FACULTY OF SCIENCES

DEPARTMENT OF ANALYTICAL CHEMISTRY
X-RAY MICROSPECTROSCOPY AND IMAGING (XMI)

DEVELOPMENT OF X-RAY ABSORPTION AND FLUORESCENCE MICROSPECTROSCOPIC IMAGING USING NOVEL DETECTION SYSTEMS

Pieter Tack
Student number: 00602412

Supervisor(s): Prof. Dr. Laszlo Vincze, Dr. Wim Bras, Dr. Bart Vekemans

A dissertation submitted to Ghent University in partial fulfilment of the requirements for the degree of Doctor of Science: Chemistry

Academic year: 2016 - 2017

GHENT UNIVERSITY

"I'm a scientist and I know what constitutes proof. But the reason I call myself by my childhood name is to remind myself that a scientist must also be absolutely like a child. If he sees a thing, he must say that he sees it, whether it was what he thought he was going to see or not. See first, think later, then test. But always see first. Otherwise you will only see what you were expecting. Most scientists forget that."

- Douglas Adams in So Long, and Thanks for All the Fish.

Acknowledgment

It is a rare feature when a person has nobody to thank after four years of scientific research, and I certainly am not one of those people. During my PhD studies I have received input, ideas, comfort and needed distractions from many people. It is thanks to them I have finally been able to write this manuscript, and a special thanks to some people is due.

During my research I could always ask my supervisor, Prof. Dr. Laszlo Vincze, for help and inspiration. Never did I leave his office without having gained new ideas or confirmation that the road I was travelling was the right one. It was my great pleasure to be your PhD student and I hope to continue our collaboration for a long time still. A great thanks also goes out to my co-supervisor in Grenoble, Dr. Wim Bras. It is always a great pleasure to talk to you during the sparse moments of reduced activity during the many beamtimes at DUBBLE. I would also like to thank you for your continued efforts to provide new and interesting samples to investigate. Investigating new methodologies is very interesting work, but it quickly loses its shine without appropriate samples. I would also like to thank Dr. Bart Vekemans for his (co)supervision. Our trips to Grenoble and Hamburg are well remembered. Thanks to your extensive music collection that guided us on our travels we now know to "Blame the Machines", a song that was particularly appropriate during that first confocal experiment in the starting days of my PhD.

I would also like to thank the Agency for Innovation by Science and Technology (IWT) for their financial support during my PhD. Also the FWO and NWO are acknowledged for their support of the DUBBLE beamline. This joint Dutch-Belgian collaboration opens the door to and facilitates synchrotron radiation research for the Dutch-Belgian community, the importance of which is easily displayed by the sheer amount of publications released annually containing DUBBLE data.

Days at the office or during beamtime experiments would have been a lot more dull without my fellow group members. Björn, we haven't had the opportunity to share a beamtime yet but I always like our kitchen and hallway talks. I admire your ability to keep digging a data set to extract the very last grain of information, far beyond the point where most would give up. Jan, we go a long way back as it was you who guided me during my Master's thesis, after which we became colleagues. You also, by accident, got me to know the beautiful town of Schopsdorf (Germany), which will always have a special place in our heart. Lien, I knew you since before I joined the XMI group and as such I already knew you were a great person. This was confirmed again when we decided to 'conquer' the third floor, or as we called it 'the cool floor'. The first few months after you left were certainly the loneliest months of my PhD, displaying how much we always supported and advised each other. Eva, having started our chemistry studies together I arrived in the XMI group a year later. You were always an example of well-planned and organised work. I loved our chats about our hobbies, research and, sometimes, the students we taught during the radiochemistry practicals. Stephen, you're my DUBBLE-buddy and it is/was always a pleasure to work together during our various beamtimes, even when our perfectly synchronised teamwork was the only thing going for us. May your pitch ever be perfect and your books abundantly marked! Brecht, it was great fun to work together and share jokes over lunch. I cannot count the amount of times we just glanced at each other during lunch conversations, realising we were both thinking exactly the same, wondering who of us both would voice the thought. Ella, although you only joined our group recently, I had the honour of guiding you last year. It was my great pleasure to teach you as much as possible, made even more pleasurable by your eternal enthusiastic attitude. You have a long way ahead of you, but from what I've seen up to now I'm sure you will be great. Glob, Glob. Eddy, I admire your choice and courage to become a PhD student after your career. I am grateful for the fresh breath of samples you brought to our research group and I hope there will be many more to come.

In addition to my fellow group members, I would also like to thank my other Department of Analytical Chemistry of Ghent University colleagues. In particular, I would like to thank the people who joined me for lunch in the kitchen of S12 and were not afraid to discuss science and daily matters alike, along with a healthy dose of humour. Karen, Lana, Veerle, Tine, Philip, Sylvia, Jolien, Steven, Debbie, Stijn, Rosie, Jorge, Peter, Yulia, Balázs, Thibaut, Jacotte: thank you for entertaining me during lunch, it was often a welcome diversion from work. A special thanks also goes out to the members of the Ramspec

group, who I often supported with IDL programming or AXIL trouble shooting. Sylvia, Jolien, Possum, Alessia, Anastasia, Debbie: it was always my pleasure to figure out and solve the issues with the programs as they fuelled my passion for programming. Pieter-Jan, you I thank for our interesting discussions on XEOL and XAS and how they relate to each other. Additionally, it was a great pleasure to teach radiochemistry practicals with you. I would also like to thank Davy for his great craftsmanship in making last-minute orders in the workshop. Without your talents I'm sure many experiments would have been a lot more challenging.

Thanks is also in order for my SLcam friends who have shared important roads of the Ghent SLcam history. I would like to thank Oliver for his meticulous work on the SLcam software package and unrelenting efforts in error handling whenever we had a new and inexplicable bug. I am also grateful for Matthieu's help with the SLcam, particularly in the initial years of my PhD research when the SLcam suffered from many child diseases. We have been frustrated together many times, but together we have raised the SLcam to the nicely behaving camera it is today.

Most of my synchrotron radiation experiments were performed at the DUBBLE beamline at the ESRF in Grenoble, France. I would like to thank the DUBBLE staff for their efforts in supporting our experiments during my frequent visits. I have spent quite some time at your beamline, and through it all I always felt welcome and appreciated in what is best described as the DUBBLE family. Dip, you were usually our local contact and I am very grateful for arranging all the administration and trying to fulfil our heart's desire. Alessandro, it was always fun to talk to you and I learned a lot with respect to XAS simulation from you. Dirk, your great skills in implementing detectors and motor systems in SPEC, making sure our experiments could operate as precise and automated as possible were a huge help in all our experiments. Florian, as the power house of DUBBLE I always admired the strength and eternal kindness you could muster to lift and replace heavy objects to make place for our confocal setup.

Years of methodological research may be all in vain if one lacks interesting samples to apply the methods to. Additionally, even though my research was mainly focussed on full-field XAS experiments, I was also involved in many 'side projects'. For these reasons I would like to thank my colleagues from the Inorganic and Physical Chemistry department, in particular Karen, Hannes, Irena, Yesid and Katrien, for their interest in XAS spectroscopy. It was always a welcome change to perform experiments in which the applied methodology posed

the easiest part of the experiment, with the data processing and information extraction being the most challenging and fun part. I would also like to thank Prof. Van Ranst for supplying us with interesting samples, seemingly ideal for the methodologies I applied. Additionally, I would like to thank Prof. Lichtenegger and Tilman for their interest in using the SLcam for white-beam ED-XRD experiments. I remain convinced that this technique is one of the most rewarding for the SLcam, making use of and challenging all its characteristics simultaneously. Furthermore, I have rarely joined an experiment that was as well prepared as those prepared by Tilman. It was always a great pleasure and even exciting to find out which difficult challenges you imposed on yourself and your environment this time.

Without a break now and then, it is difficult to keep going. Fortunately, I could always count on friends and family to provide the necessary distractions. Christophe, Dries, Michiel, Sven: we started our studies together and have tried to keep in touch every since. Even though we haven't seen each other as frequent as we would like, your friendship has always been a great support to me. Jonas, in our studies and after we have shared a great deal of things. I hope we can keep on sharing experiences through life. Dieter, Jeroen, Nicolai: we have been friends since a long time and I'm certain we will be for a long time to come. Our regular get-togheters were always fun to attend and it was great to notice we always supported each other in whatever plans we had. Niels, Peter: although I knew the card game Magic the Gathering well before I knew you, it is because of your friendship that I continue playing it. I have often joined you for a few games after a stressful working day, and I always went home completely relieved of stress, for which I am very grateful.

At last, and definitely not least, I would like to thank my partner in life, Mieke. It seems like a very long time ago, but we started living together, as a family, at the start of our PhD. Since that time we have become husband and wife, celebrating our mutual love with the rest of the world. Now, recently, you gifted me with the birth of our wonderful baby girl, Febe. Of course, we have also had our differences and rough patches, and I'm sure there will be more to come. However, I know that we will face them together, eventually turning them into loving memories, and that makes it worthwhile. Thank you for being you, and wanting to be with me. Always.

Yours truly,

Ghent, March 2017
Pieter Tack

Table of Contents

Chapter 1

Introduction

This thesis revolves around X-ray absorption and fluorescence spectroscopy (XAS and XRF), non-destructive analytical techniques that are regularly applied in the fields of chemistry, biology, geology, archeometry, engineering and more. XRF spectroscopy provides information on the elemental composition of a sample: the sample is illuminated with X-ray photons, which lead to the production of secondary characteristic radiation from the sample. This radiation contains qualitative and quantitative information as the energy of the emitted radiation is characteristic for the emitting element, whereas the amount of photons emitted by a sample volume correlates to the concentration of these elements in the sample. XAS in turn allows for the investigation of the local chemical structure of an element of interest by monitoring the X-ray photon absorption when tuning the primary X-ray photon energy over the absorption edge of a given element. As such, information on the oxidation state of the probed element is derived based on the energy position of the absorption edge, but also chemical compounds and local structures can be determined based on the fluctuations of the X-ray photon absorption with energy. The focus of this work is mainly on the application of XAS following several challenging methodologies towards 2D and 3D chemical structure analysis on a microscopic level. Several methodologies, i.e. bulk mode, (con)focal and full-field XAS, are explained and presented by means of typical applications for which the discussed methodology is generally and ideal choice. The aim is to guide users to the appropriate XAS methodology based on the specific research question as imposed by the sample of interest, as well as present the capabilities of state-of-the-art full-field methodologies.

This work follows a trend from most general to more specialised and advanced methodologies. Chapter 2 provides a theoretical background on XRF and XAS required to understand the remainder of this work. The physical processes involved in these analytical techniques are explained, followed by an overview in Chapter 3 of common instrumentation used when applying these techniques.

Chapter 4 discusses bulk XAS in which a sample is illuminated with a broad X-ray beam, providing limited spatially resolved information. Nevertheless, this approach is widely used due to the quality and speed of data acquisition. Two applications are discussed, providing an insight in the usefulness of this method.

In Chapter 5 the use of a micro-focus XRF/XAS setup, specifically developed for the BM26A (DUBBLE) beam line at the European Synchrotron Radiation Facility (ESRF, Grenoble, France) is discussed. Using this setup information can be acquired from a micrometre sized sample area, allowing for the investigation of heterogeneous samples. By moving the sample through the X-ray beam, 2D images can be constructed displaying the elemental and local chemical structure variations in a sample.

In order to obtain direct 3D resolved information from a sample volume one can make use of a confocal approach. The modification of the BM26A focal setup to a confocal one is discussed in Chapter 6, along with several applications displaying its use. The implementation of this (con)focal setup at the BM26A beamline presents the first milestone of transforming the previously macro-beamline to a microscopic beamline.

Chapter 7 in turn discusses the application of a full-field approach towards XAS, using the SLcam: a "colour X-ray camera" designed to detect X-rays in a spatially resolved manner. By illuminating a sample with a broad beam and monitoring the emitted radiation with the SLcam, nearly 70 thousand spectra, arranged in a square of 264 pixels wide, are acquired at once with a microscopic spatial resolution. This device means a significant increase in measurement speed for both 2D and 3D XRF and XAS applications. The implementation of full-field XAS experiments proves a significant improvement in spatially and depth resolved XAS data acquisition in previously infeasible measurement times, paving the way to more specific and performing XAS analyses.

Finally, all methods are compared in Chapter 8, along with a number of conclusions and future prospects.

Chapter 2

X-ray Fluorescence and Absorption Spectroscopy: basic principles

2.1 Photon-matter Interactions

2.1.1 X-rays

Discovered by Wilhelm C. Röntgen in 1895, X-rays are, based on their wave characteristics, a type of short wavelength electromagnetic (EM) radiation with a wavelength ranging from 0.01 nm to 10 nm.[1] The discovery of this, invisible to the human eye, radiation led to Röntgen being awarded the first Nobel prize of physics in 1901.[2] Based on its wavelength, X-rays are classified as a part of the electromagnetic radiation spectrum, with a wavelength range spanning from the UV to gamma ray radiation (Figure 2.1).[3] Additionally, X-rays can be distinguished from gamma rays as X-rays are emitted by electronic interactions whereas gamma rays are originating from nuclear transitions.

The energy of electromagnetic radiation can be determined based on their wavelength following Equation 2.1, or in the practical case of X-rays using the approximated Equation 2.2.[5, 6] In these equations E represents the energy, h Planck's constant ($6.626{\cdot}10^{-34}\,\mathrm{m^2kg/s}$), ν the frequency, c the light velocity and λ the photon wavelength.

$$E = h\nu = \frac{hc}{\lambda} \tag{2.1}$$

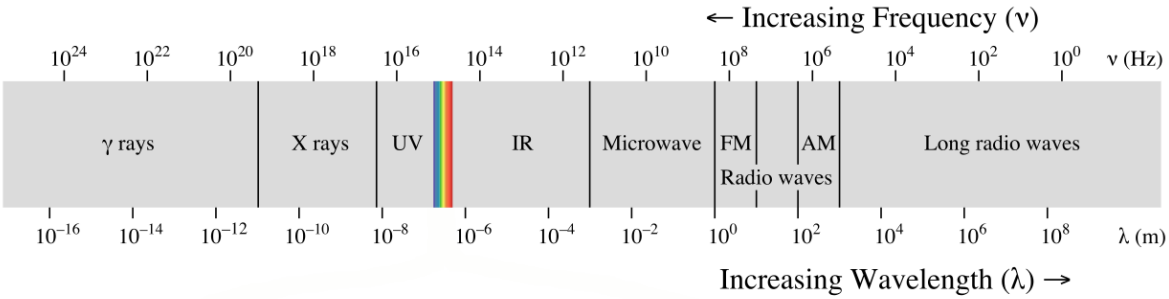

Figure 2.1: Wavelength scale of the electromagnetic spectrum. Figure adapted from.[4]

$$E[\text{keV}] = \frac{12.39}{\lambda[\text{Å}]} \tag{2.2}$$

As EM radiation in general, X-rays are characterised by the wave-particle duality, displaying properties of both waves and particles.[7] Interesting X-ray properties, resulting in their use in multiple analytical techniques, are their high penetrating character, their propagation in straight lines between interactions combined with the ability to interact with matter on the atomic scale.

In the following sections, more information is provided about these interactions and the information that can be extracted from them.

2.1.2 Photoelectric Effect

When an X-ray photon interacting with an atom has an energy greater than the electron binding energy, it is capable of ejecting the electron from the atom to the electronic continuum. In the photoelectric effect, the energy of the X-ray photon is fully transferred to the electron, aptly named the photoelectron and the photon is absorbed. The photoelectron will have en energy E_{e^-} equal to $E_0 - E_b$ with E_0 the energy of the incident X-ray photon and E_b the binding energy of the ejected electron.

The photoelectric cross-section τ is correlated with the X-ray photon E_0 energy and the atomic number Z of the interacting atom (Equation 2.3).[8] A schematic representation of the photoelectric effect is displayed in Figure 2.2, the photoelectric cross-section for Cu as a function X-ray photon energy is shown in Figure 2.5.

$$\tau \sim \frac{Z^4}{E_0^3} \tag{2.3}$$

2.1.3 X-ray fluorescence

As a result of the photoelectric effect, the interacting atom is in an excited state with a shell vacancy, e.g. an inner shell vacancy of the K shell. This vacancy is filled by the transition of a higher energy shell electron to the shell vacancy. During this process the excess energy can be emitted in the form of an X-ray photon, corresponding to the phenomenon of X-ray fluorescence, a process which competes with Auger electron emission (Figure 2.2). The resulting X-ray photon, the fluorescent photon, has an energy value equal to the difference in binding energy between the two shells involved. It was Moseley who discovered in 1913 that the wavelength/frequency of this fluorescence radiation is unique for a given element (Figure 2.3).[10] This is easily understood as the electronic orbital energies are dependent on the charge and mass of the nucleus, as well as the amount of electrons surrounding the nucleus; as such also the difference between such energy values will be unique for a given element.

Depending on the shell the electron originates from to fill the lower level electron shell vacancy, the fluorescent photon will have a different energy. To differentiate between these photons with differing energies, usually the Siegbahn notation is used (Figure 2.3). In this notation, the first letter corresponds to the shell on which the electron vacancy was present (K,L,M) and the following Greek letter and its subscript give information on the intensity

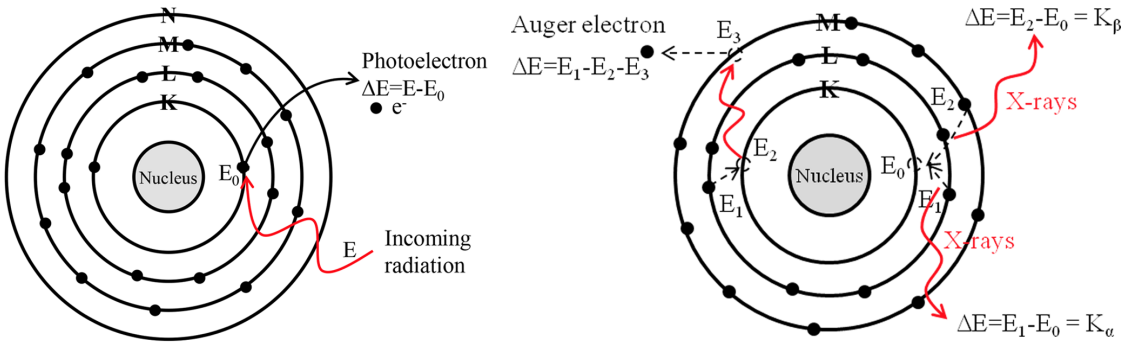

Figure 2.2: Schematic representations of the photoelectric effect (left) and X-ray fluorescence (right). The Auger electron generation principle is also displayed. Figure adapted from.[9]

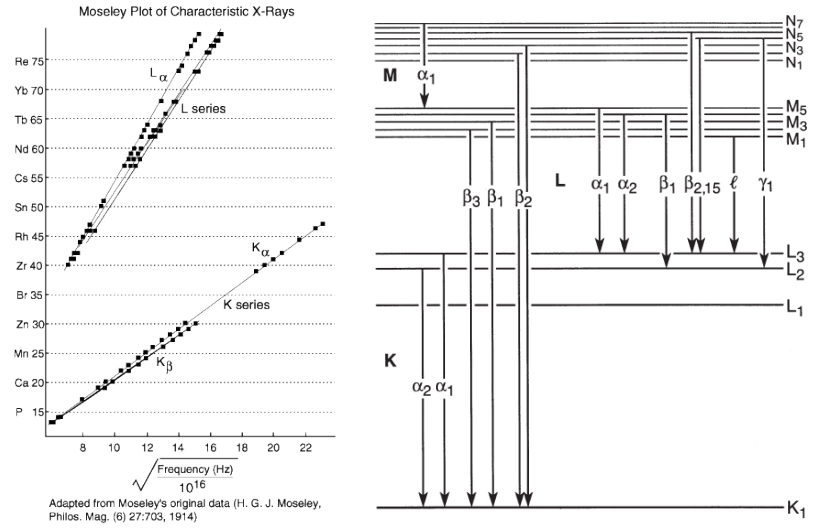

Figure 2.3: Left: X-ray fluorescence line frequencies ($E = h\nu$) as a function of atomic number, adapted from.[11] Right: Siegbahn notations for the different allowed electronic transitions, adapted from xrdb.[5] IUPAC notations are defined by the initial and final X-ray level, separated by a hyphen (e.g. K-L_3 for $K_{\alpha 1}$).[12]

(probability) of a given transition.

After the fluorescent effect occurred, and a higher shell electron filled the inner shell electron vacancy created during the photoelectric effect, a new electron vacancy is present in the higher energy shell. This state allows for a subsequent electron transition from an even higher electronic shell. This process continues in a cascade-like manner, with a probability of X-ray photon emission at each step.[13]

The probability that an X-ray photon is emitted as a result of the electron transition is called the fluorescent yield ω. A second process possible after the photoelectric effect is the radiationless Auger electron emission.[14, 15] In this interaction, first the electron vacancy is filled by a higher shell electron, and the excess in energy results in the emission of a less tightly bound electron, the Auger electron (Figure 2.2). This process is the dominant one for low Z atoms, rendering X-ray fluorescence spectroscopy less sensitive for these elements.[16] A special case of Auger electron emission consists in the Coster-Kronig transition in which the electron vacancy is filled by an electron from a higher subshell of the same shell, e.g. $L_3 \rightarrow L_1$.

2.1.4 Rayleigh Scattering

When X-rays are scattered elastically by a free electron, the phenomenon is commonly referred to as Thomson scattering which is a type of elastic/coherent scattering.[1] Rayleigh scattering is the same process, in which the scattering electron is bound to a nucleus. Upon elastically interacting with the atomic shell, acting as a dipole, the X-ray photon is emitted in a different direction of propagation without energy loss (Figure 2.4).

The Rayleigh scatter probability, which is linearly proportional to the Rayleigh scattering cross-section σ_R, is dependent on the X-ray photon energy E and the atomic number Z of the scattering atom. In general, σ_R is the spherical integral of the Rayleigh differential scattering cross-section $\frac{d\sigma_R}{d\Omega(\vartheta,\phi,E)}$ over the full solid angle 4π with the scattering angle ϑ and the azimuthal angle ϕ. The differential scattering cross-section $\frac{d\sigma_R}{d\Omega(\theta,\phi,E)}$ characterizes the angular distribution of the scattered photons at a given X-ray energy E and atomic number Z (Equation 2.4). This equation is valid in a spherical coordinate system defined by the direction of propagation and the orientation of electric and magnetic field vectors of the incident photons, where p represents the degree of polarization, r_e the classical electron radius, and $F(x, Z)$, with $x = sin(\vartheta/2)/\lambda$, refers to the atomic form factor, describing the influence of the (bound) atomic electron cloud as a whole as opposed to that of a single electron.[3, 17] Rayleigh scattering is the most important scattering interaction mechanism in case of heavier atoms and low energy X-rays (Figure 2.5).

$$\frac{d\sigma_R}{d\Omega}(\vartheta, \phi, E) = \frac{r_e^2}{2}[2 - sin^2\vartheta \times (1 - p + 2pcos^2\phi)]F^2(x, Z) \tag{2.4}$$

2.1.5 Compton Scattering

Compton, or incoherent scattering, is an inelastic process. As such, when an X-ray interacts with an electron, typically a loosely bound valence electron, part of the X-ray energy is transferred to the electron which is subsequently ejected from the atom. A schematic of this process is shown in Figure 2.4.

The energy of the scattered X-ray E_{scat} is related to the scattering angle ϑ, following Equation 2.5.[3] $m_e c^2$ represents the rest mass energy of an electron which is approximately 511 keV. This equation shows that larger scattering angles result in larger energy shifts of

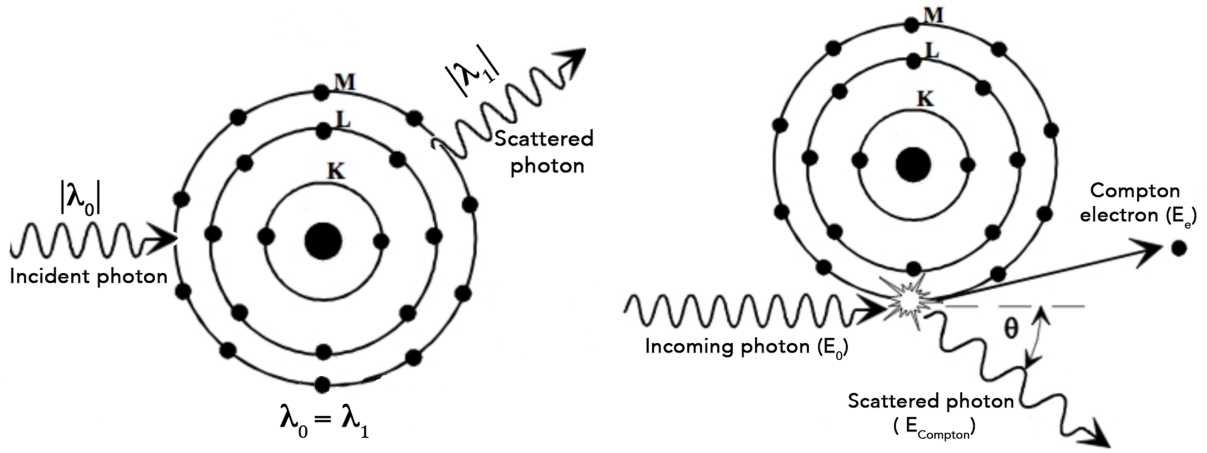

Figure 2.4: Schematic representation of elastic Rayleigh (left) and inelastic Compton scattering (right). Figures adapted from Wikipedia: Basic Physics of Digital Radiography.

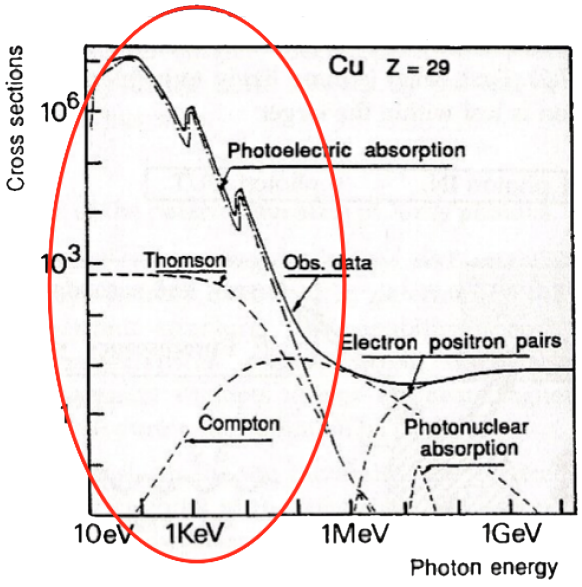

Figure 2.5: Cross sections of X-ray interactions on Cu as a function of energy. Figure adapted from.[5] The area marked in red represents the X-ray region.

the scattered photon (E_{scat}).

$$E_{scat} = \frac{E_0}{1 + \frac{E_0}{m_e c^2}(1 - cos\vartheta)} \tag{2.5}$$

As is the case with Rayleigh scattering, the probability of Compton scattering is characterized by the Compton scattering cross-section, σ_C, which is a function of the X-ray energy and the atomic number Z of the scattering atom. Analogous with the Rayleigh scattering, the Compton scattering cross-section is the spherical integral of the differential scattering cross section $\frac{d\sigma_C}{d\Omega}(\vartheta, \phi, E_{scat})$ over 4π. The differential scattering cross-section for Compton scattering is given by Equation 2.6, being the function of the scattering angle ϑ and the azimuthal angle ϕ.[18] $S(x, Z)$ is the incoherent scattering function, which is a function of the atomic number Z, the energy E_{scat} and the scatter angle ϑ. As can be derived from these equations, the Compton scattering probability is minimal for a scatter angle ϑ of 90° in the plane of linear polarisation.

$$\begin{aligned} \frac{d\sigma_C}{d\Omega}(\vartheta, \phi, E_{scat}) &= \frac{r_e^2}{2}\left(\frac{E_{scat}}{E_0}\right)^2 \\ \left[\frac{E_{scat}}{E_0} + \frac{E_0}{E_{scat}} - sin^2\vartheta \times (1 - p + 2pcos^2\phi)\right] S(x, Z) \end{aligned} \tag{2.6}$$

$$x(\text{Å}) = sin(\vartheta/2)\frac{E_0(\text{keV})}{12.39}$$

Compton scattering is relatively more probable to occur for high energy X-rays (Figure 2.5) and light elements.[5, 19] Based on the Compton peak intensity, information can be obtained on the irradiated sample mass. Additionally, the ratio between Rayleigh and Compton peak intensity can give one information on the mean atomic number of the sample, which is useful in case the matrix elements do not emit detectable XRF lines (so-called 'dark matrix'). E.g. when the matrix consists of low Z elements.

2.2 X-ray Fluorescence Spectroscopy

In X-ray fluorescence (XRF) spectroscopy the elemental constituents of a sample are determined in a qualitative or quantitative way.[1, 3] To do so, a sample is illuminated by X-rays,

resulting in, among others, the emission of characteristic fluorescent photons (Section 2.1). In case of energy dispersive XRF, an energy dispersive detector, typically positioned perpendicular to the primary X-ray beam, under an angle of 45 ° with the sample surface, detects the intensity of the emitted X-ray photons as a function of their energy. This geometrical setup is often preferred as under these conditions X-ray scattering is reduced to a minimum, and almost no risk occurs of shielding (part of) the detector by the sample from fluorescence radiation.

By scanning a sample through an X-ray (micro/nano) beam, or illuminating a given sample area and monitor the emission using a position sensitive energy dispersive (ED) detector,[20–27] an elemental overview map of the sample can be obtained. Additionally, 3D elemental distribution information can be obtained.[28–31]

Examples of these approaches, for X-ray absorption and fluorescence spectroscopy, are presented in the following chapters.

2.2.1 Spectral Evaluation

In order to extract information from an XRF spectroscopy experiment, some form of data processing has to be performed. The most crucial step in this process is the interpretation of the measured XRF spectrum.

As discussed above, an energy-dispersive XRF spectrum consists of peaks with certain intensities as a function of energy. As each element emits fluorescent X-rays with characteristic energies, the peaks can be related to their respective element by comparing the energies with a database. An example of a database containing all fluorescent K, L and M line energies for elements up to U in atomic number, is XRaylib.[19]

In a number of cases, a spectral overlap can occur. For instance, the Fe-K_β line (7.058 keV) overlaps with the Co-K_α line (6.920 keV) due to the limited energy resolution of most ED detectors. These occurrences can be resolved by performing an iterative least squares fitting, taking into account the matrix dependent K_α and K_β relative intensities. The same is true for L and M lines. Next to resolving peak overlap, the main purpose of spectral evaluation is the determination of net peak intensities by fitting and subtracting the spectral background from the detected XRF spectrum. Another important aspect of spectral evaluation is related to the determination of peak intensities corresponding to

detector artefacts.

A detector artefact that occurs is represented by escape peaks. Escape peaks correspond to the energy loss from the true/full-energy peaks do to fluorescent photons of the detector material escaping from the active detection volume. These peaks can be recognized as they are registered as photons with a total energy equal to the characteristic energy of the original photon, minus the characteristic energy of the XRF photons emitted by the detector material (e.g. Si-K_α : 1.740 keV).

The other important class of detector artefacts is represented by the so-called sum peaks. These peaks appear in a spectrum when two photons are absorbed by the active detector crystal in a time frame too short for the detector to register them as two separate photons. The result is that the detector registers a single photon, with energy equal to the sum of energies of the two photons. The occurrence of sum peaks can be prevented by reducing the detector peaking time or reducing the flux on the detector, e.g. by implementing filters or decreasing the detector solid angle.

Once all peaks are identified, their respective areas have to be determined by the aforementioned fitting process. To do so, software packages exist such as AXIL and PyMCA.[32, 33] These programs perform a background subtraction, followed by integration of the peaks using Gaussian-like functions. Once the intensity contribution of each element is known, further steps can be made towards quantification of the data.

2.2.2 XRF Quantification

As the intensity of the emitted X-ray fluorescence is a function of the analyte concentration, XRF spectroscopy is an ideal tool to obtain quantitative results for the detectable elements (i.e. Z≥14 in air or Z≥5 in vacuum, making use of thin polymer windows on the detector side.).

The most straightforward quantification method relies on comparing the intensity $I_{RM,i}$ of an element measured in a reference material (RM) with known concentration $c_{RM,i}$, to the intensity $I_{u,i}$ of the same element in the sample with unknown concentration $c_{u,i}$:

$$c_{u,i} = \frac{I_{u,i}}{I_{RM,i}} \cdot c_{RM,i} \tag{2.7}$$

A correction for illuminated sample mass can be made by normalizing each element intensity by the Compton signal of the respective measurement. However, this equation only gives good results when the matrices of the RM and investigated sample are matrix matched. Otherwise, errors due to self-absorption/matrix effects will occur.

To resolve this issue, the Fundamental Parameter Method (FPM) was proposed by Sherman, making use of the theoretical relationship between net line intensities and elemental concentrations.[34]

Assume a homogeneous sample with thickness T, density ρ, composed of n elements with weight fraction w_i ($\sum w_i = 1$), irradiated by a parallel, monochromatic X-ray beam with energy E_0, intensity I_0 and incidence angle with respect to the sample surface α. Fluorescent X-rays are detected by a detector with active area A_{DET} at distance D, oriented under constant take-off angle β with respect to the sample surface Figure 2.6.

Combining the Lambert-Beer equation with the appropriate X-ray interaction/emission probabilities, the net fluorescent intensity of element i in the interval $[x, x + dx]$ can be derived:

$$\begin{aligned} dI^*_{i,K_\alpha} &= I_0 e^{-\mu_0 \rho x} \mu_0 \rho dx \frac{w_i \tau_{i,K}}{\mu_0} p_{K_\alpha} \omega_K \\ &= I_0 e^{-\mu_0 \rho x} w_i Q_{i,K_\alpha} \rho dx \end{aligned} \tag{2.8}$$

with:

- μ_0: the mass attenuation coefficient for the sample of the primary X-ray beam (E_0). $\mu_0 = \sum w_j \mu_{j,E_0}$;
- $\tau_{i,K}$: K-shell partial photoionisation cross section for element i;
- p_{K_α}: transition probability for K_α emission;
- ω_K: fluorescence yield of K shell emission;
- $Q_{i,K_\alpha} = \tau_{i,K} p_{K_\alpha} \omega_K$: XRF production cross section.

Similarly, the detected K_α intensity of element i, generated in depth $[z, dz]$ is:

$$\begin{aligned} dI_{i,K_\alpha} &= dI^*_{i,K_\alpha} \frac{\Omega_{DET}}{4\pi} e^{-\mu_1 \rho y} \\ &= I_0 G w_i Q_{i,K_\alpha} e^{-\chi \rho z} \rho dz \end{aligned} \tag{2.9}$$

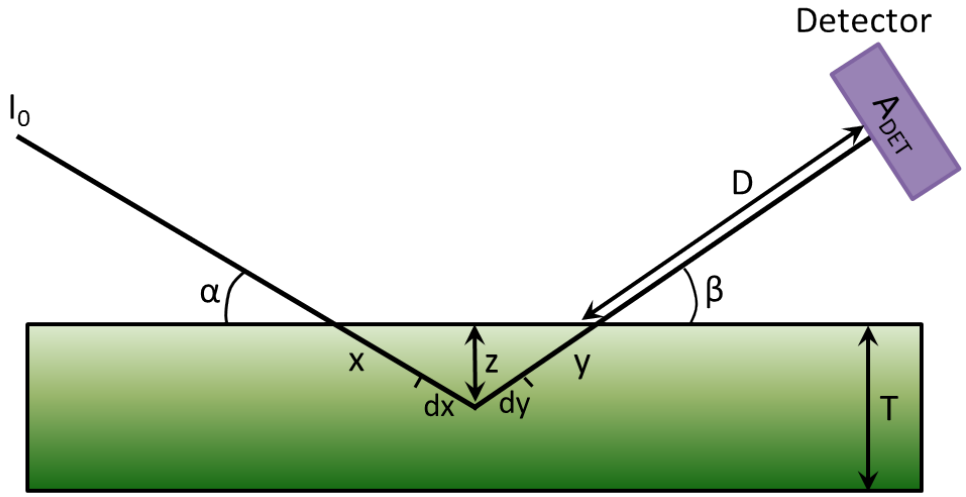

Figure 2.6: Schematic of the experimental conditions included in the fundamental parameter equation: a homogeneous sample with thickness T is illuminated by a monochromatic X-ray beam with incident angle α and intensity I_0. The fluorescent radiation with take-off angle β is detected by a detector at distance D and detector area A_{DET}.

with:

- $\chi = \frac{\mu_0}{sin\alpha} + \frac{\mu_1}{sin\beta}$;
- μ_1: the attentuation coefficient of the material for energy E_{i,K_α};
- Ω_{DET}: the detector solid angle;
- $G = \frac{\Omega_{DET}}{4\pi sin\alpha} \approx \frac{A_{DET}}{4\pi D^2 sin\alpha}$: the geometry factor.

By integrating over the sample thickness T, the final form of the FPM is obtained:

$$\begin{aligned} I_{i,K_\alpha} &= I_0 G w_i Q_{i,K_\alpha} \rho T \left(\frac{1 - e^{-\chi\rho T}}{\chi\rho T} \right) \\ &= I_0 G w_i Q_{i,K_\alpha} \rho T A_{corr} \end{aligned} \tag{2.10}$$

With A_{corr} the absorption correction factor, representing the absorption caused by the sample matrix. In the infinitesimally thin sample approximation, this parameter approximates to 1.

The main disadvantage of this first order approach is that it neglects the effect of secondary interactions. Although these effects, as well as non-homogeneous and non-flat samples and

non-perfect detectors, can be accounted for in variations on this equation, the resulting equations rapidly become very complex.

An alternative to this quantitative method is Monte Carlo based quantification for XRF spectroscopy.[13, 35] In this approach, the path of a photon through a sample up to the point of detection is simulated as a sequence of interactions with given probabilities. By applying a random number generator and simulating a sufficiently large amount of photons, a theoretical XRF spectrum can be built for a given sample and measurement geometry. By iteratively comparing the theoretical XRF spectrum to the experimentally measured spectrum, the sample composition can be determined, taking into account secondary effects and the detector response function.

2.3 X-ray Absorption Spectroscopy

X-ray absorption spectroscopy (XAS), or X-ray absorption fine structure spectroscopy (XAFS), allows the investigation of the local chemical structure of an element of investigation.[36, 37] Unlike X-ray diffraction (XRD), samples are not required to be crystalline for XAFS experiments.

Figure 2.7 shows the theoretical attenuation coefficient for different elements as a function of X-ray energy. By scanning the X-ray beam energy and measuring the X-ray attenuation at each step, the elemental constituents of a sample can be determined based on the position of their edges - sharp increases in attenuation as a function of energy.

The X-ray attenuation can be measured in two ways: transmission and emission mode.[38] In transmission mode the X-ray flux is measured before (I_0) and after the sample (I_t), making use of Equation 2.11 as derived from Lambert-Beer's law. In emission mode, two methods can be distinguished: measuring of the attenuation through detection of XRF emission, or through detection of photoelectrons. In both cases, the attenuation coefficient (mainly governed by the photoelectric cross section) is proportional to the emitted intensity I_f following Equation 2.12.

The main advantage of transmission mode measurements is the improved signal statistics, i.e. a higher count rate can be measured. However, in this method samples are limited in terms of thickness and concentration as too thick samples will absorb all X-rays, whereas in too low concentrated samples barely any change in beam flux below and above the edge

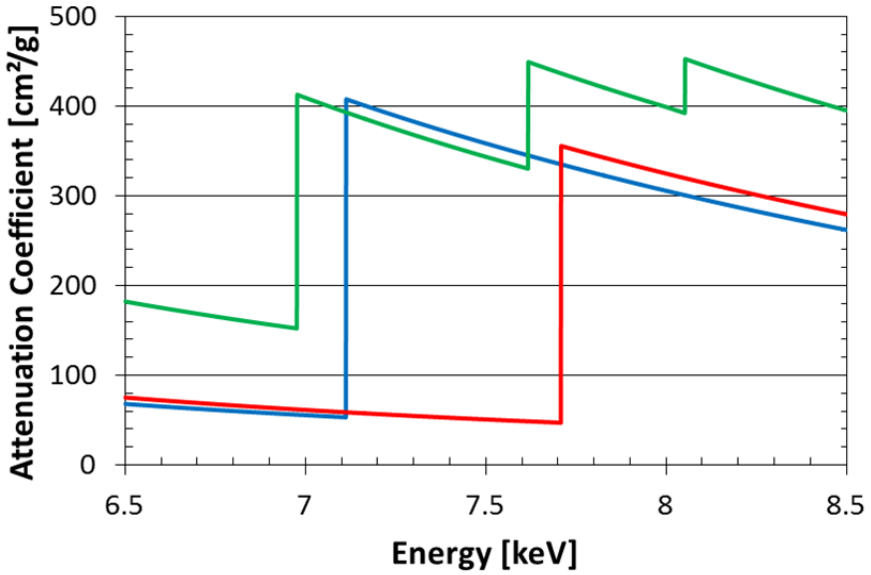

Figure 2.7: Theoretical attenuation coefficient as a function of X-ray energy for Fe (blue), Co (red) and Eu (green). Values obtained from XRayLib.[19]

energy of a given element of interest will be detected. Under these boundary conditions, emission mode experiments provide an elegant solution, despite the intrinsically longer measurement times due to the poorer counting statistics.

$$\mu d = ln\left(\frac{I_0}{I_t}\right) \tag{2.11}$$

$$\mu \propto \frac{I_f}{I_0} \tag{2.12}$$

When an atom is surrounded by other atoms, additional fluctuations in attenuation will appear close to the edge (X-ray absorption near-edge structure, XANES) or further away from the edge (extended X-ray absorption fine structure, EXAFS) due to multiple scattering of the photoelectron wave and various electronic transitions. These fluctuations are characteristic for a given compound and are treated differently depending on the energy region (XANES or EXAFS) during data treatment.

2.3.1 X-ray Absorption Near Edge Structure Spectroscopy

The XANES region is arbitrarily defined as the part of the XAS spectrum up to 30 eV beyond the main edge energy E_0 and provides information on the local chemical structure (Figure 2.8).[39] As in this low energy region beyond E_0 the core-hole lifetime of the probed atom is significantly long, XANES contains major contributions from multiple scattering effects of the photoelectron wave, resulting in chemical information from a larger volume than compared to EXAFS.[40]

Besides the determination of the local chemical structure, XANES is often applied to obtain specific information on the oxidation state and coordination geometry of the investigated element.[41–43] The oxidation state determination is easily understood as the main edge position corresponds to the energy required to emit a bound electron to an unbound state. For an atom with different oxidation state, the attraction of its electrons will be higher (in case of higher oxidation state) or lower (in case of lower oxidation state). As such, the edge position will also typically shift with increasing oxidation state. The coordination geometry can be recognized in the XANES spectrum by the pre-edge peak intensity (Figure 2.8, 5470 eV). This peak corresponds to a quantum chemically forbidden transition, e.g. 1s→3d in the case of V K-edge XANES, for centro-symmetric coordination geometries (e.g. octahedral). This forbidden transition becomes partially allowed when the structure deviates from a centro-symmetric coordination geometry, thus allowing for the presence of a pre-edge peak in the XANES spectrum. Consequently, the pre-edge peak intensity can be linked to the specific coordination number of the investigated element.[44, 45] It should be noted at this point that these trends in main edge position versus oxidation state and pre-edge peak intensity versus coordination number only work when monitoring a chemical surrounding consisting of a single type of counter-ions. For example, Fe(II)O and Fe(II)Cl_2, despite both having Fe oxidation state 2+, will have a different main edge position due to the higher electronegativity of Cl compared to O.

Typically, XANES data are compared to spectra obtained from reference compounds to recognize the presence of these compounds through a fingerprint-like method. Mixtures of compounds can be resolved this way as the measured XANES profile is a linear combination of the pure compounds' XANES, multiplied by their relative contribution to the total amount of the given element in the sample.[36]

More recently, thanks to the improvement of computing speed and better understanding

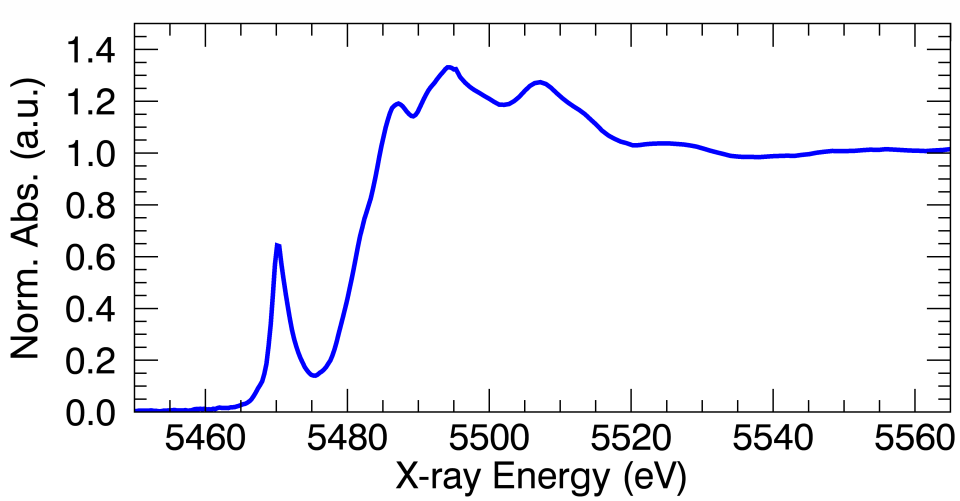

Figure 2.8: Vanadium K-edge XANES spectrum of V_2O_5 measured at the DUBBLE beamline (BM26A, Grenoble, France).

of the physical processes contributing to the XANES spectrum, more accurate *ab initio* XANES simulations can be made.[46–48] This method is very valuable to obtain information on the electronic configuration of a system, yet rapidly becomes very complicated when mixtures of different compounds are concerned. Additionally, the simulation of a single XANES spectrum easily takes 24 hours when performed on a standard computer (date of writing), rendering this approach impossible for large datasets.

2.3.2 Extended X-ray Absorption Fine Structure

The EXAFS region, arbitrarily defined as the spectral range starting at 30 eV beyond the main edge E_0 up to 1000 eV beyond E_0 (Figure 2.10), contains information on bond distances, amount and type of neighbouring atoms and the Debye-Waller factor, providing information on the standard deviation of the respective bond distances.[49–51]

The EXAFS signal is created by a scattering of the photoelectron wave, emitted by the excited atom, on nearby atoms, eventually generating constructive or destructive interference of the photoelectron wave at the excited atom's position.[52] In case of constructive interference, the probability of X-ray absorption increases with respect to the atomic absorption μ_0, whereas the opposite is true for destructive interference of the photoelectron wave. The fluctuations in X-ray absorption with respect to μ_0 are called the EXAFS function χ, which is usually expressed as a function of wavenumber k following Equation 2.13.[36]

Section 2.3.3 discusses how one obtains χ from experimental data.

$$\begin{aligned} \chi(k) =& S_0^2 \sum_i N_i \frac{f_i(k)}{kD_i^2} e^{-\frac{2D_i}{\lambda(k)}} e^{-2k^2\sigma_i^2} sin(2kD_i + \delta_i(k)) \\ k =& \frac{2\pi}{h}\sqrt{2m_e(E - E_0)} \end{aligned} \tag{2.13}$$

with:

- S_0^2: the amplitude reduction factor, denoting the amplitude reduction due to experimental conditions and intrinsic photoelectron energy losses;
- N_i: the degeneracy, amount of neighbouring scattering atoms on coordination shell i;
- $f_i(k)$: the photoelectron elastic scattering probability;
- kD_i^2: the correction factor to the EXAFS equation due to the photoelectron wave being emitted spherically instead of planar with D_i representing the half path length: the distance travelled by the scattered photoelectron wave divided by two;
- $e^{-\frac{2D_i}{\lambda(k)}}$: the mean free path correction, limiting the information to approximately 10 Å with $\lambda(k)$ the photoelectron mean free path;
- $e^{-2k^2\sigma_i^2}$: a disorder and vibration correction factor with σ_i^2 the Debye-Waller factor;
- $sin(2kD_i + \delta_i(k))$: the sinusoidal term resulting in constructive interference when $n\lambda = 2kD_i$, including a phase shift parameter $\delta_i(k)$ due to deceleration and acceleration of the photoelectron wave when leaving and entering atom potential wells.

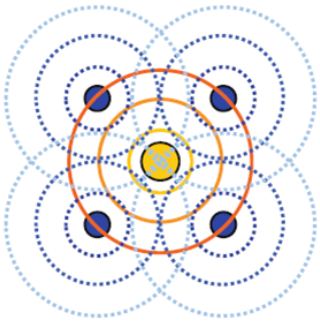

Figure 2.9: Schematic representation of the scattering of a planar photoelectron wave emitted by a central absorbing atom (yellow) on neighbouring atoms (blue).[39]

By obtaining the Fourier transform of Equation 2.13 a pseudo radial distribution function (PRDF) is obtained, in which peaks are recognized corresponding to a certain scatter path of which the position corresponds to the half path length and the amplitude is related to the degeneracy of the scatter path (Figure 2.10). In case of single scatter paths (absorber → scattering atom → absorber) the half path length is equal to the bond distance. By also interpreting multiple scatter paths (e.g. absorber → scatterer1 → scatterer2 → absorber) the local structure can be determined with greater detail due to the derivation of bond angles.

2.3.3 Spectral Evaluation

Several software packages are available to aid in the spectral evaluation of XAS data sets. Amongst those, one of the most known is the Athena software package, dedicated to XANES analysis, and the Artemis package, dedicated to EXAFS analysis.[53] Alternatively, Viper is also a widely used EXAFS analysis software tool, which was most commonly used in this work.[54] Analysis of X-ray absorption data usually starts with the normalisation of the attenuation spectrum. This is mainly done to remove concentration effects, as they have a large impact on the amplitude of the absorption spectra features.

An initial step consists of calculating the X-ray attenuation (Equation 2.12 and Equation 2.11) and removing the pre-edge background by fitting a linear or higher order curve to the pre-edge region (Figure 2.11) and subtracting this curve from the attenuation data, effectively aligning the pre-edge region with an attenuation of zero.

Subsequently, a linear trend line is fitted through the post-edge region in order to normalise the edge jump, the intensity difference between pre-edge and post-edge, to 1. This is usually done by dividing the spectrum by a scaling factor, defined as the value of the post-edge trendline at position $E_0 + 50\,\text{eV}$. Sometimes, an additional step is performed in which the post-edge region is 'flattened', during which the complete post-edge region is divided by the value of the corresponding data point of the trendline, effectively forcing the post-edge trendline to coincide with 1. This flattening procedure is mainly done in order to facilitate visual comparison of XANES data.

Once this normalisation procedure has been performed, the data is in a state ready to use it for further analysis. For XANES data this usually entails comparison to reference compounds, whereas for EXAFS data further steps are made by fitting a spline through,

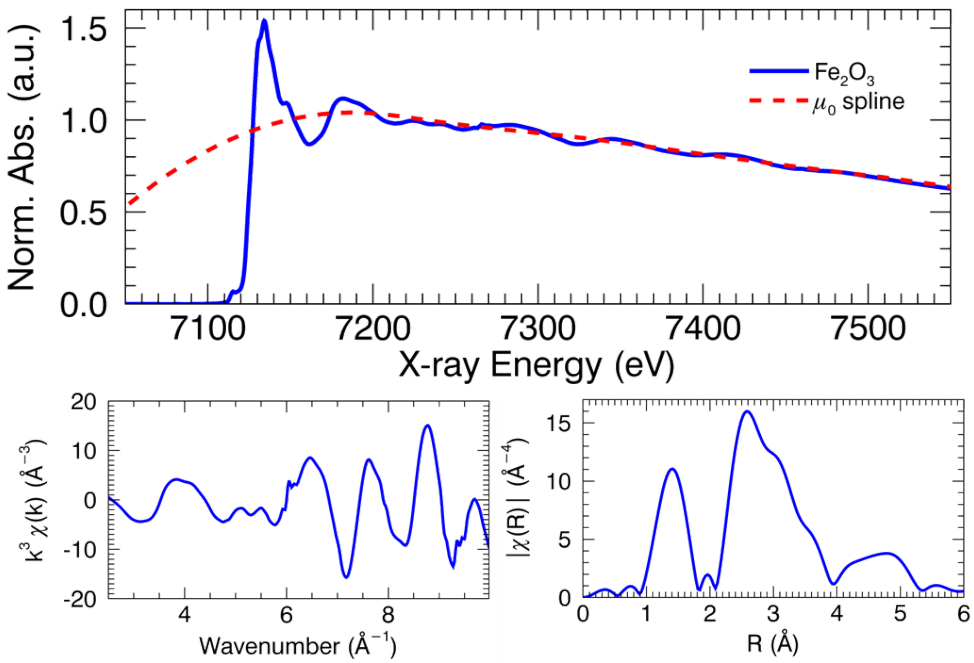

Figure 2.10: Fe K-edge EXAFS of Fe_2O_3 with corresponding μ_0 spline function to simulate the atomic absorption (top), the resulting k^3 weighed $\chi(k)$ spectrum (bottom left) and the pseudo radial distribution function resulting from the Fourier transform of $\chi(k)$ (bottom right). Data acquired at the DUBBLE beamline (BM26A, Grenoble, France).

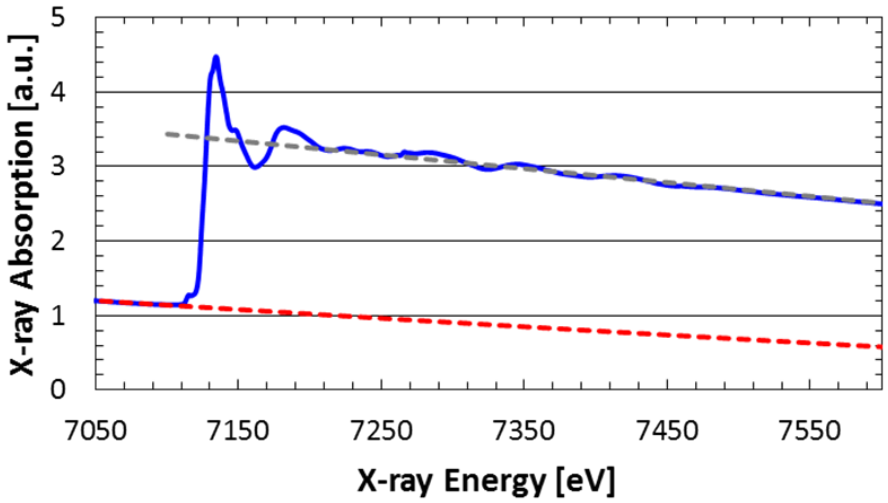

Figure 2.11: Fe K-edge EXAFS of Fe_2O_3 (blue) with pre-edge (red) and post-edge (grey) linear trendlines used during XAFS normalisation. Data acquired at the DUBBLE beamline (BM26A, Grenoble, France).

and subtracting it from, the post-edge region in order to extract the EXAFS function $\chi(E)$ (Figure 2.10). A subsequent step consists of the conversion of $\chi(E)$ to $\chi(k)$ using Equation 2.13, usually paired with a multiplication of the $\chi(k)$ spectrum by a higher order of k, typically k^2 or k^3, in order to magnify the far k-region.

The EXAFS frequencies can then be filtered using a Fourier transform, providing a pseudo-radial distribution function (PRDF). This PRDF is subsequently fitted using simulated scatter path intensities, as generated by programs such as FEFF,[46, 47] in order to determine the scatter path length, type and amount of scatterers, and the corresponding Debye-Waller factors.

References

[1] Beckhoff, B., Kanngießer, B., Langhoff, N., Wedell, R. & Wolff, H. *Handbook of Practical X-Ray Fluorescence Analysis* (Springer, 2007).

[2] Nobel prize. `http://www.nobelprize.org/`.

[3] Grieken, R. E. V. & Markowicz, A. A. *Handbook of X-Ray Spectrometry Second Edition, Revised and Expanded* (Marcel Dekker, Inc., 2002).

[4] Wikipedia. Electromagnetic radiation. `https://commons.wikimedia.org/wiki/EM_spectrum.svg` (2016).

[5] Albert, T., David, A., Eric, G., Malcolm, H., Kwang-Je, K., Janos, K., Jeffrey, K., Herman, W., Ingolf, L., Yanwei, L., Piero, P., Arthur, R., James, S., James, U. & Gwyn, W. *X-ray Data Booklet* (Center for X-ray Optics and Advanced Light Source, Berkeley, 2009).

[6] Attwood, D. *Soft X-Rays and Extreme Ultraviolet Radiation Principles and Applications* (Cambridge University Press, 2007).

[7] Einstein, A. & Infeld, L. *The Evolution of Physics* (Simon & Schuster, 1938).

[8] Tsuji, K., Injuk, J. & Grieken, R. V. *X-Ray Spectrometry: Recent Technological Advances* (Wiley & Sons Ltd., 2004).

[9] Voorde, L. V. d. *Optimization and applications of mobile, laboratory and synchrotron X-ray based non-destructive microanalysis techniques for the study of cultural heritage objects*. Ph.D. thesis, Ghent University (2015).

[10] Moseley, H. G. J. Lxxx.the high-frequency spectra of the elements. part ii. *Philosophical Magazine Series 6* **27**, 703–713 (1914).

[11] Hyperphysics. `http://hyperphysics.phy-astr.gsu.edu/hbase/quantum/moseley.html`.

[12] Jenkins, R., Manne, R., Robin, R. & Senemaud, C. Iupac—nomenclature system for x-ray spectroscopy. *X-Ray Spectrometry* **20**, 149–155 (1991).

[13] Schoonjans, T., Vincze, L., Solé, V. A., Sanchez del Rio, M., Brondeel, P., Silversmit, G., Appel, K. & Ferrero, C. A general monte carlo simulation of energy dispersive x-ray fluorescence spectrometers — part 5. *Spectrochimica Acta, Part B* **70**, 10–23 (2012).

[14] Meitner, L. Uber die entstehung der β-strahl-spektren radioaktiver substanzen. *Zeitschrift fur Physik* **9**, 131–144 (1922).

[15] Auger, P. Sur les rayons β secondaires produits dans un gaz par des rayons x. *Comptes rendus hebdomadaires des séances de l'Académie des sciences* (1923).

[16] Feldman, L. & Mayer, J. *Fundamentals of Surface Thin Film Analysis* (Upper Saddle River: Prentice Hall, 1986).

[17] Vincze, L., Janssens, K., Vekemans, B. & Adams, F. Monte carlo simulation of x-ray fluorescence spectra: Part 4. photon scattering at high x-ray energies. *Spectrochimica Acta Part B-Atomic Spectroscopy* **54**, 1711–1722 (1999).

[18] Vincze, L., Janssens, K., Adams, F., Rivers, M. & Jones, A. M. A general monte carlo simulation of ed-xrf spectrometers. ii: Polarized monochromatic radiation, homogeneous samples. *Spectrochimica Acta Part B-Atomic Spectroscopy* **50**, 127–147 (1995).

[19] Schoonjans, T., Brunetti, A., Golosio, B., del Rio, M. S., Sole, V. A., Ferrero, C. & Vincze, L. The xraylib library for x-ray-matter interactions. recent developments. *Spectrochimica Acta, Part B* **66**, 776–784 (2011).

[20] Kaulich, B. *et al.* Twinmic: A european twin microscope station combining full-field imaging and scanning microscopy. *Journal De Physique Iv* **104**, 103–107 (2003).

[21] Kirkham, R. *et al.* The maia spectroscopy detector system: Engineering for integrated pulse capture, low-latency scanning and real-time processing. In *The 10th International Conference on Synchrotron Radiation Instrumentation*, vol. CP1234, 240–243 (American Institute of Physics, 2010).

[22] Ryan, C. G., Kirkham, R., Hough, R. M., Moorhead, G., Siddons, D. P., de Jonge, M. D., Paterson, D. J., De Geronimo, G., Howard, D. L. & Cleverley, J. S. Elemental x-ray imaging using the maia detector array: The benefits and challenges of large solid-angle. *Nuclear Instruments & Methods in Physics Research Section a-Accelerators Spectrometers Detectors and Associated Equipment* **619**, 37–43 (2010).

[23] Ryan, C., Siddons, D., Kirkham, R., Dunn, P., Kuczewski, A., Moorhead, G., Geronimo, G. D., Paterson, D., Jonge, M. d., Hough, R., Lintern, M., Howard, D., Kappen, P. & Cleverley, J. The new maia detector system: Methods for high definition trace element imaging of natural material. In Denecke, M. & Walker, C. (eds.) *X-ray Optics and Microanalysis, Proceedings of the 20th International Congress*, vol. CP1221, 9–17 (American Intitute of Physics, 2010).

[24] Alfeld, M., De Nolf, W., Cagno, S., Appel, K., Siddons, D. P., Kuczewski, A., Janssens, K., Dik, J., Trentelman, K., Walton, M. & Sartorius, A. Revealing hidden paint layers in oil paintings by means of scanning macro-xrf: a mock-up study based on rembrandt's "an old man in military costume". *Journal of Analytical Atomic Spectrometry* **28**, 40 (2013).

[25] Ordavo, I., Ihle, S., Arkadiev, V. & Scharf, O. A new pnccd-based color x-ray camera for fast spatial and energy-resolved measurements. *Nuclear Instruments and Methods in Physics Research A* **doi:10.1016/j.nima.2011.05.080** (2010).

[26] Scharf, O. *et al.* Compact pnccd-based x-ray camera with high spatial and energy resolution: a color x-ray camera. *Anal Chem* **83**, 2532–2538 (2011).

[27] Reiche, I., Muller, K., Alberic, M., Scharf, O., Wahning, A., Bjeoumikhov, A., Radtke, M. & Simon, R. Discovering vanished paints and naturally formed gold nanoparticles on 2800 years old phoenician ivories using sr-ff-microxrf with the color x-ray camera. *Anal Chem* **85**, 5857–5866 (2013).

[28] Kanngiesser, B., Malzer, W., Mantouvalou, I., Sokaras, D. & Karydas, A. G. A deep view in cultural heritage—confocal micro x-ray spectroscopy for depth resolved elemental analysis. *Applied Physics A* **106**, 325–338 (2011).

[29] Luhl, L., Mantouvalou, I., Malzer, W., Schaumann, I., Vogt, C., Hahn, O. & Kanngiesser, B. Reconstruction procedure for 3d micro x-ray absorption fine structure. *Anal Chem* **84**, 1907–1914 (2012).

[30] Radtke, M., Buzanich, G., Curado, J., Reinholz, U., Riesemeier, H. & Scharf, O. Slicing – a new method for non destructive 3d elemental sensitive characterization of materials. *J. Anal. At. Spectrom.* **29**, 1339–1344 (2014).

[31] Garrevoet, J., Vekemans, B., Tack, P., De Samber, B., Schmitz, S., Brenker, F. E., Falkenberg, G. & Vincze, L. Methodology toward 3d micro x-ray fluorescence imaging using an energy dispersive charge-coupled device detector. *Anal Chem* **86**, 11826–11832 (2014).

[32] Vekemans, B., Janssens, K., Vincze, L., Adams, F. & Vanespen, P. Analysis of x-ray-spectra by iterative least-squares (axil) - new developments. *X-Ray Spectrometry* **23**, 278–285 (1994).

[33] Solé, V. A., Papillon, E., Cotte, M., Walter, P. & Susini, J. A multiplatform code for the analysis of energy-dispersive x-ray fluorescence spectra. *Spectrochimica Acta Part B: Atomic Spectroscopy* **62**, 63–68 (2007).

[34] Sherman, J. The theoretical derivation of fluorescent x-ray intensities from mixtures. *Spectrochimica Acta* **7**, 283–306 (1955).

[35] Schoonjans, T., Solé, V. A., Vincze, L., Sanchez del Rio, M., Appel, K. & Ferrero, C. A general monte carlo simulation of energy-dispersive x-ray fluorescence spectrometers — part 6. quantification through iterative simulations. *Spectrochimica Acta, Part B* **82**, 36–41 (2013).

[36] Calvin, S. *XAFS for Everyone* (Taylor & Francis, 2013).

[37] Koningsberger, D. & Prins, R. *X-ray absorption: Principles, applications, techniques of EXAFS, SEXAFS and XANES* (Wiley, 1987).

[38] Bunker, G. *Introduction to XAFS A Practical Guide to X-ray Absorption Fine Structure Spectroscopy* (Cambridge University Press, 2010).

[39] Schnohr, C. S. & Ridgway, M. C. *X-Ray Absorption Spectroscopy of Semiconductors* (Springer, 2015).

[40] Bianconi, A. Surface x-ray absorption-spectroscopy - surface exafs and surface xanes. *Applied Surface Science* **6**, 392–418 (1980).

[41] Wilke, M., Partzsch, G. M., Bernhardt, R. & Lattard, D. Determination of the iron oxidation state in basaltic glasses using xanes at the k-edge (vol 213, 71, 2004). *Chemical Geology* **220**, 141–161 (2005).

[42] Farges, F., Rossano, S., Lefrere, Y., Wilke, M. & Brown, G. E. Iron in silicate glasses: a systematic analysis of pre-edge, xanes and exafs features. *Physica Scripta* **T115**, 957–959 (2005).

[43] Tack, P., Bauters, S., Mauro, J. C., Smedskjaer, M. M., Vekemans, B., Banerjee, D., Bras, W. & Vincze, L. Confocal depth-resolved micro-x-ray absorption spectroscopy study of chemically strengthened boroaluminosilicate glasses. *RSC Adv.* **6**, 24060–24065 (2016).

[44] Silversmit, G., van Bokhoven, J. A., Poelman, H., van der Eerden, A., Marin, G. B., Reyniers, M.-F. & De Gryse, R. The structure of avox/tio2(anatase) powder catalyst under reduction and oxidation at 623k. *Physica Scripta.* **T115**, 798–801 (2005).

[45] Silversmit, G., van Bokhoven, J. A., Poelman, H., van der Eerden, A. M. J., Marin, G. B., Reyniers, M.-F. & De Gryse, R. The structure of supported and unsupported vanadium oxide under calcination, reduction and oxidation determined with xas. *Applied Catalysis A: General* **285**, 151–162 (2005).

[46] Ankudinov, A. L. & Rehr, J. J. Relativistic calculations of spin-dependent x-ray-absorption spectra. *Physical Review B* **56**, R1712–R1715 (1997).

[47] Ankudinov, A. *Relativistic Spin-dependent X-ray Absorption Theory.* Ph.D. thesis, University of Washington (1996).

[48] Joly, Y. X-ray absorption near-edge structure calculations beyond the muffin-tin approximation. *Physical Review B* **63** (2001).

[49] Sayers, D. E., Stern, E. A. & Lytle, F. W. New technique for investigating noncrystalline structures: Fourier analysis of the extended x-ray—absorption fine structure. *Physical Review Letters* **27**, 1204–1207 (1971).

[50] Stern, E. A., Sayers, D. E. & Lytle, F. W. Extended x-ray-absorption fine-structure technique. iii. determination of physical parameters. *Physical Review B* **11**, 4836–4846 (1975).

[51] Lytle, F. W., Sayers, D. E. & Stern, E. A. Extended x-ray-absorption fine-structure technique. ii. experimental practice and selected results. *Physical Review B* **11**, 4825–4835 (1975).

[52] Medjo, R. E. *Characterization of Carbon Nanotubes*, chap. 7 (InTech, 2013).

[53] Ravel, B. & Newville, M. Athena, artemis, hephaestus: data analysis for x-ray absorption spectroscopy using ifeffit. *J Synchrotron Radiat* **12**, 537–541 (2005).

[54] Klementev, K. V. Deconvolution problems in x-ray absorption fine structure spectroscopy. *Journal of Physics D-Applied Physics* **34**, 2241–2247 (2001).

Chapter 3

Instrumental Aspects

3.1 Generation of X-rays

X-rays can be generated in a number of ways. Here, some of the most frequent ways in which X-rays are generated for analytical purposes are discussed.

3.1.1 Natural Sources

The biggest source of X-rays in our Solar System is the Sun.[1] Due to a combination of various nuclear processes, X-rays with a wide range of energies are emitted as a part of the solar electromagnetic spectrum. However, most of these high energy photons emitted towards Earth are absorbed by the atmosphere, preventing their interaction with matter on Earth's surface. X-rays originating from the Sun or other celestial bodies are part of the cosmic radiation spectrum.[2, 3]

Besides cosmic radiation, a natural source of X-rays exists in radioisotopes. Isotopes of the same element are atoms with a specific atomic number, or number of protons contained in the nucleus, but which have a different number of neutrons. When an isotope has more or less neutrons than its stable counterpart, nuclear decay is possible during which the emission of X-rays is a possibility.

A common example of a radionuclide emitting X-rays is iron-55 (^{55}Fe). This iron isotope has a neutron less than its stable counterpart and decays through the electron capture

process, in which a proton and inner shell electron are converted to a neutron.[4] This process is associated with the emission of a neutrino. After the electron capture process, the atom is essentially transformed to a Mn atom, with an electron hole in the K shell. Due to an electron transition this core hole can be filled by an electron from a higher electron shell, resulting in the emission of characteristic Mn-K_α, Mn-K_β X-ray photons or Auger electrons, each with well-defined probabilities (Section 2.1.3).

Radionuclides are particularly useful when calibrating the energy scale of energy dispersive detectors, as the sources emit X-rays of well-defined energies. Furthermore, radionuclides are also used in medicine to aid in the imaging of internal organs, making use of the high penetrating character of X-rays.[5] Additionally, in cases where the availability of electric power is limited, or due to weight and/or size restrictions, radioisotopes can be used as X-ray sources in (e.g. portable) XRF spectrometers.

3.1.2 X-ray Tubes

For laboratory based X-ray analysis, most often X-ray tubes are used to generate X-rays.[6] It was from a predecessor of one such device, the so-called Crookes tube, that Röntgen discovered the emission of an unknown type of radiation, later named X-rays.[7] Despite the large variety in X-ray tubes, each with their own characteristics, they are all based on the same principle. A diagram of an X-ray tube is shown in Figure 3.1.

When a high voltage is set over an electrically heated filament (typically made of tungsten), serving as cathode, and an anode material (e.g. Mo), electrons are emitted by the filament and accelerated towards the anode. When reaching the anode material, the electrons can gradually lose their kinetic energy by interaction with the electrons and the target nuclei. A small part of the lost energy is emitted as X-rays, resulting in the emission of a continuous polychromatic spectrum.[8] This type of radiation is called Bremsstrahlung, or braking radiation. A secondary interaction that may occur is similar to the photoelectric effect, in which the impinging electron ejects a bound electron from the anode material. The resulting electron hole is filled by an electronic transition, causing the emission of a characteristic X-ray of the anode material. The total resulting emitted X-ray spectrum will consist of a continuous Bremsstrahlung background, superimposed by characteristic X-ray fluorescence peaks (Figure 3.1, right).

Due to the continuous electron bombardment, and the large amount of energy deposition

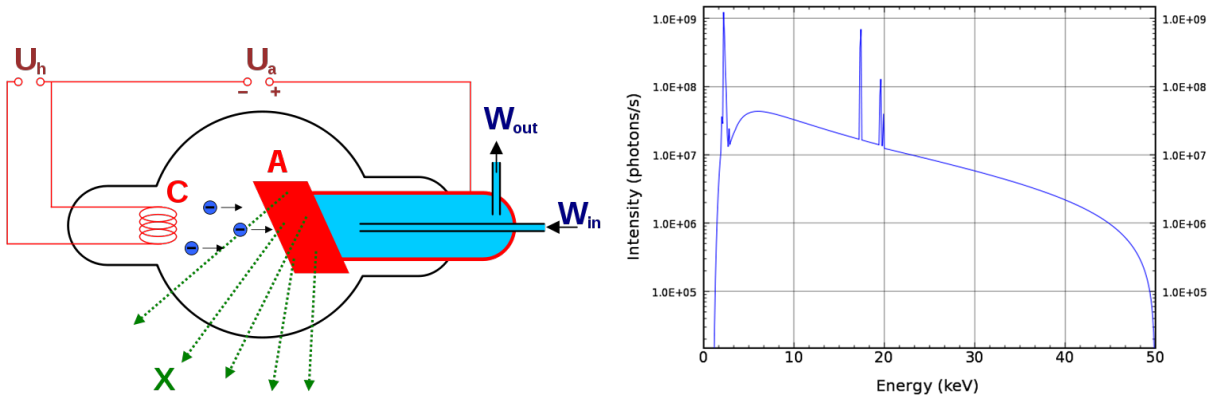

Figure 3.1: Schematic representation of a Coolidge X-ray tube[9] (left) and the emitted spectrum of an X-ray tube with 50 kV voltage and Mo anode material (right).

in the form of heat, the anode material must be cooled. Modern X-ray tubes typically use water or air cooled systems. Additionally, the output power of an X-ray tube is usually limited by this heat dissipation. To overcome this limitation in applicable power, rotating anode X-rays tubes are employed in which the anode is continuously rotated, providing a better heat dissipation and thus higher X-ray flux output. An even newer development is the invention of liquid metal jet X-ray sources, which eliminate the cooling issues altogether.

3.1.3 Synchrotron Radiation Sources

X-ray beams of extreme intensity and laser-like qualities are generated in synchrotron radiation (SR) facilities. These facilities make use of charged elementary particles (e.g. electrons or positrons),accelerated to relativistic speeds, that pass through strong magnetic fields of various types of SR sources.[10] Due to the magnetic field, Lorentz forces are induced and the path of the charged particles will be curved, resulting in a strong acceleration coupled with the emission of electromagnetic radiation, part of which in the X-ray region.[11]

The first large scale synchrotrons, so-called first generation synchrotrons, were built mainly for particle physics research. As such, the loss of energy of the particles when passing through the magnetic fields was considered a nuisance.

Fairly soon after building the first generation synchrotrons, researchers recognised the use of these synchrotron generated X-rays for analytical purposes. Due to the unique characteristics of SR-beams, synchrotrons were built for the specific purpose of emitting X-rays, thus introducing second generation SR facilities.[12] The actual X-ray sources in

these facilities are the so-called bending magnets, deflecting the particle beam at given positions of the storage ring.

Third generation SR facilities were introduced when so-called insertion devices were applied, providing more intense and collimated X-ray beam fluxes compared to the second generation facilities. Below a short description is provided on the different parts of a third generation SR facility.

Synchrotron Radiation Characteristics

Synchrotron radiation has distinct characteristics,[13] rendering it the source of choice for many X-ray based analytical applications. Below, a short description of these characteristics is listed.

Flux and Brilliance. The flux is defined as the amount of photons per second. Brilliance defines the amount of flux, normalized by the source size and emission solid angle. Due to the high energy of the charged particles and the high magnetic fields applied at synchrotrons, a very high flux is obtained. Additionally, the application of insertion devices and dedicated focussing optics provides a significant increase in brilliance. The high flux and brilliance result in the possibility to perform measurements using shorter measurement times, a useful asset considering the limited available beam time at a SR facility

Polarisation. Due to the way synchrotron radiation is generated, a high degree of polarisation (nearly 100 %) in the particle orbit plane can be obtained. This results in the minimization of scattering effects when measuring in this plane of polarisation (horizontally).

Coherence. There are two types of coherence: longitudinal or temporal coherence, and transversal or spatial coherence. The first denotes the extent to which the radiation maintains its phase at two different times. The latter describes the correlation of the wave phase at two distinct points, and is an expression for the degree of collimation. SR is characterized by a high degree of natural collimation, allowing for better focussing of the X-ray beam using dedicated X-ray optics.

Energy Tunability. The X-ray photons emitted by SR sources cover a wide energetic spectrum. Using dedicated X-ray optics (monochromators) or adjusting certain parameters of the particular SR sources, the X-ray energy can be tuned.

Time Structure. Due to the presence of the charged particles in bunches in the synchrotron ring, X-rays are emitted with a pulsed time structure. This creates the possibility to perform time resolved experiments at SR facilities. The filling mode of the storage ring defines the time between pulses. When fewer bunches are present in the ring, more time is available between pulses. However, fewer bunches also generate lower X-ray fluxes. Typical pulse lengths are in the range of 40 to 400 ps.

Facility Outline

A SR facility can be split in four general parts: the linear accelerator (linac), booster ring, storage ring and the beamlines. The linac is used to pre-accelerate the charged particles to a few hundred MeV before injecting them in the booster synchrotron. Inside the booster ring, the energy of the particles is increased until the particles reach their final energy (e.g. 6 GeV in case of the ESRF), at which time they are introduced in the storage ring (Figure 3.2).

The storage ring contains the magnetic structures that are used to generate X-ray radiation. It is actually a polygon, with bending magnets at the corner positions. In the straight parts of the polygon, insertion devices can be installed. Radiation generated by each of the separate magnetic structures can be guided through a series of X-ray mirrors and optics, down the so-called beam lines.

The beam lines themselves can be described as consisting of three parts. The first part are the X-ray optics, used to define beam dimensions, select appropriate photon energies and guide the beam towards the experimental hutch, which is the second major part of a beam line. Inside the experimental hutch, the researchers can place their sample in the path of the beam, allowing for intricate sample environments when required. To protect the researchers from exposure to the X-ray beam, the experimental hutch is typically lined by lead panels. When researchers are inside the experimental hutch, the X-ray beam path is blocked by a so-called shutter system, existing of a lead metal plate cutting the beam path. During operation, the experimental hutch is closed, preventing anyone from entering, and researchers can control their experiment from the control room.

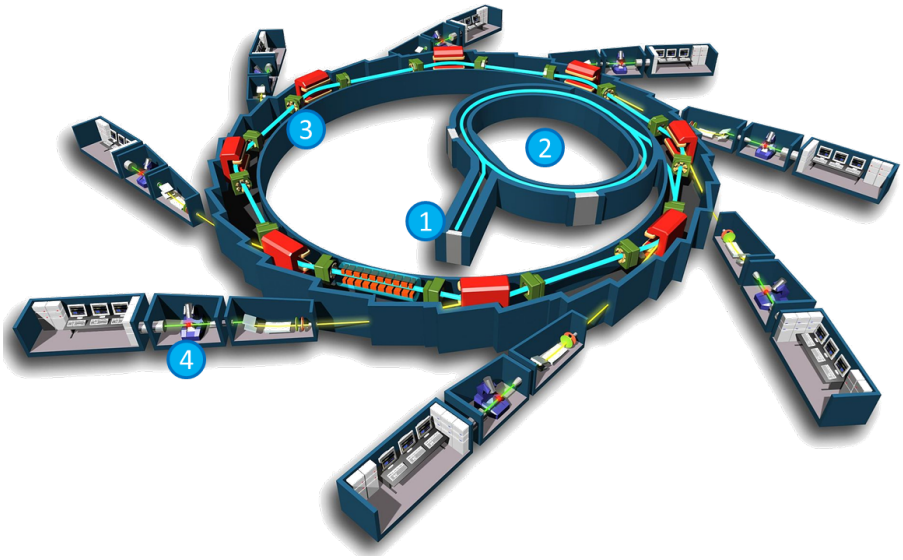

Figure 3.2: A schematic overview of a synchrotron radiation facility. Depicted are the linear accelerator (1), booster ring (2), storage ring with bending magnets and insertion devices (3) and beam lines (4). Figure adapted from.[14]

Bending Magnet

Located at the vertices of the synchrotron's polygon shape, bending magnets are ultimately used to force the charged particles' path into a closed orbit, as well as generate X-ray radiation. Bending magnets are usually permanent magnets with strong magnetic fields, e.g. 0.4 T at BM26A (DUBBLE, ESRF),[15, 16] emitting radiation in a wide fan. A section of the fan can be selected using a slit system, improving on the horizontal collimation at the cost of beam flux.

The emitted radiation has a smooth continuous spectrum (Figure 3.3), characterised by a critical energy E_C defined by Equation 3.1.[17] Here, E is the electron energy and B is the bending magnet's magnetic field strength. The critical energy is the energy value at half the integrated radiative power of the continuous emission spectrum. With higher E_C, higher energy photons are generated.

$$E_C[\text{keV}] = 0.665 \cdot E^2[\text{GeV}] \cdot B[\text{T}] \tag{3.1}$$

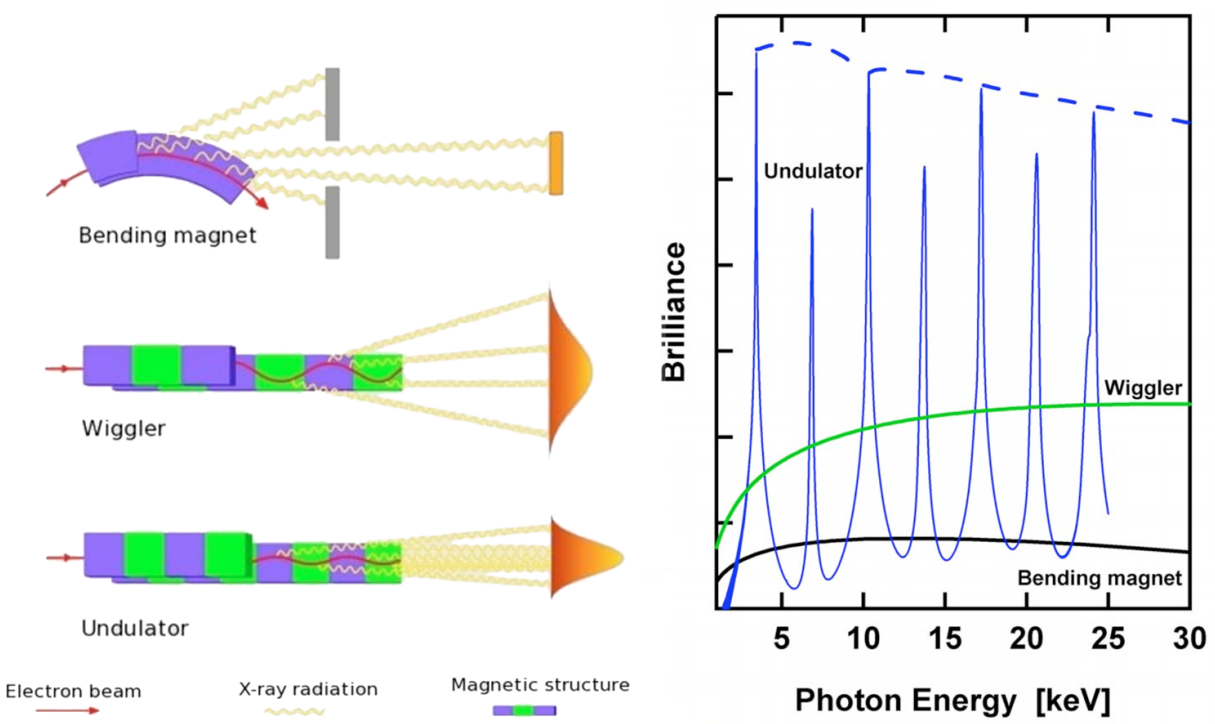

Figure 3.3: Left: schematic representation of (top to bottom) a bending magnet, wiggler and undulator. Right: emission spectra of the devices depicted to the left. Figures adapted from.[18]

Insertion Device

In the search for more intense X-ray beams insertion devices were developed, introducing the third generation of SR facilities.[12] These magnetic structures are installed in the straight parts of the synchrotron and consist of arrays of magnets with alternating poles. When charged particles propagate through the thus created magnetic field, many oscillations perpendicular to their direction of movement are induced. At each bend, as is also the case for bending magnets, the particles will lose part of their energy by the emission of electromagnetic radiation. Due to the large amount of bends, a substantially higher synchrotron radiation intensity is generated when compared to a bending magnet.

There are two types of insertion devices: a wiggler and undulator. Both are described by the deflection parameter K (Equation 3.2).[17] In this equation, B_0 is the peak magnetic field of the magnets and λ_p is the period of the magnetic poles.

$$K = \frac{[c] \cdot e \cdot B_0}{m \cdot c^2} \cdot \frac{\lambda_p}{2\pi} = 0.934 \cdot B_0 \cdot \lambda_p[\text{cm}] \tag{3.2}$$

A wiggler is characterised by large deflection angles ($K \gg 1$) and n poles. Due to the overlap of the emission cones, an emission spectrum similar in shape to that of a bending magnet, but more intense due to its proportionality to $2n$, is generated (Equation 3.3).

In the case of an undulator, the deflection angles are small ($K \leq 1$) due to weaker magnetic fields, resulting in small on-axis deviations of the charged particles.[17] This results in coherent addition of the emissions cones, generating an emission spectrum characterised by several sharp peaks (Figure 3.3). Additionally, undulators usually consist of more magnetic poles than wigglers, further increasing the intensity of the spectrum, proportional to n^2. The position of the sharp spectral peaks in the undulator spectrum can be shifted by adjusting the gap: the distance between the south and north poles.

3.2 X-ray Detectors

As X-rays are not visible to the human eye, dedicated instruments are required in order to determine the amount and energy of X-ray photons originating from a sample. Röntgen first discovered X-rays by the visible fluorescence they induced on a barium platinocyanide screen. However, no quantitative information on the energy of X-rays is obtained from such

photosensitive plates, rendering them less useful for spectroscopic purposes. Below, a short description is supplied concerning the currently most frequently used X-ray detectors.

3.2.1 Ion Chambers

Ionisation or ion chambers are amongst the simplest X-ray detectors, consisting of two electrodes over which a high potential is placed with a gas contained in between.[19] When an X-ray photon enters the ion chamber, it can interact with the gas atoms by ionising them. The resulting (positively charged) ion and electron will be attracted to the cathode and anode respectively, generating an electrical pulse. As a result, a current is measured corresponding to the flux of X-rays entering the ion chamber.

Despite its inability to determine the energy of the detected X-rays, ion chambers are commonly used to determine beam fluxes for spectral normalisation purposes. By modifying the gas mixture, the ion chamber can be optimized to detect X-rays of a specific energy for a given amount. E.g. in X-ray absorption spectroscopy it is customary to use two ion chambers, one before the sample and one after the sample in transmission mode, where the first ion chamber has a gas mixture absorbing approximately 20 % of the X-rays, whereas the second ion chamber usually is set to absorb 75 % of the X-rays. The second ion chamber preferably does not absorb 100 % of the X-rays in transmission mode X-ray absorption measurements in case one prefers the simultaneous measurement of a reference sample, by making use of a third ion chamber.

3.2.2 Semiconductor Detectors

Semiconductor detectors are made of a semiconducting material, typically Si(Li) or Ge(Li), applied with an electric field and can provide information on both the X-ray flux and energy. As such, they are often utilized as energy dispersive (ED) detectors.

When an X-ray photon enters the detector material, it can dissipate its energy by generating multiple electron-hole pairs in a sequence of interactions initiated by the photo-electric effect.[19] The generation of each electron-hole pair has a well defined energy depending on the detector material (a few eV), thus the initial X-ray photon energy is correlated to the amount of generated electron-hole pairs.[20]

Upon determination of the total charge generated by an X-ray photon, which is proportional to the deposited X-ray energy, the detector readout adds a count to the channel corresponding to this charge, thus creating a spectrum. Due to thermal noise (dark current) and the occasional recombination of an electron-hole pair before detection, a peak is formed in the spectrum instead of a fine line at a specific energy. The width of the peak is expressed by the energy resolution, which is typically 140-150 eV at 5.9 keV (Mn-K_α) for Si(Li) detectors. The theoretical energy resolution E_{res} of a detector is expressed by the Fano factor F and the electronic noise N.[7, 17] Here, E represents the energy of the fluorescent photon and ε is a conversion factor from the energy to the number of charge carriers (For Si based detectors, $\varepsilon = 3.65\,\text{eV}$).

$$E_{res} = 2.35 \cdot \sqrt{FE\varepsilon} + N \tag{3.3}$$

The amount of X-rays detected with respect to the amount incident on the detector material is expressed by the quantum efficiency of the detector. This parameter is dependent on the X-ray energy, as well as the detector material and thickness. Generally, Si(Li) detector crystals are relatively thick, between 3-5 mm. Nevertheless, even for several mm thickness, due to the low atomic number of Si, the detector crystal becomes transparent above 40 keV, rendering them sensitive to X-ray energies between 1 and 40 keV. For higher energies, best use is made of Ge(Li), or more recently HPGe, based detectors due to the increased density (Si: $2.33\,\frac{\text{g}}{\text{cm}^3}$, Ge: $5.46\,\frac{\text{g}}{\text{cm}^3}$) and higher atomic number (14 and 32 for Si and Ge respectively).

The main disadvantage of photon counting semiconductor detectors is their low count rate, typically being significantly saturated by fluxes of 10 kcps. Additionally, cooling by liquid nitrogen is often required in order to reduce thermal noise contribution and prevent drifting of the Li atoms throughout the detector material.

3.2.3 Silicon Drift Detectors

An enhancement in semiconductor detectors was introduced in 1983 by Gatti and Rehad, by the invention of the silicon drift detector (SDD).[21, 22] This detector consists of a circular design of p+ electrodes surrounding a n- anode, on top of a n- Si bulk with a back contact consisting of a single p+ electrode (Figure 3.4).

This design has the advantage that full bulk depletion can be achieved with significantly lower voltages with respect to traditional Si(Li) detectors. Furthermore, incorporation of the electron drift principle and on-chip field effect transistors (FET) reduce electronic noise contributions and required signal shaping times, resulting in increased count rates and enhanced energy resolution. Further advances in detector count rates without loss of energy resolution exist in the implementation of improved pulse processors and the coupling of separate SDD detectors into a multichannel drift detector.[23] Additionally, cooling can be performed by Peltier based systems instead of using liquid nitrogen, thus leading to more compact devices.

3.2.4 Spatially Resolved Detectors

Both Si(Li) and SDD detectors provide information on the energy of the X-ray photon, as well as the amount of incident photons. However, when information is required on the exact place of the detector on which the X-ray photon entered, a spatially resolved detector is needed.

For this purpose, typically charge coupled device (CCD) detectors are used. However, complementary metal oxide semiconductor (CMOS) detectors are also applicable.[24, 25] The main difference between these two types of detectors is the way in which they read out the collected signals. A CMOS detector will read out each pixel separately, where a CCD detector will transfer the photo-generated charge from pixel to pixel and convert this charge to a voltage at an output node.[25–27]

The charge collection in spatially resolved detectors happens in the same way as in a normal Si(Li) detector. The detector chip is usually built up out of silicon, which will absorb incoming X-rays and transfer them into electron hole-pairs. In a CMOS detector every pixel of the detector has its own readout technology, resulting in very fast signal readout. In fact, one could picture this CMOS detector as a collection of multiple miniaturized Si(Li) detectors. A CCD detector reads out the signal in a somewhat more complex way, resulting in slower count rates.[20, 24, 25] However, a CCD chip is less complex to manufacture than a CMOS chip, as the electron to volt conversion occurs on a separate circuit board.[24]

Figure 3.5 shows a cross section of a pnCCD detector chip. The generated electron cloud prefers to be at the bottom of the electron potential surface. This minimum in the potential surface is created by applying a somewhat higher voltage in a p^+ register implant, when

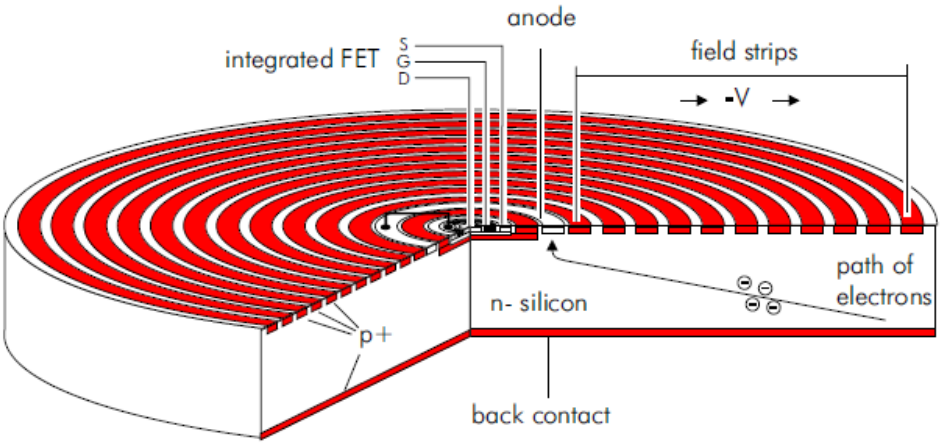

Figure 3.4: Schematic overview of a SDD consisting of p+ electroces, n- anode and Si bulk, as well as integrated front-end transistor (FET). Figure adapted from.[23]

compared to the neighbouring register implants. The collected electron clouds will be transferred to the readout anode by changing the voltages of the register implants relative to each other. The detector depicted is characterised by a 3-phase readout schematic: an electron cloud will be shifted to the next pixel by changing the voltages of the p^+ register implants in three steps. Once the electron cloud reaches the readout anode a charge will be created which can be amplified and interpreted to give the correct energy of the incident X-ray photon.

The full pnCCD chip consists of rows and columns of pixels. Often the readout of such a chip will occur by moving the collected electron clouds one pixel to the side, followed by a complete readout of the last column before the process is repeated by moving each row one pixel to the side again. This is a relatively time consuming process. Even though transporting all electron clouds in one direction is fairly fast, the movement in the perpendicular direction creates a bottleneck which slows down the whole readout process.

Furthermore, if a photon reaches the detector while the readout process is occurring, the exact incident location cannot be determined. As long as the photons hit the CCD before the readout process has started, the correct place of incidence can be determined. However if a photon hits the detector after the readout process has started, the location of incidence of this photon will be assigned to the wrong pixel.

The slow readout is a weak spot for many CCD detectors. However, several solutions have been found to solve this problem. A first possibility is splitting the chip in two or

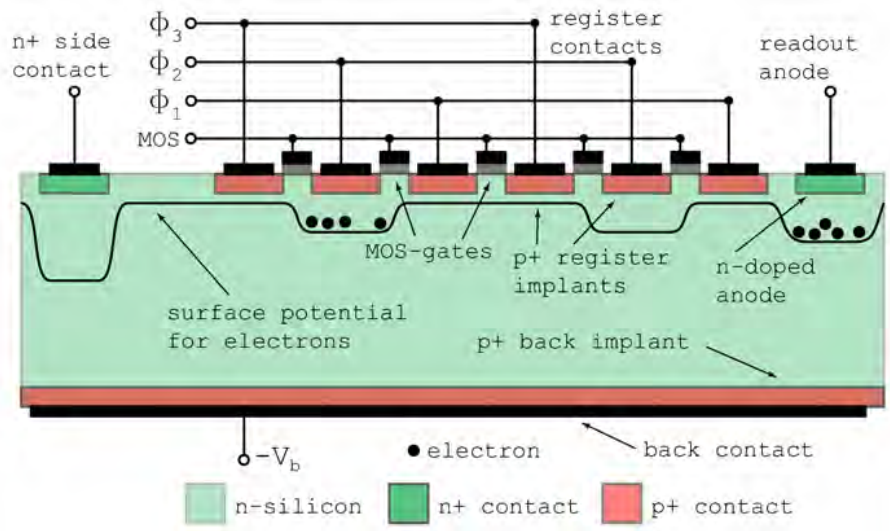

Figure 3.5: Schematic cross section of a pnCCD chip. Depicted are the p- and n-junctions as well as the arbitrarily chosen front- and backside. Electrons will gather in electron potential surface minima and can be transferred by changing the voltages over the p^+ register implants.[20]

more separate segments for the readout process. This way the electron clouds pass a lower amount of pixels before they reach the readout anode. Consequently the signals are read out more quickly. An additional option is the 'frame store' mode.[20] In this mode the CCD chip is split in two halves: one half is used for photon detection, while the other half is used for electron storage only. The readout process then quickly transfers all electron clouds from the detecting half to the storage half, after which the storage half can commence depletion. As soon as the detecting half of the chip is empty, the chip can collect new photons and subsequently the detector's dead time has been reduced.

Most CCD detectors are described as working under 'backside illumination'. As can be seen in Figure 3.5 the backside has a thin, more or less homogeneous layer covering the detector. The front side has many electronic components on it of different thicknesses and sizes, causing the X-rays to be attenuated differently based on their point of impact to the detector. A difference can even be perceived between different points in one pixel. When illuminating under backside illumination conditions, it is safe to say every X-ray photon beam of a certain energy will be attenuated up to the same degree at any point of incidence of the detector before it enters the depleted silicon region, since it passed the same material of roughly the same dimensions on the way.

Despite the possibility of CCD devices to perform energy dispersive measurements, often

this option is not used to further improve the count rate. X-ray photon energy determination in spatially resolved detectors requires recognition of the generated electron charge cloud, as this typically bleeds over several pixels. This step requires significant computing time, thus increasing detector dead time.

3.3 X-ray Optics

Synchrotron radiation is characterized by a large electromagnetic radiation spectral range. Researchers often wish to select a narrow energy band for the X-ray beam with which to excite their samples. Additionally, it is often necessary to decrease the X-ray beam spot size at the sample position in order to obtain better spatial resolution.

The most straightforward way of defining the beam size is by using slit systems or pinholes. These essentially consist of metallic plates (W, Mo, ...) blocking part of the beam. The main disadvantage of these beam defining optics is their lack of focussing.

Here some of the X-ray optics used for the micro-spectroscopic research presented in this thesis are discussed.

3.3.1 Monochromators

Monochromators are used to select a narrow band of the X-ray energy range to propagate beyond the optic, whereas the rest are blocked. The width of this energy range band is expressed by the energy resolution of the monochromator $\frac{\Delta E}{E}$. Commonly, an X-ray monochromator is either a perfect crystal or multilayer, selecting a specific wavelength based on the Bragg principle (Equation 3.4).[7] In Bragg's equation, n is an integer denoting the order of diffraction (n = 1, 2, 3, ...), λ the X-ray photon wavelength, d the distance between crystal layers and ϑ the angle of diffraction between crystal surface and X-ray photon. a is the crystal lattice spacing and h, k and l are the Miller indices of the Bragg plane. The bottom equation in Equation 3.4 is correct only for cubic systems. Based on the crystal material and the specific plane being diffracted on, the energy resolution will change. E.g. Si(111) has a typical energy resolution in the order of $\Delta E/E = 1 \times 10^{-4}$, whereas Si(311) achieves $\Delta E/E = 2 \times 10^{-5}$.[28, 29]

$$n\lambda = 2 \cdot d \cdot sin(\vartheta)$$
$$d = \frac{a}{\sqrt{h^2 + k^2 + l^2}} \tag{3.4}$$

By changing the angle between crystal surface and the X-ray beam, a different wavelength can be selected. This way, one can scan through X-ray beam energies by tilting the monochromator crystal with respect to the beam. Based on the precision of the crystal tilt motor and the angular dependence of the X-ray wavelength, different crystal types are used for different energy regions. Si(111) is most often used for energies between 5-20 keV whereas beyond 20 keV better use is made of a Si(311) crystal due to angular limitations.

In order to not change the beam direction after diffraction by the monochromator, typically a second crystal is used fixed parallel or slightly offset to the first crystal. The slight offset of the second crystal serves the purpose of rejecting higher order harmonics that can potentially interfere with the experiment. Higher order harmonics can also be removed by inserting a mirror in the beampath as a higher energy cut-off or slightly detuning the second monochromator crystal. To prevent changes in beam position during monochromator movement, often a translation of the second crystal is performed simultaneously. A monochromator equipped to do so operates in 'fixed-exit' mode.

Besides energy bandwidth selection, monochromator crystals can also be used to (pre)focus the X-ray beam by applying curved monochromator crystals. Typically, this does come at the cost of a slightly decreased energy resolution.

3.3.2 Capillaries

An elegant way of focusing an X-ray beam, thus decreasing the beam dimensions while increasing the brilliance, is the use of (poly)capillary optics.[30–35] These optics are typically made of a bundle of Si-based glass fibres through which the photons are guided to a focal point by means of repeated total reflection. A polycapillary optic consists of hundreds of thousand single fibres, fused together. Depending on the shape of the polycapillary optic, the X-ray beam can be focussed or collimated (Figure 3.6).

In order for a photon (with energy E) to reflect on the glass, it must reflect on the glass under an angle smaller than the critical angle of total reflection ϑ_C (Equation 3.5).[17, 37] The

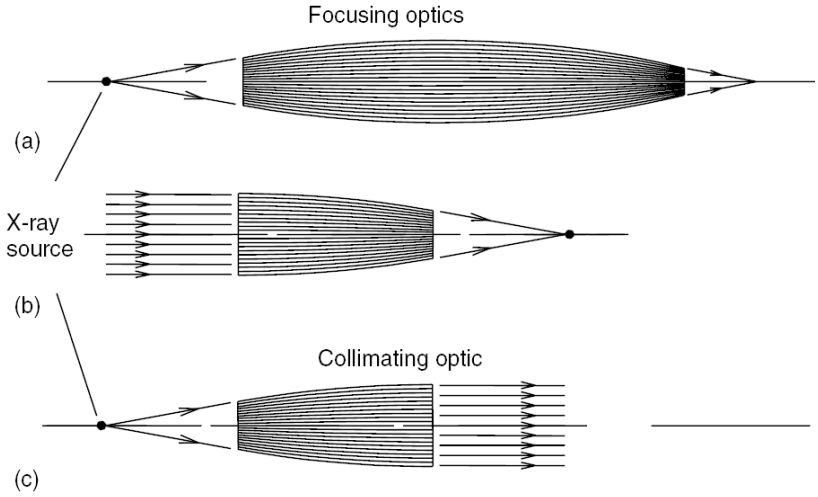

Figure 3.6: Polycapillary X-ray optics that produce a focused (a,b) or parallel beam (c), starting from an X-ray point source (micro-focus X-ray tube (a,c) or a quasi-parallel X-ray source (e.g. synchrotron (b)).[31, 36]

critical angle of total reflection is inversely proportional to the energy, resulting in higher energies reflecting under smaller angles. This ensures that with higher energies, smaller beam sizes can be obtained. However, the smaller critical angle of total reflection boundary also results in a lower probability of transmission of X-ray photons through the optic, denoted by the transmission efficiency.[38] The transmission efficiency of a polycapillary half-lens optic as a function of X-ray energy is presented in Figure 3.7. The sharp drop in efficiency around 1.8 keV is due to the Si K-shell absorption edge.

$$\vartheta_C[\text{mrad}] \approx \frac{30}{E[\text{keV}]} \tag{3.5}$$

Despite the high degree of manual labour required during the manufacturing of polycapillary optics, these optics are very cost efficient. Beam sizes down to 5 μm at the focal point can be obtained for energies above 10 keV. Additionally, polycapillary optics are fairly straightforward to align and can be designed specifically for a given beam shape in order to obtain the highest possible transmission efficiency and lowest beam spot. It should be noted that for focussing polycapillary optics often the divergence of the beam is increased, thus complicating their use for analytical techniques requiring collimated X-ray beams such as XRD.

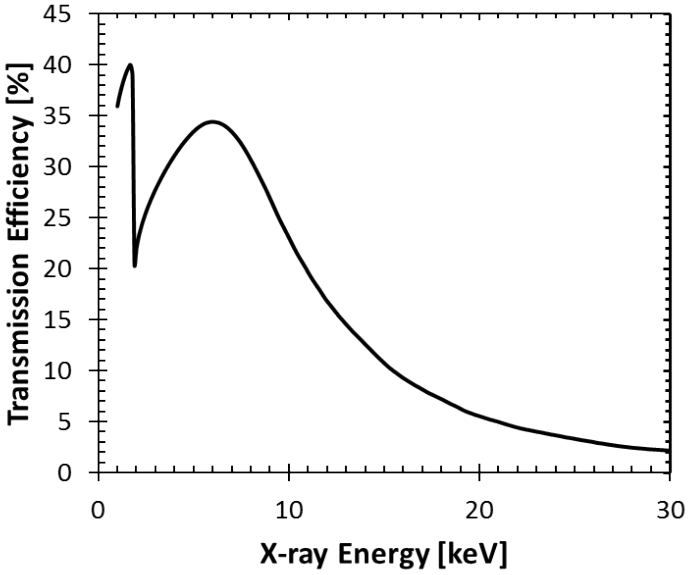

Figure 3.7: Transmission efficiency as a function of X-ray energy for a polycapillary half-lens optic with length 9 cm, focal distance of 5 mm and outer entrance diameter of 4.13 mm and exit diameter of 1.17 cm. The polycapillary optic consists of 200000 capillaries diminishing in diameter from 7 to 2 μm.

3.3.3 Kirkpatrick-Baez Mirrors

An additional X-ray optic based on total reflection are Kirkpatrick-Baez mirrors or KB-mirrors.[39–42] This optic consists of two mirrors curved in one dimension, one to focus in the horizontal and one to focus in vertical direction (Figure 3.8). By adjusting the curvature of the mirrors, beam spots down to sub-micrometre dimensions with working distances considerably larger than those of polycapillary optics (>10 mm) can be obtained.[43, 44] Additionally, by using only a single mirror of the system, a vertical or horizontal sheet beam can be obtained. A feature which is particularly interesting with respect to confocal full-field experiments.[45]

Despite the fairly simple working principle, these optics come at a fairly high cost due to the manufacturing of bendable mirrors with very low surface roughness, as well as the high precision motor systems required to position the mirrors in the path of the beam.

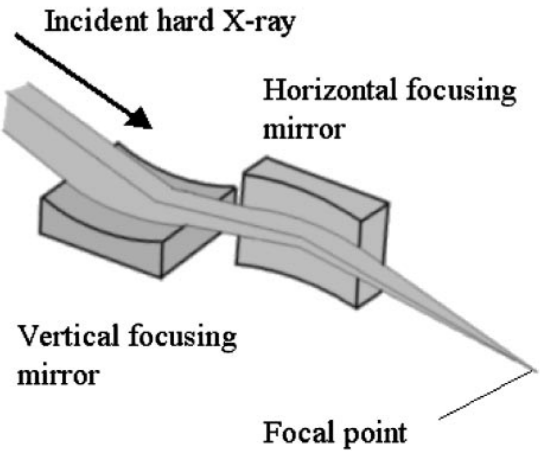

Figure 3.8: X-ray guiding scheme of a Kirkpatrick-Baez mirror system. Figure adapted from H. Mimura *et al.*[46]

References

[1] Parker, E. N. Nanoflares and the solar x-ray corona. *The Astrophysical Journal* **330**, 474 (1988).

[2] Sharma, S. *Atomic And Nuclear Physics Chapter 18* (Pearson Education, 2008).

[3] Alfvén, H. & Herlofson, N. Cosmic radiation and radio stars. *Physical Review* **78**, 616 (1950).

[4] Alvarez, L. W. Nuclear k electron capture. *Physical Review* **52**, 134–135 (1937).

[5] Henkin, R. E. *Nuclear Medicine 2nd ed.* (Elsevier Mosby, 2006).

[6] Behling, R. *Modern Diagnostic X-Ray Sources: Technology, Manufacturing, Reliability* (CRC Press, 2015).

[7] Grieken, R. E. V. & Markowicz, A. A. *Handbook of X-Ray Spectrometry Second Edition, Revised and Expanded* (Marcel Dekker, Inc., 2002).

[8] Bethe, H. & Heitler, W. On the stopping of fast particles and on the creation of positive electrons. *Proceedings of the Royal Society A: Mathematical, Physical and Engineering Sciences* **146**, 83–112 (1934).

[9] Wikipedia. X-ray tube. `https://en.wikipedia.org/wiki/X-ray_tube` (2016).

[10] Elder, F. R., Gurewitsch, A. M., Langmuir, R. V. & Pollock, H. C. Radiation from electrons in a synchrotron. *Physical Review* **71**, 829–830 (1947).

[11] Schwinger, J. On the classical radiation of accelerated electrons. *Physical Review* **75**, 1912–1925 (1949).

[12] Albert, T., David, A., Eric, G., Malcolm, H., Kwang-Je, K., Janos, K., Jeffrey, K., Herman, W., Ingolf, L., Yanwei, L., Piero, P., Arthur, R., James, S., James, U. & Gwyn, W. *X-ray Data Booklet* (Center for X-ray Optics and Advanced Light Source, Berkeley, 2009).

[13] Kim, K.-J. Characteristics of synchrotron radiation. *AIP Conf. Proc.* **184**, 565 (1989).

[14] French national synchrotron facility soleil. `http://www.synchrotron-soleil.fr`.

[15] Tack, P., Bauters, S., Mauro, J. C., Smedskjaer, M. M., Vekemans, B., Banerjee, D., Bras, W. & Vincze, L. Confocal depth-resolved micro-x-ray absorption spectroscopy study of chemically strengthened boroaluminosilicate glasses. *RSC Adv.* **6**, 24060–24065 (2016).

[16] Nikitenko, S., Beale, A. M., van der Eerden, A. M., Jacques, S. D., Leynaud, O., O'Brien, M. G., Detollenaere, D., Kaptein, R., Weckhuysen, B. M. & Bras, W. Implementation of a combined saxs/waxs/qexafs set-up for time-resolved in situexperiments. *J Synchrotron Radiat* **15**, 632–640 (2008).

[17] Beckhoff, B., Kanngießer, B., Langhoff, N., Wedell, R. & Wolff, H. *Handbook of Practical X-Ray Fluorescence Analysis* (Springer, 2007).

[18] Deutches elektronen synchrotron desy. `http://photon-science.desy.de/`.

[19] Knoll, G. F. *Radiation Detection and Measurement 4th Ed.* (Wiley & Sons, Inc., 2010).

[20] Kimmel, N. *Analysis of the charge collection process in solid state X–ray detectors.* Ph.D. thesis, Universität Siegen (2008).

[21] Tsuji, K., Injuk, J. & Grieken, R. V. *X-Ray Spectrometry: Recent Technological Advances* (Wiley & Sons Ltd., 2004).

[22] Gatti, E. & Rehak, P. Semiconductor drift chamber — an application of a novel charge transport scheme. *Nuclear Instruments and Methods in Physics Research* **225**, 608–614 (1984).

[23] Lechner, P., Fiorini, C., Longoni, A., Lutz, G., Pahlke, A., Soltau, H. & Strüder, L. Silicon drift detectors for high resolution, high count rate x-ray spectroscopy at room temperature. *Advances in X-ray Analysis* **47**, 53–58 (2004).

[24] Litwiller, D. Ccd vs. cmos: Facts and fiction. *Photonics Spectra* (2001).

[25] Litwiller, D. Cmos vs. ccd: Maturing technologies, maturing markets. *Photonics Spectra* **39**, 54 (2005).

[26] Kimmel, N., Hartmann, R., Holl, P., Meidinger, N., Richter, R. & Strüder, L. Analysis of the charge collection process in pnccds (2006). Date od event: 2006-05-24 - 2006-05-27.

[27] Kimmel, N., Hiraga, J. S., Hartmann, R., Meidinger, N. & Struder, L. The direct measurement of the signal charge behavior in pnccds with subpixel resolution. *Nuclear Instruments & Methods in Physics Research Section a-Accelerators Spectrometers Detectors and Associated Equipment* **568**, 128–133 (2006).

[28] Evans, G. *The method of Multiple wavelength Anomalous Diffraction using Synchrotron Radiation at optimal X-ray energies: Application to Protein Crystallography.* Ph.D. thesis, University of Warwick (1994).

[29] Beaumont, J. H. & Hart, M. Multiple bragg reflection monochromators for synchrotron-x radiation. *Journal of Physics E-Scientific Instruments* **7**, 823–829 (1974).

[30] Bjeoumikhov, A., Langhoff, N., Wedell, R., Beloglazov, V., Lebed'ev, N. & Skibina, N. New generation of polycapillary lenses: manufacture and applications. *X-Ray Spectrometry* **32**, 172–178 (2003).

[31] Gao, N. & Janssens, K. *Polycapillary X-Ray Optics*, chap. 3.3, 89–110 (Wiley&Sons Ltd., 2004).

[32] Gao, N. & Ponomarev, I. Y. Polycapillary x-ray optics: manufacturing status, characterization and the future of the technology. *X-Ray Spectrometry* **32**, 186–194 (2003).

[33] Gao, N., Ponomarev, I. Y., Xiao, Q. F., Gibson, W. M. & Carpenter, D. A. Monolithic polycapillary focusing optics and their applications in microbeam x-ray fluorescence. *Applied Physics Letters* **69**, 1529–1531 (1996).

[34] MacDonald, C. A. & Gibson, W. M. Applications and advances in polycapillary optics. *X-Ray Spectrometry* **32**, 258–268 (2003).

[35] Proost, K., Vincze, L., Janssens, K., Gao, N., Bulska, E., Schreiner, M. & Falkenberg, G. Characterization of a polycapillary lens for use in micro-xanes experiments. *X-Ray Spectrometry* **32**, 215–222 (2003).

[36] Samber, B. D. *Spatially Resolved X-Ray Micro/Nano-Spectroscopy and Imaging on the Model Organism Daphnia Magna Using Laboratory and Synchrotron Sources.* Ph.D. thesis, Universiteit Gent (2010).

[37] Schields, P. J., Gibson, D. M., Gibson, W. M., Gao, N., Huang, H. P. & Ponomarev, I. Y. Overview of polycapillary x-ray optics. *Powder Diffraction* **17**, 70–80 (2002).

[38] Vincze, L., Janssens, K., Adams, F., Rindby, A. & Engstrom, P. Interpretation of capillary generated spatial and angular distributions of x rays: Theoretical modeling and experimental verification using the european synchrotron radiation facility optical beam line. *Review of Scientific Instruments* **69**, 3494–3503 (1998).

[39] Kirkpatrick, P. & Baez, A. V. Formation of optical images by x-rays. *J Opt Soc Am* **38**, 766–774 (1948).

[40] Yumoto, H. *et al.* Focusing of x-ray free-electron laser pulses with reflective optics. *Nature Photonics* **7**, 43–47 (2013).

[41] Hignette, O., Rostaing, G., Cloetens, P., Rommeveaux, A., Ludwig, W. & Freund, A. Submicron focusing of hard x-rays with reflecting surfaces at the esrf. *X-Ray Micro- and Nano-Focusing: Applications and Techniques Ii* **4499**, 105–116 (2001).

[42] Dabin, Y., Rostaing, G., Hignette, O., Rommeveaux, A. & Freund, A. The present state of kirkpatrickbaez mirror systems at the esrf. *X-Ray Mirrors, Crystals, and Multilayers II* **4782**, 235–245 (2002).

[43] Hignette, O., Cloetens, P., Rostaing, G., Bernard, P. & Morawe, C. Efficient sub 100nm focusing of hard x rays. *Review of Scientific Instruments* **76**, 063709 (2005).

[44] Hignette, O., Cloetens, P., Morawe, C., Borel, C., Ludwig, W., Bernard, P., Rommeveaux, A. & Bohic, S. Nanofocusing at esrf using graded multilayer mirrors. *Synchrotron Radiation Instrumentation, Pts 1 and 2* **879**, 792–795 (2007).

[45] Garrevoet, J., Vekemans, B., Tack, P., De Samber, B., Schmitz, S., Brenker, F. E., Falkenberg, G. & Vincze, L. Methodology toward 3d micro x-ray fluorescence imaging using an energy dispersive charge-coupled device detector. *Anal Chem* **86**, 11826–11832 (2014).

[46] Mimura, H., Matsuyama, S., Yumoto, H., Hara, H., Yamamura, K., Sano, Y., Shibahara, M., End, K., Mori, Y., Nishino, Y., Tamasaku, K., Yabashi, M., Ishikawa, T. & Yamauchi, K. Hard x-ray diffraction-limited nanofocusing with kirkpatrick-baez mirrors. *Japanese Journal of Applied Physics Part 2-Letters and Express Letters* **44**, L539–L542 (2005).

Chapter 4

Bulk XAS

4.1 Introduction

Bulk X-ray absorption spectroscopy (XAS) is the "mother technique" from which micro- and nano-XAS were eventually developed. In this approach, the sample is illuminated by a 'large' X-ray beam with a size of the order of a few millimetres. The absorption spectrum, resulting from an experiment illustrated by Figure 4.1, represents the average response of the entire illuminated sample volume. Despite the current synchrotron radiation development trend towards smaller beam sizes, currently achieving sizes down to only a few nanometres,[1] bulk XAS experiments remain very popular as they are the ideal approach when studying samples with millimetre sized homogeneity length scales.

This method is not ideal when investigating materials containing chemical structure hetero-

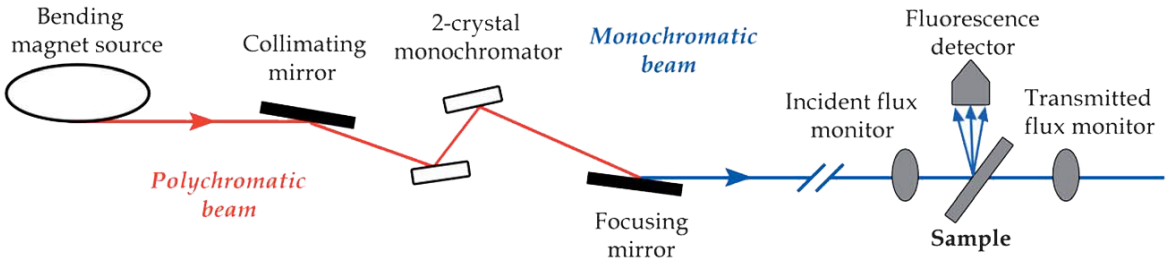

Figure 4.1: Schematic representation of a X-ray absorption experiment using synchrotron radiation. Represented are transmission mode, making use of the incident and transmitted flux monitors, and fluorescence emission mode, making use of the incident flux monitor and fluorescence detector. Figure adapted from Ortega, R. *et al.*[2]

geneities. Nevertheless, in case of applications when the samples can be considered locally homogeneous, or in cases when the investigation of the (sub-mm scale) chemical heterogeneity in a spatially resolved manner is of lesser importance, bulk XAS measurements offer an easily applicable, methodologically less demanding approach.

An advantageous property of bulk XAS is the higher flux and stability of the primary X-ray beam interacting with the sample compared to that achievable in a micro-focus setup, resulting in better signal to noise ratios. Additionally, due to the homogeneous nature of the sample - or at least the assumption that this is the case on a scale comparable to the utilized beam size - most samples can be optimized in such a way that transmission mode experiments are possible, which again provide better counting statistics (Section 2.3).

Due to the high flux attainable at synchrotron radiation facilities, bulk XANES experiments can be performed at a rate of less than a minute per spectrum, even down to a sub-second frequency, creating the opportunity of in-situ experiments such as those following catalytic processes.[3–6] Due to the time required for EXAFS measurements, in-situ experiments are typically not feasible. Exceptions include the application of quick-scanning EXAFS (QEXAFS or Q-XAS)[7, 8] and the study of relatively slow reactions, coupled with sufficient repeats of the experiments. Both bulk XANES and EXAFS experiments can also be coupled with several specialized sample environments such as cryo chambers or high pressure and temperature cells.[9–13] This is often difficult for microspectroscopic approaches due to spatial constraints. As such, bulk XAS is often the most fruitful approach towards XAS if spatially resolved information is not relevant.

Below, two applications of bulk XANES and EXAFS are presented, illustrating the possibilities of these methods.

4.2 Application: Study of V on metal-organic framework materials

This section is partially adapted from Wang *et al.*[a]

[a] G. Wang, K. Leus, S. Couck, P. Tack, H. Depauw, Y. Y. Liu, L. Vincze, J. F. Denayer, P. Van Der Voort, Enhanced gas sorption and breathing properties of the new sulfone functionalized COMOC-2 metal organic framework. *Dalton transactions* **45**, 9485-9491, doi:10.1039/c6dt01355d (2016).

4.2.1 Introduction

Metal-organic frameworks (MOFs) or coordination polymers (PCPs) are crystalline and porous materials consisting of metal ions or clusters coordinated to multidentate organic ligands.[14] They are characterized by high chemical tunability, framework flexibility, large surface area and pore volume and are regularly studied in the framework of gas adsorption, separation and as heterogeneous catalysts.[15–27] For instance, the gas sorption behaviour of MOFs toward different adsorbates as well as their thermal and chemical stability and catalytic activity for selected reactions can be functionalized by employing different linkers, as well as careful selection of the metal ion or cluster.[28, 29]

A series of Al/V doped MOFs (COMOC-2 and MIL-53) were investigated using XANES and EXAFS to provide information on the structure of MIL-53-Al (Al^{III}(OH)BDC, MIL: Matériaux de l'Institut Lavoisier) after replacing the Al(III) centre by $V^{(III/IV/V)}$ resulting in a mixed-metal MOF MIL-53-Al/V. More specifically, the oxidation state and the coordination environment can reveal essential information on structural changes that occur during vanadium incorporation. Doping MIL-53-Al with vanadium offers the opportunity to incorporate a catalytically active element in an ultra-stable framework. The fact that this framework shows extreme flexibility is also of great scientific interest. The incorporation of vanadium in the MIL-53-Al framework is of significant interest to understand in more detail its breathing behaviour (open and closing of the structure by external stimuli such as exposure to CO_2, temperature, moisture) and the catalytic activity, as studying the coordination environment and oxidation state are essential to gather information on what the trigger for this breathing phenomena is.[30, 31] Additionally, a comparison is made between sulfone based and non-sulfone based COMOC-2 MOFs. Both materials display breathing behaviour, although the sulfone based COMOC-2 MOF (SO_2-COMOC-2) has a decreased barrier for this structural transition.[32]

4.2.2 Experimental

XAS measurements were performed onbeamline BM26A (Dutch-Belgian beamline, DUBBLE) at the ESRF (Grenoble, France).[33] The X-ray beam, originating from a 0.4 T bending magnet, was monochromatised using a Si(111) crystal monochromator. Higher harmonics were rejected and vertical focussing is obtained by using a Si and Pt coated mirror downstream from the monochromator. The primary and transmitted beam intensities were

monitored using ionization chambers, filled with gasses to provide approximately 10 % and 70 % absorption before and after the sample position respectively. The sample was cooled to 80 K using a He gas filled cryostat (Oxford Instruments, Figure 4.2) to reduce thermal vibration effects, expressed in part by the Debye-Waller factor (Section 2.3.2), perturbing the true EXAFS signal. In order to prevent the presence of pinhole effects, ultimately attenuating the XAS signal, the samples were prepared as pressed pellets, containing an amount of analyte providing a theoretical absorption of two absorption lengths at 5515 eV. When necessary, cellulose was added as a binding agent. XANES scans were performed over the V K-edge (E_0: 5465 eV) with 0.3 eV steps over the pre-edge peak and edge regions. Multiple repetitions were performed to obtain better data quality. XANES data were normalized and processed using the Athena software package.[34] The pre-edge peak, corresponding to the 1s–3d electron transition, was fitted with a pseudo-voigt function, after subtracting an error function corresponding to the rising edge.

EXAFS data was acquired up to 9 $Å^{-1}$ in steps of 0.025 $Å^{-1}$.The Viper[36] software package was used to process the EXAFS data and fit FEFF7[37, 38] calculated scatter paths in order to determine the amount of neighbouring atoms and bond distances. The amplitude reduction factor S_0^2 was determined to be 0.72 by fitting a vanadium foil EXAFS Fourier transform between 1.5 and 5.4 Å (Figure 4.3). E_0 and Debye-Waller factor for the V-O scatter paths were constrained to -2 eV and 0.025 respectively. Each first scatter (1 to 2.5 Å) shell was fitted by two separate V-O scatter paths with V-O starting value distances of 2 and 2.5 Å respectively.

4.2.3 Results and Discussion

As shown by Silversmit *et al.*, the main edge (μx = 0.5) and "white line" (1s $\rightarrow$ 4p transition) energy position is dependent on the V oxidation state.[4, 39] Here, the main edge position was used to determine the nominal oxidation state, as this approach is less sensitive to fluctuations caused by varying counter ion types. The XANES spectra of the reference compounds with varying V oxidation states and the COMOC-2 MOF samples are shown in Figure 4.4. The linear correlation between oxidation state and main edge position is displayed in Figure 4.5. Nominal oxidation states for COMOC-2 and SO_2-COMOC-2 are determined to be 4.03 and 3.7, respectively. Provided the presence of V^{III} and/or V^{IV} cations, it can be concluded that in COMOC-2 all V atoms are in the +IV state, whereas the SO_2-COMOC-2 materials exhibit a V^{III}/V^{IV} ratio of 30/70 (0.43).

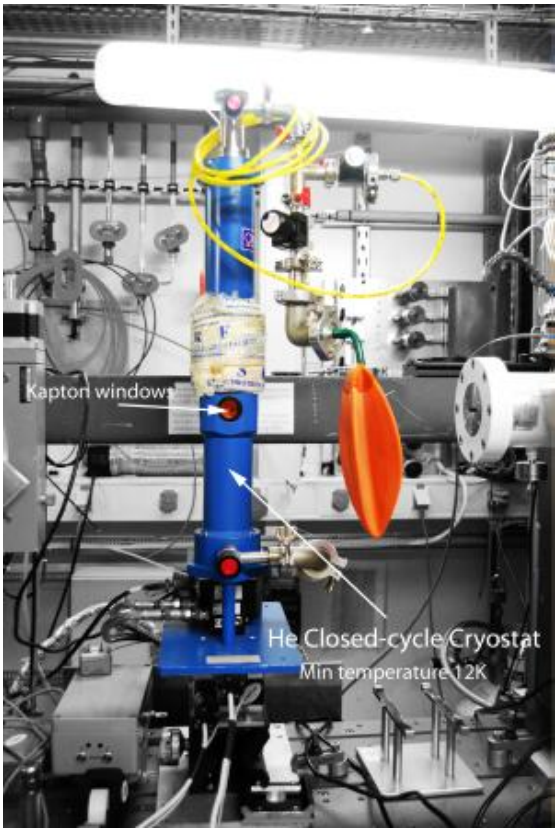

Figure 4.2: Photograph of the BM26A beam line Oxford Instruments cryostat. Right in view is a picture of the first ionisation chamber, monitoring the primary X-ray beam flux. The cryostat can be operated in both transmission and emission. Photograph adapted from the ESRF - DUBBLE website.[35]

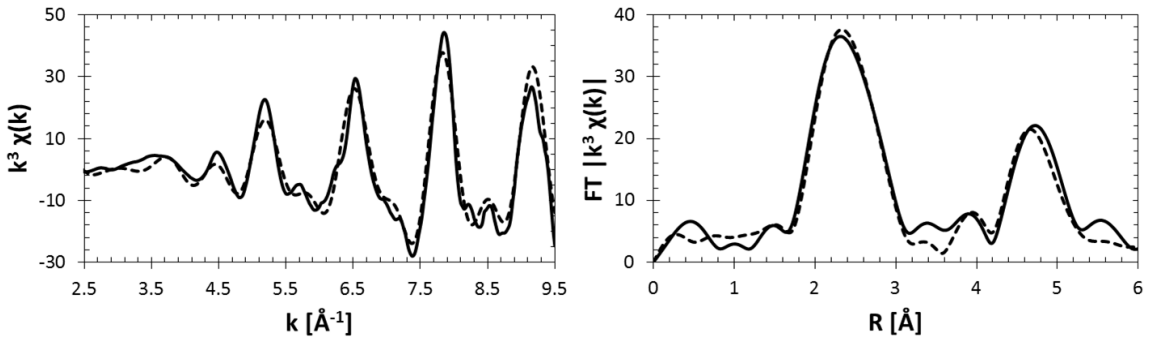

Figure 4.3: Vanadium K-edge EXAFS $k^3 \cdot \chi(k)$ spectrum (left) and Fourier transform (right), with respective fits, of a V foil measured at the DUBBLE beamline (BM26A, Grenoble, France).

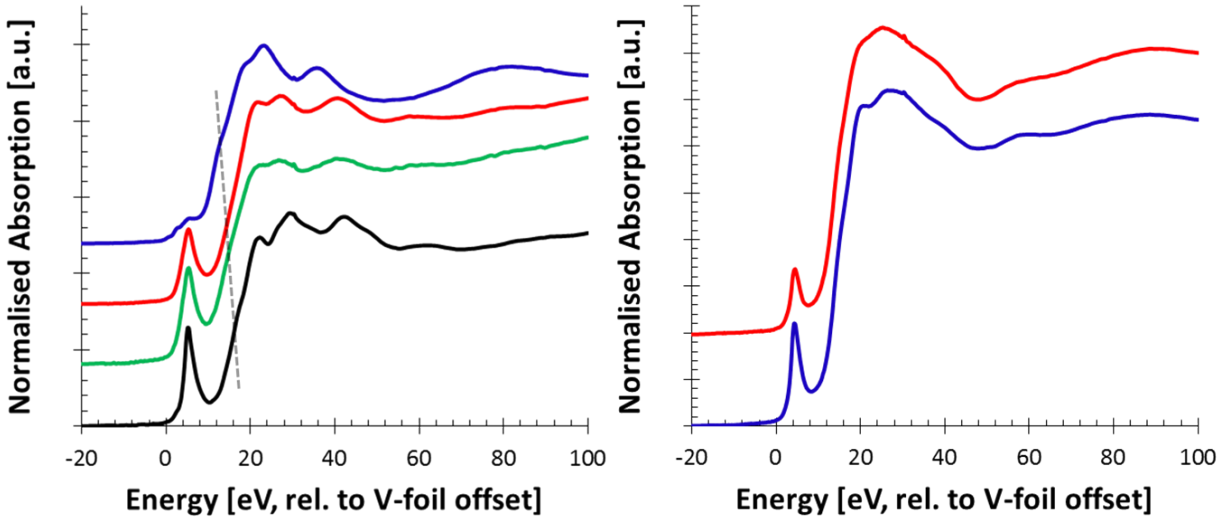

Figure 4.4: Vanadium K-edge XANES. Left, from bottom to top, nominal oxidation state in parenthesis: V_2O_5 (black, +5), V_6O_{13} (green, +4.3), VO_2 (red, +4) and V_2O_3 (blue, +3). A line guide is displayed to show the relation between V oxidation state and main edge position; Right: SO_2-COMOC-2 MOF (top, red) and COMOC-2 MOF (bottom, blue).

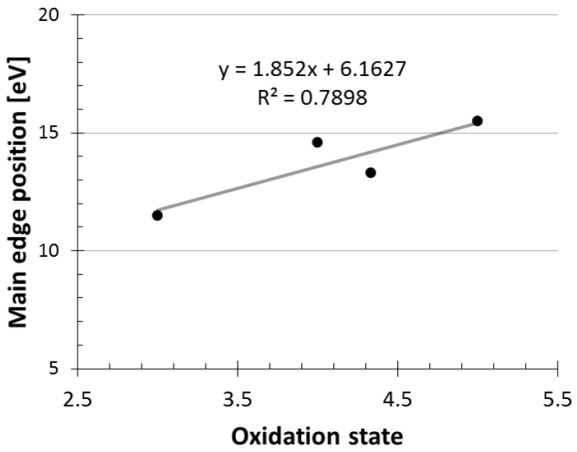

Figure 4.5: Vanadium K-edge XANES main edge ($\mu x = 0.5$) position trend as a function of oxidation state for the pure vanadium oxides V_2O_5, V_6O_{13}, VO_2 and V_2O_3. Energy positions are relative to the V-foil offset.

Similarly, the oxidation state of a series of MIL-53 MOFs with variable Al/V content was measured, the results of which are displayed in Table 4.1. It is clear from this data that the as synthesized vanadium samples have a nominal oxidation state of approximately 3.5, denoting a 50/50 V^{III}/V^{IV} ratio. By performing a calcination step, the vanadium is changed to pure V^{IV}. The Al/V content or type of MOF does not appear to influence the V oxidation state.

Additionally, the V K-edge XANES pre-edge peak supplies information on the vanadium coordination with a large pre-edge peak denoting coordination without inversion symmetry (e.g. tetrahedral or distorted octahedral) and a small to no pre-edge peak represents coordination with inversion symmetry (e.g. octahedral).[40] A decrease in pre-edge peak area is seen from COMOC-2 (2.36), to SO_2-COMOC-2 (0.88), showing a transformation of V coordination from a lack of inversion symmetry for COMOC-2 to more inversion symmetry for SO_2-COMOC-2. Additionally, calcined samples have a larger pre-edge peak and thus less inversion symmetry. A similar trend can be seen for increasing V content: with higher V content, the average V symmetry shows less inversion symmetry.

In this MOF structure, the closest neighbouring atoms (first coordination shell) to V and Al are O atoms. EXAFS experiments were performed to obtain more information on the amount and distance of these atoms. The $\chi(k)$ results and corresponding Fourier transform fits are displayed in Figure 4.6 and Table 4.2. Despite the unrealistically large fluctuation of the amount of neighbouring atoms N, caused by fitting uncertainties concerning the E_0 value, spline subtraction and its influence on N, a general trend can be perceived nonetheless. As such, these results for N should be considered only as a qualitative result.

It appears that with increasing amount of V, values for N decrease. A similar trend, although admittedly less convincing, is seen when comparing N for a sample before calcination (as synthesized, a.s.) and after. Also an increase in photoelectron scatter path length R, denoting the V-O bond distance, with increasing V content can be perceived for as synthesized samples, however this trend is less clear for calcined samples. In general, scatter path lengths increase when comparing a sample before (a.s.) and after calcination.

4.2.4 Conclusion

Interpreting the XANES and EXAFS results, a chemical transition of V in the samples can be seen when increasing the V content. Initially, in a sample with high Al/V content,

Table 4.1: Overview of V K-edge XANES results on Al/V MOFs, displaying integrated pre-edge peak area and oxidation state with varying Al/V content and the calcination during MOF synthesis. Missing values (-) are due to the lack of a pre-edge peak in the XANES spectrum.

Compound	**Al/V content**	**Integrated Area**	**Main edge position [eV]**	**Rel. edge position***	**Oxidation State**
SO_2-COMOC-2	0/100	0.66	5478.1	13.1	3.7
COMOC-2	20/80	1.69	5478.2	13.2	3.8
	10/90	1.77	5478.6	13.6	4.0
	0/100	2.36	5478.6	13.6	4.0
MIL-47 a.s.	0/100	0.26	5477.5	12.5	3.4
MIL-47 calc.	0/100	2.12	5479.0	14.0	4.2
MIL-47 calc.†	0/100	2.77	5478.5	13.5	4.0
MIL-53 a.s.	99/1	-	5477.4	12.4	3.4
	98/2	0.35	5477.6	12.6	3.5
	95/5	0.50	5477.4	12.4	3.4
	75/25	0.37	5477.3	12.3	3.3
	50/50	0.35	5477.8	12.8	3.6
MIL-53 calc.	99/1	1.44	5478.8	13.8	4.1
	98/2	0.61	5479.0	14.0	4.2
	95/5	0.77	5479.0	14.0	4.2
	75/25	1.39	5478.7	13.7	4.1
	50/50	1.86	5478.7	13.7	4.1

*Rel.: relative to E_0; a.s.: as synthesized; calc.: calcined
†: calcined at 380 °C

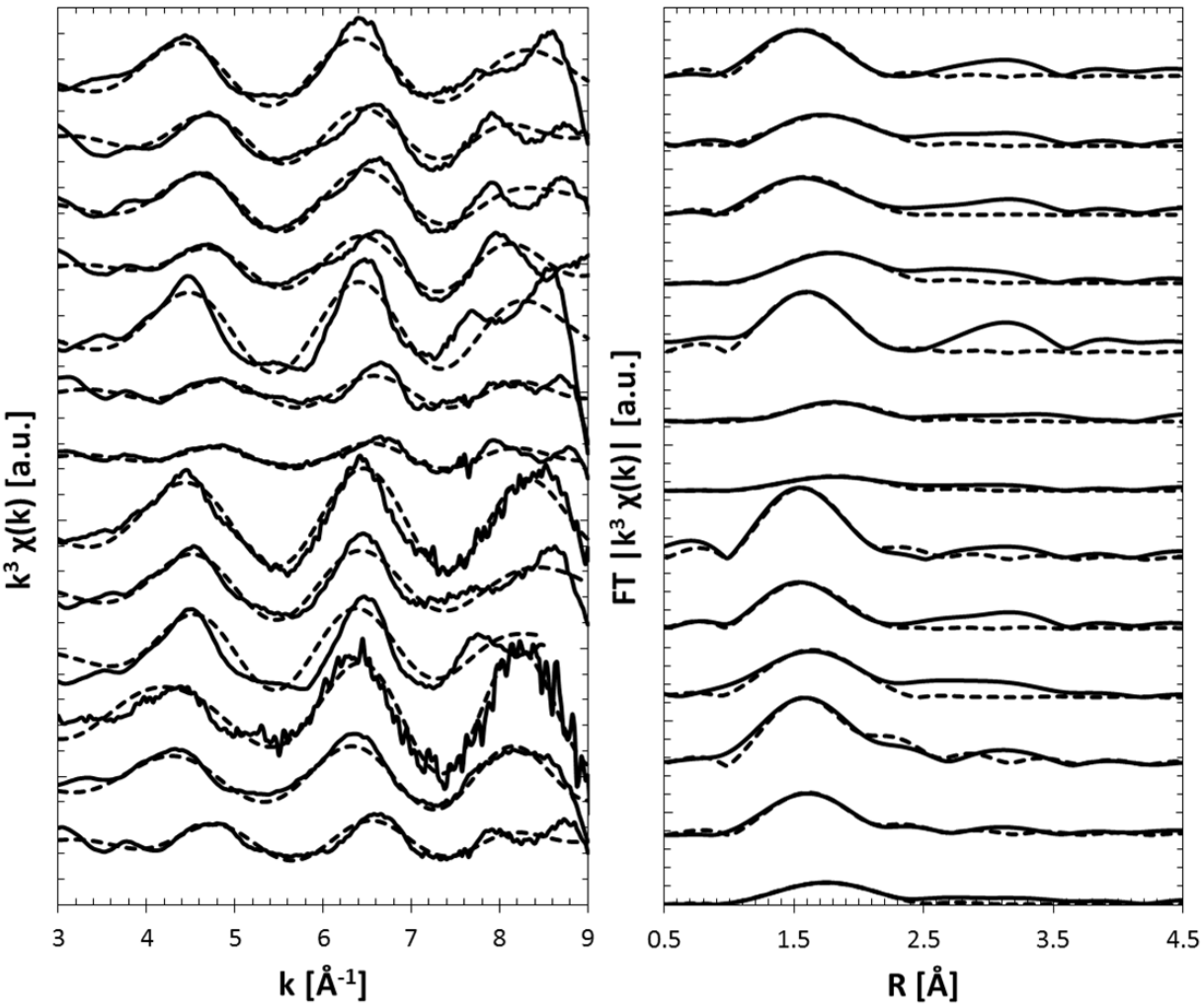

Figure 4.6: Vanadium K-edge EXAFS $k^3 \cdot \chi(k)$ spectra (left) and their Fourier transform (right) (solid curves) and respective fits (dotted curves) for a series of Al/V MOFs. Top to bottom (Al/V): SO_2-COMOC-2 (0/100), COMOC-2 (20/100), COMOC-2 (10/90), COMOC-2 (0/100), MIL-47 a.s (0/100), MIL-47 calc. (0/100), MIL-47 calc. 380 °C (0/100), MIL-53 a.s. (98/2), MIL-53 a.s. (75/25), MIL-53 a.s. (50/50), MIL-53 calc. (98/2), MIL-53 calc. (75/25), MIL-53 calc. (50/50).

Table 4.2: Overview of V K-edge EXAFS results on Al/V MOFs, displaying the nearest neighbour degeneracy N, scatter path length R, Debye-Waller factor σ_w and theoretical FEFF edge shift E_0. Standard deviations are noted in between brackets.

Compound	**Al/V content**	**N**	**R** [Å]	σ_w [Å^2]	$\mathbf{E_0}$ **[eV]**
SO_2-COMOC-2	0/100	6.1 (1.3)	2.13 (0.02)	0.0025	-2.0
COMOC-2	20/80	5.8 (1.3)	2.29 (0.02)	0.0025	-2.0
	10/90	6.0 (0.3)	2.19 (0.01)	0.0025	-2.0
	0/100	5.7 (0.9)	2.29 (0.02)	0.0025	-2.0
MIL-47 a.s.	0/100	8.6 (1.2)	2.17 (0.01)	0.0025	-2.0
MIL-47 calc.	0/100	3.4 (0.6)	2.30 (0.03)	0.0025	-2.0
MIL-47 calc.†	0/100	2.7 (0.5)	2.30 (0.01)	0.0025	-2.0
MIL-53 a.s.	98/2	9.1 (1.6)	2.11 (0.01)	0.0025	-2.0
	75/25	6.5 (1.1)	2.17 (0.01)	0.0025	-2.0
	50/50	8.1 (2.1)	2.26 (0.03)	0.0025	-2.0
MIL-53 calc.	98/2	12.8 (1.5)	2.18 (0.01)	0.0025	-2.0
	75/25	6.0 (0.6)	2.15 (0.01)	0.0025	-2.0
	50/50	4.1 (0.5)	2.28 (0.01)	0.0025	-2.0

a.s.: as synthesized; calc.: calcined, $S_0^2 = 0.72$
†: calcined at 380 °C

the V is fixed in a centrosymmetric, high N geometry with comparably short V-O bond distances. As more V is added to the system, it is capable of changing the structure which was previously defined by the Al ions, turning into a non-centrosymmetric, lower N geometry with generally larger V-O bond distances. As such, a transition from octahedral V-O surrounding to pyramidal V-O surrounding with increasing V content is suggested. Additionally, calcination of the sample further increases the transition of octahedral V-O to pyramidal V-O. It should be noted that this structural transition is merely a hypothesis based on the XAS results, and should be confirmed by additional experiments.

4.3 Application: Study of Au on photocatalytic Au/TiO_2 materials[41]

This section is adapted from Meire *et al.*[b]

[b]M. Meire, P. Tack, K. De Keukeleere, L. Balcaen, G. Pollefeyt, F. Vanhaecke, L. Vincze, P. Van Der Voort, I. Van Driessche, P. Lommens, Gold/titania composites: An X-ray absorption spectroscopy study

4.3.1 Introduction

Gold/titania (Au/TiO_2) composite materials have a wide range of applications including catalysis (e.g. water–gas shift reaction), photocatalysis (e.g.water purification, H_2 production), photovoltaics and photoelectrochemical solar cells.[42–45] These materials can be synthesized following several approaches.[46–54] Here, Au/TiO_2 composite materials were prepared by impregnating a mesoporous titania powder with an aqueous solution of $HAuCl_4$. In a subsequent step, the salt is reduced using one of the following reduction methods: chemical (citrate, $NaBH_4$),[49, 55] thermal (H_2 atmosphere)[50, 56] or by UV irradiation.[51, 57]

Although the changes in gold particle size, specific surface area of the titania matrix and (photo)catalytic activity as a function of the synthesis method are well discussed,[50, 56, 58–61] the influence of the above reduction methods on the Au oxidation state is not,[62, 63] despite its large effect on the catalytic activity of the materials. For instance, a positive charge on gold particles increases the activity in the case of CO conversion due to a better adsorption of CO,[62] yet the photocatalytic hydrogen production on Pt/TiO_2 is less influenced by a charge on the Pt atoms.[64] XANES experiments were performed on a set of Au/TiO_2 composite materials in order to obtain additional information on the Au state as a function of the reduction method used during synthesis.

4.3.2 Experimental

Details on how the Au/TiO_2 materials were synthesized are outside the scope of this thesis, and are published elsewhere.[41] All samples have a gold loading of approximately 0.3 w%. Different procedures to reduce the gold salt in the samples were applied:

- illumination during 6 h with a UV black light (Vilber, 136 $\mu W/cm^2$, maximum intensity at 365 nm),
- thermal reduction for 2 h at 200 °C under 5% H_2/Ar atmosphere,
- microwave (MW) irradiation for 1 h at 120 °C, dispersed in 4 mL aqueous solution of NaOH (pH = 10). The powder was washed with water and dried at room temperature in the dark,

on the influence of the reduction method. *Spectrochimica Acta Part B: Atomic Spectroscopy* **110**, 45-50, doi:10.1016/j.sab.2015.05.007 (2015).

- 0.2 mL of 0.1 M $NaBH_4$ was added to a dispersion of Au/TiO_2 in 15 mL deionized water and stirred for 3 h. Afterwards, the powder was washed with deionized water and dried at room temperature in the dark.

All samples were stored in the dark at 25 °C and the whole characterization was performed within a week after synthesis to prevent change of the Au oxidation state by exposure to air or light.

XANES spectroscopy experiments were performed at BM26A, the XAS station of the Dutch–Belgian beamline (DUBBLE) at the ESRF.[33] The beam size at the sample position was approximately $3\times1\,mm^2$, defined by slit systems. Samples were fixed as powder between two 25 μm polyimide tapes (Goodfellow SARL) in a circular holder with surface area of 1.3 cm^2. The X-ray absorption signal was monitored in emission mode using a Vortex-EM silicon drift detector. A XANES scan consisted of 139 energy steps, with an acquisition time of 1 s/step.

In addition, high resolution XANES data were acquired at ID26 (ESRF, Grenoble, France) using a Si(311) monochromator (energy resolution $\Delta E/E$ of $\sim 0.3\times10^{-4}$). A wavelength dispersive spectrometer with an energy resolution lower than the core-hole lifetime (5.41 eV for the Au-L_3 edge[65]) was used to monitor the emitted radiation, resulting in significantly sharpened spectral features.[66–69] The spectrometer was tuned to 9.713 keV (Au-L_α fluorescence line) using the spherically bent Ge(600) wafer Bragg reflection. A beam size of $0.3(V)\times1(H)\,mm^2$ at the sample position was used. Samples were pressed to pellets (5 mg powder dispersed in cellulose) and moved through the beam to illuminate a new area after each scan to avoid beam induced changes. A XANES scan consisted of 1003 energy steps, with an acquisition time of 30 s/scan. 60 scans were averaged to obtain better counting statistics. At both beamlines experiments were performed at room temperature (298 K).

Raw XANES data were normalized for incident beam flux using the primary ionization chamber signal, pre-edge subtracted using a linear function and post-edge normalized at an energy of E_0+50 eV. Additionally, the slow variations caused by the atomic absorption profile before and after the edge were subtracted to facilitate linear combination analysis spectra comparisons.[70] The obtained XANES profiles were compared to the transmission mode XANES profiles of a series of reference compounds (Au foil, AuCN, $KAu(CN)_2$ and $HAuCl_4$) by means of linear combination fitting, resulting in the semiquantitative chemical speciation of the gold in the sample.[71, 72]

4.3.3 Results and Discussion

Beam induced changes were detected by performing multiple fast scans as a function of energy. The XANES spectra of the non-reduced and UV reduced samples clearly present an intense peak after the absorption edge (∼11.918 keV), historically known as the white line, which decreases in intensity as a function of time (amount of scans) (Figure 4.7A). For this reason only the first measured XANES scan of these samples was used as representative of the sample's initial state.

The XANES spectra measured at BM26A are displayed in Figure 4.8. The white line represents the 2p→5d electron transition, providing information on the density of the unoccupied 5d states near the Fermi level and thus is closely related to the oxidation state of the gold atoms.[73, 74] The decrease of the white line represents a smaller density of unoccupied 5d states and thus a reduction in oxidation state.

The white line of the UV reduced sample was significantly smaller than the one of the unreduced sample, indicating that UV irradiation partially reduced the gold. In the other samples no white line was present and the spectra did not change as a function of time, hinting at the presence of fully reduced Au^0 particles.

XANES linear combination fitting was performed using an Au foil and the unreduced sample XANES spectra. The XANES spectrum of the unreduced sample was used as a reference for the sample's initial state instead of the pure $HAuCl_4$ XANES spectrum, as the surrounding titania matrix has an influence on the XANES shape. The fitting results showed that in case of the thermal and chemical reduction, transformation from Au^{3+} to Au^0 was complete, while MW reduction left 4 % unreduced and UV irradiation only reduced half (52 %) of the gold atoms.

Using high energy resolution fluorescence detection (HERFD) XANES at ID26, the energy dependent post-edge features can be observed in more detail showing more fluctuations and more pronounced amplitudes, allowing for better determination of the chemical surroundings of the adsorbing atom. No spectral changes as a function of time were observed as the sample was scanned through the beam during the HERFD XANES experiments, illuminating a fresh part of the sample during each energy scan.

As a correlation exists between the size and shape of the Au-L_3 XANES post-edge features and the probed particle size for gold (nano)particles,[75, 76] it was decided to perform HERFD

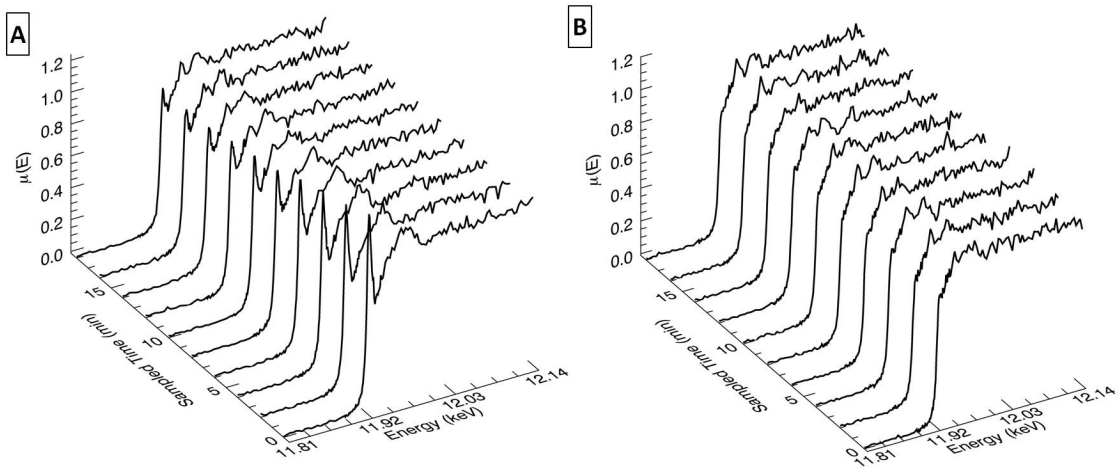

Figure 4.7: Au L_3-edge XANES profiles of unreduced (A) and microwave reduced (B) Au/TiO_2 as a function of time, displaying the beam induced changes for the unreduced sample.

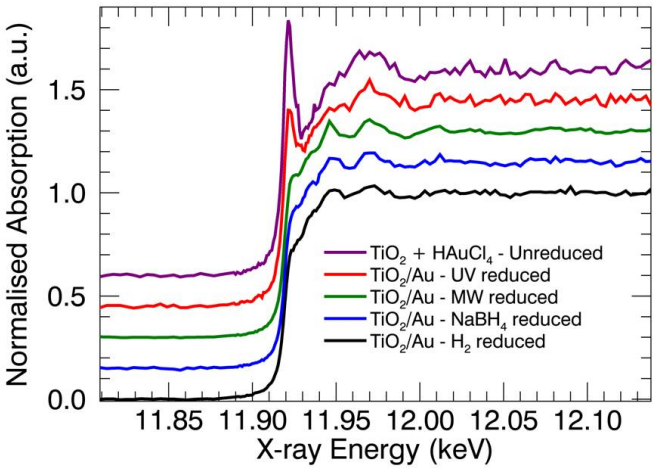

Figure 4.8: Au L_3-edge XANES profiles for Au/TiO_2 composite materials with different reduction methods, as measured at beamline BM26A.

XANES measurements for the microwave and UV reduced Au/TiO_2 samples with gold particles of 11.5 nm and 10.5 nm, respectively (Figure 4.9). For the two samples, the post-edge features are nearly identical, except for the white line, which is more intense in the case of the UV reduced sample suggesting a larger density of unoccupied 5d states and thus (partial) oxidation of the metal particles in case of the UV reduced sample. Additionally, the absorption edge position of the two Au/TiO_2 samples and the gold foil reference coincide, showing that the gold in the composite materials has the same oxidation state as the metal foil. As also the post-edge features of the XANES spectra of the samples are similar to those of the XANES features of the metal foil, it can be concluded that the gold in the Au/TiO_2 samples has a similar chemical surrounding as found in metallic gold.

Therefore, the oxidized Au species in the UV reduced sample cannot simply be identified as unreduced salt ($HAuCl_4$), as then the absorption edge should be shifted to lower energies and the post-edge features observed for the Au/TiO_2 samples should clearly differ from those of the Au foil. The increase of the white line intensity of the UV reduced sample can as such only be explained as originating from a positive charge on the gold particles. As the charge is likely to be spread over the gold particle, resulting in a small charge on each gold atom in the cluster, it is not impossible that the local Au structure does not change significantly compared to the case with no charge, as seen in Figure 4.9 when comparing the XANES post-edge regions.

4.3.4 Conclusion

XANES experiments were performed on a series of Au/TiO_2 composite materials, which were treated by different reduction procedures. The increase in white line intensity of the UV reduced sample can be explained by a different interaction with the titania support compared to the microwave (MW) reduced sample. As the MW reduced sample does not show an increased white line intensity, the gold nanoparticles have only limited interaction with the titania support. An explanation for the positive charge might be found in the used reduction method: UV reduction is the only method that uses the photoelectrical properties of the titania matrix to reduce the gold salt. The other reduction methods use 'external' influences to reduce the gold salt. The use of the titania matrix during the reduction step might cause a stronger interaction between the gold nanoparticles and the titania matrix.

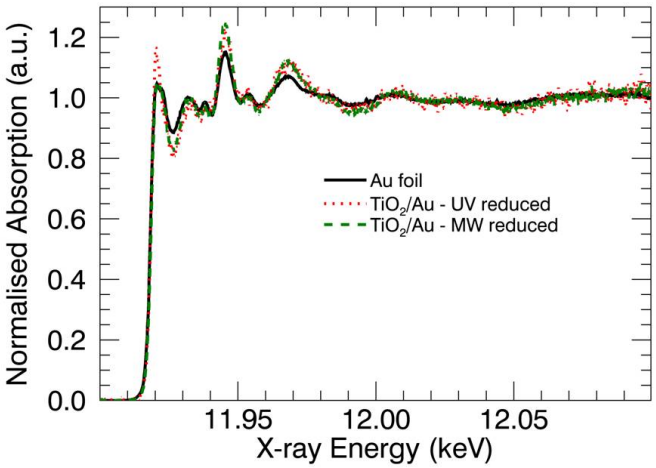

Figure 4.9: Au L_3-edge XANES profiles for Au/TiO_2 composite materials with different reduction methods, as measured at beamline BM26A.

The positive charge on the gold nanoparticles could be explained as follows. During UV illumination, electron and hole pairs are formed in the titania matrix. The electrons will reduce the gold ions to form gold nanoparticles, and the holes will be scavenged by surface bound hydroxyl groups. As the experiment is performed on dry Au^{3+}/TiO_2 powder, the amount of surface bound hydroxyl groups might not be sufficient to scavenge all photogenerated holes produced during 6 h of illumination and part of these photogenerated holes will oxidize the gold nanoparticles, generating a partial positive charge.

A positive charge on the gold nanoparticles can lead to a reduction in photocatalytic activity of the composite materials as photogenerated electrons will neutralize this positive charge and therefore will not participate in the generation of a photocurrent.

4.4 Summary

Bulk XAS experiments are performed by illuminating the sample with a broad beam, resulting in spectra which represent the average response from the illuminated sample volume. Despite this lack of spatially resolved information, bulk XAS experiments are useful due to their general applicability and fairly simple measurement setup.

Additionally, bulk XAS experiments are easily extended by inserting special sample environment chambers and/or simultaneously coupling different X-ray based analytical tech-

niques. Furthermore, bulk XAS experiments are often performed *in situ*, assisted by the fairly fast data acquisition scheme, often providing useful insights in chemical reactions that are otherwise difficult to monitor.

As such, XAS analyses should always be considered whether to be performed in bulk mode or whether spatial resolution is of higher priority, as the achieved data quality in a given time frame is significantly different for both approaches. When spatially resolved information is essential, the X-ray beam size can be limited to excite only a small (micro- or nanoscopic) area of the sample, after which the sample can be raster scanned through this micro- or nanobeam providing spatially resolved information. This approach, focussing down the X-ray beam to microscopic dimensions, is further discussed in Chapter 5.

References

[1] Laforce, B., Schmitz, S., Vekemans, B., Rudloff, J., Garrevoet, J., Tucoulou, R., Brenker, F. E., Martinez-Criado, G. & Vincze, L. Nanoscopic x-ray fluorescence imaging of meteoritic particles and diamond inclusions. *Anal Chem* **86**, 12369–12374 (2014).

[2] Ortega, R., Carmona, A., Llorens, I. & Solari, P. L. X-ray absorption spectroscopy of biological samples. a tutorial. *Journal of Analytical Atomic Spectrometry* **27**, 2054–2065 (2012).

[3] Sherborne, G. J. & Nguyen, B. N. Recent xas studies into homogeneous metal catalyst in fine chemical and pharmaceutical syntheses. *Chem Cent J* **9**, 37 (2015).

[4] Silversmit, G., Poelman, H., Sack, I., Buyle, G., Marin, G. B. & De Gryse, R. An in-situ reduction/oxidation xas study on the el10v8 vox/tio2(anatase) powder catalyst. *Catalysis Letters* **107**, 61–71 (2006).

[5] Silversmit, G., Poelman, H., Balcaen, V., Heynderickx, P. M., Olea, M., Nikitenko, S., Bras, W., Smet, P. F., Poelman, D., Gryse, R. D., Reniers, M.-F. & Marin, G. B. In-situ xas study on the cu and ce local structural changes in a cuo–ceo2/al2o3 catalyst under propane reduction and re-oxidation. *Journal of Physics and Chemistry of Solids* **70**, 1274–1284 (2009).

[6] Bazin, D. & Guczi, L. A review of in situ xas study on co-based bimetallic catalysts relevant to co hydrogenation. *Natural Gas Conversion Vii* **147**, 343–348 (2004).

[7] Stotzel, J., Lutzenkirchen-Hecht, D. & Frahm, R. A new stand-alone qexafs data acquisition system for in situ studies. *J Synchrotron Radiat* **18**, 165–175 (2011).

[8] Siebecker, M., Li, W., Khalid, S. & Sparks, D. Real-time qexafs spectroscopy measures rapid precipitate formation at the mineral-water interface. *Nat Commun* **5**, 5003 (2014).

[9] Badro, J., Gillet, P., McMillan, P. F., Polian, A. & Itié, J.-P. A combined xas and xrd study of the high-pressure behaviour of gaaso 4 berlinite. *EPL (Europhysics Letters)* **40**, 533 (1997). URL `http://stacks.iop.org/0295-5075/40/i=5/a=533`.

[10] Taguchi, T., Harada, J., Kiku, A., Tohji, K. & Shinoda, K. Development of a new in-laboratory xafs apparatus based on new concept. *J Synchrotron Radiat* **8**, 363–365 (2001).

[11] Pascarelli, S. & Mathon, O. Advances in high brilliance energy dispersive x-ray absorption spectroscopy. *Phys Chem Chem Phys* **12**, 5535–5546 (2010).

[12] Poe, B. T., Romano, C. & Henderson, G. Raman and xanes spectroscopy of permanently densified vitreous silica. *Journal of Non-Crystalline Solids* **341**, 162–169 (2004).

[13] Poe, B. T., Romano, C., Zotov, N., Cibin, G. & Marcelli, A. Compression mechanisms in aluminosilicate melts: Raman and xanes spectroscopy of glasses quenched from pressures up to 10 gpa. *Chemical Geology* **174**, 21–31 (2001).

[14] Long, J. R. & Yaghi, O. M. The pervasive chemistry of metal-organic frameworks. *Chem Soc Rev* **38**, 1213–1214 (2009).

[15] Paz, F. A., Klinowski, J., Vilela, S. M., Tome, J. P., Cavaleiro, J. A. & Rocha, J. Ligand design for functional metal-organic frameworks. *Chem Soc Rev* **41**, 1088–110 (2012).

[16] Farha, O. K., Yazaydin, A. O., Eryazici, I., Malliakas, C. D., Hauser, B. G., Kanatzidis, M. G., Nguyen, S. T., Snurr, R. Q. & Hupp, J. T. De novo synthesis of a metal-organic framework material featuring ultrahigh surface area and gas storage capacities. *Nat Chem* **2**, 944–948 (2010).

[17] Furukawa, H., Ko, N., Go, Y. B., Aratani, N., Choi, S. B., Choi, E., Yazaydin, A. O., Snurr, R. Q., O'Keeffe, M., Kim, J. & Yaghi, O. M. Ultrahigh porosity in metal-organic frameworks. *Science* **329**, 424–428 (2010).

[18] Serre, C., Millange, F., Thouvenot, C., Nogues, M., Marsolier, G., Louer, D. & Ferey, G. Very large breathing effect in the first nanoporous chromium(iii)-based solids: Mil-53 or cr-iii(oh)center dotO2C-C6H4-CO2center dotHO2C-C6H4-CO2H(x)center dot h2oy. *Journal of the American Chemical Society* **124**, 13519–13526 (2002).

[19] Schneemann, A., Bon, V., Schwedler, I., Senkovska, I., Kaskel, S. & Fischer, R. A. Flexible metal-organic frameworks. *Chem Soc Rev* **43**, 6062–6096 (2014).

[20] Chang, Z., Yang, D. H., Xu, J., Hu, T. L. & Bu, X. H. Flexible metal-organic frameworks: Recent advances and potential applications. *Adv Mater* **27**, 5432–5441 (2015).

[21] Lescouet, T., Kockrick, E., Bergeret, G., Pera-Titus, M. & Farrusseng, D. An alternative pathway for the synthesis of isocyanato- and urea-functionalised metal–organic frameworks. *Dalton Trans* **40**, 11359–11361 (2011).

[22] Sumida, K., Rogow, D. L., Mason, J. A., McDonald, T. M., Bloch, E. D., Herm, Z. R., Bae, T. H. & Long, J. R. Carbon dioxide capture in metal-organic frameworks. *Chem Rev* **112**, 724–781 (2012).

[23] Suh, M. P., Park, H. J., Prasad, T. K. & Lim, D. W. Hydrogen storage in metal-organic frameworks. *Chem Rev* **112**, 782–835 (2012).

[24] Li, J. R., Sculley, J. & Zhou, H. C. Metal-organic frameworks for separations. *Chem Rev* **112**, 869–932 (2012).

[25] Zlotea, C., Phanon, D., Mazaj, M., Heurtaux, D., Guillerm, V., Serre, C., Horcajada, P., Devic, T., Magnier, E., Cuevas, F., Ferey, G., Llewellyn, P. L. & Latroche, M. Effect of nh2 and cf3 functionalization on the hydrogen sorption properties of mofs. *Dalton Trans* **40**, 4879–4881 (2011).

[26] Lee, J., Farha, O. K., Roberts, J., Scheidt, K. A., Nguyen, S. T. & Hupp, J. T. Metal-organic framework materials as catalysts. *Chemical Society Reviews* **38**, 1450–1459 (2009).

[27] Farrusseng, D., Aguado, S. & Pinel, C. Metal-organic frameworks: opportunities for catalysis. *Angew Chem Int Ed Engl* **48**, 7502–7513 (2009).

[28] Burrows, A. D., Frost, C. G., Mahon, M. F. & Richardson, C. Post-synthetic modification of tagged metal-organic frameworks. *Angew Chem Int Ed Engl* **47**, 8482–8486 (2008).

[29] Tanabe, K. K., Wang, Z. & Cohen, S. M. Systematic functionalization of a metal-organic framework via a postsynthetic modification approach. *J Am Chem Soc* **130**, 8508–8517 (2008).

[30] Van der Voort, P., Leus, K., Liu, Y., Vandichel, M., Van Speybroeck, V., Waroquier, M. & Biswas, S. Vanadium metal–organic frameworks: structures and applications. *New J Chem* **38**, 1853–1867 (2014).

[31] Biswas, S., Couck, S., Denysenko, D., Bhunia, A., Grzywa, M., Denayer, J. F. M., Volkmer, D., Janiak, C. & Van Der Voort, P. Sorption and breathing properties of difluorinated mil-47 and al-mil-53 frameworks. *Microporous and Mesoporous Materials* **181**, 175–181 (2013).

[32] Wang, G., Leus, K., Couck, S., Tack, P., Depauw, H., Liu, Y. Y., Vincze, L., Denayer, J. F. & Van Der Voort, P. Enhanced gas sorption and breathing properties of the new sulfone functionalized comoc-2 metal organic framework. *Dalton Trans* **45**, 9485–9491 (2016).

[33] Nikitenko, S., Beale, A. M., van der Eerden, A. M., Jacques, S. D., Leynaud, O., O'Brien, M. G., Detollenaere, D., Kaptein, R., Weckhuysen, B. M. & Bras, W. Implementation of a combined saxs/waxs/qexafs set-up for time-resolved in situexperiments. *J Synchrotron Radiat* **15**, 632–640 (2008).

[34] Ravel, B. & Newville, M. Athena, artemis, hephaestus: data analysis for x-ray absorption spectroscopy using ifeffit. *J Synchrotron Radiat* **12**, 537–541 (2005).

[35] European synchrotron radiation facility bm26 cryostat. `http://www.esrf.eu/UsersAndScience/Experiments/CRG/BM26/Xafs/sample-environment`.

[36] Klementev, K. V. Deconvolution problems in x-ray absorption fine structure spectroscopy. *Journal of Physics D-Applied Physics* **34**, 2241–2247 (2001).

[37] Ankudinov, A. L. & Rehr, J. J. Relativistic calculations of spin-dependent x-ray-absorption spectra. *Physical Review B* **56**, R1712–R1715 (1997).

[38] Ankudinov, A. *Relativistic Spin-dependent X-ray Absorption Theory.* Ph.D. thesis, University of Washington (1996).

[39] Silversmit, G., Poelman, H., Degryse, R., Bras, W., Nikitenko, S., Florea, M., Grange, P. & Delsarte, S. Effect of nitridation on the electronic environment of vanadium in valo(n) powder catalysts, used for the ammoxidation of propane. *Catalysis Today* **118**, 344–352 (2006).

[40] Wong, J., Lytle, F. W., Messmer, R. P. & Maylotte, D. H. K-edge absorption spectra of selected vanadium compounds. *Physical Review B* **30**, 5596–5610 (1984).

[41] Meire, M., Tack, P., De Keukeleere, K., Balcaen, L., Pollefeyt, G., Vanhaecke, F., Vincze, L., Van Der Voort, P., Van Driessche, I. & Lommens, P. Gold/titania composites: An x-ray absorption spectroscopy study on the influence of the reduction method. *Spectrochimica Acta Part B: Atomic Spectroscopy* **110**, 45–50 (2015).

[42] Kubacka, A., Fernandez-Garcia, M. & Colon, G. Advanced nanoarchitectures for solar photocatalytic applications. *Chem. Rev.* **112**, 1555–1614 (2012).

[43] Idakiev, V., Tabakova, T., Yuan, Z. Y. & Su, B. L. Gold catalysts supported on mesoporous titania for low-temperature water-gas shift reaction. *Appl. Catal. A* **270**, 135–141 (2004).

[44] Guo, Y. G., Wan, L. J. & Bai, C. L. Gold/titania core/sheath nanowires prepared by layer-by-layer assembly. *J. Phys. Chem. B* **107**, 5441–5444 (2003).

[45] Chandrasekharan, N. & Kamat, P. V. Improving the photoelectrochemical performance of nanostructured TiO_2 films by adsorption of gold nanoparticles. *J. Phys. Chem. B* **104**, 10851–10857 (2000).

[46] Wang, X. D. & Caruso, R. A. Enhancing photocatalytic activity of titania materials by using porous structures and the addition of gold nanoparticles. *J. Mater. Chem.* **21**, 20–28 (2011).

[47] Li, J. & Zeng, H. C. Preparation of monodisperse Au/TiO_2 nanocatalysts via self-assembly. *Chem. Mater.* **18**, 4270–4277 (2006).

[48] Subramanian, V., Wolf, E. E. & Kamat, P. V. Catalysis with TiO_2/gold nanocomposites. effect of metal particle size on the fermi level equilibration. *J. Am. Chem. Soc.* **126**, 4943–4950 (2004).

[49] Zheng, N. & Stucky, G. D. A general synthetic strategy for oxide-supported metal nanoparticle catalysts. *J. Am. Chem. Soc.* **128**, 14278–14280 (2006).

[50] Claus, P., Bruckner, A., Mohr, C. & Hofmeister, H. Supported gold nanoparticles from quantum dot to mesoscopic size scale: Effect of electronic and structural properties on catalytic hydrogenation of conjugated functional groups. *J. Am. Chem. Soc.* **122**, 11430–11439 (2000).

[51] Kowalska, E., Abe, R. & Ohtani, B. Visible light-induced photocatalytic reaction of gold-modified titanium(iv) oxide particles: action spectrum analysis. *Chem. Commun.* **2**, 241–243 (2009).

[52] Pradhan, S., Ghosh, D. & Chen, S. W. Janus nanostructures based on Au-TiO_2 heterodimers and their photocatalytic activity in the oxidation of methanol. *Acs Appl. Mater. Interfaces* **1**, 2060–2065 (2009).

[53] Xie, Y., Ding, K., Liu, Z., Tao, R., Sun, Z., Zhang, H. & An, G. In situ controllable loading of ultrafine noble metal particles on titania. *J. Am. Chem. Soc.* **131**, 6648–6649 (2009).

[54] Wang, P., Xie, T.-F., Li, H.-Y., Peng, L., Zhang, Y., Wu, T.-S., Pang, S., Zhao, Y.-F. & Wanga, D.-J. Synthesis and plasmon-induced charge-transfer properties of monodisperse gold-doped titania microspheres. *Chem.-Eur. J.* **15**, 4366–4372 (2009).

[55] Hidalgo, M. C., Maicu, M., Navio, J. A. & Colon, G. Effect of sulfate pretreatment on gold-modified TiO_2 for photocatalytic applications. *J. Phys. Chem. C* **113**, 12840–12847 (2009).

[56] Bamwenda, G. R., Tsubota, S., Nakamura, T. & Haruta, M. The influence of the preparation methods on the catalytic activity of platinum and gold supported on TiO_2 for CO oxidation. *Catal. Lett.* **44**, 83–87 (1997).

[57] Zhang, D. Q., Wen, M. C., Zhang, S. S., Liu, P. J., Zhu, W., Li, G. S. & Li, H. X. Au nanoparticles enhanced rutile TiO_2 nanorod bundles with high visible-light photocatalytic performance for no oxidation. *Appl. Catal. B-Environ.* **147**, 610–616 (2014).

[58] Dozzi, M. V., Prati, L., Canton, P. & Selli, E. Effects of gold nanoparticles deposition on the photocatalytic activity of titanium dioxide under visible light. *Phys. Chem. Chem. Phys.* **11**, 7171–7180 (2009).

[59] Haruta, M. Size- and support-dependency in the catalysis of gold. *Catal. Today* **36**, 153–166 (1997).

[60] Haruta, M., Tsubota, S., Kobayashi, T., Kageyama, H., Genet, M. J. & Delmon, B. Low-temperature oxidation of co over gold supported on TiO_2, α-Fe_2O_3, and Co_3O_4. *J. Catal.* **144**, 175–192 (1993).

[61] Grunwaldt, J. D. & Baiker, A. Gold/titania interfaces and their role in carbon monoxide oxidation. *J. Phys. Chem. B* **103**, 1002–1012 (1999).

[62] Casaletto, M. P., Longo, A., Martorana, A., Prestianni, A. & Venezia, A. M. Xps study of supported gold catalysts: the role of au^0 and $au^+\delta$ species as active sites. *Surf. Interface Anal.* **38**, 215–218 (2006).

[63] Li, H., Bian, Z., Zhu, J., Zhang, D., Li, G., Huo, Y., Li, H. & Lu, Y. Mesoporous titania spheres with tunable chamber stucture and enhanced photocatalytic activity. *Journal of the American Chemical Society* **129**, 8406–8407 (2007).

[64] Parayil, S. K., Kibombo, H. S., Wu, C.-M., Peng, R., Kindle, T., Mishra, S., Ahrenkiel, S. P., Baltrusaitis, J., Dimitrijevic, N. M., Rajh, T. & Koodali, R. T. Synthesis-dependent oxidation state of platinum on TiO_2 and their influences on the solar simulated photocatalytic hydrogen production from water. *J. Phys. Chem. C* **117**, 16850–16862 (2013).

[65] Krause, M. O. & Oliver, J. H. Natural widths of atomic k and l levels, ka x-ray lines and several kll auger lines. *J. Phys. Chem. Ref. Data* **8**, 329–338 (1979).

[66] de Groot, F. M. F., Krisch, M. H. & Vogel, J. Spectral sharpening of the ptledges by high-resolution x-ray emission. *Physical Review B* **66** (2002).

[67] Glatzel, P., Singh, J., Kvashnina, K. O. & van Bokhoven, J. A. In situ characterization of the 5d density of states of pt nanoparticles upon adsorption of co. *Journal of the American Chemical Society* **132**, 2555 (2010).

[68] Glatzel, P., Weng, T.-C., Kvashnina, K., Swarbrick, J., Sikora, M., Gallo, E., Smolentsev, N. & Mori, R. A. Reflections on hard x-ray photon-in/photon-out spectroscopy for

electronic structure studies. *Journal of Electron Spectroscopy and Related Phenomena* **188**, 17–25 (2013).

[69] Hämäläinen, K., Siddons, D. P., Hastings, J. B. & Berman, L. E. Elimination of the inner-shell lifetime broadening in x-ray-absorption spectroscopy. *Physical Review Letters* **67**, 2850–2853 (1991).

[70] Calvin, S. *XAFS for Everyone* (Taylor & Francis, 2013).

[71] Samain, L., Silversmit, G., Sanyova, J., Vekemans, B., Salomon, H., Gilbert, B., Grandjean, F., Long, G. J., Hermann, R. P., Vincze, L. & Strivay, D. Fading of modern prussian blue pigments in linseed oil medium. *Journal of Analytical Atomic Spectrometry* **26**, 930–941 (2011).

[72] Silversmit, G., Vekemans, B., Appel, K., Schmitz, S., Schoonjans, T., Brenker, F. E., Kaminsky, F. & Vincze, L. Three-dimensional fe speciation of an inclusion cloud within an ultradeep diamond by confocal µ-x-ray absorption near edge structure: Evidence for late stage overprint. *Anal. Chem.* **83**, 6294–6299 (2011).

[73] Longo, A., Liotta, L. F., Pantaleo, G., Giannici, F., Venezia, A. M. & Martorana, A. Structure of the metal–support interface and oxidation state of gold nanoparticles supported on ceria. *The Journal of Physical Chemistry C* **116**, 2960–2966 (2012).

[74] Reifsnyder, S. N. & Lamb, H. H. Characterization of silica-supported pd-au clusters by x-ray absorption spectroscopy. *Journal of Physical Chemistry B* **103**, 321–329 (1999).

[75] Schwartz, V., Mullins, D. R., Yan, W. F., Chen, B., Dai, S. & Overbury, S. H. XAS study of Au supported on TiO_2: Influence of oxidation state and particle size on catalytic activity. *Journal of Physical Chemistry B* **108**, 15782–15790 (2004).

[76] Miller, J. T., Kropf, A. J., Zha, Y., Regalbuto, J. R., Delannoy, L., Louis, C., Bus, E. & van Bokhoven, J. A. The effect of gold particle size on au-au bond length and reactivity toward oxygen in supported catalysts. *J. Catal.* **240**, 222–234 (2006).

Chapter 5

Micro-focus XRF/XAS

5.1 Introduction

In many research areas, spatially resolved information is essential: for example, the spatial distribution of nickel poisoning inside a catalyst particle can heavily influence the reactivity of the catalyst, the location of Cu contamination in a biological organism can tell us more on the biological effects of the contamination, the presence of a given element in a specific region of a painting can tell us which pigment was used.

In order to perform micro-focus XRF or XAS experiments, an X-ray beam is focussed down to a few micrometers or even to sub-micrometer dimensions. Subsequently, the sample is scanned through the beam using steps equal to or slightly smaller than the beam size while acquiring information at each individual step of the scan. Alternatively, a continuous movement of the sample through the beam can be performed, during which the emitted radiation is repeatedly sampled in preset time intervals during this continuous or dynamic scanning. The latter approach is usually followed in order to e.g. increase the scanning speed or reduce the probability of beam induced alteration of the illuminated sample areas due to prolonged exposure to the intense X-ray microbeam. Two dimensional scans, or mappings, are obtained by moving the sample through the beam, making use of two separate motor systems. Three dimensional scans can be obtained by introducing an additional (rotational) movement, around the sample's axis of rotation. The 3D computed tomography (CT) scans are typically combined to reconstruct a 3D volume by filtered backprojection[1] or algebraic reconstruction[2] techniques. This XRF/XAS tomo-

graphic method, however, is rather time consuming as measurement time scales with the third power of the number of scan points required in a given dimension. Additionally, algorithms required for these reconstruction methods are often computationally expensive and may induce artefacts in the rendered 3D volume.

It is clear that for 2D and 3D mappings, the measurement time increases significantly with the amount of investigated data points and thus by the covered area/volume. For XAS, a full energy scan has to be performed at each data point, essentially adding an extra data dimension and increasing measurement times. As such, most micro-XAS experiments are limited to an initial XRF-based overview mapping of the sample's region of interest, followed by XAS scans at a select number of points of interest. It is then assumed that, based on the co-distribution of elemental constituents as determined by the XRF analysis or additional techniques, the obtained XAS spectra are representative for compositionally similar phases in the scanned region. However, it is not hard to imagine that in some cases this assumption cannot be made. As such, the need for full-field XAS arose, in which a XAS spectrum is obtained in a spatially resolved way for each pixel/voxel within a given sample area or volume. One approach makes use of a position sensitive energy dispersive CCD detector, as discussed in Chapter 7. A second approach applies a large area (multi-element) ED detector, coupled with fast detector readout electronics to perform so-called fast scanning XRF/XAS. As such, a large fraction of the fluorescence radiation emitted by the sample can be processed in very short times, resulting in measurement times of only a few milliseconds per point. A noteworthy detector for fast-scanning approaches is the Maia detector, consisting of 384 $1\times1\,\mathrm{mm}^2$ Si-based detector elements arrayed in a 20×20 raster with the central 4×4 elements removed to allow for beam passage.[3–8] A Mo mask is implemented to minimize charge sharing between elements. In combination with a dedicated dynamic analysis method, the Maia can reputedly handle 100 million events per second, allowing for sub-ms scan times per pixel for concentrated samples. Alternatively, similar results towards large solid angle fast-scanning can be obtained using e.g. a Vortex ME4 multi-element detector in combination with a Quantum Detectors Xspress 3 system, capable of handling count rates of several million counts per second.[9]

In this chapter, the application of a polycapillary based microbeam XRF/XAS setup developed by our group at a bending magnet beam line (DUBBLE BM26A) of the ESRF is discussed. Additionally, an example is shown of the XAS and XRF investigation of ancient carbonized Herculaneum papyrus scroll fragments in quest of the origin and composition of the writing ink on these scrolls.

5.2 The DUBBLE (BM26A) Micro-focus Setup

5.2.1 From macro to microbeam XAS

Historically, the DUBBLE BM26A beam line (ESRF, Grenoble) has been mainly specialized in on-line catalysis research by means of X-ray absorption spectroscopy. For these purposes, it uses a 0.4 T bending magnet generated beam of approximately 1×10^{11} ph/s and energy tunability in the 4.5 to 30 keV range with an energy resolution ΔE of 1.7 eV at 9.689 keV. Typically applied beam sizes at the sample position are of the order of $5\times1\,mm^2$, resulting in most of the experiments performed at BM26A to classify as bulk experiments.

In order to make micro-XAS and -XRF experiments possible at BM26A, a micro-focus setup was built in collaboration with Drs. Stephen Bauters. During the development of this setup, it was of great importance that this setup could be removed and inserted in the beamline at will, as a sort of 'plug-and-play' system, thus retaining the large beam and very flexible sample environment characteristics of BM26A. For this purpose, it was opted to focus the X-rays down to a microscopic sized beam using a polycapillary X-ray optic (Section 3.3.2). More information on this subject can be found in S. Bauter's work.

5.2.2 Micro-focus Setup Outline

An elliptically shaped polycapillary optic[10–12] was obtained from XOS (X-ray Optical Systems, NY, USA) consisting of a large acceptance window ($7.5\times3\,mm^2$), a focal distance of approximately 2.5 mm and an estimated focal spot size of 10 μm at 6.4 keV. The 6 cm long polycapillary optic is contained in a housing with entrance window diameter of 10 mm and exit window diameter of 2.8 mm. Due to the large acceptance window, a large fraction of the BM26A X-ray beam is guided through the optical system, resulting in a flux as high as possible impinging on the sample. Purging holes to flow He through the polycapillary optic, decreasing absorption of X-ray photons by air, are foreseen in the optic's housing design.

The alignment of a polycapillary optic is particularly sensitive to rotations around the directions orthogonal to its optical axis. Tilt angles with respect to the incident beam direction should be minimized, as the condition of (repeated) total reflection within the hollow glass channels of the polycapillary needs to be fulfilled in order to transmit X-

rays through the optic. As such, the polycapillary optic has to be mounted coaxially to the unfocussed X-ray beam. To pre-align the polycapillary optic, a straight 16 cm long rail equipped with 1 mm sized pinholes on both ends is inserted in the path of the beam. Translation and rotation of the rail with respect to the primary beam is allowed by a motorized H206 6-axis precision alignment system (Physik Instruments) with c-887 hexapod controller (PI), while the transmission of the primary X-ray beam through both pinholes is monitored using a gas ionisation chamber. Once the pre-alignment rail is oriented parallel to the beam, the pinholes are removed and the polycapillary optic is inserted in the rail. The polycapillary optic is then aligned by iteratively making minute rotational and translational adjustments until a maximal transmitted flux is measured.

A photograph of the aligned micro-focus setup is displayed in Figure 5.1. A Vortex-EM SDD (Hitachi High-Technologies Science America Inc.) with 450 μm thick Si crystal was mounted at 90° with respect to the polycapillary optic, in the plane of polarization, equiped with an Al collimator to further reduce background scattering. Any additional energy dispersive detectors could be applied in this setup, although geometric restrictions have to be considered due to the short focal distance of the polycapillary optic. A SteREO Discovery V20 microscope (Carl Zeiss AG) is used to visualise the sample to facilitate sample alignment.

The sample can be mounted on a goniometer sample holder (HUBER Diffraktionstechnik GmbH & Co. KG), fixed on a XYZ motorized system (Micro-Translation stages, Physik Instruments) allowing for translation along each axis of 3D space. Additionally, a manual rotation stage was installed to allow for reproducible sample placement in grazing angle entry or exit conditions.

5.2.3 Analytical Characterisation

The beam size of the DUBBLE micro-focus setup was determined by scanning a 10 μm stainless steel wire (Goodfellow Inc.) through the beam. The transmission signal shows a Gaussian beam profile, which is a convolution of the actual beam size at the sample position and the thickness of the metal wire. At 9.029 keV, the 10 μm diameter stainless steel wire can be considered to be a perfect beam stop. However, at 18.048 keV, the stainless steel wire becomes partially transparent to the beam. As such, a correction to the beamsize was made by calculating the amount of transmission through the wire at each point, resulting

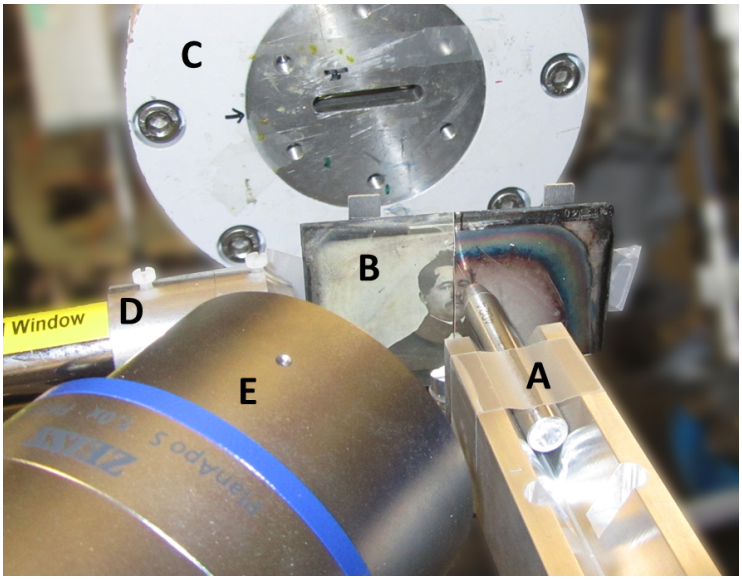

Figure 5.1: Photograph of the BM26A DUBBLE micro-focus setup displaying the 6 cm long polycapillary optic in its holder rail (A), Daguerreotype sample (B), transmission signal monitoring ion chamber (C), energy dispersive SDD detector with Al collimator (D) and Zeiss microscope (E).

in an effective wire thickness of ∼6.3 μm. This method results in a beam size diameter at the sample position of 8-11 μm depending on the excitation beam energy, with higher beam energies resulting in smaller focal spot sizes. Furthermore, the focussed beam has a divergence of ∼4 ° in the horizontal and ∼0.4 ° in the vertical direction as determined by performing wire line scans at varying optic-wire distances.

The beam flux at the sample position was approximated by monitoring the difference in transmission signal before and after polycapillary optic insertion and alignment. A focussed beam flux of approximately 1×10^9 ph/s was estimated this way at an energy of 9.029 keV.

Figure 5.3 displays the elemental detection limit (DL) values for the macro and micro-focal setup for a NIST SRM 1577c bovine liver sample. The sample was illuminated for 1000 seconds with an energy of 9.029 keV. It is clear that the DL values are lower for macro (5×1 mm^2 at the sample position) compared to micro-beam conditions as part of the primary X-ray beam flux is lost due to imperfect polycapillary optic transmission efficiency and limited incident beam acceptance, although the DL is sub-ppm level for elements with atomic number >19 (K) for both approaches.

However, most XAS applications do not lend themselves to measurement times of 1000 seconds

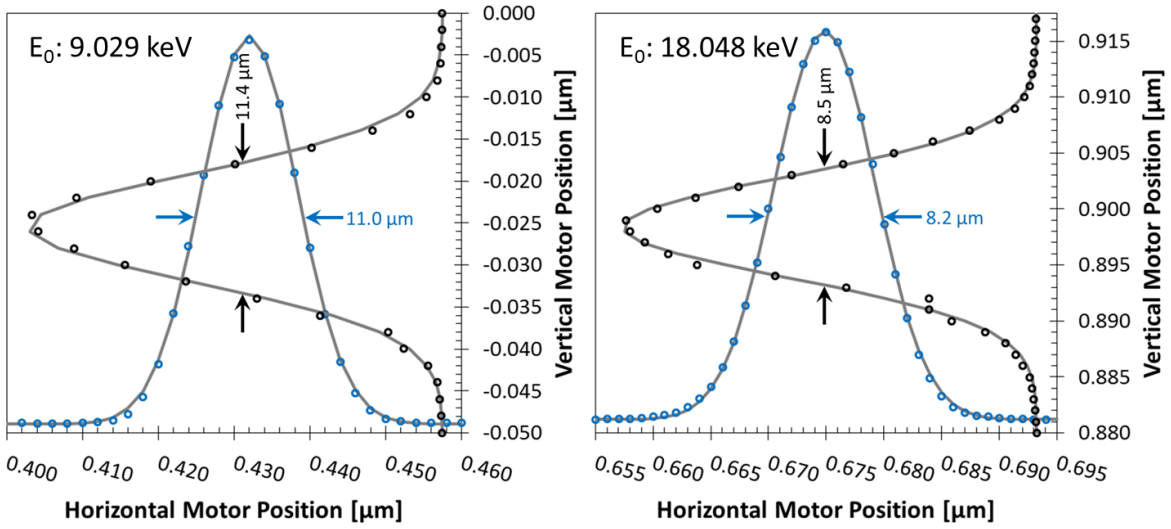

Figure 5.2: Transmission intensity curves derived from a wire scan in the vertical (black) and horizontal (blue) direction over a 10 μm stainless steel wire at different energies. Beam sizes are presented for each scan direction.

per point, per energy step. As the DL scales inversely to the square root of the measurement time, it is found that for K (Z=19) to Cu (Z=29) detection limits of 1-20 ppm and 2-35 ppm for 1 s exposure time are acquired for macro- and micro-beam applications respectively.

5.2.4 Conclusion

The DUBBLE BM26A micro-focus setup consists of a polycapillary optic allowing the focussing of a large part of the unfocussed broad beam down to beam sizes of $\sim 8 \times 8\,\mu m^2$. Slightly higher detection limit values are found for the micro-setup when compared to the unfocussed beam, although they are well within the 1-50 ppm range for transition metals, allowing for fast measurements on diluted samples.

The sample can be scanned through the X-ray beam in XYZ direction, while the fluorescence and scatter radiation is detected by an energy dispersive detector for each point in a spatially resolved manner. Due to the "plug-and-play" design of the setup, fairly fast transitions between focussing and non-focussing setup can be made. An improvement in this transition rate can be made by implementing a motorised retraction of the polycapillary optic, without changing the sample position. Currently, this is not available due to the limited travel range of the hexapod on which the polycapillary optic is mounted.

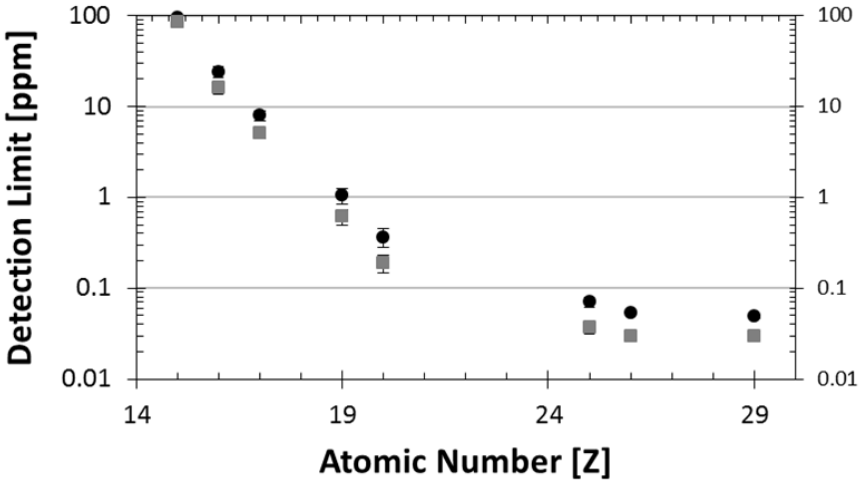

Figure 5.3: Detection limits for the DUBBLE BM26A (ESRF, Grenoble, France) macro (gray squares) and micro-beam (black circles) setup on a NIST SRM 1577c bovine liver sample. 1000 s exposure time, E_0: 9.029 keV. Error bars represent 3σ confidence level and are occasionally covered by the data point symbol. The beam size of the micro-beam at the sample position is 8 μm whereas the macro beam has a beam size of $5\times1\,\mathrm{mm}^2$.

Due to the divergence of the focussed X-ray beam, a spot size at the sample position can be selected according to the requirements of the experiment by translating the sample along the longitudinal axis of the polycapillary optic. The usable size range is approximately from 10 μm to 50 μm.

5.3 Application: Herculaneum Papyrus Scrolls

The experiment and results described in this section have been presented in Scientific Reports published by the Nature Publishing group.[a]

[a] P. Tack, M. Cotte, S. Bauters, E. Brun, D. Banerjee, W. Bras, C. Ferrero, D. Delattre, V. Mocella, L. Vincze, Tracking ink composition on Herculaneum papyrus scrolls: quantification and speciation of lead by X-ray based techniques and Monte Carlo simulations. *Scientific Reports* **6**, 20763, doi:10.1038/srep20763 (2016).

5.3.1 Introduction

Recently, the writing in rolled Herculaneum papyri was successfully explored by X-ray phase-contrast tomography.[13, 14] These scrolls are part of a complete library, containing hundreds of such papyrus scrolls. This library was discovered between 1752 and 1754 in the small city of Herculaneum, which was covered and preserved by layers of volcanic material in 79 AD.[15–18] This is the only library passed on from Antiquity, and is therefore an inestimable treasure. Due to the pyroclastic events associated with the eruption, the scrolls were carbonized and locked-up, rendering the writing on the scrolls unreadable. Previously, it was attempted to read these scrolls by mechanically unrolling them.[19] These attempts, however, usually led to the irretrievable loss of large parts of the text due to the brittle nature of the carbonized scrolls.

As demonstrated by the work of Mocella *et al.*, the writing in the scrolls can now be, at least partially, recovered by non-destructive X-ray imaging methods, without the need of unrolling the scrolls.[13] The readability of the text is however not optimal due to interference of the papyrus fibres, running vertically and horizontally across the document. Recently, Brun *et al.* showed the presence of lead in the papyrus writing, rendering the text more readable when monitoring the Pb X-ray fluorescence (XRF) signal.[20]

Several hypotheses to explain the presence of Pb and other elements in the sample are assessed using a sequence of non-destructive, X-ray based analytical techniques, providing further insights into the production and history of the Herculaneum manuscripts.

The goal of the experiment described in this section was to determine which Pb compound was used. Lead could have been introduced unknowingly, or on purpose:

- An initial hypothesis is Pb contamination of the water used as a solvent for the ink.
- A second hypothesis states that Pb could be present as a contaminant from a bronze container in which the ink was stored, as discussed by Canevali *et al.*[21]
- Alternatively, Pb could have been knowingly introduced to the ink in a controlled fashion. Lead-based pigments, being a black mineral galena (PbS) or lead white (different mixtures of cerusite ($PbCO_3$) and hydrocerusite ($2PbCO_3$,$Pb(OH)_2$)), were frequently used in ancient times as a pigment for cosmetic products.[22–24] Galena has been proposed as a pigment in black inks in Egyptian papyrus before,[25] whereas minium ($Pb_2^{2+}Pb^{4+}O_4$) has been reported as a red pigment in Roman writing.[26, 27]

- Additionally, Pb could originate from a binding medium in the ink: Pb compounds have been used extensively as dryers in paintings as they speed up the process of oil drying.[28, 29] The use of litharge (PbO) as oil drier is already mentioned by Galen at the 2nd C. A.D. and by Marcellus at the 4th C. A.D.[30, 31] Furthermore, the use of a lipid-based ink to draft the papyrus writing can be hypothesized.[21, 32, 33]

5.3.2 Methods

Description of the samples

Two fragments of Herculaneum papyrus scrolls were investigated. The large fragment measures approximately $0.9\times1.2\,\mathrm{cm}^2$, whereas the small fragment is approximately $0.5\times0.8\,\mathrm{cm}^2$ large. Both samples are originating from unrolled scrolls and have an average thickness of approximately 0.3 mm with a surface roughness of approximately $30\,\mu m$.[34] The samples were sandwiched between two $4\,\mu m$ thick ultralene foils (Spex, Certiprep).

XRF mapping acquisition

Microbeam measurements were performed at the X-ray microscopy beam line ID21 at the ESRF (Grenoble, France). The primary beam energy was tuned by the use of a Si(111) monochromator. To define the beam spot size on the sample for a general overview mapping, a pinhole ($50\,\mu m$ for the large fragment and $100\,\mu m$ for the small fragment) was used. An incident beam flux monitoring pin diode was used continuously to correct for intensity variations. An average beam flux of 3.7×10^9 ph/s and 6.9×10^9 ph/s was obtained during the measurements on the large and small fragments respectively. The sample to detector chip distance was set to 3 cm and 3.1 cm for the large and small fragments, respectively. Scans were performed by moving the sample through the X-ray beam and acquiring an XRF spectrum at each step (38×31 $100\,\mu m$ steps for the small fragment and 160×175 $50\,\mu m$ steps for the large one). Acquisition times of 0.26 s and 1 s per step were used for the large and small fragments respectively. High resolution spatially resolved XRF measurements were performed using progressively smaller pixel size (10, 5 and $1\,\mu m$), the beam being focused down to $0.3\times0.6\,\mu m^2$ using a Kirkpatrick-Baez mirror system.[35]

The microscope is operated under vacuum and samples were placed under an angle of 62° with respect to the primary X-ray beam. The XRF (and scatter) radiation was detected

using a Bruker (Germany) XFlash 5100 silicon drift detector (SDD), equipped with a Moxtek AP3.3 polymer window,[36] mounted under 69° with respect to the primary X-ray beam. An additional ultralene foil (4 μm) further covers the detector. XRF spectra were processed using PyMCA[37] as well as the AXIL and IDL based Microxrf2 software packages.[38, 39] Pixels contributing to the writing on the papyrus were isolated using K-means clustering routines, as incorporated in the Microxrf2 software.[40]

XRF quantification

The XRF data were quantified using Monte Carlo based simulations, as calculated by the XMI-MSIM simulation code.[41–43] Sample position and orientation as well as detector position and orientation were calculated based on the information as noted above. A detector active area of 0.8 cm^2 was supplied without a collimator. Slits sizes were set to the size of the used pinhole. Additionally, the SDD detector crystal was simulated to consist of pure Si (ρ = 2.33 g/cm^3) with a 450 μm thickness. The primary X-ray beam was set to a monochromatic value of 3.5 keV with a 100% polarization in the horizontal plane. A source size equal to the pinhole size with a zero radian divergence was used. The experimentally used 4 μm ultralene foils were approximated during the simulation as 4 μm Kapton polyimide foils, the composition of which was supplied by the built-in XMI-MSIM catalogue. Due to the small foil thickness and similar energy dependent X-ray absorption this approximation will not have a significant influence on the outcome of the quantification. The Moxtek AP3.3 window, consisting of a thin (<4 μm) polymer foil on top of a 100 μm or more silicon grid,[36] cannot be simulated in the XMI-MSIM program due to its heterogeneous nature. As 100 μm Si is virtually a beam stop to 3.5 keV X-ray photons (approximately 3×10^{-5}% transmission), regions covered by the Moxtek window grid will not transmit photons to the detector. Provided a 70% open grid area, the Moxtek window Si grid was simulated in the XMI-MSIM program by reducing the initial X-ray beam flux by 30%. The live acquisition time corresponding to the writing sum spectrum was derived from the amount of pixels contributing to the writing and the acquisition time per point, taking into account an average dead time of 5% for the large and 15% for the small fragment. The sample thickness was estimated to be 300 μm and the sample density was calculated to be 0.36 g/cm^3, based on the dimensions of the approximately cylindrical scroll with a diameter of 5 cm, length of 20 cm and weight of 141 g.

XAFS

Pb L_3-edge (13.035 keV) XAFS experiments were performed at the EXAFS station of the Dutch-Belgian beam line (DUBBLE, BM26A) at the ESRF (Grenoble, France).[44] The energy of the X-ray beam was tuned using a Si(111) monochromator operating in fixed-exit mode, with an energy resolution of approximately 1.7×10^{-4} at 9.659 keV. Higher harmonics were rejected by using a vertically focusing Pt-coated mirror behind the monochromator. The primary X-ray beam was confined to $1\times3\,mm^2$ (V)×(H) using a slit system and further focused down to approximately $20(V)\times60(H)\,\mu m^2$ at the sample position using polycapillary optics. The primary X-ray beam and transmitted beam intensities were monitored using ionisation chambers, filled with a gas mixture to absorb approximately 10% and 70% of the beam respectively. The XRF/scattered radiation was detected using a Vortex-EM silicon drift detector.

XAFS energy scans were performed over the Pb L_3-edge (calibrated using a metallic Pb foil, setting the maximum of the first derivative to 13.035 keV), starting at E_0-100 eV up to E_0+100 eV. Acquisition times per energy step were chosen based on data statistics and available beam time. Additional XANES acquisitions were performed at ID21, at the sulphur and chlorine K-edges. XANES spectra were recorded in XRF mode (same set-up as above), with a beam of 100, 50 and 0.4 μm diameter. The monochromator was calibrated setting the maximum of absorption at 2.483 keV for $CaSO_4{\cdot}2H_2O$ reference and at 2.828 keV for NaCl reference. XANES spectra were acquired from 2.46 to 2.58 keV with 400 steps of 0.3 eV at S K-edge and from 2.795 to 2.895 keV with 400 steps of 0.25 eV at Cl K-edge. Linear combination fitting of the XANES spectra was performed to identify and quantify mixtures of pure compounds, which were prepared as powder pressed to pellets and measured in transmission mode.

5.3.3 Results and Discussion

To be able to (dis)prove the origin of the Pb in the ink, two fragments (referred to as the "large" and "small" fragments) from unrolled scrolls were investigated. The two fragments are flat pieces of papyrus, made of different sheets, and showing E, Π , I, N, I, A and O, Λ letters on their surface, respectively. A picture of the large sample is shown in Figure 5.4A. In terms of analytical techniques, considering the precious nature of the samples, priority was given to non-destructive imaging methods. Besides, the heterogeneity of the

samples at both micro- and millimetric scales motivated the implementation of a multi-scale analysis. Accordingly, macro and micro XRF and XAS techniques were used, at ID21[45] and BM26A[44] of the European Synchrotron Radiation Facility (Grenoble, France). In order to have a good statistics record of XRF data in and out of the ink, XRF 2D maps were acquired over the full surface of the samples, with a sub-millimetre beam. As detailed in Brun *et al.*,[20] the XRF map of Pb perfectly matches with the ink distribution (Figure 5.4B) as the writing, faintly visible in Figure 5.4A as well, is revealed. From this map, two average XRF spectra were extracted, by summing the pixel spectra corresponding to i) the writing using K-means clustering[40] and visually comparing the clusters to the XRF distribution images, ii) the papyrus alone, excluding the written areas. The qualitative comparison of these two spectra reveals an increased concentration in Pb, Al and P in the written area, which is also observable on the XRF map (Figure 5.5).

In order to quantitatively determine the ink composition, XRF results were simulated by means of Monte Carlo calculations.[41–43] These simulations model all relevant photon-matter interactions, simulating the trajectories of a large number of photons originating from an X-ray source and undergoing interactions in the sample, to the point of possible detection in a detector. The occurrence of each photon-matter interaction[46] (photoelectric effect/fluorescence, Rayleigh and Compton scattering) as well as direction of propagation and distance between interactions of the photons are simulated. By iteratively comparing the simulated spectrum to its experimental equivalent and adjusting the simulated sample composition after each iteration, the experimental sample composition is determined.

Figure 5.4C shows the result of the Monte Carlo simulation based XRF spectrum. A clear match is seen between the experimental spectrum and the theoretical simulation. The main differences are attributed to the lack of simulation for X-rays below 1 keV[43] and a slight underestimation of the generated pulse pile-up (3.05 keV and >3.5 keV) due to the uncertainty on the simulated detector's pulse width. Elemental concentrations are shown in Table 5.1. Both fragments show a similar C and Si content. The writing on the large fragment contains significantly more Pb, and slightly more Na, Al, P and Cl. The S concentration is lower in the large fragment than in the small one. When comparing the quantification results of the writing to the papyrus matrix, a characteristic increase in Al, P, Pb and to a lesser amount Cl is perceived, showing these elements are clearly associated with the writing. This was further investigated using μ-XRF, as discussed below (Figure 5.6). Additionally, the papyrus in both fragments has a fairly similar composition, only Na and S quantities seem to vary. It should be noted that these quantification results do

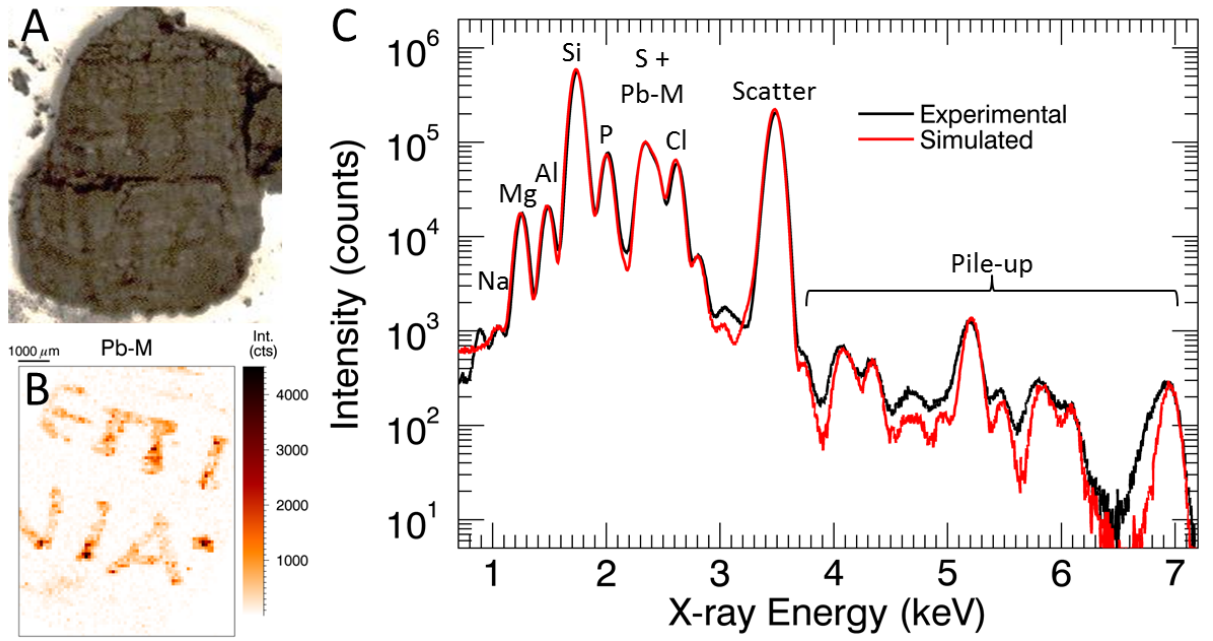

Figure 5.4: Contrast and brightness enhanced photograph (A) and Pb-M XRF signal (B) of the large papyrus fragment. The XRF spectra of the writing (C) on the large papyrus fragment (Experimental, black curve) and Monte Carlo simulation (Simulated, red curve) using the XMI-MSIM software.

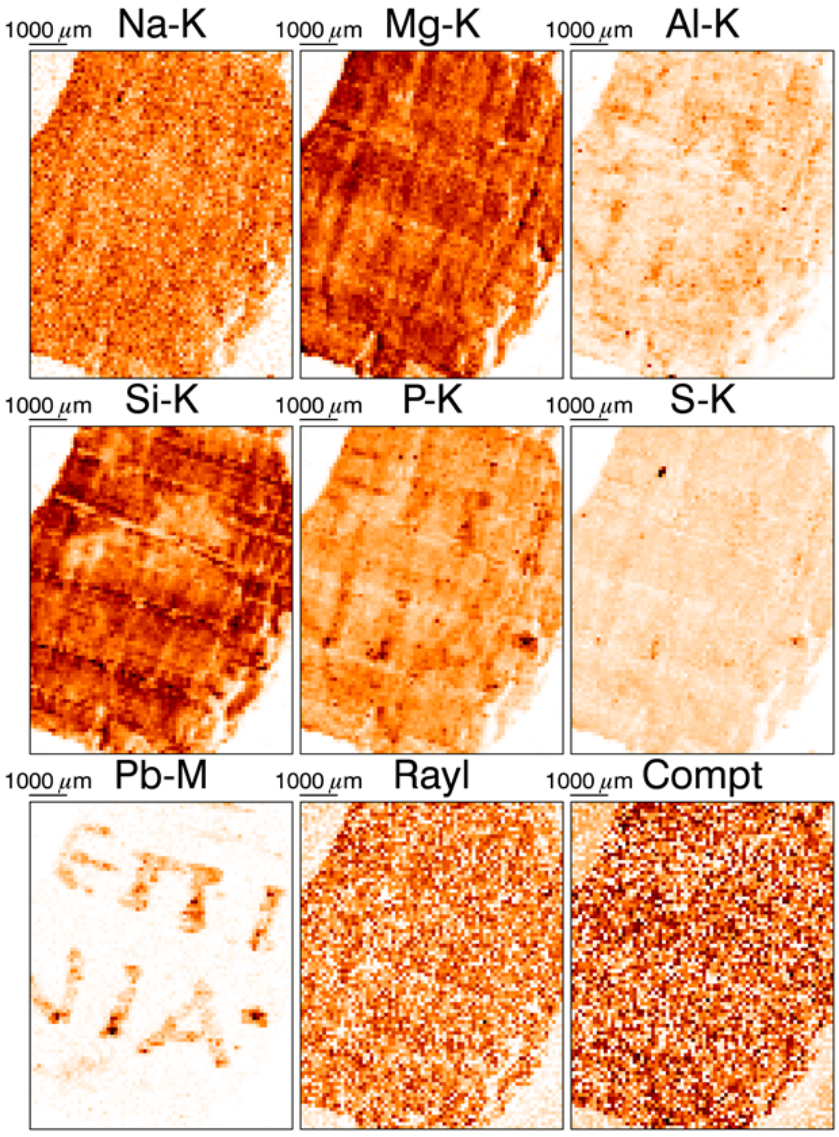

Figure 5.5: XRF Elemental distribution images of the large papyrus fragment. The writing is visible in the Al, P and Pb signals.

not represent the composition of the pure ink, but rather represent a mixture of the ink and the underlying papyrus due to the penetrating character of X-rays. Nevertheless, as the writing was mainly visible through the Pb signal, it is safe to say the Pb concentration calculated by the simulation can be mainly attributed to the ink, and not the underlying papyrus. Taking into account the total area covered by the writing on each fragment and the average sample density, the Pb concentration in the ink is approximately $16\pm5\,\mu g/cm^2$ for the small and $84\pm5\,\mu g/cm^2$ for the large fragment.

Based on the work of Kim *et al.*[47] and Delile *et al.*[48] it is clear that these Pb contents are too high to be caused by the contamination of lead in the water (<1.5 mg/L), used as a solvent for the ink, or as a contaminant from a bronze container. Additionally, Cu was found to show no co-distribution with the writing on the papyrus, which would be expected if Pb in the writing was a contaminant from a bronze container (Figure 5.7).

To obtain a better insight into the ink elemental composition, the same μ-XRF maps were acquired, but zooming on a particular part of the ink, with a smaller beam (down to sub-micrometric probe). It was of particular interest to see if elements, correlated on the millimetre scale, were also correlated on the micro-scale (hence potentially chemically associated). Figure 5.6 shows the Pb distribution on the large fragment on both macroscopic and microscopic levels, as well as the distribution of Al, P and S at different zoom levels down to the microscopic levels. It is clear from these results that Pb, P and Cl show a co-distribution (Figure 5.6 and Figure 5.8). Similar results are obtained through PCA analysis of the data set by means of the Microxrf2 software package (Figure 5.9).[39] Even though Al is co-localized with the Pb at the macro level (Figure 5.6 and Figure 5.5), it is clear from the micro-scale images Pb is not chemically associated with Al due to their lack

Table 5.1: Monte Carlo quantification results in w% using the XMI-MSIM software on the sum spectra corresponding to the writing (Ink) on the large (L) and small (S) papyrus fragments, as well as on the surrounding papyrus (Pap). Elements present in the simulation but not shown here are Mg, K, Ca, Ti, Mn, Fe, Ni and Ba. The estimated error for these values is 5 %.

Fragment	**C[a]**	**Na**	**Al**	**Si**	**P**	**S**	**Cl**	**Pb**
L-Ink	75.14	0.65	1	8.8	0.6	0.01	0.12	0.78
L-Pap	76.56	0.65	0.5	8.8	0.4	0.07	0.08	0.05
S-Ink	77.06	0.35	0.75	8.3	0.35	0.08	0.07	0.15
S-Pap	77.42	0.35	0.6	8.3	0.25	0.07	0.07	0.05

[a]The C content is determined indirectly by difference and may be a mixture of C, H and O.

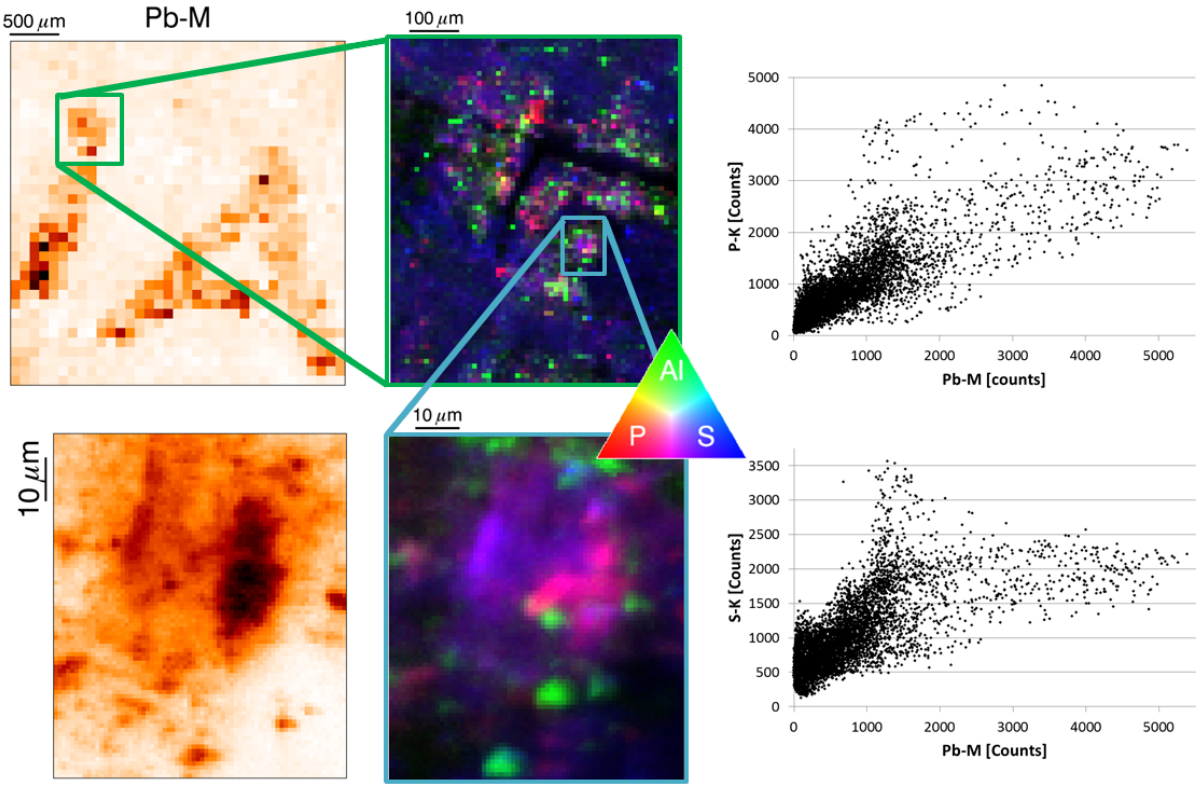

Figure 5.6: Micro-XRF Pb elemental distribution images on macroscopic (top left, 100 μm step size) to microscopic (bottom left, 1 μm step size) level. Red (P) Green (Al) Blue (S) images are displayed in the centre for different zoom modes (top right: 10 μm step size, bottom right: 1 μm step size) to display the co-localization of Al, P and S with Pb. Pb-P and Pb-S correlation plots are displayed to the right to show the correlation of Pb with P and partial correlation with S.

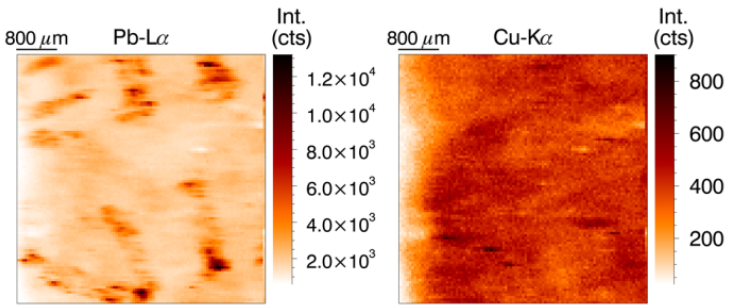

Figure 5.7: Pb-L_α and Cu-K_α elemental distribution of the large papyrus fragment as measured at BM26A using an excitation energy of 13.133 keV.

of co-distribution at the micro level. This demonstrates that the used ink has a complex composition, with different ingredients of which the distribution is homogeneous at the millimetre scale, but not at the microscopic level. The S signal shows a fairly homogeneous distribution over the papyrus, with occasional hot spots which are only partially co-distributed with Pb (Figure 5.6). Taking into account the quantification results, it is thus unlikely that PbS is the main constituent of the papyrus ink.

Additionally, X-ray absorption near-edge structure (XANES) spectroscopy was performed at the Pb L_3- and S K-edges to identify the chemical state and speciation of the Pb and S, by comparison with the XANES spectra of known compounds. Figure 5.10 displays the Pb L_3-edge XANES of the Pb in the writing, compared to several other reference compounds. It is clear from this image that Pb in the writing is in a state very similar to that of lead(II)acetate. Linear combination fitting of the papyrus data with the reference compound XANES shows there may be a partial contribution of PbS (up to 45%), along with lead(II)acetate. However, it should be noted the PbS XANES post-edge is fairly featureless; PbS contributes to the fit mainly to correct for a small edge shift and shaping of the post-edge feature at 13.085 keV compared to the lead(II)acetate reference. Comparing the papyrus writing Pb-L_3-edge XANES curve with those measured for minium in literature,[49, 50] it is clear no contribution of minium is found in the papyrus writing XANES due to the lack of contribution of the minium white line ($\sim$13.055 keV). As such, if minium was used to draft the writing, the compound was not preserved over the centuries.

As shown in Figure 5.11, S K-edge XANES shows complex features, characteristic of a mixture of different species. The primary information is obtained by comparing the signal in and next to the ink. The spectra are quite similar, demonstrating that most of the signal in the area covered by the ink is most probably due to the papyrus behind the ink. The spectra exhibit features similar to those recorded on plants or wood, with both reduced and oxidized sulphur species. Cheah *et al.* discuss the speciation of sulphur in biochar, displaying a S K-edge XANES spectrum very similar to the one obtained from the papyrus and ink.[51] A good match for the reduced S contribution is found with an unknown organic sulphur compound as well as a sulphate, represented here as a dibenzothiophene and Ca-sulphate respectively, as in Cheah *et al.*[51] More particularly, the presence of PbS in the papyrus writing is not indicated due to the absence of a sulphide peak at 2.4725 keV. A Cl K-edge XANES, measured on the writing, is shown to the right in Figure 5.11. Based on comparison to reference materials available (among which $PbCl_2$, NaCl, PVC) no match was found. However, comparison to literature shows that the probed Cl

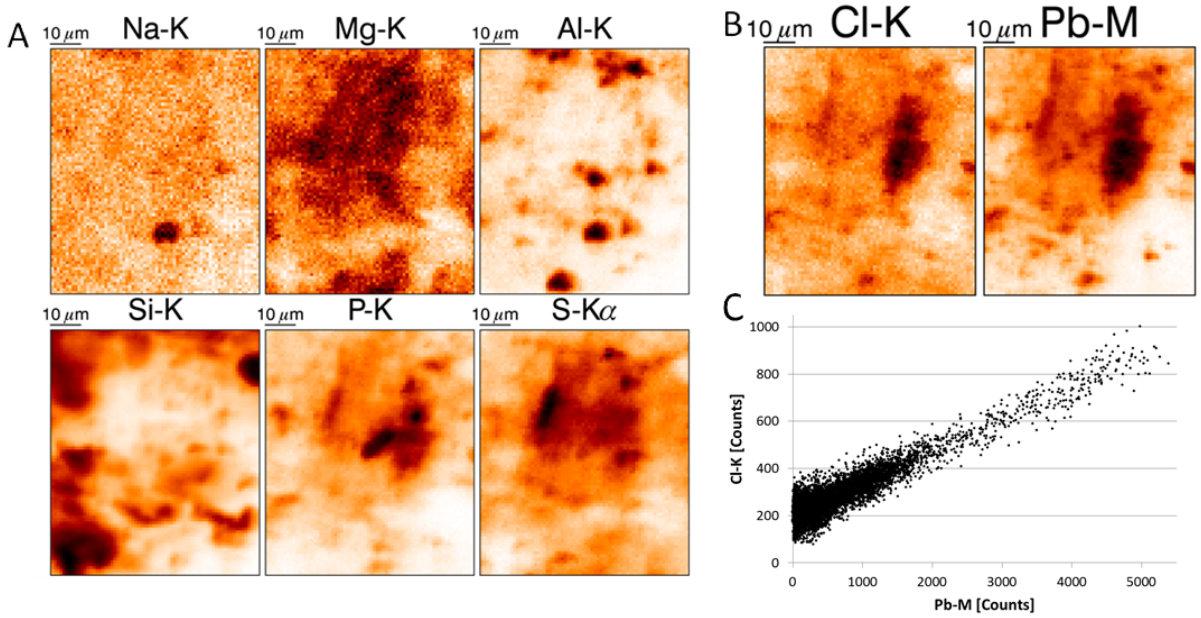

Figure 5.8: XRF elemental distribution images at the micro-scale (1 μm step size) displaying the co-distribution of P, Cl, Pb and partially S. Mappings in A were measured with an incident beam energy of 2.48 keV, thus not exciting the Pb-M and Cl-K shells electrons. Mappings in B were acquired at E_0 equal 3.00 keV (above the Cl-K and Pb-M shells). C shows the Pb-Cl correlation plot for the micro-scale XRF mapping.

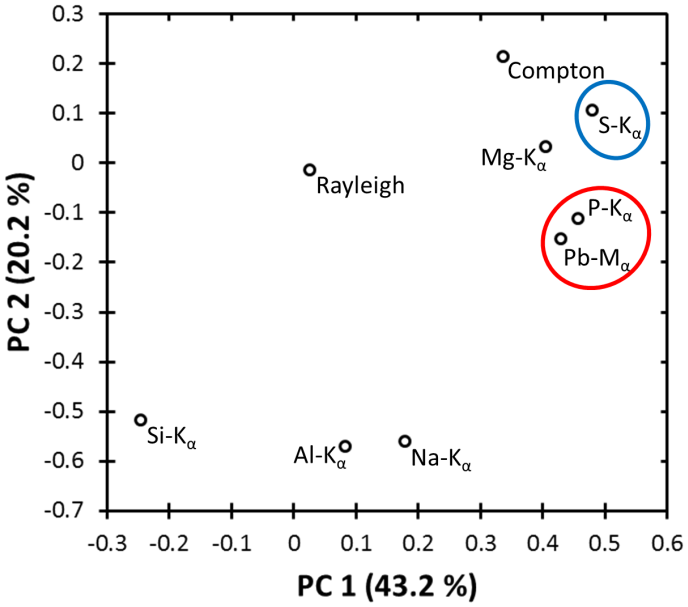

Figure 5.9: PCA loading plot presenting principal component 2 as a function of principal component 1. A clear separation between Pb and P on one hand (red circle) and S (blue circle) on the other is perceived along the principal component 2 axes.

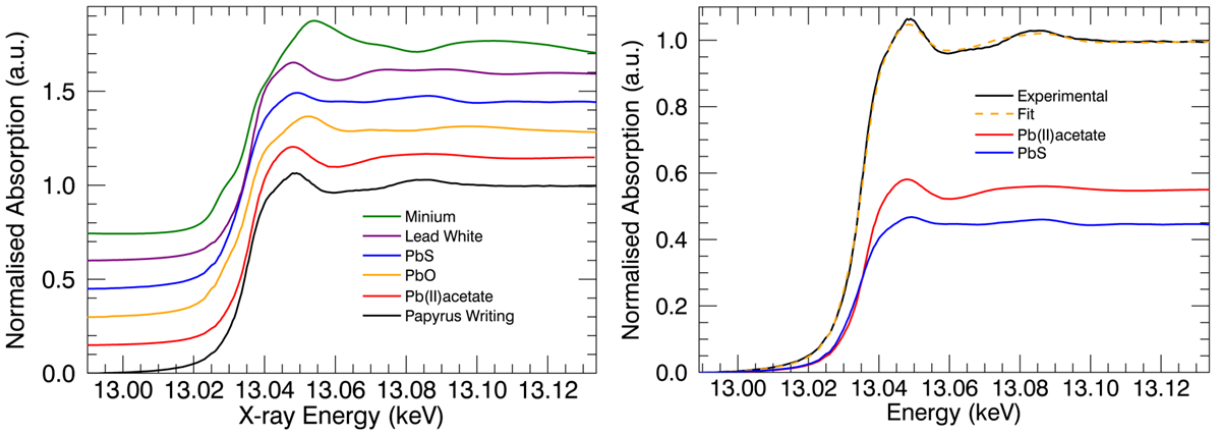

Figure 5.10: Left: Pb L_3-edge XANES spectra measured on the writing (black) compared to several other reference compounds. Right: Linear combination fitting showing a clear contribution of lead(II)acetate (red) in the papyrus writing lead content.

compound resembles organochlorine compounds as found in coal fuels.[52] Thus, despite the co-localization of Pb and Cl, they seem not directly chemically bonded in the papyrus ink.

As an alternative to the use of lead as a pigment, lead could have been introduced as a drier. As mentioned earlier, litharge was used in Antiquity as an oil drier.[30, 31] As PbO is very prompt to react (*e.g.* with oil or another reactive), the detection of PbO "as is" is improbable. Previous analyses including among others Fourier-transform infrared (FTIR) spectroscopy, Raman spectroscopy, gas chromatography coupled with mass spectrometry and pyrolysis, applied to nine black powders found in Pompeii houses (possibly used as ink and cosmetics), revealed in eight samples the presence of lipids, of animal and/or plant origin.[19] The FTIR spectrum of one sample shows features characteristic of fatty soaps similar to those found in some Egyptian cosmetics.[22] The hypothesis of Pb being present as lead carboxylates, following the use of a Pb-based drier and provided the organic lead species are original, is further strengthened by the Pb L_3-edge XANES as discussed above. Here, μ-FTIR was not attempted on the papyrus fragments as it would have required the destruction of the sample. Therefore, information about organic components is rather limited. The distinction between a lead pigment and a lead drier can only be estimated based on the lead concentration in ink. A survey of several oil paint medium recipes from the XV$^{\text{th}}$ to the XX$^{\text{th}}$ century states that the mass proportions of litharge:oil can vary from 1:4 to 1:1633. Using the latter fraction, an estimated writing thickness of 50 μm and an oil density of 0.93 g/mL, a theoretical concentration of 290 μg/cm^2 of Pb is found. Concentrations obtained through the Monte Carlo quantification are lower ($\sim$80 μg/cm^2).

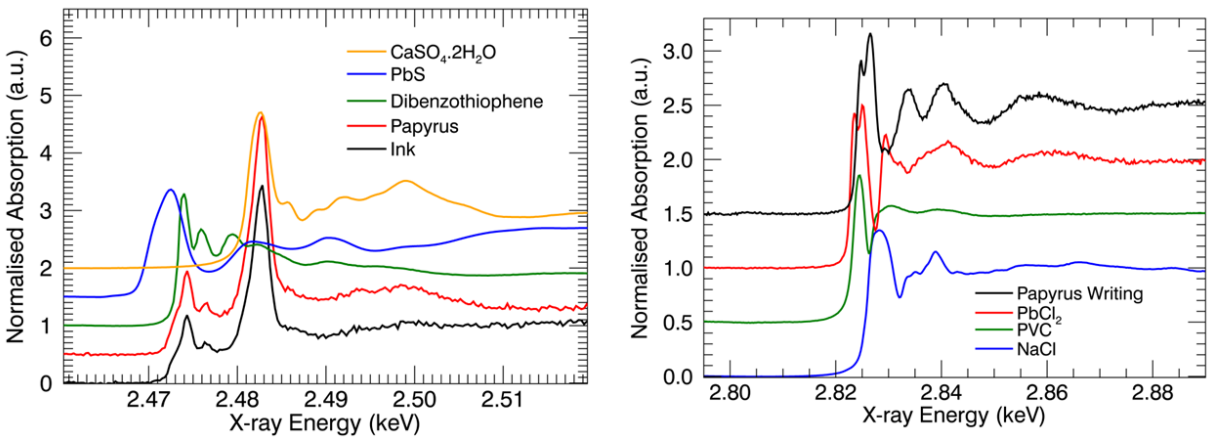

Figure 5.11: Left: S K-edge XANES spectra measured on the writing (black) and besides the writing (red) on the papyrus. Several reference compounds' XANES are displayed for comparison. Right: Cl K-edge XANES spectra measured on the writing, along with several reference spectra.

However, the actual ink layer thickness may be thinner than what was estimated here, and the proportion of the drier with respect to the "lead-based medium" could be lower too. Additionally, the drying medium may have been diluted with other organic binders. It can also be argued that for Pb to originate from a pigment, the Pb concentration should be larger than Pb introduced via a drying agent. As such, the quantified Pb content is an additional argument for Pb originating from an admixture to the ink rather than the main constituent.

Finally, the presence of galena in the writing is not confirmed by the S K-edge XANES and the only partial co-distribution of S and Pb on the micro-scale. However, it should be noted that PbS, if originally present, could have oxidized to PbO during the pyroclastic events that carbonized the scrolls. After the scrolls were discovered and dug out in 1754[13, 16–18] they were stored in wooden cabinets, which are known to emanate acetic acid vapours and can slowly react with PbO to form lead(II)acetate or other lead carboxylates.[53, 54] The latter reaction scheme could also explain the presence of lead(II)acetate, or similar carboxylates, as found by the Pb L_3-edge XANES.

5.3.4 Conclusion

In conclusion, two Herculaneum papyrus fragments were investigated aiming at the non-destructive identification, localization, quantification and speciation of Pb by X-ray based

techniques and Monte Carlo simulations.

Several hypotheses were postulated about the origin of Pb in the scrolls, and assessed using the aforementioned analytical techniques. Based on the Pb concentration and lack of co-distribution with Cu, it was determined that Pb is not originating from a contaminant in the ink solvent or container. It is deemed more likely that Pb was intentionally added to the ink, either as a pigment or as a drying agent. However, due to the changes the samples have likely undergone during the pyroclastic events and subsequent exhumation, we are not in the position of providing a definite answer to the question of the origin of Pb in the writing on the scrolls.

Nevertheless, the applied analytical methodologies provide important insights into the manufacturing and history of these and similar precious artefacts and should be similarly applied to other papyri, preserved in better conditions. Moreover, the concentrations found in the fragments could provide important information for optimizing the future tomography experiments on the rolled-up Herculaneum scrolls, provided they contain lead-rich writing as well. Further studies, in particular focusing on the speciation of organic compounds, may provide additional information required to give a definite answer to the origin of Pb in the scrolls, despite the often invasive nature of such techniques.

5.4 Summary

Micro-focus XRF and XAS provide information in a spatially resolved manner allowing for the study of the distribution of detectable elements and chemical species in the sample, with a spatial resolution level on the micron scale which is not achievable by broad beam excitation combined with a conventional detection system. Many approaches towards microbeam XRF/XAS are available. Here, the initial characterisation and application of a self-developed "plug-and-play" polycapillary based micro-focal setup at the DUBBLE BM26A (ESRF, Grenoble) was discussed. This setup allows the focussing of the typical $5\times1\,\mathrm{mm}^2$ broad beam down to $8\times8\,\mu\mathrm{m}^2$ for a 18 keV beam. Detection limits in the range of 1-35 ppm for a 1 s exposure (0.03-1 ppm for 1000 s) on a NIST SRM 1577c bovine liver sample were obtained, rendering the system applicable to diluted systems.

The use of this setup in combination with the ID21 KB-mirror based instrument was illustrated by investigating a rare set of carbonised Herculaneum papyrus scroll fragments.

An intriguing, so far unseen correlation between the writing on the papyrus fragment and lead distribution was found. Micro-XRF and XAS were used to quantify the amount of lead in the ancient text which provided information on the potential origin of lead in the ink.

Future advances in the field of emission-mode micro-focus XAS at a bending magnet source like DUBBLE could take substantial advantage in the application of larger effective solid angle and faster energy dispersive detectors, with energy resolution similar to the currently available silicon drift detectors (150 eV at 5.89 keV). Alternatively, the application of so-called full-field detectors in combination with a large beam also proves an interesting alternative to the currently available micro-XRF and XAS methodologies (Chapter 7).

In many cases, 2D visualisation of the sample top layers is however insufficient and one would like to investigate the full 3D structure of a sample or differentiate between top layers. To do so, one can either perform tomographic experiments, requiring significantly more measurement time, or one can investigate the sample using so-called confocal detection methods. The latter is discussed in Chapter 6 for a polycapillary optic based setup whereas in Section 7.4 a confocal full-field approach is discussed.

References

[1] Schroer, C. G. Reconstructing x-ray fluorescence microtomograms. *Applied Physics Letters* **79**, 1912–1914 (2001).

[2] Golosio, B., Simionovici, A., Somogyi, A., Lemelle, L., Chukalina, M. & Brunetti, A. Internal elemental microanalysis combining x-ray fluorescence, compton and transmission tomography. *Journal of Applied Physics* **94**, 145–156 (2003).

[3] Ryan, C. G., Kirkham, R., Hough, R. M., Moorhead, G., Siddons, D. P., de Jonge, M. D., Paterson, D. J., De Geronimo, G., Howard, D. L. & Cleverley, J. S. Elemental x-ray imaging using the maia detector array: The benefits and challenges of large solid-angle. *Nuclear Instruments & Methods in Physics Research Section a-Accelerators Spectrometers Detectors and Associated Equipment* **619**, 37–43 (2010).

[4] Ryan, C., Siddons, D., Kirkham, R., Dunn, P., Kuczewski, A., Moorhead, G., Geronimo, G. D., Paterson, D., Jonge, M. d., Hough, R., Lintern, M., Howard, D., Kappen,

P. & Cleverley, J. The new maia detector system: Methods for high definition trace element imaging of natural material. In Denecke, M. & Walker, C. (eds.) *X-ray Optics and Microanalysis, Proceedings of the 20th International Congress*, vol. CP1221, 9–17 (American Intitute of Physics, 2010).

[5] Howard, D. L., de Jonge, M. D., Lau, D., Hay, D., Varcoe-Cocks, M., Ryan, C. G., Kirkham, R., Moorhead, G., Paterson, D. & Thurrowgood, D. High-definition x-ray fluorescence elemental mapping of paintings. *Anal Chem* **84**, 3278–3286 (2012).

[6] Kirkham, R. *et al.* The maia spectroscopy detector system: Engineering for integrated pulse capture, low-latency scanning and real-time processing. In *The 10th International Conference on Synchrotron Radiation Instrumentation*, vol. CP1234, 240–243 (American Institute of Physics, 2010).

[7] Ryan, C. G. *et al.* Maia x-ray fluorescence imaging: Capturing detail in complex natural samples. *22nd International Congress on X-Ray Optics and Microanalysis* **499**, 012002 (2014).

[8] Monico, L., Janssens, K., Alfeld, M., Cotte, M., Vanmeert, F., Ryan, C. G., Falkenberg, G., Howard, D. L., Brunetti, B. G. & Miliani, C. Full spectral xanes imaging using the maia detector array as a new tool for the study of the alteration process of chrome yellow pigments in paintings by vincent van gogh. *J. Anal. At. Spectrom.* **30**, 613 (2015).

[9] Quantum detectors xspress 3: The next generation of solid state detector readout. `http://www.quantumdetectors.com/xspress3/`.

[10] Gao, N., Ponomarev, I. Y., Xiao, Q. F., Gibson, W. M. & Carpenter, D. A. Monolithic polycapillary focusing optics and their applications in microbeam x-ray fluorescence. *Applied Physics Letters* **69**, 1529–1531 (1996).

[11] Gao, N. & Ponomarev, I. Y. Polycapillary x-ray optics: manufacturing status, characterization and the future of the technology. *X-Ray Spectrometry* **32**, 186–194 (2003).

[12] Gao, N. & Janssens, K. *Polycapillary X-Ray Optics*, chap. 3.3, 89–110 (Wiley&Sons Ltd., 2004).

[13] Mocella, V., Brun, E., Ferrero, C. & Delattre, D. Revealing letters in rolled herculaneum papyri by x-ray phase-contrast imaging. *Nat Commun* **6**, 5895 (2015).

[14] Seales, W. & Delattre, D. Virtual unrolling of carbonized herculaneum scrolls: Research status (2007-2012). *Cronache Ercolanesi* **43**, 191–208 (2013).

[15] Mattusch, C. C. & Lie, H. The villa dei papiri at herculaneum: Life and afterlife of a sculpture collection. *Getty Publications* (2005).

[16] Paderni, C. Extract of a letter from signor camillo paderni, to dr. mead, concerning the antiquities dug up from the ancient herculaneum, dated from naples. *Philos. Trans.* **48**, 71–73 (1753).

[17] Paderni, C. Extract of a letter from camillo paderni, keeper of the museum herculaneum, to thomas hollis, esq. *Philos. Trans.* **48**, 634–638 (1754).

[18] Paderni, C. Extract of a letter from camillo paderni, keeper of the herculaneum museum, to thomas hollis, esq., relating to the late discoveries at herculaneum. *Philos. Trans.* **48**, 821–825 (1753).

[19] Delattre, D. Le point sur les travaux relatifs au pherc. paris 2. *Comptes rendus des séances de l'Académie des Inscriptions et Belles-Lettres* **153-2**, 925–943 (2009).

[20] Brun, E., Cotte, M., Wright, J., Ruat, M., Tack, P., Vincze, L., Ferrero, C., Delattre, D. & Mocella, V. Revealing metallic ink in herculaneum papyri. *Proc Natl Acad Sci U S A* **113**, 3751–3754 (2016).

[21] Canevali, C., Gentile, P., Orlandi, M., Modugno, F., Lucejko, J. J., Colombini, M. P., Brambilla, L., Goidanich, S., Riedo, C., Chiantore, O., Baraldi, P., Baraldi, C. & Gamberini, M. C. A multi-analytical approach for the characterization of powders from the pompeii archaeological site. *Anal Bioanal Chem* **401**, 1801–1814 (2011).

[22] Martinetto, P., Anne, M., Dooryhée, E., Drakopoulos, M., Dubus, M., Salomon, J., Simionovici, A. & Walter, P. Synchrotron x-ray micro-beam studies of ancient egyption make-up. *Nucl. Instr. and Meth. in Phys. Rev. B* **181**, 744–748 (2001).

[23] Cotte, M., Dumas, P., Richard, G., Breniaux, R. & Walter, P. New insight on ancient cosmetic preparation by synchrotron-based infrared microscopy. *Analytica Chimica Acta* **553**, 105–110 (2005).

[24] Walter, P., Martinetto, P., Tsoucaris, G., Breniaux, R., Lefebvre, M. A., Richard, G., Talabot, J. & Dooryhee, E. Making make-up in ancient egypt. *Nature* **397**, 483–484 (1999).

[25] Wagner, B., Donten, M. L., Donten, M., Bulska, E., Jackowska, A. & Sobucki, W. Analytical approach to the conservation of the ancient egyptian manuscript "bakai book of the dead": a case study. *Microchimica Acta* **159**, 101–108 (2007).

[26] Baraldi, P., Moscardi, G., Bensi, P., Aceto, M. & Tassi, L. An investigation of the palette and techniques of some high medieval codices by raman microscopy. *Pigment and ink analysis of medieval codices, e-PS* **6**, 163–168 (2009).

[27] Vornicu, N., Melniciuc-Puică, N. & Ardelean, E. Red pigments used for writing and illuminating manuscripts. *Scientific Annals of the Alexandru Ioan Cuza University of Iasi Orthodox Theology* **1**, 75–87 (2013).

[28] Maroger, J. *The Secret Formulas and Techniques of the Masters* (Hacker Art Books, 1948).

[29] Cotte, M., Checroun, E., Susini, J., Dumas, P., Tchoreloff, P., Besnard, M. & Walter, P. Kinetics of oil saponification by lead salts in ancient preparations of pharmaceutical lead plasters and painting lead mediums. *Talanta* **70**, 1136–1142 (2006).

[30] Kastens, M. L. & Hansen, F. R. Drier soap manufacture. *Industrial and Engineering Chemistry* **41**, 2080–2090 (1949).

[31] Sabin, A. H. *Industrial and artistic technology of paint and varnish* (New York,: J. Wiley & Sons, Inc.; London,; Chapman & Hall, limited, 1927).

[32] Winckelmann, J. J., Jansen, H., Brühl, H. & Barrois, L.-F. *Recueil de lettres de M. Winckelmann, sur les découvertes faites à Herculanum, à Pompeii, à Stabia, à Caserte & à Rome* (A Paris : Chez Barrois l'Aîné, libraire, quai des Augustins, 1784).

[33] Boot, J. C. G. *Notice sur les manuscrits trouvés à Herculanum* (Amsterdam, J. Müller, 1841).

[34] Tack, P., Cotte, M., Bauters, S., Brun, E., Banerjee, D., Bras, W., Ferrero, C., Delattre, D., Mocella, V. & Vincze, L. Tracking ink composition on herculaneum papyrus scrolls: quantification and speciation of lead by x-ray based techniques and monte carlo simulations. *Scientific Reports* **6**, 20763 (2016).

[35] Kirkpatrick, P. & Baez, A. V. Formation of optical images by x-rays. *J Opt Soc Am* **38**, 766–774 (1948).

[36] Decker, K. W., Lines, M., Xu, D. & Perkins, R. Radiation window with coated silicon support structure; patent - us 7,709,820 b2 (2010).

[37] Solé, V. A., Papillon, E., Cotte, M., Walter, P. & Susini, J. A multiplatform code for the analysis of energy-dispersive x-ray fluorescence spectra. *Spectrochimica Acta Part B: Atomic Spectroscopy* **62**, 63–68 (2007).

[38] Vekemans, B., Janssens, K., Vincze, L., Adams, F. & Vanespen, P. Analysis of x-ray-spectra by iterative least-squares (axil) - new developments. *X-Ray Spectrometry* **23**, 278–285 (1994).

[39] Vekemans, B., Janssens, K., Vincze, L., Aerts, A., Adams, F. & Hertogen, J. Automated segmentation of l-xrf image sets. *X-Ray Spectrometry* **26**, 333–346 (1997).

[40] Vekemans, B., Vincze, L., Brenker, F. E. & Adams, F. Processing of three-dimensional microscopic x-ray fluorescence data. *Journal of Analytical Atomic Spectrometry* **19**, 1302–1308 (2004).

[41] Schoonjans, T., Brunetti, A., Golosio, B., del Rio, M. S., Sole, V. A., Ferrero, C. & Vincze, L. The xraylib library for x-ray-matter interactions. recent developments. *Spectrochimica Acta, Part B* **66**, 776–784 (2011).

[42] Schoonjans, T., Vincze, L., Solé, V. A., Sanchez del Rio, M., Brondeel, P., Silversmit, G., Appel, K. & Ferrero, C. A general monte carlo simulation of energy dispersive x-ray fluorescence spectrometers — part 5. *Spectrochimica Acta, Part B* **70**, 10–23 (2012).

[43] Schoonjans, T., Solé, V. A., Vincze, L., Sanchez del Rio, M., Appel, K. & Ferrero, C. A general monte carlo simulation of energy-dispersive x-ray fluorescence spectrometers — part 6. quantification through iterative simulations. *Spectrochimica Acta, Part B* **82**, 36–41 (2013).

[44] Nikitenko, S., Beale, A. M., van der Eerden, A. M., Jacques, S. D., Leynaud, O., O'Brien, M. G., Detollenaere, D., Kaptein, R., Weckhuysen, B. M. & Bras, W. Implementation of a combined saxs/waxs/qexafs set-up for time-resolved in situexperiments. *J Synchrotron Radiat* **15**, 632–640 (2008).

[45] Salomé, M. *et al.* The id21 scanning x-ray microscope at esrf. *Journal of Physics: Conference Series* **425**, 182004 (2013).

[46] Knoll, G. F. *Radiation Detection and Measurement 4th Ed.* (Wiley & Sons, Inc., 2010).

[47] Kim, E. J., Herrera, J. E., Huggins, D., Braam, J. & Koshowski, S. Effect of ph on the concentrations of lead and trace contaminants in drinking water: a combined batch, pipe loop and sentinel home study. *Water Res* **45**, 2763–2774 (2011).

[48] Delile, H., Blichert-Toft, J., Goiran, J. P., Keay, S. & Albarede, F. Lead in ancient rome's city waters. *Proc Natl Acad Sci U S A* **111**, 6594–6599 (2014).

[49] Gabuda, S., Kozlova, S., Erenburg, S. B. & Bausk, N. Xanes pb liii spectra of mixed-valence compound: Minium, pb3o4. *Nuclear Inst. and Methods in Physics Research, A* **543**, 184–187 (2005).

[50] Figueiredo, M. O., Silva, T. P. & Veiga, J. P. A xanes study of the structural role of lead in glazes from decorated tiles, xvi to xviii century manufacture. *Applied Physics A* **83**, 209–211 (2006).

[51] Cheah, S., Malone, S. C. & Feik, C. J. Speciation of sulfur in biochar produced from pyrolysis and gasification of oak and corn stover. *Environ Sci Technol* **48**, 8474–8480 (2014).

[52] Huggins, F. E. & Huffman, G. P. Chlorine in coal - an xafs spectroscopic investigation. *Fuel* **74**, 556–569 (1995).

[53] Niklasson, A., Johansson, L.-G. & Svensson, J.-E. The influence of relative humidity and temperature on the acetic acid vapour-induced atmospheric corrosion of lead. *Corrosion Science* **50**, 3031–3037 (2008).

[54] Arni, P. C., Cochrane, G. C. & Gray, J. D. The emission of corrosive vapours by wood. i. survey of the acid-release properties of certain freshly felled hardwoods and softwoods. *Journal of Applied Chemistry* **15**, 305–313 (1965).

Chapter 6

Confocal XRF/XAS

6.1 Introduction

In order to obtain cross-sectional or fully 3D information using a micro-focus X-ray beam, a computed tomography (CT) approach can be used for XRF/XAS. For each investigated sample cross-section, repeated translational (linear) scans are performed over a large number of sample rotations at a given height (longitudinal position) of the sample. The resulting tomographic data-set, represented by so-called elemental sinograms, is then reconstructed by specialized tomographic reconstruction methods,[1, 2] providing the distribution of elemental constituents in the investigated cross-section within the limitations imposed by sample self-absorption effects. By repeating this process for different sample heights, a three dimensional volume of a sample is probed. Unfortunately, this approach is rather time consuming due to relatively slow motor movement, limited signal intensity and/or detector throughput and, more importantly, the sheer amount of data points that have to be measured. One enormous draw-back is a general lack of local tomographic approaches for XRF, in which limited sub-volumes of the sample can be analyzed relatively rapidly, without having to use artefact prone tomographic reconstruction methods.

However, an alternative approach exists to acquire information from a select sub-volume within a sample. This can be done by applying a confocal detection scheme, in which the detector field of view is limited to a (microscopic) volume by applying X-ray focussing optics in front of the detector and overlapping this optic focal point with that of the primary X-ray beam's focal point, thus generating a confocal volume (Figure 6.1).[3–7] By moving

a sample through this confocal volume, 3D and depth resolved information is acquired selectively from this volume, without the need of sample rotation during data acquisition.

This method is useful when studying layered samples,[8] or heterogeneous samples with specific subvolumes that are of interest.[4, 6, 9] A specific example of the latter are inclusions in natural diamonds originating from deep Earth (reaching depths in some cases exceeding 670 km): these inclusions contain unique and otherwise difficult to access information on deep Earth geology. The diamond host encapsulating these inclusions assures that the chemical structure and contents of the minerals in these inclusions do not change during exhumation. The X-ray scattering is a problematically large fraction of the emitted radiation during XRF and XAS analysis due to the diamond's carbon matrix. However, by measuring in confocal mode the scattering contribution can be decreased significantly, thus allowing for the selective investigation of the separate inclusions with dramatically improved signal-to-noise ratios.

The remainder of this chapter discusses the BM26A DUBBLE micro-confocal setup, and presents some applications for which the setup was used to obtain 3D XAS information.

6.2 The DUBBLE (BM26A) Micro-Confocal Setup

6.2.1 Introduction

In the scope of the development of a micro-focus setup at the DUBBLE beamline (Section 5.2), also the extension to a confocal measurement methodology was implemented. In this approach, the Vortex-EM SDD detector (Hitachi High-Technologies Science America Inc.) is equipped with a XOS (X-ray Optical Systems, NY, USA) manufactured, elliptically shaped polycapillary optic.[10]

This collimating detector optic has a length of 4 cm, a 2 mm diameter entrance window and 10 mm diameter exit window. The focal spot distance is 2 mm away from the entrance window and purge holes to allow for He flushing through the polycapillary optic are foreseen in the polycapillary housing. Due to the low critical angle for total reflection at higher energies, polycapillary optics are characterised by low transmission efficiencies for higher energies (e.g. E >25 keV), rendering them less useful in these energy ranges.

The detector is mounted on three (XYZ) LS-120 linear translation stages (PI miCos

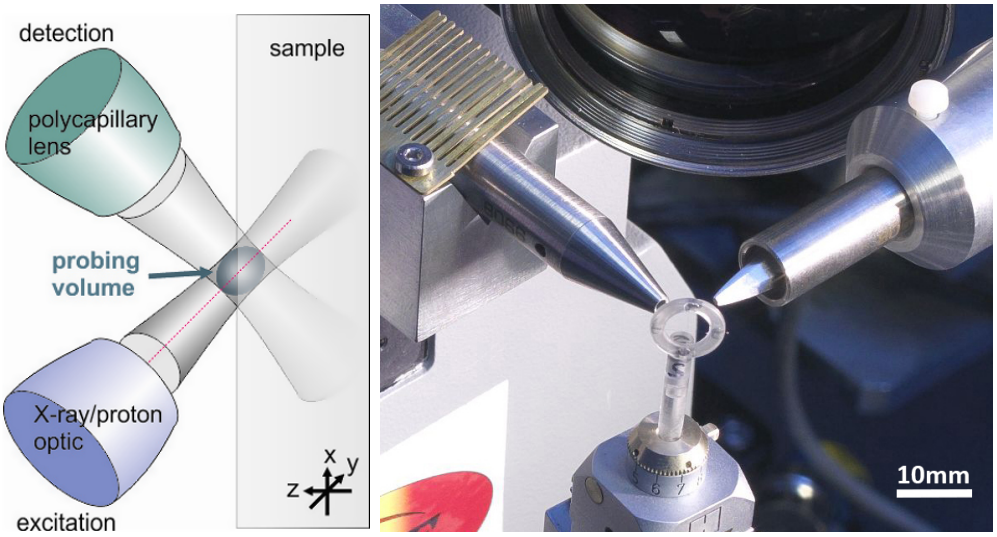

Figure 6.1: Left: Principle of the confocal detection scheme. Figure adapted from Kanngiesser *et al.*[3] Right: Photograph of the polycapillary based confocal setup at beam line BM26A (DUBBLE, ESRF) showing the focussing optic on the left, confocal optic on the right and a 10 μm stainless steel wire cross in a plastic holder ring as a sample.

GmbH). By inserting a metallic wire in the focal spot of the focussing polycapillary optic, the confocal volume can be optimised through an iterative process in which the detector is moved towards the wire and a translational scan of the detector orthogonal to this direction of movement is performed. The iterative process, and thus confocal alignment, is completed when the characteristic emission of the wire shows a minimal full width at half maximum. More information on this setup and its use can be found in S. Bauter's work.

6.2.2 Characterization

For the DUBBLE confocal setup, two dimensions of the confocal volume are defined by the focussing optic focal spot size, thus resulting in a width and height of ~8 μm each (Section 5.2). The depth of the confocal volume is determined by the confocal optic mounted on the detector as described above. Figure 6.2 shows that a confocal volume depth of ~10 μm can be achieved, depending on the energy. This results in a total confocal volume of ~8×8×10 μm^3 from which information can be selectively detected.

Similar to the focal setup, the volume from which information is detected can be adjusted by moving the detector closer to or further away from the point in which both the polycapillary focii overlap. Similar to the focal optic, the divergence of the confocal optic's field of view

is 4.2 °. This option is useful when a confocal volume of slightly larger dimensions than what was attained above is preferred.

Detection limits (DL) were determined for a NIST SRM 1577c bovine liver sample, measured for 1000 s using a 9.029 keV excitation beam (Figure 6.3). For the confocal setup the sample was scanned through the confocal volume and the DL was determined for the sample position providing the highest intensity, corresponding to the point when the confocal volume is filled by the sample surface.

A slightly higher DL is found for the confocal approach when compared to the focal setup as presented in Chapter 5. This is because in focal mode, the $\sim$100 μm thick sample is illuminated and radiation is detected from the full depth of the sample. However, in confocal mode, only information from the top 10 μm is detected, resulting in lower count rates and thus higher, i.e. worse, DL. Additionally, part of the X-ray photons entering the confocal optic are not transmitted to the detector. The corresponding DL for 1 s exposure and elements with atomic number Z between 19 (K) and 29 (Cu) of 1.5-35 ppm are found for the focal setup compared to 3.5-40 ppm for the confocal approach, displaying only a minor difference in sensitivity.

The main disadvantage of the confocal measurement approach is the reduction in detector count rate due to the imperfect and energy dependent confocal optic photon transmission efficiency, and the rather small detector solid angle ($\sim \frac{1}{4}$ sr). These disadvantages can be reduced by applying a polycapillary optic with a larger entrance area, thus increasing the solid angle, or with a different shape, providing a higher transmission efficiency. However, such optics typically also have larger focal spot sizes, thus a balance has to be achieved between sensitivity, spatial resolution and working distances.

Of particular interest to confocal-XAS is the energy dependent primary beam intensity modification by the sample itself: the primary beam intensity as a function of energy impinging the top layer of a sample is different from the one experienced by layers deeper in the sample. This is because the top layer of the sample will partially absorb the beam in an energy dependent manner, thus the primary beam intensity reaching a layer at a given depth is modified by the exponential attenuation term corresponding to the line integral of the energy dependent linear absorption coefficient along the beam path in the sample. In the literature several ways are described to correct for these effects,[9, 11, 12] however nearly all of them assume the composition, or at least the energy dependent absorption, of each layer to be known. It is clear that for most samples this is not the case. Additionally, this

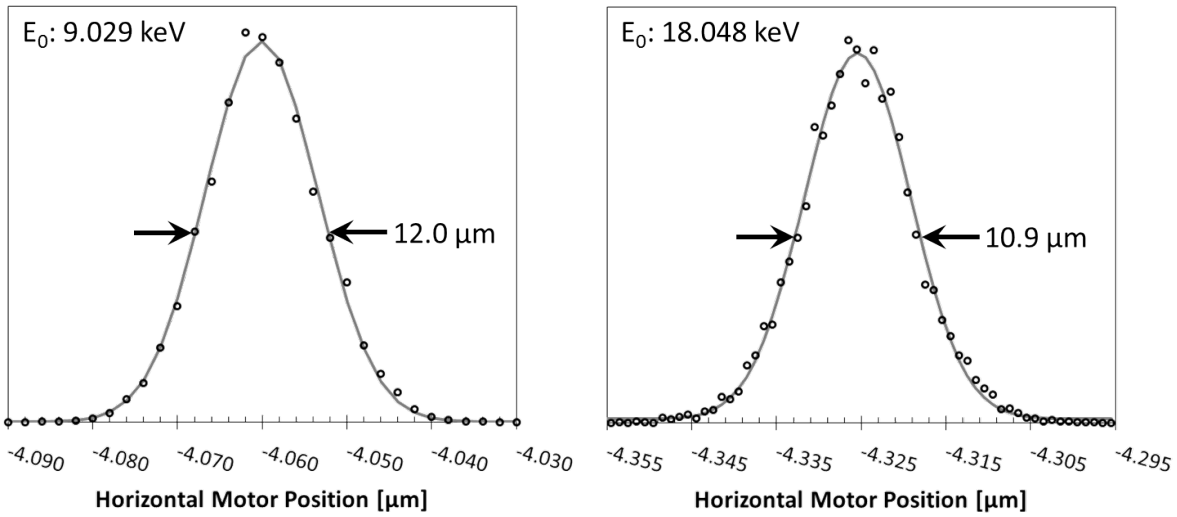

Figure 6.2: Fluorescence intensity curves corresponding to a detector scan in horizontal direction over a 10 μm stainless steel wire at different energies using the DUBBLE BM26A micro-confocal setup (ESRF, Grenoble). Beam sizes are displayed for each scan.

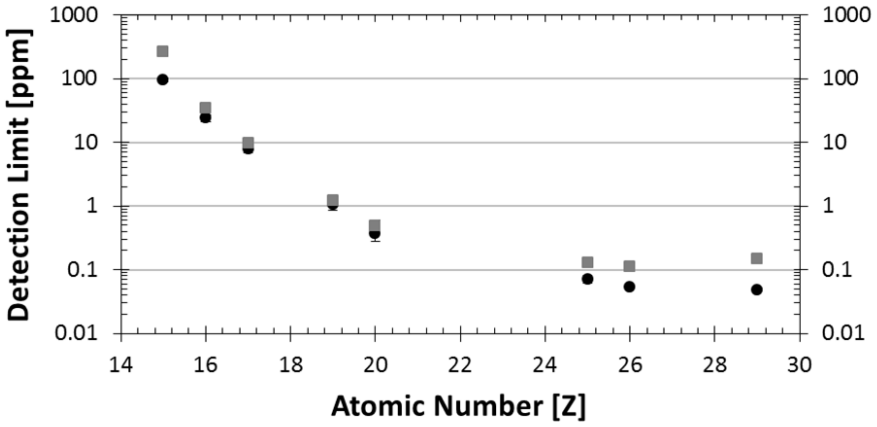

Figure 6.3: Detection limits for the DUBBLE BM26A (ESRF, Grenoble, France) micro-focal (black circles) and micro-confocal (gray squares) setup on a NIST SRM 1577c bovine liver sample. 1000 s exposure time, E_0: 9.029 keV. Error bars represent 3σ confidence level and are occasionally covered by the data point symbol.

effect only visible influences the obtained XAS data when the sample matrix is composed of a significant amount (>5 w%) of the analyte over whose absorption edge an energy scan is performed. Alternatively, a primary beam intensity correction can be performed based on the fluorescence signal of an element with absorption edge well below the edge over which a XAS scan is performed.

6.2.3 Future Prospects

Despite the fact that the confocal volume attainable at BM26A (DUBBLE, ESRF) using the setup described above is amongst the smallest in the world for polycapillary-based confocal setups, many applications could profit from even smaller beam sizes. Additionally, the limited working distance of the confocal setup also limits the combination of confocal measurements with challenging sample environments such as catalytic reactor cells or cryogenic cooling. As such, a future prospect for the DUBBLE confocal setup is to replace the primary focussing optic by a Kirkpatrick-Baez mirror system. This optic not only provides potentially sub-μm beam sizes, it also has a much longer working distance than most polycapillary optics. Additionally, the beam divergence is much lower than for polycapillary optics, rendering this optic useful for SAXS and XRD experiments as well, which can potentially be performed simultaneously with confocal XRF and XAS measurements.

An additional drawback at present concerns the quantitave evaluation of confocal XRF data. For example, Monte Carlo based quantification algorithms currently have not incorporated polycapillary optic simulation. This simulation is particularly problematic for the confocal optic, as radiation from a different sized volume can be detected depending on the X-ray energy. Additionally, the currently applied detector response function should be adjusted to account for the energy dependent transmission efficiency of the polycapillary optic, which is computationally demanding to simulate. Future prospects of the setup exist in the implementation of a confocal XRF quantification routine in the currently available XMI-MSIM software.[13–15]

6.3 Application: Corning Gorilla Glass

This section is adapted from Tack *et al.*[a]

6.3.1 Introduction

Understanding the structural origins of macroscopic properties in silicate glasses is crucial for their high-tech applications. The properties of glasses not only depend on the chemical composition, but also on the processing history. Thermal, pressure and chemical treatments can influence the macroscopic material properties to a large degree. For example, it is known that the coordination number (CN) of atoms or ions in materials increases through application of a sufficiently high pressure,[16–19] a phenomenon that also applies to glassy materials.[20–23] These modifications due to processing conditions are not necessarily uniform throughout the material, as part of the manufacturing process might cause depth dependent modifications. An example of this is the ion exchange process (IX), widely used in the glass industry.

In this process, the glass object to be processed is placed in a molten inorganic salt bath (e.g. KNO_3) at elevated temperatures whereupon smaller alkali ions (e.g. Na^+) from the glass are partially exchanged by larger ones (e.g. K^+) from the molten salt bath via diffusion. As a result, the outer layers of the glass have a different proportion of K_2O and Na_2O while the core of the material remains unchanged.

This exchange leads to formation of a compressive stress layer near the surface of the glass; it is well known and widely used by industry for production of chemically strengthened scratch and damage resistant glasses.[24, 25] As electronics devices are more and more portable, consumer demand drives the devices toward not only having a physically pleasant appearance and functionality but also having excellent mechanical properties, including damage and scratch resistant surfaces. Some of the most successful examples are smartphones and tablets with cover glass post-treated by the IX process. The resulting high compressive stress of the material is the basis of the excellent mechanical properties of these cover glasses.

[a] P. Tack, S. Bauters, J. C. Mauro, M. M. Smedskjaer, B. Vekemans, D. Banerjee, W. Bras, L. Vincze, Confocal depth-resolved micro-X-ray absorption spectroscopy study of chemically strengthened boroaluminosilicate glasses. *RSC Adv.* **6**, 24060-24065, doi:10.1039/C6RA01839D10.1039/c6ra01839d (2016).

Although the ion exchange process is empirically reasonably well understood,[24, 25] much less is known about the fundamental physics of the process. For instance, it is not known which chemical state the dopant elements are in as a function of diffusion depth in alkali-aluminosilicate glasses. According to molecular dynamics simulations of ion-exchanged glass, the CN of network formers is unchanged due to the IX process, whereas the invading alkali ions induce unique structures unattainable via standard melt-quenching processes.[26–28] However, this has not yet been confirmed experimentally.

In this study, a set of boroaluminosilicate glasses, containing 1 mol% of Fe_2O_3 as dopant material, with varying SiO_2 and Al_2O_3 concentrations are provided by Corning Inc. (NY, USA).[29] Fe atoms are used here as a suitable probe for monitoring chemical stress-induced changes in CN, oxidation state, and bond distances in the glasses.[30] Previous studies reported on the changes in CN of B, Al and the presence of non-bridging oxygen (NBO) in these glasses as a result of the different SiO_2/Al_2O_3 ratios.[31–34]

Here we used depth-resolved X-ray absorption spectroscopy (XAS) to determine the chemical state and CN of Fe in the glasses. To monitor depth resolved differences in Fe state in the top 50 μm of the glass and in the bulk ($\sim$100 μm depth), i.e., in compressive and tensile stress regions, respectively, polycapillary optics based confocal XAS measurements are performed, applying a rarely achieved $10\times10\times15\,\mu m^3$ spatial resolution. The Fe–K X-ray absorption near-edge structure (XANES) spectroscopy pre-edge peak contains information on both the oxidation state and CN of the absorbing atom.[35–41]

Conventionally, information on the CN and local structure of the absorbing atom is obtained through extended X-ray absorption fine structure (EXAFS) spectroscopy experiments. Here, we opt not to perform EXAFS measurements for each sample at each depth due to the inherently long acquisition time compared to XANES experiments (easily a factor 10 difference). Instead, EXAFS experiments are performed on a few selected samples at a depth near the surface (25 μm depth) and closer to the bulk (55 μm depth). This is done in order to compare with the XANES results and verify that the conclusions based upon the XANES results are valid even beyond the structural length scale for which XANES normally would render results.

A major objective of this approach is to minimize the local absorbed radiation dose since it has become clear in recent years that when glassy material is exposed to a too high local Xray dose, the structural and chemical information obtained via X-ray based techniques might be compromised due to the generation of a high local concentration of photoelec-

trons.[42–45] The radiation dose required to obtain valid XANES results is only a fraction from the dose required to obtain a complete EXAFS spectrum and therefore an assessment is made if the information rendered by XANES is sufficient or if complete EXAFS scans have to be made.

6.3.2 Materials and Methods

Glass Samples

A series of 10 boroaluminosilicate glass samples with varying SiO_2 and Al_2O_3 concentration (Table 6.1) and each containing approximately 1 mol% Fe_2O_3 were prepared by melt-quenching, as described in detail elsewhere.[32] The glasses will be further referred to by their code as shown in the top row of Table 6.1. To induce a high compressive stress in the surface layers of the glasses, each glass sample was cut to a size of $2\times2\times0.1\,cm^3$ and ion exchanged in a refined grade KNO_3 molten salt bath for 4 hours at 410 °C. During this ion exchange process, Na^+ ions are replaced by the larger K^+ ions, generating a compressive stress in the glass surface, thereby improving its mechanical durability. Due to the nature of the diffusion-limited ion exchange process, more Na^+ ions are replaced at the surface of the glass compared to the bulk of the glass.

XAS

Confocal XAS experiments were performed at BM26A, part of the Dutch-Belgian beam line (DUBBLE) at the ESRF.[46] The beam line receives the radiation from a 0.40 T ESRF bending magnet. A double crystal Si(111) monochromator operating in a fixed exit mode in combination with a collimating mirror allows an energy resolution $\Delta E/E$ of 1.7×10^{-4} at

Table 6.1: Glass composition in mol% before applying the ion exchange process.

	Al0	**Al1**	**Al2.5**	**Al5**	**Al7.5**	**Al10**	**Al12.5**	**Al15**	**Al17.5**	**Al20**
SiO_2	79.4	78.9	77.4	74.7	71.8	68.9	67.1	64.1	62.3	61.1
Al_2O_3	0.3	0.7	2.2	4.7	7.6	10.3	12.6	15.6	17.9	19.4
Na_2O	14.6	14.5	14.6	14.6	14.7	14.8	14.3	14.3	13.7	13.6
B_2O_3	4.9	4.9	4.9	5.0	4.9	5.0	5.0	5.0	5.1	5.0
Fe_2O_3	0.9	0.9	0.9	1.0	1.0	1.0	1.0	1.0	0.9	0.9

9.659 keV. A vertically focusing mirror behind the monochromator allows vertical focusing and higher energy harmonic suppression.

The primary intensity was determined with a gas-filled ion chamber and the transmitted intensity was determined with an identical device. The gas mixtures in both ionization chambers were adjusted to allow approximately 10% absorption in the first and about 70% absorption in the second ionization chamber at 7.212 keV. The photon flux was $\sim 6 \times 10^9$ photons per s at the sample position at the Fe K-edge energy (7112 eV). A 4 μm thick pure iron foil (Goodfellow SARL, Lille, France) was measured in transmission mode at regular time intervals during the experiment to correct for monochromator energy shifts by setting the first inflection point of the XANES profile to 7112 eV.

The incident X-ray beam was focused down to a 10(V)×10(H) μm^2 (FWHM) spot size at the sample position at the Fe K-edge energy using a polycapillary X-ray lens (XOS, NY, USA). A Vortex-EM silicon drift detector (Hitachi High-Technologies Science America Inc., California, USA), equipped with a collimating polycapillary optic lens (XOS, NY, USA), was placed perpendicular to the incident X-ray beam in the plane of polarization. The foci of both polycapillaries were aligned to coincide, thus obtaining a confocal detection scheme in which information can be selectively obtained from a 10(V)×10(H)×15(D) μm^3 volume inside the sample matrix at the Fe K-edge energy. By scanning the sample through this confocal volume, direct 3D spatially resolved sample data can be collected.[5, 6, 47] A schematic of the setup is shown in Figure 6.4.

Depth resolved XANES scans were acquired in 5 μm steps for the first 50 μm of the glass surface, and an additional XANES scan was performed at a depth of 105 μm, representative for the bulk of the glasses. The reported depths correspond to the maximal depth probed by the confocal volume, e.g. a reported depth of 20 μm corresponds to the volume 5-20 μm. A single XANES scan was split up in energy as follows: from 7012.0 eV to 7092.0 eV in 3.8 eV steps, from 7093.0 eV to 7110.0 eV in 0.9 eV steps, from 7110.5 eV to 7120.5 eV in 0.5 eV steps, from 7121.0 eV to 7132.0 eV in 0.9 eV steps and from 7133.0 eV to 7343.0 eV in 3.0 eV steps. The total integration time per energy step was adjusted for each depth and sample based on a visual inspection of the obtained XANES spectrum.

Raw XANES data were normalized for incident beam flux using the primary ionization chamber signal, pre-edge subtracted using a linear function and post-edge normalized at an energy of E_0+50 eV. Additionally, the slow variations caused by the atomic absorption profile before and after the edge were subtracted to facilitate linear combination analysis

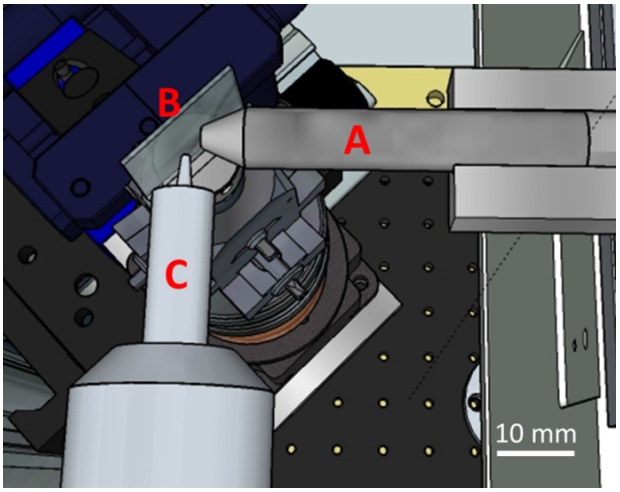

Figure 6.4: Schematic overview of the confocal micro-XAS setup at BM26A. Displayed are the focusing optic (A), focusing the primary beam on the sample (B), mounted on a goniometer head. The focus of confocal optic (C) mounted on the SDD detector coincides with that of the focusing optic, thus creating a confocal volume from which information is selectively acquired.

spectra comparisons.[48] Due to the high absorbing nature of the glass matrix and the intrinsic properties of the confocal detection method, no self-absorption effects are expected and thus were not corrected for. To obtain data on the Fe oxidation state and coordination number (CN), the pre-edge peak, originating from the 1s→3d electron transition, was fitted using a Gaussian function on top of an arctangent background, in line with previous research performed by Wilke *et al.*,[36] Giuli *et al.*[37] and others.[35, 38–41]

EXAFS data were acquired at a depth of 25 μm and 55 μm in the glass, up to 11 $Å^{-1}$ in k-space using 0.05 $Å^{-1}$ steps. The data was processed using the VIPER software package[[49] and fitted using FEFF7[50, 51] calculated scatter paths. A spline was fitted using the VIPER "through the knots" routine, applying 7 knots spaced evenly over the Fourier transformed k-range from 3 to 10.5 $Å^{-1}$. The first coordination shell was fitted in R-space, fitting the module and imaginary space from 0.7 to 2.0 Å (before phase shift correction). During the fitting process, an amplitude reduction factor S_0^2 equal to 0.43 was used, as determined by fitting a hematite structure to have 6 O neighboring atoms (N) around the absorbing Fe atom. Due to the strong correlation between N and S_0^2, the Debye-Waller-like factors were constrained between 0.0025 and 0.0035 $Å^2$.

6.3.3 Results and Discussion

XANES profiles for the Al10 glass, after IX had been performed, at various depths are displayed in Figure 6.5. No clear difference is visible in general between the curves, aside from the different degrees of noise. The curves corresponding to points deeper inside the glass matrix show poorer signal to noise ratios as a result of the decreased intensity measured at these points, which in turn is due to increased absorption related to the larger X-ray path length in the sample. Similar XANES curves are found for each of the ion-exchanged boroaluminosilicate glasses (not shown). When monitoring the Fe–K XANES pre-edge peak (Figure 6.5 inset), subtle differences between the curves are visible. The results of the pre-edge peak surface area and position as a function of depth are shown in Figure 6.6.

A systematic change in pre-edge peak position as a function of Al_2O_3 content is observed (Figure 6.6, right image): an increase in $[Al_2O_3]/[SiO_2]$ ratio corresponds to a decrease in pre-edge peak position. Additionally, a slight decrease in pre-edge peak position with increasing sample depth can be seen, which is discussed in more detail below. No clear trend with pre-edge peak integrated area and glass composition or depth is observed in Figure 6.6, although it appears the pre-edge peak integrated area is slightly larger in the bulk compared to the surface. This is discussed as well in greater detail below.

Since the pre-edge peak position is related to the oxidation state of Fe in the sample,[35–41] a comparison of the pre-edge peak position values obtained from known structures (not displayed) provides insights in the Fe oxidation in the glasses, which is between 2+ and 3+. A gradual decrease in oxidation state with increased $[Al_2O_3]/[SiO_2]$ molar concentration ratio is observed, but an exact quantification of the Fe^{3+}/Fe^{2+} ratio is not performed in this case as an insufficient amount of reference compounds with known Fe^{3+}/Fe^{2+} ratio were available. An attempt was made to compare using database extracted reference spectra. However, a large uncertainty in the results arose due to the difference in energy resolution and smaller step size applied during the scans acquired from the databases.

When comparing the average pre-edge peak area and position for the surface (0–50 μm) with those in the bulk (105 μm), a more clear change in CN and oxidation state of Fe as a function of depth in the glasses is found (Figure 6.7). One can note that this is the average CN for both Fe^{2+} and Fe^{3+} states since it is not possible to differentiate between these two contributions using XAS. Again, the trend in oxidation state (pre-edge peak

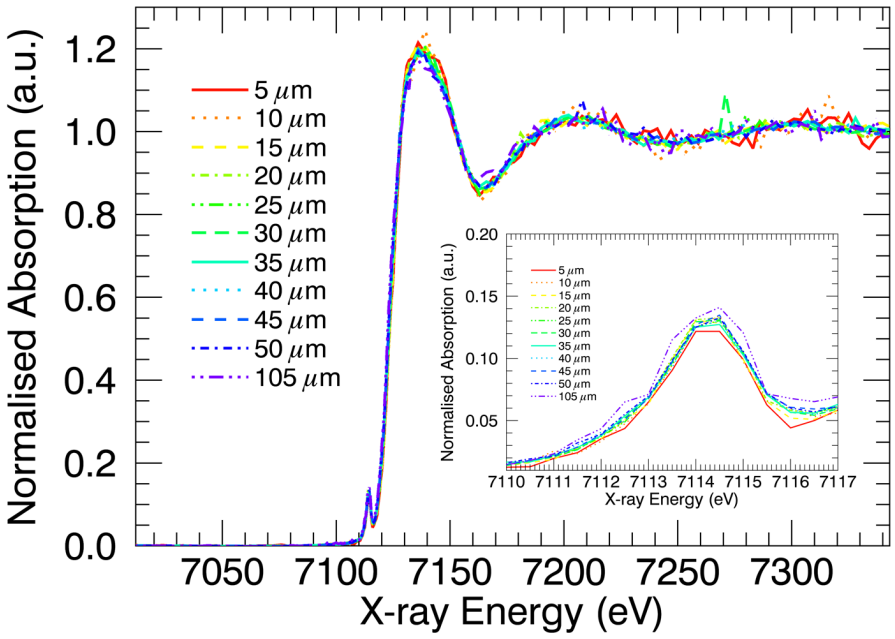

Figure 6.5: Al10 Fe K-edge XANES profiles as a function of probed sample depth with magnification of the pre-edge peak region in the inset, containing information on the Fe oxidation state and coordination number.

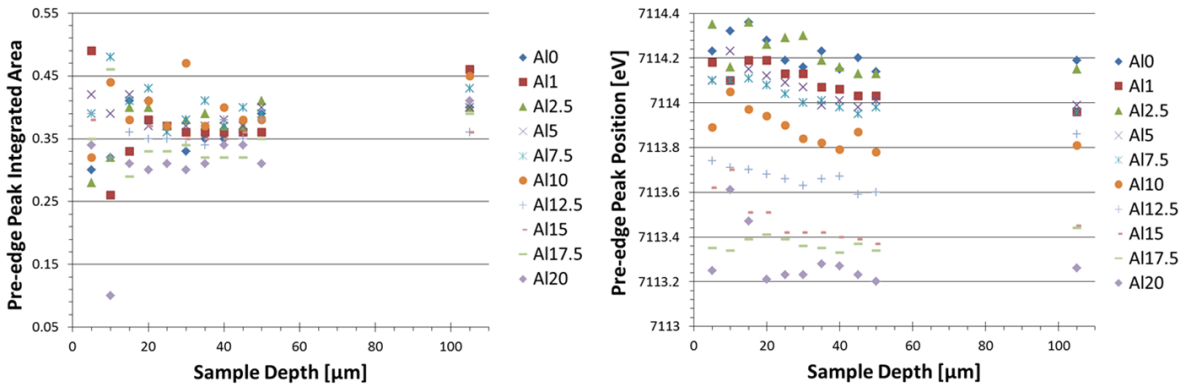

Figure 6.6: Pre-edge peak integrated area (left) and position (right) as a function of sample depth and glass composition. An increase in pre-edge peak integrated area corresponds to a decrease in coordination number; an increase in pre-edge peak position relates to an increase in oxidation state.

position) as a function of glass composition is clearly visible. Additionally, the bulk is generally characterized by an increased pre-edge peak area and slightly decreased pre-edge peak position, respectively, indicating a lower CN and a slightly lower oxidation state for Fe atoms in the bulk as compared to the surface.

In order to obtain more quantitative information on the CN of Fe in the glasses, EXAFS experiments were performed in Al0, Al10, and Al20 glasses at two depths: near the surface (25 μm) and deeper in the bulk (55 μm). The data fits are shown in Figure 6.8, and a graphical representation of the obtained CNs and bond distances is displayed in Figure 6.9. A CN between 4 and 6 was found for Fe at the surface of the glasses, showing a fluctuation as a function of glass composition. This is in full agreement with the XANES pre-edge peak results. Generally, a higher CN is found for Fe at the surface, which is also confirmed by the XANES data (Figure 6.7). Additionally, a change in Fe–O bond distance at the surface of the glasses as a function of glass composition can be seen, with shorter bonds at higher $[Al_2O_3]/[SiO_2]$ ratio. Deeper in the glass sample (55 μm depth), the Fe–O bond distance is found to be independent of $[Al_2O_3]/[SiO_2]$ ratio.

Mysen *et al.* reported that an increase in $Fe^{3+}/\Sigma Fe$ results in an overall decrease in CN of Fe in glasses.[52] Here, a decrease in CN and oxidation state with increasing Al_2O_3 content was perceived, suggesting an opposite trend to what was reported by Mysen *et al.* It should however be noted that the glasses discussed here were ion-exchanged, resulting in a compressive stress of the surface layers. This compressive stress typically increases with $[Al_2O_3]/[SiO_2]$ ratio[53] and may potentially lead to differences in CN for the different glasses. The change in oxidation state with glass composition on the other hand can be explained as a result of the differences in homogenization temperature for glasses with different Al_2O_3/SiO_2 ratios, as was suggested in Smedskjaer *et al.*[32]

The decrease in CN and the increase of the Fe–O bond distances with increasing sample depth can be understood by considering the effect of the IX process on the local atomic structure. Closer to the surface more Na atoms will have been replaced by the larger K atoms, resulting in a compression of the surface layers. As the surface layers are compressed, the bond distances will decrease and even the arrangement of O atoms around Fe can change to a more tightly packed structure, increasing the Fe CN. Deeper in the sample less Na atoms will have been replaced due to the limited diffusion depth of the K atoms and a lower stress is observed, resulting in a less pronounced decrease in bond length or increase of CN. This suggests that high compressive stress plays a similar role as

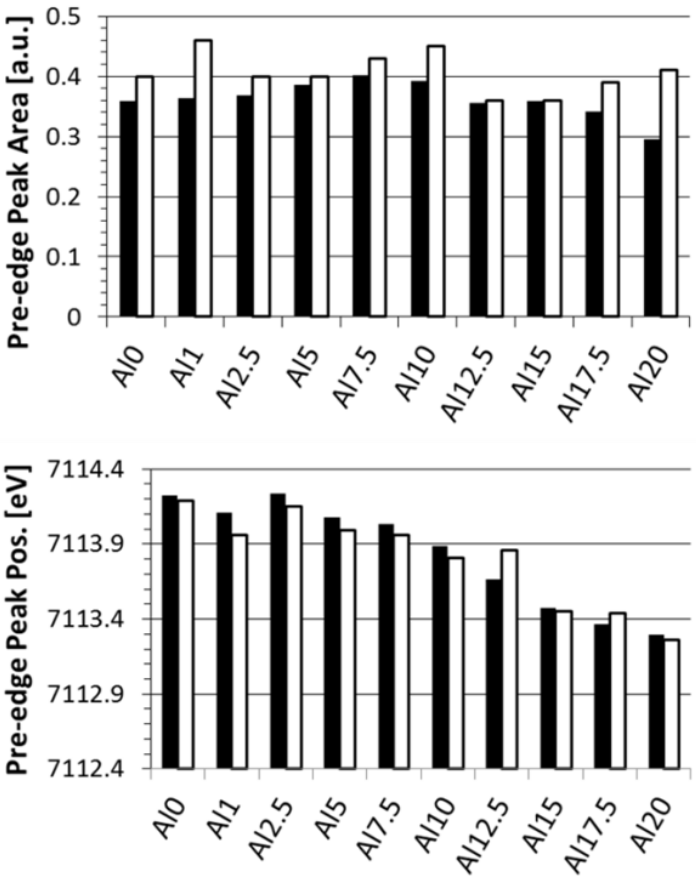

Figure 6.7: Pre-edge peak integrated area (top) and position (bottom) for the averaged surface (0–50 μm; black) and bulk (105 μm; white) regions. The top panel indicates that the bulk is characterized by decrease in coordination number and the bottom panel panel shows a decrease in Fe oxidation state with increasing Al content.

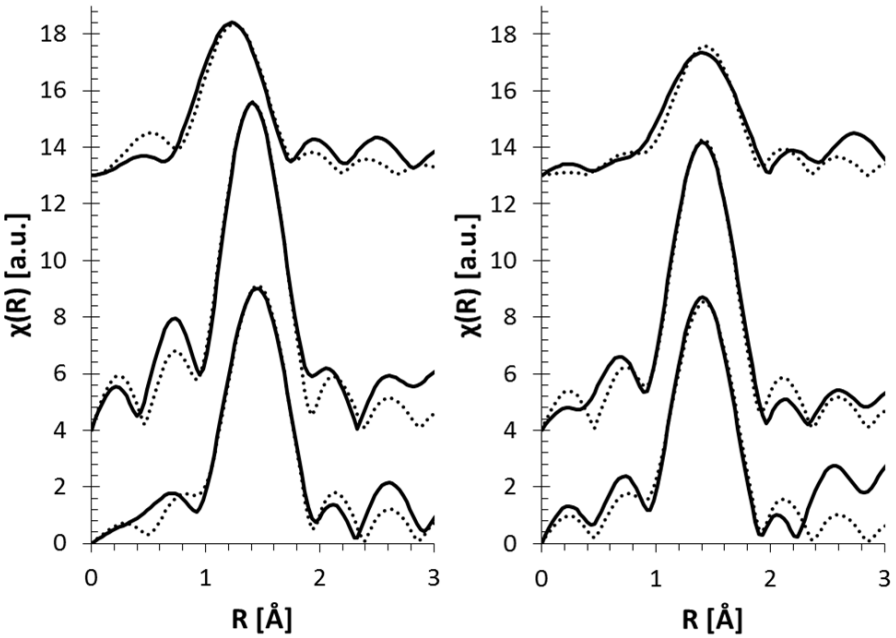

Figure 6.8: EXAFS pseudo radial distribution magnitude plots (solid curve) and their fits (dotted curve) for glasses at 25 μm (left) and 55 μm depth (right).

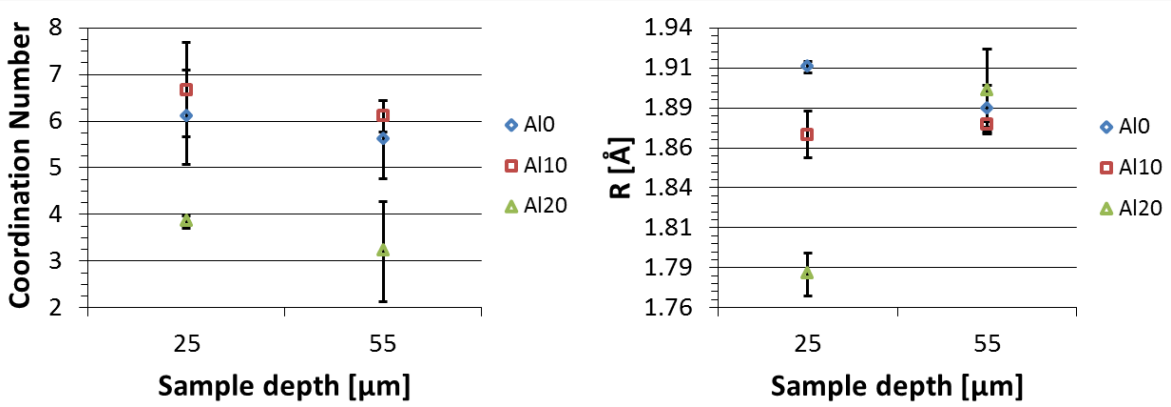

Figure 6.9: EXAFS fitting results for multiple glasses at two different depths. The fitted coordination number (left) and nearest neighbour Fe–O scatter path length (right) are displayed.

high pressure in the glasses.

6.3.4 Conclusion

Fe K-edge confocal micro-XANES and -EXAFS experiments have been performed to study the Fe oxidation state and coordination number (CN) as a function of depth and glass composition in a series of ion-exchanged (IX) boroaluminosilicate glasses in order to determine the structural and chemical differences of the Fe environment as a function of depth below the surface. It was found that XANES experiments are well suited and sufficient to obtain information on the oxidation state of transition metals (e.g., Fe) in these glasses, avoiding the need to perform full EXAFS scans and thus decreasing the exposure of the sample to radiation. However, in order to obtain quantitative information on the CN, EXAFS experiments are more conclusive.

The Fe oxidation state decreases with increasing $[Al_2O_3]/[SiO_2]$ ratio in the bulk of the glasses. This feature is believed to originate from the different homogenization temperatures applied to the different glasses. Also a decrease in CN was observed with increased alumina content. Additionally, the depth-resolved data show an increase of CN and decrease of Fe–O bond distance at the surface compared to deeper inside the glass matrix, which is also explained by the IX process induced stress.

These findings represent previously unknown information on the impact of the IX-generated compressive stress and K-for-Na substitution on the local atomic structure and will aid in further developing and improving the unique characteristics and functionalities of such damage-resistant glasses. Moreover, it is shown that confocal micro-XAS experiments are a useful addition to analytical research in order to obtain unique information on a large variation of samples, not excluding *in situ* or similarly challenging experiments.

6.4 Application: Rare Natural Deep Earth Diamond Inclusions

6.4.1 Introduction

Deep Earth (>670 km below the surface) is typically studied through indirect methods based on high-pressure techniques and seismological data as direct sampling is problematic.[54, 55] However, some rare geological materials can be regarded as unique messengers from deep Earth. Such samples are diamonds which, in certain cases, carry precious sources of geological information on the mantle in the form of tiny heterogeneities, i.e. inclusions, trapped within the diamond host during their formation. Most natural diamonds are formed in the lithospheric upper mantle (<200 km), however a few sources provide diamonds from depths below the lithosphere, of several hundreds of km depth. Fluids, minerals and rock fragments can be trapped during the growth of these diamonds. As the inclusions' original composition and sometimes high pressure structure is preserved during transport of the diamond towards Earth's surface and exhumation, these diamonds provide one of the few tools to obtain direct information on deep Earth composition.[56–62]

Performing XANES experiments on these inclusions allows for the identification of the mineral phases present in the inclusions. Due to the high scattering power of the diamond matrix, the confocal detection scheme is a necessity in order to improve signal-to-scatter background ratios. Additionally, the direct spatially resolved 3D XRF information can determine the variation of chemical composition within the studied inclusions. The volume ratios/shapes of chemically characterised phases in turn gives information on the formation of the diamond and its inclusions.

The investigation of a set of diamonds originating from the Sao Luis area in Brazil is reported below, which was made possible at ESRF DUBBLE by the development of the above described confocal XRF/XAS setup. The diamonds were investigated at the BM26A beamline, using the confocal setup which has been described in detail above. A confocal volume of $14\times13\times17\,\mu m^3$ (W×H×D) was used to allow for the investigation of large sample volumes (cross-sectional slices of $>1.5\times1.5\,mm^2$) in reasonable time frames (∼2 h/slice).

6.4.2 Results and Discussion

As the diamond inclusions of interest mainly contain iron rich minerals, the primary beam excitation energy was set to 7.21 keV, slightly above the Fe K-edge. A cross-sectional slice consisting of 76×76 points with a 20 μm step size was performed on diamond SL-FFM-13, representing a volume slice of $1.5\times1.5\times0.015\,\mathrm{mm}^3$ in the diamond. An exposure time of 1 s/voxel was applied. XRF elemental composition maps are shown in Figure 6.10.

Judging by the scatter images (Compton and Rayleigh) most Fe hot spots, i.e. high Fe concentrations, in Figure 6.10 appear to be located on or close to the sample surface . As such, it is not certain whether these inclusions are open to air and thus have been potentially changed in chemical structure and composition. A XANES scan was performed on the inclusion deeper in the sample, and compared to several Fe containing minerals. The closest resemblance was found to magnetite (Fe_3O_4) and hematite (Fe_2O_3). Linear combination analysis showed a 30±4 % and 67±3 % contribution of magnetite and hematite respectively.

Investigation of another diamond, SL-FFM-15 (Figure 6.11) shows several inclusions that are bridged either by a narrow crack just below the diamond surface, or by the diamond surface itself. In contrast to the inclusion investigated in SL-FFM-13, the inclusions in SL-FFM-15 also show the presence of several other elements such as K, Ca, Ti, V, Cr and Mn. Two XANES scans at separate parts of the inclusion were performed to investigate whether the mineral phase in both inclusions is the same. In both inclusions the Fe content was nearly pure Fe_2O_3.

A third diamond, SL-FFM-16, was investigated at two different sample height positions (Figure 6.12). Each height reveals an inclusion with a circular shape composed of K, Ca, Ti, V, Cr, Mn and Fe. Fe K-edge XANES reveals that both inclusions contain an olivine-like mineral. This mineral is of particular interest as it is a low pressure equivalent of ringwoodite, which in turn is a mineral that can incorporate percentage levels by weight of water in its structure. As such, the presence of ringwoodite in a deep Earth diamond is proof for the presence of a large reservoir of water in deep Earth.[7, 63, 64] The olivine XANES spectrum is not identical to that of the diamond inclusions, which suggests the Fe is in a chemical state very similar to olivine. Further analyses, i.e. confocal Raman spectroscopy, will show whether the mineral present is indeed ringwoodite, or another olivine-like mineral.

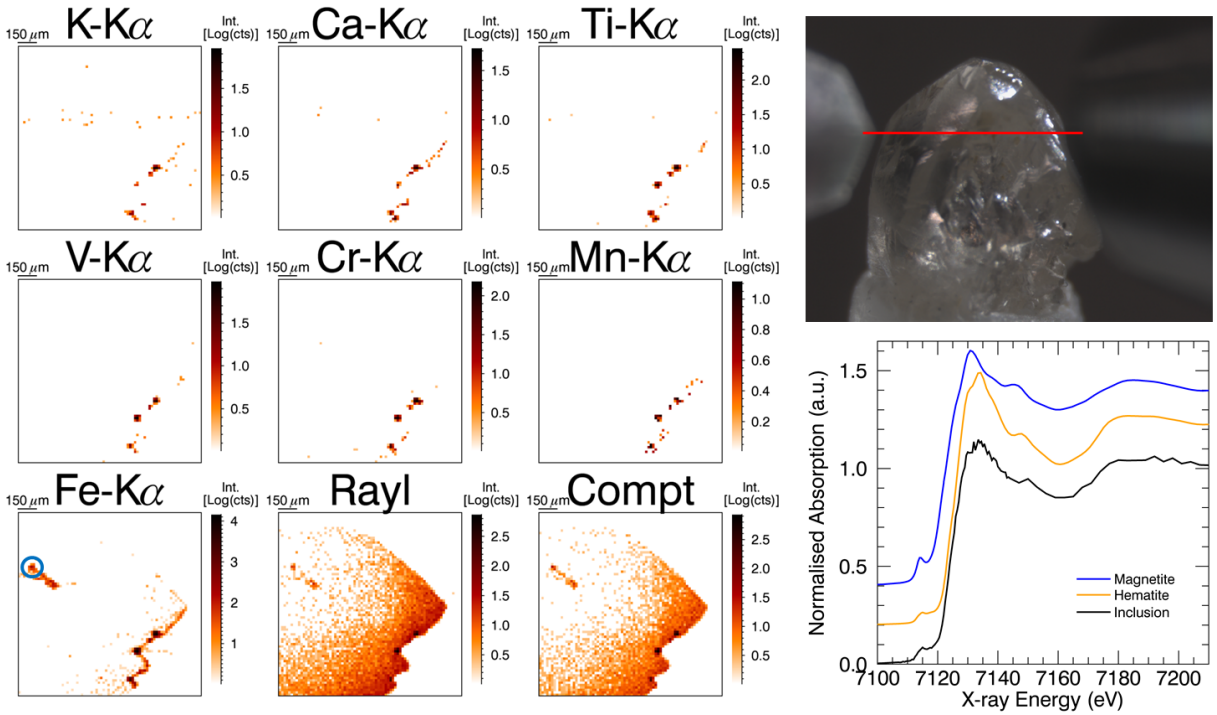

Figure 6.10: X-ray fluorescence spectroscopy elemental composition maps of a cross-sectional volume slice in diamond SL-FFM-13 acquired at BM26A (left) with a photograph denoting the region in which the scan was performed (top right) and the XANES scan of the inclusion marked on the XRF Fe K_α composition image (blue circle), compared to reference compound spectra (bottom right).

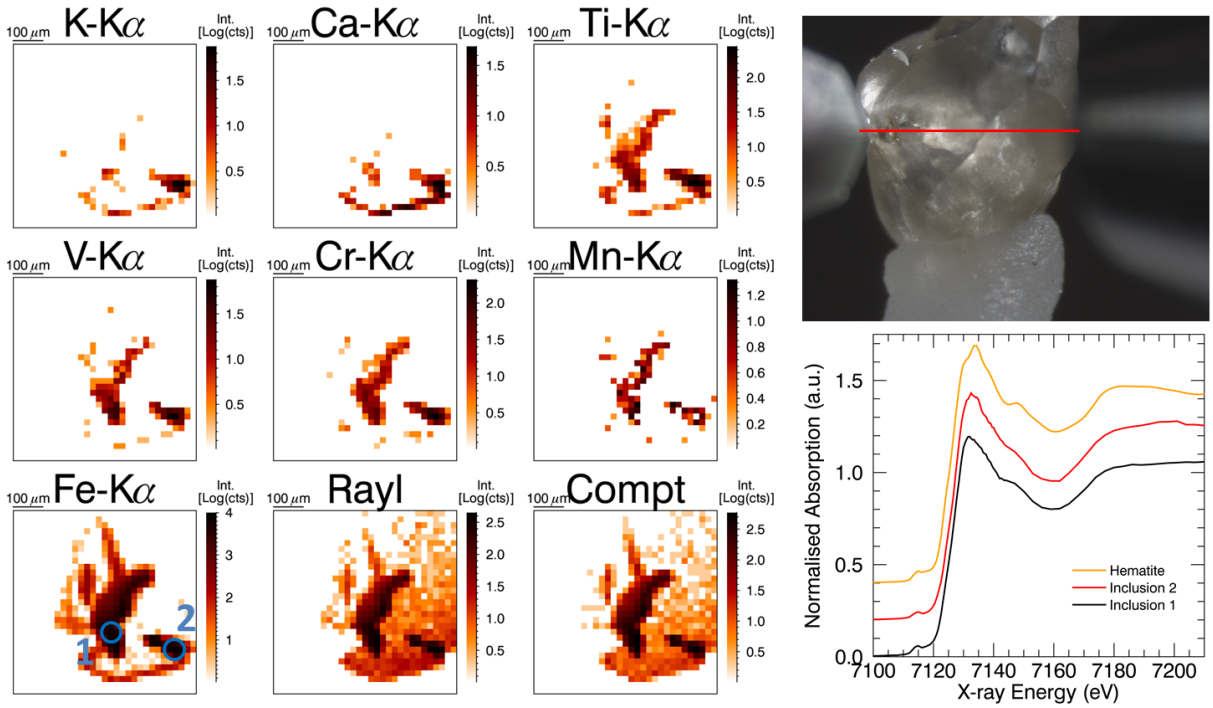

Figure 6.11: X-ray fluorescence spectroscopy elemental composition maps of a cross-sectional volume slice in diamond SL-FFM-15 acquired at BM26A (left) with a photograph denoting the region in which the scan was performed (top right) and the XANES scan of the inclusions marked on the XRF Fe K_α composition image (blue circles), compared to the hematite spectrum (bottom right).

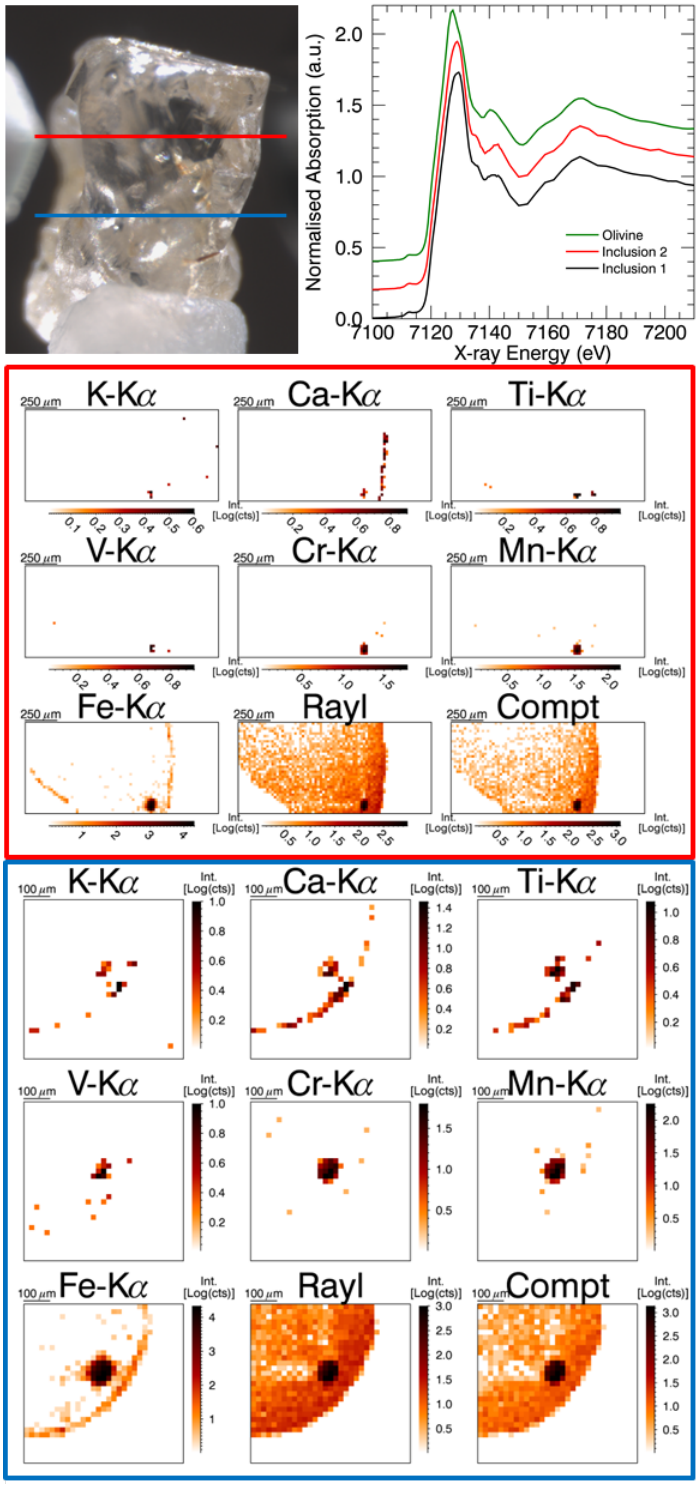

Figure 6.12: X-ray fluorescence spectroscopy elemental composition maps of 2 cross-sectional volume slices in diamond SL-FFM-16 acquired at BM26A (bottom) with a photograph denoting the regions in which the scan was performed (top left) and the XANES scan of the inclusions of each slice, compared to the olivine spectrum (top right).

6.4.3 Conclusion

Confocal XRF and XAS experiments have been performed at BM26A, measuring natural deep Earth diamond inclusions. These experiments represent a milestone of development at beamline BM26A, demonstrating the application of previously not possible micro-beam based confocal XRF/XAS technigues on unique geological materials.

Several inclusions were located by means of XRF cross-sectional slicing of the diamond, followed by XAS scans in selected points of interest of the found inclusions. It was attempted to perform full-3D XANES experiments, during which a full energy range XANES scan is recorded for each voxel of a selected volume. However, the measurement time coupled to such a measurement, given the low flux of detected Fe radiation, was too high with respect to the available beam time and the amount of samples that should be investigated, as well as the likelihood of finding heterogeneously distributed minerals within a single inclusion. As such, it was decided to measure confocal micro-XANES spectra only in selected regions of interest, under the assumption that the entire inclusion is represented by this single micro-volume.

Based on the confocal XRF measurements on these inclusions scientists are capable of directly probing the composition of deep Earth. The composition, volume and structure of the inclusions can give information on the formation and exhumation process of the diamond. Additional XAS experiments give information on the chemical structure of compounds in the inclusions, which were unchanged during exhumation due to the protective shielding of the diamond surrounding. A good signal-to-scatter ratio is obtained due to the confocal detection scheme, reducing the monitoring of the intense diamond matrix scattering.

The presence of an olivine-like phase, magnetite and hematite was shown in the diamonds. The olivine-like phase can be ringwoodite, which is indicative for an aquas deposit in deep Earth. According to McCammon *et al.* the presence hematite also hints at the presence of hydrous regions in deep Earth.[65]

6.5 Summary

The confocal detection scheme, in which the detector field of view is limited to a (microscopic) volume by applying an X-ray focussing optic in front of the detector and overlapping this optic's focal point with that of the primary X-ray beam's focal point, allows for direct 3D scanning of a select sub-volume of a sample. A polycapillary based 'plug-and-play' confocal setup was designed and developed at the BM26A DUBBLE beamline at the ESRF.

This setup provides confocal volumes down to the order of $8{\times}8{\times}10\,\mu\text{m}^3$ depending on excitation and detected X-ray energy, which is amongst the smallest reported confocal volumes. The application of the setup towards spatially depth-resolved EXAFS in high compressive strength boroaluminosilicate glasses and 3D confocal slicing of natural deep Earth diamond inclusions was displayed.

It has been shown that depth resolved studies are feasible, which could open up a new research area, for instance industrial research. Full volume 3D XAS experiments, in which a full energy scan is performed for each sample voxel within a selected sample volume, was not performed as this approach is inherently time consuming due to the relatively low count rates and comparably long motor movement overhead time. Future prospects consist of the implementation of a KB mirror as focussing optic of the primary X-ray beam, allowing for larger working distance and thus more diverse sample environments as well as the combination of confocal XRF/XAS with XRD and SAXS.

3D mapping of a sample rapidly becomes very time consuming with increasing volume size. As such, an alternative was developed in full-field XRF/XAS, where spatially resolved information is acquired from a large area/surface in a single measurement, without the need for raster scanning of the sample through the beam position, presenting a significant decrease in required measurement time. This full-field approach is discussed in the next chapter (Chapter 7).

References

[1] Schroer, C. G. Reconstructing x-ray fluorescence microtomograms. *Applied Physics Letters* **79**, 1912–1914 (2001).

[2] Golosio, B., Simionovici, A., Somogyi, A., Lemelle, L., Chukalina, M. & Brunetti, A. Internal elemental microanalysis combining x-ray fluorescence, compton and transmission tomography. *Journal of Applied Physics* **94**, 145–156 (2003).

[3] Kanngiesser, B., Malzer, W., Mantouvalou, I., Sokaras, D. & Karydas, A. G. A deep view in cultural heritage—confocal micro x-ray spectroscopy for depth resolved elemental analysis. *Applied Physics A* **106**, 325–338 (2011).

[4] Laclavetine, K., Ager, F. J., Arquillo, J., Respaldiza, M. n. & Scrivano, S. Characterization of the new mobile confocal micro x-ray fluorescence (cxrf) system for in situ non-destructive cultural heritage analysis at the cna: μxrf-concha. *Microchemical Journal* **125**, 62–68 (2016).

[5] Silversmit, G., Vekemans, B., Nikitenko, S., Tirez, K., Bras, W., Brenker, F. E. & Vincze, L. Polycapillary based µ-xas and confocal µ-xanes at a bending magnet source of the esrf (2009).

[6] Silversmit, G., Vekemans, B., Nikitenko, S., Schmitz, S., Schoonjans, T., Brenker, F. E. & Vincze, L. Spatially resolved 3d micro-xanes by a confocal detection scheme. *Phys Chem Chem Phys* **12**, 5653–5659 (2010).

[7] Silversmit, G., Vekemans, B., T.Schoonjans, Voorde, L. V. D., Schmitz, S., Appel, K., Brenker, F. & Vincze, L. Three-dimensional confocal μ-xanes on mineral inclusions in natural diamonds. *Photon Science 2009 : highlights and HASYLAB annual report : author contributions* (2010).

[8] Tack, P., Bauters, S., Mauro, J. C., Smedskjaer, M. M., Vekemans, B., Banerjee, D., Bras, W. & Vincze, L. Confocal depth-resolved micro-x-ray absorption spectroscopy study of chemically strengthened boroaluminosilicate glasses. *RSC Adv.* **6**, 24060–24065 (2016).

[9] Luhl, L., Hesse, B., Mantouvalou, I., Wilke, M., Mahlkow, S., Aloupi-Siotis, E. & Kanngiesser, B. Confocal xanes and the attic black glaze: the three-stage firing process through modern reproduction. *Anal Chem* **86**, 6924–6930 (2014).

[10] Gao, N. & Janssens, K. *Polycapillary X-Ray Optics*, chap. 3.3, 89–110 (Wiley&Sons Ltd., 2004).

[11] Luhl, L., Mantouvalou, I., Malzer, W., Schaumann, I., Vogt, C., Hahn, O. & Kanngiesser, B. Reconstruction procedure for 3d micro x-ray absorption fine structure. *Anal Chem* **84**, 1907–1914 (2012).

[12] Luhl, L., Mantouvalou, I., Schaumann, I., Vogt, C. & Kanngiesser, B. Three-dimensional chemical mapping with a confocal xrf setup. *Anal Chem* **85**, 3682–3689 (2013).

[13] Schoonjans, T., Brunetti, A., Golosio, B., del Rio, M. S., Sole, V. A., Ferrero, C. & Vincze, L. The xraylib library for x-ray-matter interactions. recent developments. *Spectrochimica Acta, Part B* **66**, 776–784 (2011).

[14] Schoonjans, T., Vincze, L., Solé, V. A., Sanchez del Rio, M., Brondeel, P., Silversmit, G., Appel, K. & Ferrero, C. A general monte carlo simulation of energy dispersive x-ray fluorescence spectrometers — part 5. *Spectrochimica Acta, Part B* **70**, 10–23 (2012).

[15] Schoonjans, T., Solé, V. A., Vincze, L., Sanchez del Rio, M., Appel, K. & Ferrero, C. A general monte carlo simulation of energy-dispersive x-ray fluorescence spectrometers — part 6. quantification through iterative simulations. *Spectrochimica Acta, Part B* **82**, 36–41 (2013).

[16] Elliott, S. R. *Physics of Amorphous Materials* (Wiley, New York, 1988).

[17] Guthrie, M., Tulk, C., Benmore, C., Xu, J., Yarger, J., Klug, D., Tse, J., Mao, H. k. & Hemley, R. Formation and structure of a dense octahedral glass. *Physical Review Letters* **93** (2004).

[18] Meng, Y., Mao, H. K., Eng, P. J., Trainor, T. P., Newville, M., Hu, M. Y., Kao, C., Shu, J., Hausermann, D. & Hemley, R. J. The formation of sp3 bonding in compressed bn. *Nat Mater* **3**, 111–114 (2004).

[19] Yarger, J. L., Smith, K. H., Nieman, R. A., Diefenbacher, J., Wolf, G. H., Poe, B. T. & Mcmillan, P. F. Al coordination changes in high-pressure aluminosilicate liquids. *Science* **270**, 1964–1967 (1995).

[20] Grimsditch, M., Polian, A. & Wright, A. C. Irreversible structural changes in vitreous b2o3 under pressure. *Phys Rev B Condens Matter* **54**, 152–155 (1996).

[21] Lee, S. K., Eng, P. J., Mao, H.-k., Meng, Y., Newville, M., Hu, M. Y. & Shu, J. Probing of bonding changes in b2o3 glasses at high pressure with inelastic x-ray scattering. *Nature Materials* **4**, 851–854 (2005).

[22] Wondraczek, L., Sen, S., Behrens, H. & Youngman, R. E. Structure-energy map of alkali borosilicate glasses: Effects of pressure and temperature. *Physical Review B* **76** (2007).

[23] Wu, J., Deubener, J., Stebbins, J. F., Grygarova, L., Behrens, H., Wondraczek, L. & Yue, Y. Structural response of a highly viscous aluminoborosilicate melt to isotropic and anisotropic compressions. *The Journal of Chemical Physics* **131**, 104504 (2009).

[24] Tyagi, V. & Varshneya, A. K. Measurement of progressive stress buildup during ion exchange in alkali aluminosilicate glass. *Journal of Non-Crystalline Solids* **238**, 186–192 (1998).

[25] Varshneya, A. K. Kinetics of ion-exchange in glasses. *Journal of Non-Crystalline Solids* **19**, 355–365 (1975).

[26] Tandia, A., Vargheese, K. D. & Mauro, J. C. Elasticity of ion stuffing in chemically strengthened glass. *Journal of Non-Crystalline Solids* **358**, 1569–1574 (2012).

[27] Tandia, A., Vargheese, K. D., Mauro, J. C. & Varshneya, A. K. Atomistic understanding of the network dilation anomaly in ion-exchanged glass. *Journal of Non-Crystalline Solids* **358**, 316–320 (2012).

[28] Vargheese, K. D., Tandia, A. & Mauro, J. C. Molecular dynamics simulations of ion-exchanged glass. *Journal of Non-Crystalline Solids* **403**, 107–112 (2014).

[29] Boyd, D. Sodium aluminosilicate glass article strengthened by a surface compressive stress layer (1973).

[30] Myson, B. O., Seifert, F. & Virgo, D. Structure and redox equilibria of iron-bearing silicate melts. *American Mineralogist* **65**, 867–884 (1980).

[31] Smedskjaer, M. M., Mauro, J. C. & Yue, Y. Ionic diffusion and the topological origin of fragility in silicate glasses. *J Chem Phys* **131**, 244514 (2009).

[32] Smedskjaer, M. M., Zheng, Q., Mauro, J. C., Potuzak, M., Mørup, S. & Yue, Y. Sodium diffusion in boroaluminosilicate glasses. *Journal of Non-Crystalline Solids* **357**, 3744–3750 (2011).

[33] Xiang, Y., Du, J., Smedskjaer, M. M. & Mauro, J. C. Structure and properties of sodium aluminosilicate glasses from molecular dynamics simulations. *J Chem Phys* **139**, 044507 (2013).

[34] Zheng, Q. J., Youngman, R. E., Hogue, C. L., Mauro, J. C., Potuzak, M., Smedskjaer, M. M. & Yue, Y. Z. Structure of boroaluminosilicate glasses: Impact of [al2o3]/[sio2] ratio on the structural role of sodium. *Physical Review B* **86** (2012).

[35] Farges, F., Rossano, S., Lefrere, Y., Wilke, M. & Brown, G. E. Iron in silicate glasses: a systematic analysis of pre-edge, xanes and exafs features. *Physica Scripta* **T115**, 957–959 (2005).

[36] Wilke, M., Partzsch, G. M., Bernhardt, R. & Lattard, D. Determination of the iron oxidation state in basaltic glasses using xanes at the k-edge (vol 213, 71, 2004). *Chemical Geology* **220**, 141–161 (2005).

[37] Giuli, G., Eeckhout, S. G., Paris, E., Koeberl, C. & Pratesi, G. Iron oxidation state in impact glass from the k/t boundary at beloc, haiti, by high-resolution xanes spectroscopy. *Meteoritics & Planetary Science* **40**, 1575–1580 (2005).

[38] Berry, A. J., O'Neill, H. S., Jayasuriya, K. D., Campbell, S. J. & Foran, G. J. Xanes calibrations for the oxidation state of iron in a silicate glass. *American Mineralogist* **88**, 967–977 (2003).

[39] Cottrell, E., Kelley, K. A., Lanzirotti, A. & Fischer, R. A. High-precision determination of iron oxidation state in silicate glasses using xanes. *Chemical Geology* **268**, 167–179 (2009).

[40] Galoisy, L., Calas, G. & Arrio, M. A. High-resolution xanes spectra of iron in minerals and glasses: structural information from the pre-edge region. *Chemical Geology* **174**, 307–319 (2001).

[41] Jackson, W. E., Farges, F., Yeager, M., Mabrouk, P. A., Rossano, S., Waychunas, G. A., Solomon, E. I. & Brown, G. E. Multi-spectroscopic study of fe(ii) in silicate glasses: Implications for the coordination environment of fe(ii) in silicate melts. *Geochimica Et Cosmochimica Acta* **69**, 4315–4332 (2005).

[42] Fuhrmann, S., Schumacher, D., Herbst, J. & Wondraczek, L. Irradiation induced particle formation in ag-doped sulfophosphate glass. *Journal of Non-Crystalline Solids* **401**, 82–86 (2014).

[43] Gonçalves Ferreira, P., de Ligny, D., Lazzari, O., Jean, A., Cintora Gonzalez, O. & Neuville, D. R. Photoreduction of iron by a synchrotron x-ray beam in low iron content soda-lime silicate glasses. *Chemical Geology* **346**, 106–112 (2013).

[44] Martis, V., Nikitenko, S., Sen, S., Sankar, G., van Beek, W., Filinchuk, Y., Snigireva, I. & Bras, W. Effects of x-rays on crystal nucleation in lithium disilicate. *Crystal Growth & Design* **11**, 2858–2865 (2011).

[45] Stanley, H. B., Banerjee, D., van Breemen, L., Ciston, J., Liebscher, C. H., Martis, V., Merino, D. H., Longo, A., Pattison, P., Peters, G. W. M., Portale, G., Sen, S. & Bras, W. X-ray irradiation induced reduction and nanoclustering of lead in borosilicate glass. *Crystengcomm* **16**, 9331–9339 (2014).

[46] Nikitenko, S., Beale, A. M., van der Eerden, A. M., Jacques, S. D., Leynaud, O., O'Brien, M. G., Detollenaere, D., Kaptein, R., Weckhuysen, B. M. & Bras, W. Implementation of a combined saxs/waxs/qexafs set-up for time-resolved in situexperiments. *J Synchrotron Radiat* **15**, 632–640 (2008).

[47] Silversmit, G., Vekemans, B., Nikitenko, S., Bras, W., Czhech, V., Zaray, G., Szaloki, I. & Vincze, L. Polycapillary-optics-based micro-xanes and micro-exafs at a third-generation bending-magnet beamline. *Journal of Synchrotron Radiation* **16**, 237–246 (2009).

[48] Calvin, S. *XAFS for Everyone* (Taylor & Francis, 2013).

[49] Klementev, K. V. Deconvolution problems in x-ray absorption fine structure spectroscopy. *Journal of Physics D-Applied Physics* **34**, 2241–2247 (2001).

[50] Ankudinov, A. L. & Rehr, J. J. Relativistic calculations of spin-dependent x-ray-absorption spectra. *Physical Review B* **56**, R1712–R1715 (1997).

[51] Ankudinov, A. *Relativistic Spin-dependent X-ray Absorption Theory.* Ph.D. thesis, University of Washington (1996).

[52] Mysen, B. O. The structural behavior of ferric and ferrous iron in aluminosilicate glass near meta-aluminosilicate joins. *Geochimica et Cosmochimica Acta* **70**, 2337–2353 (2006).

[53] Dejneka, M. J., Mauro, J. C., Potuzak, M., Smedskjaer, M. M. & Youngman, R. E. Chemically-strengthened borosilicate glass articles (2015).

[54] Duffy, T. S. Synchrotron facilities and the study of the earth's deep interior. *Reports on Progress in Physics* **68**, 1811–1859 (2005).

[55] Romanowicz, B. Global mantle tomography: Progress status in the past 10 years. *Annual Review of Earth and Planetary Sciences* **31**, 303–328 (2003).

[56] Harte, B., Harris, J. W., Hutchison, M. T., Watt, G. R. & Wilding, M. C. Mantle petrology: Field observations and high pressure experimentation: A tribute to francis r. (joe) boyd. *Geochemical Society* **6**, 125–153 (1999).

[57] Stachel, T., Harris, J. W., Brey, G. P. & Joswig, W. Kankan diamonds (guinea) ii: lower mantle inclusion parageneses. *Contributions to Mineralogy and Petrology* **140**, 16–27 (2000).

[58] Stachel, T. Diamonds from the asthenosphere and the transition zone. *European Journal of Mineralogy* **13**, 883–892 (2001).

[59] Kaminsky, F. V., Zakharchenko, O. D., Davies, R., Griffin, W. L., Khachatryan-Blinova, G. K. & Shiryaev, A. A. Superdeep diamonds from the juina area, mato grosso state, brazil. *Contributions to Mineralogy and Petrology* **140**, 734–753 (2001).

[60] Hayman, P. C., Kopylova, M. G. & Kaminsky, F. V. Lower mantle diamonds from rio soriso (juina area, mato grosso, brazil). *Contributions to Mineralogy and Petrology* **149**, 430–445 (2005).

[61] Tappert, R., Stachel, T., Harris, J. W., Muehlenbachs, K., Ludwig, T. & Brey, G. P. Subducting oceanic crust: The source of deep diamonds. *Geology* **33**, 565–568 (2005).

[62] Kaminsky, F. Mineralogy of the lower mantle: A review of 'super-deep' mineral inclusions in diamond. *Earth-Science Reviews* **110**, 127–147 (2012).

[63] Pearson, D. G., Brenker, F. E., Nestola, F., McNeill, J., Nasdala, L., Hutchison, M. T., Matveev, S., Mather, K., Silversmit, G., Schmitz, S., Vekemans, B. & Vincze, L. Hydrous mantle transition zone indicated by ringwoodite included within diamond. *Nature* **507**, 221–224 (2014).

[64] Silversmit, G., Vekemans, B., Appel, K., Schmitz, S., Schoonjans, T., Brenker, F. E., Kaminsky, F. & Vincze, L. Three-dimensional fe speciation of an inclusion cloud within an ultradeep diamond by confocal μ-x-ray absorption near edge structure: Evidence for late stage overprint. *Anal. Chem.* **83**, 6294–6299 (2011).

[65] McCammon, C. A., Frost, D. J., Smyth, J. R., Laustsen, H. M. S., Kawamoto, T., Ross, N. L. & van Aken, P. A. Oxidation state of iron in hydrous mantle phases: implications for subduction and mantle oxygen fugacity. *Physics of the Earth and Planetary Interiors* **143-144**, 157–169 (2004).

Chapter 7

Full-field XRF/XAS: the SLcam

7.1 Introduction

Due to the time consuming nature of acquiring spatially resolved full XANES spectra for a large number of sample points using conventional (confocal) scanning approaches, the need for full-field XAS and XRF spectroscopy arose. Full-field in this context indicates a position sensitive detection scheme in which each pixel corresponds to a full XAS or XRF spectrum. For transmission mode XAS, an initial approach consists of illuminating a sample with a broad X-ray beam and measuring the energy dependent X-ray transmission using a position sensitive charge integrating detector placed behind the sample.[1–3] 3D spatially resolved information can then be obtained by implementing a rotational move, thus performing a tomographic scan.[4–6] Despite the fairly short measurement times and good data statistics inherent to this approach, it is limited to sufficiently thin and concentrated samples.

To allow for full-field experiments on thick (non-transparent) or dilute samples, the X-ray absorption has to be monitored by the emitted X-ray fluorescence. In order to achieve sufficient signal-to-background ratios, use is made of recently developed energy dispersive full-field detectors, which measure the energy of the photon as well as its point of incidence on the detector chip. Several devices for this purpose have been reported:

- Medipix: Medipix chips are available since 1998 and were originally developed for medical applications. The first generation of this CMOS-type detector, Medipix-1, consists of 64 by 64 $170\times170\,\mu\mathrm{m}^2$ pixels on a $200\,\mu\mathrm{m}$ thick Si crystal. The second

generation, Medipix-2, improves on these characteristics by presenting a 300 μm thick Si chip of 256 by 256 55×55 μm^2 pixels. Instead of measuring a full energy range spectrum (e.g. 0-20 keV), the Medipix-2 features two energy windows defining an energy range in which photons are detected. The Medipix-3 in turn improves on this by allowing 8 energy windows instead of two.[7–12]

- Hartmann *et al.*[13] reported in 2000 on a pnCCD full-field detector with a 300 μm Si crystal thickness, a 1×3 cm^2 sensitive area with 150×150 μm^2 pixels, used in the XMM and ABRIXAS astronomy satellite missions.

- A 6×6 cm^2 large pnCCD detector which would be used for several astrophysical investigations was reported by Kimmel *et al.*[14, 15] This Si detector consists of 150×150 μm^2 pixels and a 300 μm sensitive depth. While operating at temperatures below 180 K a thermal noise of less than 5 e^- and a 130 eV energy resolution for the Mn-K_α line was measured.

- In 2010, Alfeld and Janssens reported the use of a full-field pnCCD camera with 512 by 512 24×24 μm^2 pixels.[16] The Si crystal is 80 μm thick and has an active depth of nearly 20 μm. An energy resolution of 235 eV was found for the Mn-K_α line.

- JUNGFRAU: The adJUstiNg Gain detector FoR the Aramis User station, consists of 256 by 256 75×75 μm^2 pixels on a 320 μm thick Si crystal. This chips can be combined to cover larger areas, while maintaining the same readout frequency (2 kHz) due to the CMOS type detector readout.[17, 18]

An alternative detector is the SLcam,[19, 20] which is discussed in more detail below, characterised by a higher quantum efficiency than any of the detectors listed above. A big advantage of CMOS type detectors compared to pnCCD type detectors such as the SLcam is their high count rate capability. However, this usually comes with the disadvantage of lower energy resolution. The trade-off between these two parameters is an important parameter in the choice of the correct device for a given application.

The full-field XRF spectroscopy approach using energy dispersive spatially resolved detectors consists of mounting the detector orthogonal to the X-ray source - sample direction and illuminating the sample with a broad beam. Usually, the sample surface is rotated to 45 ° with respect to the incident X-ray beam to minimise shadowing of the incident and emitted X-ray photons by the sample. Additionally, this sample tilt further spreads the primary X-ray beam over the sample, thus illuminating a larger area. As the fluores-

cence radiation emitted by the sample is distributed isotropically, an X-ray optic must be mounted in front of the full-field detector in order to guide photons from each illuminated point on the sample to a corresponding pixel on the detector. XRF elemental composition images can then be acquired by extracting and interpreting the XRF spectrum for each separate pixel, and recombining the results to a 2D image. To extrapolate this approach to full-field XAS experiments, a 2D XRF image is acquired for a set of primary X-ray beam energies, where the energies vary over the absorption edge of an element of interest. By assembling the XRF images a XAS spectrum can be extracted for each separate detector pixel.

To obtain 3D volumetric full-field XRF or XAS information one can perform an additional sample rotation, where a full-field XRF/XAS map is obtained for each sample rotation and 3D information is recovered by tomographic reconstruction. Alternatively, one can illuminate the sample with a thin sheet beam instead of a broad beam spread over the sample surface (Figure 7.1). As such, a confocal volume is defined from which radiation is selectively measured. 3D information can now be obtained by performing a sample translation through this confocal volume slice, without the need for any tomographic reconstruction. Both of these 3D approaches suffer, however, from element and matrix dependent limits of information depth imposed by sample (self-)absorption effects.

Below, examples are discussed where the SLcam is used for both the broad beam approach as well as the confocal slicing method towards full-field XAS. In what follows the SLcam is used in emission modus. It should be noted that technically the SLcam could be used for transmission mode measurements as well. However, for full-field XAS in transmission mode the SLcam would quickly prove insufficient in terms of maximal count rate. Additionally, in this approach the energy dispersive character of the SLcam is not used, rendering the user to better use a non-energy dispersive CCD or CMOS detector. An attempt can be made to illuminate the sample with a polychromatic X-ray beam and monitor the absorption as a function of energy in the SLcam. However, this method is not capable of resolving the XAS fine structure and thus is better referred to as spectral imaging. For more information on spectral imaging using the SLcam the reader is guided towards the work by Boone *et al.*[22]

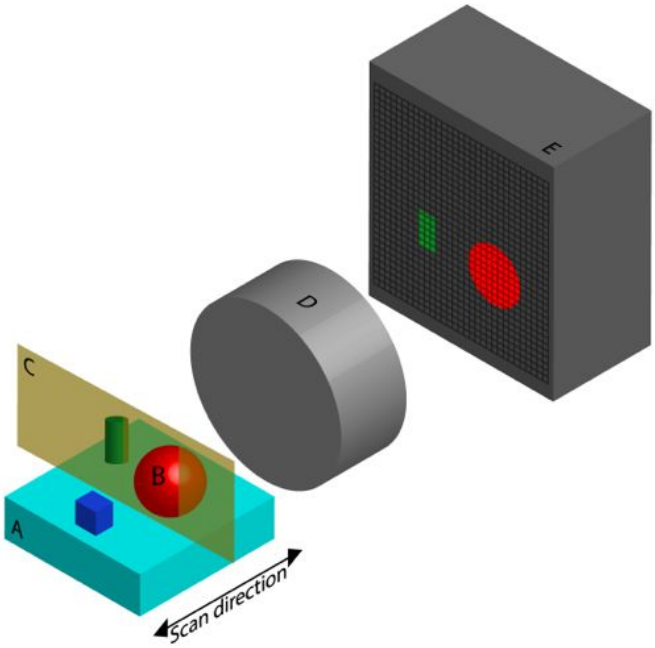

Figure 7.1: Confocal sheet beam measurement methodology representation showing the sample holder (A), sample objects (red, green, blue)(B), X-ray sheet beam (C), X-ray optic (D), and the SLcam (E). Figure adapted from[21]

7.2 SLcam Characteristics

The SLcam (Strüder-Langhoff camera, or Colour X-ray Camera) is a Si based pnCCD type energy dispersive X-ray detector, consisting of a 450 μm thick Si layer with 264 by 528 48×48 μm^2 pixels, mutually developed by PNSensor GmbH (Munich, Germany), the Institute for Scientific Instruments GmbH (IFG, Berlin, Germany), the BAM Federal Institute for Materials Research and Testing (Berlin, Germany), and the Institut für Angewandte Photonik e.V. (IAP, Berlin, Germany).[19] The outer 264 by 132 pixels on each side of the chip are covered to prevent illumination by X-rays (Figure 7.3). The chip is read out with a 400 Hz frequency, in which a fast sideways transfer of the central 264 by 264 pixels to the sides, the so-called 'dark frame storage mode', is combined with the slower read out of the dark frames by two CAMEX chips each, effectively splitting the SLcam readout window in four quarters (Figure 7.3). Currently, a 1 kHz version is also available. In both cases, the chip is back side illuminated which accounts for a homogeneous illumination over the entire chip surface.[23] An overview of the SLcam technical properties are listed in Table 7.1.

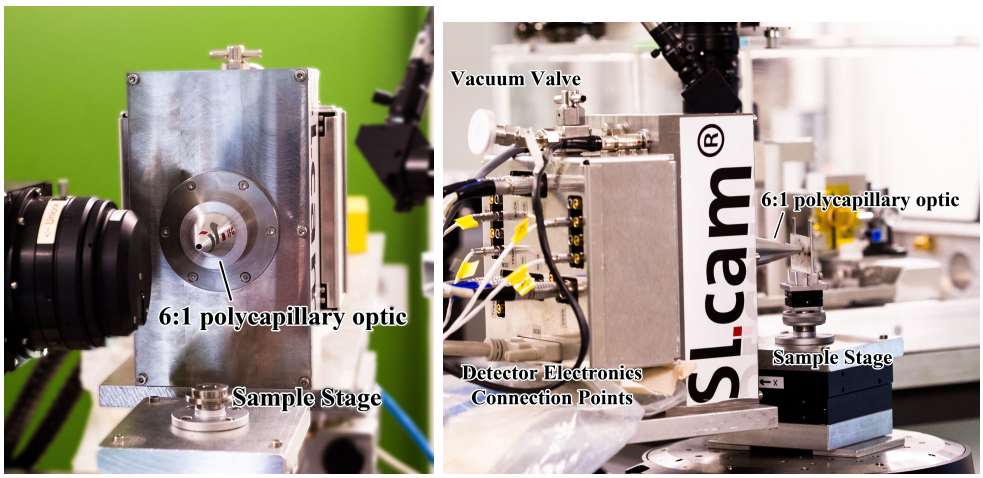

Figure 7.2: Photographs of the SLcam installed at beamline P-06 of PETRA-III at DESY, Hamburg. Left: frontal view, right: side view.

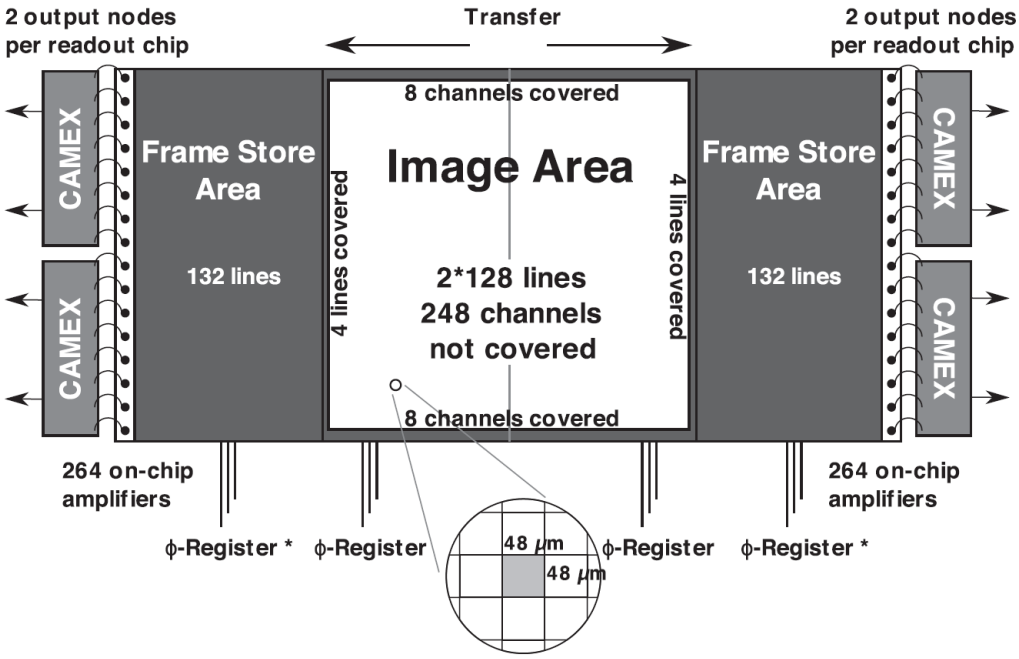

Figure 7.3: Schematic illustration of the frame store operation for high-speed readout of the SLcam. During read-out the charges in the chip are first rapidly transferred to dark chips at the sides, the frame store area, from where the system has more time to read out the charges, while new photons are being collected by the detector chip. Figure adapted from Ordavo *et al.*[20]

Table 7.1: Summary of the SLcam characteristics. Adapted from Scharf *et al.*[19]

Parameter	Value
pnCCD type	column-parallel, split frame readout
pixel size	$48\times48\,\mu m^2$
number of pixels	69,696
image area	$12.7\times12.7\,mm^2$
sensitive depth	$450\,\mu m$
frame rate	400 Hz (up to 1 kHz possible)
pixel readout speed	28 Mpixel/s
quantum efficiency	>95 % at 3 keV - 10 keV; >30 % at 20 keV
readout noise (rms)	$<3\,e^-$/pixel
charge transfer efficiency	>0.99995
energy resolution	152 eV for Mn-K_α

Two polycapillary detector lenses are currently available for the instrument: one polycapillary is a 1:1 magnification optic and the other has a 6:1 magnification. The latter has a conical shape, which results in an effective pixel size of $8\times8\,\mu m^2$, while the 1:1 polycapillary is a parallel polycapillary, providing an effective pixel size of $48\times48\,\mu m^2$. These theoretical image pixel sizes provide an upper limit of the spatial resolution one can obtain using this detector and a given detector optic. It should be noted that the distance between the sample and the detector optic has a considerable impact on the actual spatial resolution: the spatial resolution is defined by the acceptance of each individual capillary following Equation 7.1 with R_S the spatial resolution, T the capillary fibre inner diameter, d the sample-optic distance and ϑ_C the critical angle of total reflection. Here, the capillary fibre diameter T can be approximated as the projected SLcam pixel size, depending on the used polycapillary optic (e.g. 8 or $48\,\mu m$). Additionally, a subpixel resolution based on more accurate charge cloud shape recognition and center of impact determination will be available in the future, although the gain of spatial resolution also comes at the cost of longer measurement times in order to obtain similar counting statistics on a pixel-by-pixel base.[19, 20, 24]

$$R_S = T + 2 \cdot d \cdot tan\vartheta_C \tag{7.1}$$

The large image area and the relatively thick sensitive depth of the SLcam make this an ideal device to measure the elemental composition of a sample in a relatively short timespan. It should be mentioned that the $450\,\mu m$ sensitive depth also has its limitations.

The first graph of Figure 7.4 shows the thickness of pure Si needed to attenuate 99 % of the incident beam as a function of X-ray energy. The second graph of Figure 7.4 shows the fraction of the incoming X-ray photons that will be attenuated in a 450 μm thick layer of Si, when the X-rays hit the surface under an angle of 90 ° taking into account the absorption by the 50 μm Be window of the SLcam. Less than 36 % of X-ray photons with an energy higher than 20 keV will be absorbed by the chip, as the quantum efficiency in Table 7.1 expresses. The detection efficiency is reduced considerably above 25 keV, reducing to approximately 20 % at this energy. Additionally, at energies >25 keV the polycapillary X-ray optics start to loose their photon guiding properties, thus losing the imaging properties. Nevertheless, the 450 μm sensitive depth is still superior when compared to other full-field cameras, as shown in the previous section. In fact, this sensitive thickness is similar or even better than typical crystal thickness values in state-of-the-art silicon drift detectors, e.g. VORTEX-EM SDD has an active thickness of 350 μm.[25] Before X-rays reach the detector chip, they must pass a 50 μm Be window. This decreases the detectability of low energy X-ray photons (<3keV) as they are attenuated severely by the window.

In order to reduce electronic thermal noise, the detector CCD-chip is cooled. The cooling is obtained by a combination of water cooling and Peltier cooling, however more recent prototypes of this detector are supposed to be cooled by Peltier elements and active air cooling only. An operating temperature value of -25 °C is reported to be optimal.[19, 20] Figure 7.5 shows a graph of the FWHM of the Mn-K_α peak as a function of temperature, which is a typical figure-of-merit to characterize the energy resolution of an ED-detector. It is important that one operates the detector at a temperature where the FWHM is rather constant over a small temperature interval.[26] This is the case in the temperature interval of -25 °C to -15 °C. The remaining thermal noise produced by the detector is corrected for by a dark frame correction. The detector chip is operated under vacuum conditions, typically 0.1 mbar, to reduce the humidity inside the detector and avoid corrosion. This way no water condensation can take place on the CCD-surface and inner electronics.

The user can select two energy regions in which X-ray photons are collected: 0-20 keV and 0-40 keV.[19] The selected energy region is divided into 1024 channels. A maximum of 600000 cps, detected on the full image area, can be handled by the detector before the event analysis becomes cumbersome.[19, 26] This corresponds to approximately 10 cps/pixel before a single pixel is oversaturated. After event analysis, each pixel reads out a spectrum in which each channel has the same energy calibration (same energy offset and gain). In order to obtain this, the detector must be calibrated by the so-called constant-gain calibration.

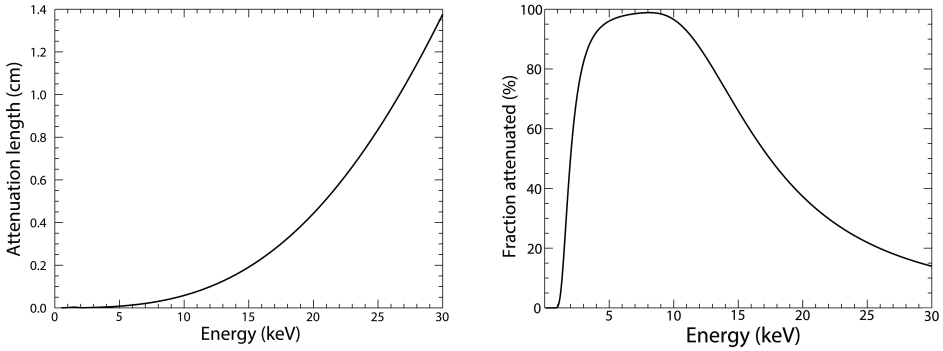

Figure 7.4: 99% attenuation length as a function of X-ray energy for pure Si (left) and the fraction of X-ray photons of a given energy that will be absorbed in a 450 μm thick layer of pure Si taking into account the 50 μm Be window(right).

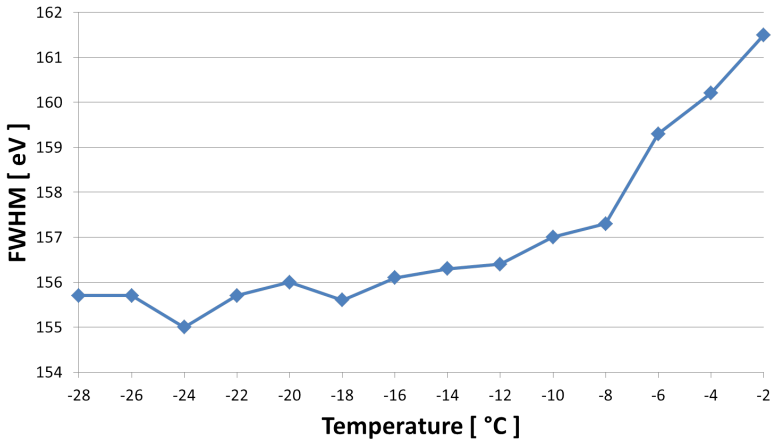

Figure 7.5: Graph of the FWHM of the Mn-K_α peak as a function of chip temperature as detected by the SLcam. The FWHM of this peak is the typical figure-of-merit characterizing the detector energy resolution. It is advised to operate at a temperature for which the FWHM is more or less constant around this temperature. Figure adapted from the Slcam manual.[26]

Once the detector is calibrated however, all 69696pixel spectra can be fitted using the same calibration model for each of these pixels. Due to the CMOS-type readout method of alternative detectors mentioned above, they can handle higher readout frequencies (several kilo-Hertz per pixel). However, it should be noted that the SLcam is rarely saturated during full-field XRF and XAS experiments except for the most concentrated samples, illuminated with the brightest sources (e.g. undulator source and multilayer monochromator for XRF applications), as such the limited SLcam readout frequency is not a limiting factor for most full-field applications, as discussed below.

7.3 Application: Fe-K edge Full-field XANES

This section is adapted from Tack *et al.*[a]

7.3.1 Introduction

X-ray absorption near edge structure (XANES) spectroscopy is a non-destructive analytical technique widely used to obtain chemical and local electronic environment information from probed atoms, which is carried out by scanning the X-ray absorption edge.[27, 28] Full-field transmission mode XANES imaging, in which a sample is illuminated with a broad X-ray beam and the transmission signal is monitored using a non-energy dispersive (ED) CCD-based detection method, has been used in the past to obtain chemical information from a large sample area with microscopic resolution.[2, 5, 29–32] This technique is a microspectroscopic analogue of bulk transmission XANES experiments in which only average information from the analysed sample volume could be obtained, and for which the assumption had to be made that this average was representative of the entire sample. However, transmission mode XANES has the drawback that the data quality is reduced when the samples are far from the optimum in terms of thickness resulting in too strong absorption of the primary beam or, conversely, too few sample−photon interactions upon transmission.[27, 28]

Fluorescence mode XANES largely eliminates thickness and/or low analyte concentration

[a] P. Tack, J. Garrevoet, S. Bauters, B. Vekemans, B. Laforce, E. Van Ranst, D. Banerjee, A. Longo, W. Bras and L. Vincze, Full-Field Fluorescence Mode Micro-XANES Imaging Using a Unique Energy Dispersive CCD Detector. Anal. Chem. 86, 8791-8797, doi:10.1021/ac502016b (2014).

related problems typically encountered in transmission mode spectroscopy and can be characterized by trace-level detection limits in dilute systems as well as providing the possibility of investigating concentrated thin films or the surface layers of thick, non-transparent samples. In a conventional fluorescence mode XANES imaging experiment, a sample is scanned through a focused pencil beam, measuring a XANES spectrum at each point.[33–36] As a result of the slow rate of data collection, the limited access to and experimental time constraints at synchrotron radiation facilities, required for X-ray absorption spectroscopy, scanning fluorescence mode XANES is rarely applied to investigate large sample areas.

In this work, a new approach to full-field fluorescence mode XANES imaging is presented, making use of an energy dispersive CCD detector, the SLcam[19, 20, 22, 37] which consists of 264×264 pixels allowing for emission mode XANES imaging of up to 12.7×12.7 mm^2 sample areas with microscopic resolution.

A proof of concept of this method is presented by experiments performed on a microscopically heterogeneous Fe^0/Fe_2O_3 model sample. To be able to handle the large data volume, represented by 69696 fluorescence mode XANES spectra obtained from a single energy scan, a multivariate analysis method for data reduction is discussed. A schematic overview of the performed experiment is shown in Figure 7.6. A XANES profile can be extracted for each SLcam pixel, with varying degrees of noise depending on the data acquisition time per energy step and the concentration of the analyte in the sample material. For this work, the data acquisition time (see the Materials and Methods section) was chosen so a pixel with average Fe intensity (∼2 Fe-K_α counts per second per pixel in the post-edge region) would result in a relatively noiseless XANES profile. As an application, this technique was used to investigate the iron chemical state in a Nitisol soil sample.[38–40] Nitisols are defined in the World Reference Base (WRB) as soils having a nitic horizon, which is a clay-rich subsurface horizon with characteristic flat-edged or nut-shaped and shiny components, and gradual diffuse boundaries to the horizons above and below.[41] The origin of the shiny surfaces typical for Nitisols is not clear. The term "metallization" has been used to indicate the accumulation of metal oxides as thin coatings on peds (soil agglomerates) giving rise to the shiny appearance. More than half of all Nitisols are found in tropical Africa, and Ethiopia is one of the mainstays of these soils. The studied sample originates from a nitic horizon in the Gilgel Gibe catchment in the Jimma zone in south-west Ethiopia, where Nitisols are very important for food production.[40]

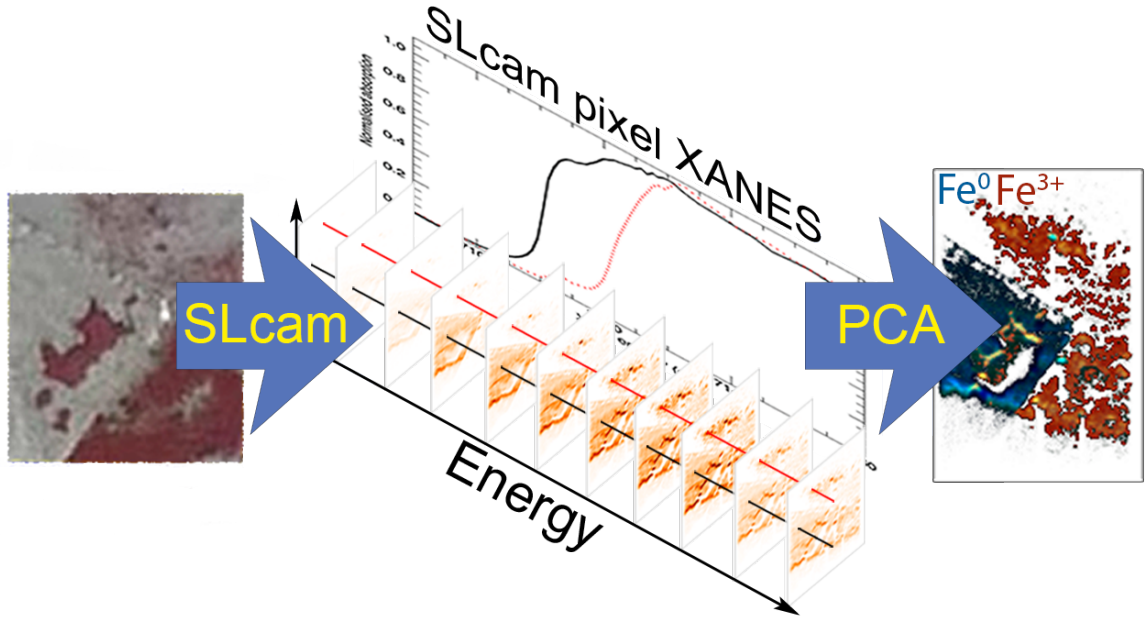

Figure 7.6: Schematic overview of the full-field emission mode XANES experiment in which the Fe-K_α signal of an Fe^0/Fe_2O_3 model sample is monitored as a function of incident X-ray beam energy, using the SLcam. A multivariate analysis method is used to reduce the data set consisting of 69696 simultaneously acquired XRF spectra per incident beam energy step.

7.3.2 Materials and Methods

SLcam: Energy Dispersive CCD Detector

As a detector, the silicon-based energy dispersive pnCCD "Colour X-ray Camera", the SLcam, was used. This pnCCD detector is characterized by its large sensitive chip area of $12.7\times12.7\,mm^2$ consisting of 264×264 pixels of $48\times48\,\mu m^2$. Because of the large depletion depth of $450\,\mu m$ and a $50\,\mu m$ beryllium window, the device has a high quantum efficiency ($95-30\,\%$) for photons with energies between 2 and 20 keV.[20]

Detector readout is performed in a column-parallel, split frame method in which each half of the illuminated pnCCD chip is physically transferred in $50\,\mu s$ to a dark frame storage area to reduce illumination during further signal processing by two dedicated CAMEX chips for each half of the pnCCD chip, effectively splitting the total illuminated chip area in four quadrants.[19, 20, 22] Event analysis is performed to determine the center of gravity and total deposited energy for each incident photon, as the corresponding electron charge cloud created in the detector material can be distributed over multiple pixels depending on

the photon energy and point of incidence with respect to the pixel boundaries, giving rise to an increase in the point spread function. Full detector readout occurs at a frequency of 400 Hz.

In this way, each pixel will collect a full energy dispersive X-ray spectrum of photons with energies up to 20 keV. At −20 °C operating chip temperature, a noise level and Fano factor[28, 42] of 34.75 eV and 0.120 were obtained, respectively, corresponding to an energy resolution of ∼150 eV for the Mn-K_α line following Equation 7.2 with F the Fano factor, E the detected X-ray energy, ε the average energy needed to generate an electron-hole pair: 3.65 eV for Si-based detectors, and N the noise level of the detector.[42, 43] For imaging purposes, the detector is coupled with polycapillary (glass fiber) based X-ray optics. In this work, two polycapillary optics provided by IFG Berlin were used: a 1:1 straight polycapillary and a 6:1 magnifying conical polycapillary, resulting in theoretical spatial resolutions of 48×48 μm^2 and 8×8 μm^2 and investigated sample areas of 12.7×12.7 mm^2 and 2.1×2.1 mm^2, respectively. The field of view using the 6:1 magnifying polycapillary optic is limited to a circular area with a diameter of 2.1 mm due to the limited polycapillary size and its housing.

$$FWHM = 2.35(FE\varepsilon)^{1/2} + N \tag{7.2}$$

Due to the small angular aperture of a single polycapillary fiber (i.e., ∼3 mrad at 10 keV) and the relatively low transmission efficiency of a conically shaped polycapillary optic (i.e., ∼5−40 % for 7−20 keV X-rays),[44] the count rate detected by a single pixel (∼10 cts/s max at 400 Hz readout frequency) will be lower than what can be acquired by a conventional solid state detector in non-imaging mode. However, as the SLcam detects 69696 spatially resolved pixels simultaneously without the need of scanning the sample through an X-ray beam, the data acquisition from a large area can be performed in a more time efficient manner when compared to the conventional acquisition methods.

Experimental Setup

The experiments were performed at BM26A, the X-ray absorption spectroscopy (XAS) station of the Dutch-Belgian beamline (DUBBLE) at the ESRF.[45] The beamline uses a 0.40 T ESRF bending magnet as a primary radiation source. The energy of the X-ray

beam is tuned by a double-crystal Si(111) monochromator (energy resolution $\Delta E/E$ of $\sim 1.7 \times 10^{-4}$ at 9.659 keV) operating in a fixed-exit mode.

A collimating mirror in front of the monochromator and a vertically focusing mirror behind the monochromator, each with Si and Pt coatings, were used to collimate/focus the beam and to suppress the higher harmonic content. For the simultaneously performed transmission mode detection, the gas mixtures in the first and second ionization chambers were adjusted to allow approximately 10 % absorption in the first and about 70 % absorption in the second ion chamber at a given energy. The beam size was $0.3(V) \times 3(H)\,mm^2$ providing a photon flux of $\sim 6 \times 10^9$ photons/s at the sample position at the Fe-K edge energy (7112 eV).

To make full use of the large field of view of the SLcam, the detector was mounted above the sample, perpendicular to the plane of polarization defined by the synchrotron ring, as shown in Figure 7.7. Additionally, the sample was mounted under a small angle ($\sim 10\,°$) with respect to the incident X-ray beam, spreading out the X-rays over the sample, increasing the illuminated sample area. This setup mode has the additional advantage of reducing image distortion effects which allows for straightforward optical feature recognition during sample alignment. Spatial resolution using the SLcam is mainly dependent on the type of X-ray optic. When using a polycapillary optic, the spatial resolution R_S is approximated according to Equation 7.1.[42]

Because the sample is placed under a small angle of incidence, nearly parallel with the detector chip and as close as possible to the polycapillary optic, the last term in Equation 7.1 can be neglected, resulting in a spatial resolution approximately equal to the channel diameter of the polycapillary fibers. For the purpose of this detector, the spatial resolution is equal to the area of the sample "seen" by one pixel. As such, the value for T in above equation is equal to the pixel size (48 μm) divided by the magnification factor defined by the polycapillary lens. For the 1:1 polycapillary optic, this results in a spatial resolution of $48 \times 48\,\mu m^2$, whereas for the 6:1 polycapillary optic, it is $8 \times 8\,\mu m^2$. Higher spatial resolutions could in principle be obtained by using optics with higher magnification factors, however, such optics were not available for the experiments discussed in this work.

Detection limits were determined using a NIST SRM 611 (400-500 ppm trace elements in a glass matrix) sample, using the SLcam with 6:1 polycapillary optic.[46] The XRF spectra of the above mentioned standard were obtained using an excitation energy of 7161 eV. For the XANES analysis, a series of reference compounds, diluted to ~ 10 wt%

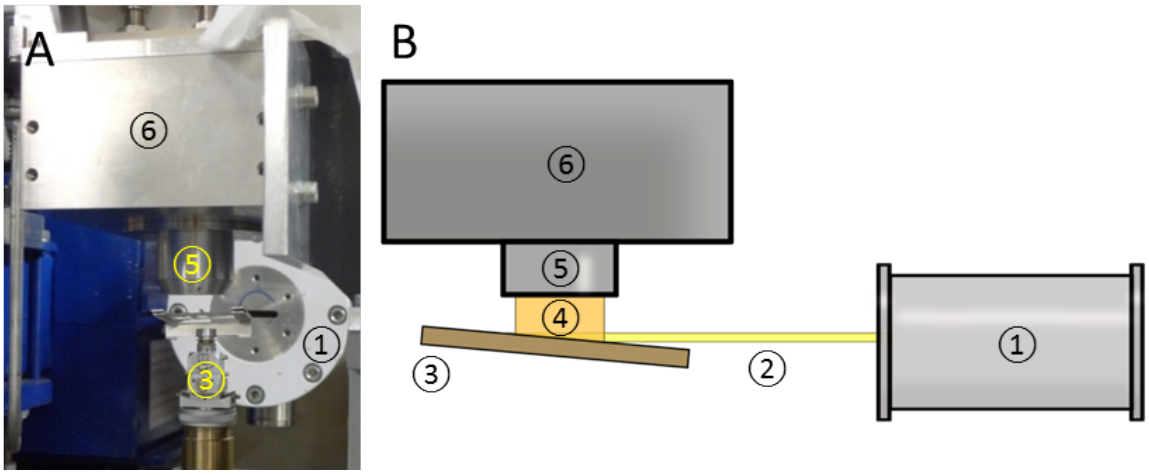

Figure 7.7: Photograph (A) and schematic drawing of the side view (B) of the SLcam setup at the DUBBLE beamline (ESRF, France). Numbered elements are the ionization chamber (I_0) (1) to monitor the primary X-ray beam flux, the X-ray beam (2), the sample mounted under a shallow angle with respect to the primary beam (3), the XRF radiation monitored by the detector (4), the SLcam X-ray optic (1:1 polycapillary optic) (5), and the SLcam detector (6).

using cellulose powder (type 20, Sigma-Aldrich) and pressed to pellets with an estimated thickness of 2.5 absorption lengths, were measured in transmission mode. A 4 μm thick pure iron foil (Goodfellow SARL, Lille, France) was measured in transmission mode after each experiment to correct for monochromator energy shifts by setting the first inflection point of the XANES profile to 7112 eV. XANES scans were performed from approximately 50 eV below the Fe−K edge up to 49 eV above the edge, with 0.2 eV energy steps and 2 s counting time per step.

As a test sample a piece of 4 μm thick iron foil and Fe_2O_3 powder (pro analysis, MERCK KGaA, Darmstadt, Germany) was fixed on a commercial tape. A fluorescence mode Fe K-edge XANES scan using the SLcam in combination with the 1:1 polycapillary optic was performed in three separate energy regions to optimize the experiment time with respect to the obtained information: the pre-edge region from 7075.5 eV up to 7100.6 eV in 2.5 eV steps for 5 min per step, the edge region from 7102.7 eV up to 7132.8 eV in 0.8 eV steps for 10 min per step, and the post-edge region from 7134.9 eV up to 7160.9 eV in 2.6 eV steps for 5 min per step resulting in a total experiment time of 7 h and 40 min.

As an application, a geological Nitisol soil sample was investigated for iron coordination state by means of fluorescence mode XANES using the SLcam equipped with the 6:1 polycapillary optic. The XANES region was split up in three parts as follows: from

7075.5 eV up to 7100.6 eV in 4.2 eV steps for 5 min per step, from 7102.7 eV up to 7132.8 eV in 1.2 eV steps for 20 min per step, and from 7134.9 eV up to 7160.9 eV in 1.29 eV steps for 10 min per step. The total experiment took 14 h and 30 min.

Comparing the above data acquisition times for emission mode full-field XANES using the SLcam with the more conventional step by step emission mode measurement strategy, it is clear the SLcam represents a significant advance in emission mode XANES measurements: the average single point emission mode XANES scan takes around 2 to 20 min. Scanning 69696 points this way would take approximately 97 to 970 days of experiment time. To measure the same amount of points as monitored simultaneously by the SLcam in the same time as was acquired here, one would need to perform a XANES scan in 0.5 to 1 s per point, which would result in low data statistics even if the monochromator and sample stage motor movements was adapted to such short measurement times and overhead time was nearly non-existent.

Data Processing

For the fluorescence mode experiments, Fe-K_α intensities were extracted from each pixel spectrum at each energy step using a region of interest (ROI) integration algorithm. This method was compared to a more time consuming iterative least-squares fitting using the AXIL software package[47, 48] showing no substantial differences in the distribution images.

Although it is possible to extract a XANES profile for each of the 69696 SLcam pixels, it was opted to group and sum pixels with similar XANES profiles by means of principal component analysis (PCA) and K-means clustering as a means of data reduction.[48] Similarities and differences in ROI integrated Fe-K_α intensity variation with excitation energy were investigated using PCA. Before PCA, square root transformation of the data was applied to reduce intensity differences due to concentration changes between sample points, resulting in a better separation between points representing different chemical compounds than obtained when performing the PCA routine without square root data transformation. Data points with similar principal component scores show similar XANES profiles and were grouped using K-means clustering, effectively grouping pixels with similar XANES profiles. Subsequently, the ROI integrated Fe-K_α intensities for each data point within a cluster were extracted and summed as a function of the excitation energy, resulting in a raw XANES profile for each cluster. Raw XANES data were normalized for incident beam flux using

the primary ionization chamber signal, pre-edge subtracted using a linear and Victoreen function for fluorescence and transmission data respectively and post-edge normalized at an energy of E_0+40 eV. Additionally, the slow variations caused by the atomic absorption profile before and after the edge were subtracted to better compare the spectra in linear combination analyses.[27]

Linear combination fitting of the normalized fluorescence XANES spectra with transmission XANES reference spectra was performed to obtain semi-quantitative results on the chemical speciation present in the sample.[36, 49]

7.3.3 Results and Discussion

Limits of Detection

With respect to elemental analysis, the detection limits (DL) in weight percentage for 1000 and 300 s measurements using the 6:1 polycapillary optic are shown in Figure 7.8. In case of the NIST SRM 611 glass matrix, for Fe-K_α , the DL for a single SLcam pixel using a data acquisition time of 1000 s measurement time is approximately 0.49±0.03 wt%. It should be noted that the MDL can be improved by binning neighbouring pixels at the expense of spatial resolution. The MDL can be further improved by using a higher exciting X-ray beam flux (e.g., by using an undulator source to generate the primary beam) and using an improved detector optic with a higher X-ray transmission efficiency.

Differential XANES Imaging Using the SLcam

Figure 7.9 shows transmission XANES reference spectra for a 4 μm thick iron foil and pure Fe_2O_3, along with their difference curve represented by the blue dashed line. From this curve, it is clear that at an energy of approximately 7120 eV the Fe^0 will absorb more X-rays when compared to Fe^{3+} in Fe_2O_3. At 7143 eV, both compounds will have a comparable level of X-ray absorption. A heterogeneous model sample consisting of a 4 μm iron foil, FeO particles and Fe_2O_3 powder fixed to an adhesive tape (Scotch) was used as a test sample for the fluorescence mode differential imaging experiment, shown in Figure 7.10A. The area marked in blue was investigated using the SLcam. The sample was illuminated for 10 min at 7120 and 7143 eV each, and the Fe-K_α signal was retrieved for each pixel of the detector resulting in elemental images of Fe at both energies.

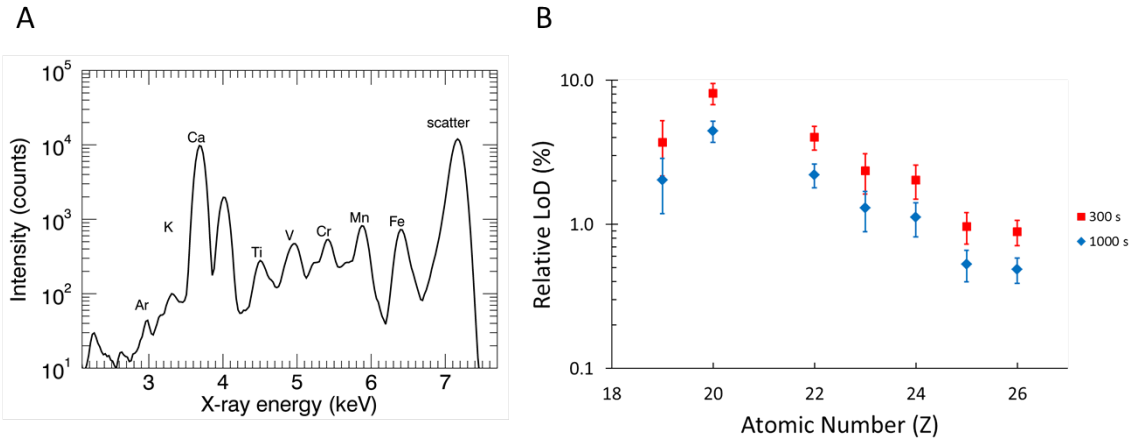

Figure 7.8: XRF spectrum of the SLcam, summed over all 69696 pixels, after 3600 s acquisition time of NIST SRM 611 using the 6:1 polycapillary optic and a 7160.9 eV excitation energy at DUBBLE (ESRF, France) (A) and the minimum detection limits for one SLcam pixel corresponding to 300 and 1000 s measuring time (B).

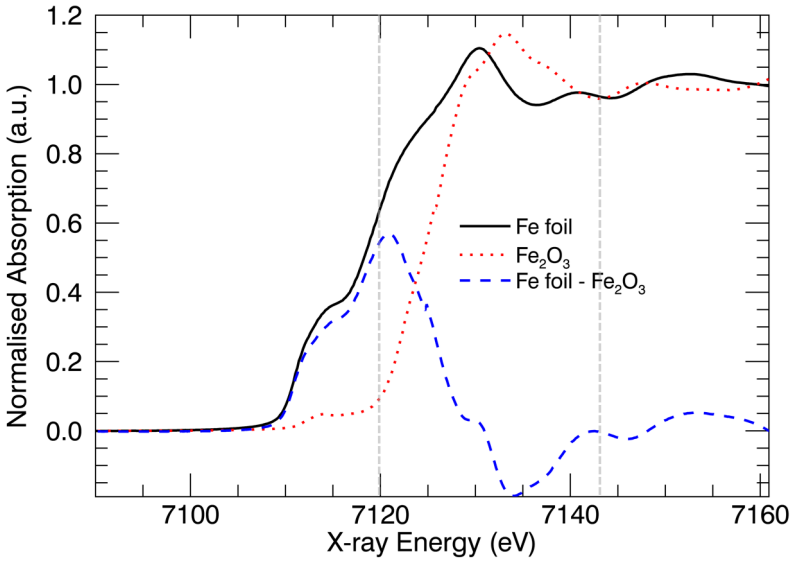

Figure 7.9: Transmission mode XANES spectra of a 4 μm thick iron foil (black) and Fe_2O_3 pressed pellet (red). The difference is presented as a blue dashed curve.

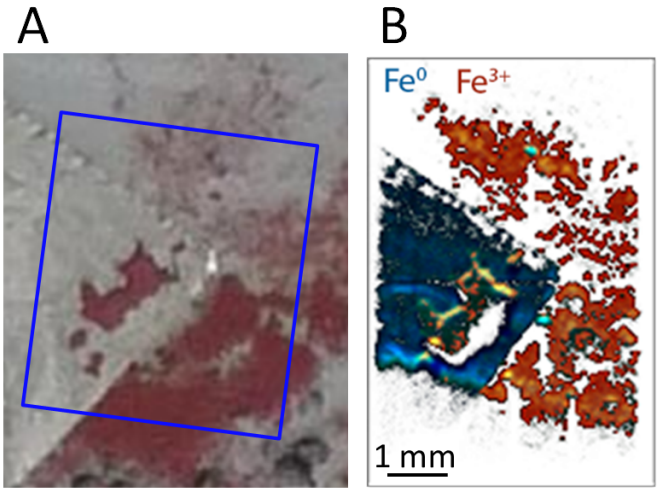

Figure 7.10: Left: Photograph of an iron test sample composed of a 4 μm thick Fe foil, FeO particles and Fe_2O_3 powder. The blue marking shows the area that was investigated using the SLcam. Right: Result of the differential imaging of the iron test sample after 20 min measuring time and monitoring the Fe-K_α signal at 7120 and 7143 eV. Spatial resolution 48×48 μm^2.

The image obtained at 7120 eV shows a distribution in which the Fe^0 is most intense. By subtracting the image retrieved at 7120 eV from that measured at 7143 eV, a differential image is obtained in which the Fe^{3+} becomes the most prominent signal as seen in Figure 7.10B. When compared to Figure 7.10A, it is clear the differential imaging method is successful at differentiating between Fe^0 and Fe^{3+} distributions in 20 min of measurement time, monitoring a sample area of approximately 3×3 mm^2 with a spatial resolution of 48×48 μm^2. Some areas in the iron foil region can be found to show zero intensity, which is attributed to shadowing effects caused by the waviness of the Fe foil surface and the presence of a thin layer of Fe_2O_3 on top of the iron foil.

Full-Field Fluorescence Mode XANES Using the SLcam

When the variations between two curves are minute one has to resort to more elaborate analysis methods in order to retrieve differences which are significant. In contrast to the differential imaging method, a XANES scan was performed by extracting the Fe-K_α intensity from each SLcam pixel at each energy step, resulting in a XANES spectrum for each of the 69696 SLcam pixels.

The large data set can be reduced by performing principal component analysis (PCA) and

K-means clustering,[48] grouping together pixels that show similar variations as a function of the X-ray beam energy. PCA is performed on the data set after extracting the Fe-K_α intensity signal for each pixel at each energy. Pixels are then grouped using K-means clustering based on the score of each pixel obtained for the second and third principal component, which can be used to identify metallic Fe and Fe_2O_3 exhibiting large negative score values (Figure 7.11).

In a subsequent step, the Fe-K_α signal of each pixel in a given cluster is extracted and summed by energy, giving the raw XANES profile corresponding to the given cluster. Figure 7.12A shows the resulting fluorescence XANES spectra, after normalization, for the clusters corresponding to the Fe foil and Fe_2O_3 regions (red curves) compared to the transmission mode reference spectra (black curves).

It is evident that the fluorescence XANES spectra differ from the reference spectra. However, the compounds used to make the test sample were pure, undiluted compounds. Additionally, the sample was measured in fluorescence mode under a shallow angle with respect to the incident X-ray beam. Both characteristics cause the distortion of the XANES spectrum due to self-absorption effects. As the composition of the separate clusters is known, the data could be corrected using an in-house developed, thickness-sensitive self-absorption correction routine (Appendix Chapter C), the results of which are represented in Figure 7.12B. The self-absorption corrected fluorescence XANES spectra resemble the reference spectra very well, confirming the validity of using the SLcam for fluorescence mode XANES experiments to investigate chemical speciation. Differences between the self-absorption corrected and reference data are likely due to noise in the uncorrected fluorescence data and the curvature of the iron foil or the unknown and varying thickness of the Fe_2O_3 powder, preventing straightforward determination of the correction parameters.

Application: Nitisol Soil Sample

The developed full-field fluorescence XANES and associated data-reduction methodology was demonstrated by spatially resolved Fe-speciation of a Nitisol[38, 39] soil sample. This iron-containing soil sample contains mineral particulates that are believed to be volcanic ash particles. The goal of this experiment was to investigate the iron oxidation state distribution throughout the sample, and whether the particle of interest shows a different iron speciation compared to the surrounding matrix. A photograph of the sample as well

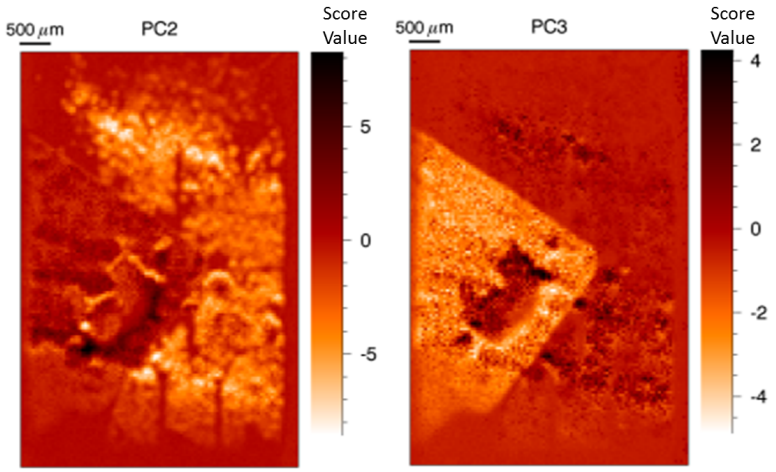

Figure 7.11: Second (left) and third (right) principal component score image of a PCA analysis on SLcam XANES data of an iron model sample. The iron foil (Fe^0) can be clearly distinguished from the Fe_2O_3 powder (Fe^{3+}). Displayed area is $4.8 \times 7.2\,mm^2$ large with a $48 \times 48\,\mu m^2$ spatial resolution.

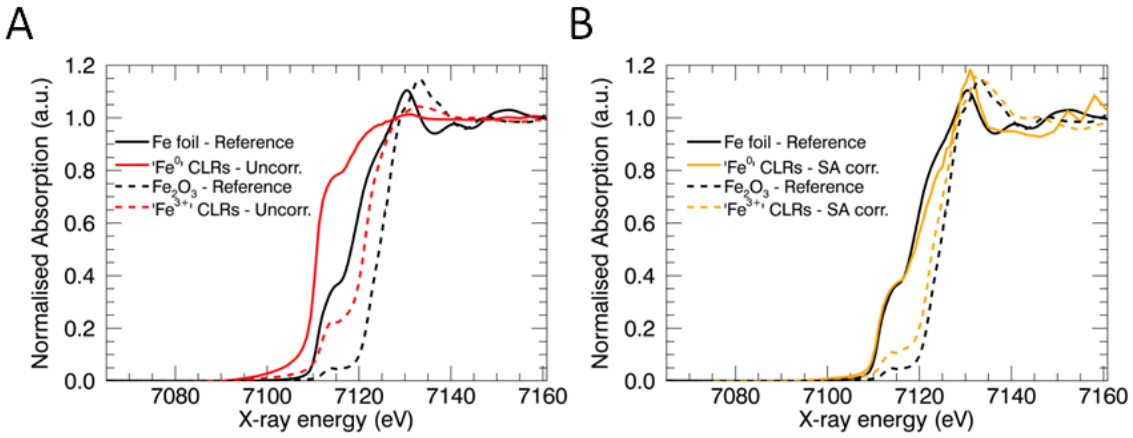

Figure 7.12: Fluorescence mode XANES obtained from the SLcam for the iron foil and Fe_2O_3 regions without self-absorption correction compared to the transmission mode reference XANES (A) and the fluorescence mode XANES curves after self-absorption correction using a thickness sensitive routine with the sample thickness set to $4\,\mu m$, an incident angle of $17°$, and an exit angle of $73°$ (B).

as the iron distribution image obtained with the SLcam using a 6:1 polycapillary optic and illuminating the sample at 7160.9 eV are displayed in Figure 7.13. The total circular field of view with 2.1 mm diameter was investigated with $8\times8\,\mu m^2$ spatial resolution in 10 min. The vertical intensity gradient perceived in the Fe distribution image is due to the non-uniform primary beam profile. A full XANES scan was performed, as discussed in the Materials and Methods section of this chapter, over the same area with the same spatial resolution in less than 15 h, mainly limited in speed by the available flux provided by the bending magnet source.

Three types of regions were selected from which XANES profiles were extracted: the surrounding matrix, the top part of the particle (indicated blue dotted line) showing increased Fe-K_α intensity, and the lower part of the particle (indicated by green dashed line) showing a lower Fe-K_α intensity. The XANES profiles were extracted from the chosen regions, marked in Figure 7.13, and presented in Figure 7.14. All three regions show similar XANES profiles. It could be argued that the spectrum from the top part of the particle (dotted blue curve) differs from the other two. However, this difference can be explained by self-absorption effects distorting the XANES spectrum. This hypothesis is further strengthened by the higher iron intensity in this region, as seen in Figure 7.13. Comparison of the fluorescence XANES spectra with reference spectra by means of linear combination analysis shows that the iron composition of the selected regions is fairly homogeneous and consists of approximately 16.8±10.1 % Fe^{2+} and 83.3±31.5 % Fe^{3+}.

7.3.4 Conclusions

Using the energy dispersive pnCCD SLcam detector for fluorescence mode XANES can yield spatially resolved coordination state and chemical speciation information from a large sample area ($12.7\times12.7\,mm^2$ or $2.1\times2.1\,mm^2$ depending on the used X-ray optic) with a microscopic resolution ($48\times48\,\mu m^2$ or $8\times8\,\mu m^2$, respectively) without the need for microbeam scanning in previously infeasible measurement times (less than 15 h). The data acquisition using the SLcam detector results in a data set of 69696 spatially resolved micro-XANES profiles in a single measurement.

Improvements can be made to the presented experimental method by using a higher primary X-ray beam flux (e.g., by utilising insertion device beamlines), which will improve the detection limits of this technique and will significantly decrease the data acquisition

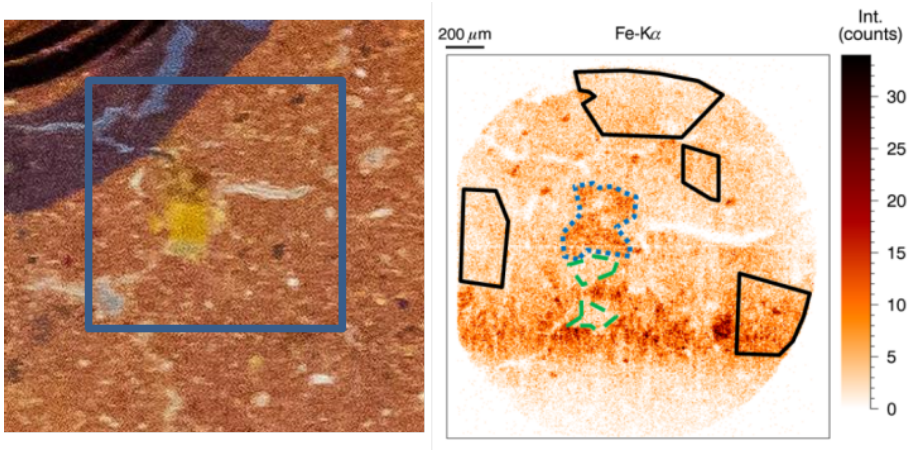

Figure 7.13: Photograph (left) and iron distribution image (right) of a Nitisol soil sample. Three types of regions are marked from which XANES profiles were extracted: the surrounding matrix (black solid line), the top part of the mineral inclusion (blue dotted line), and the lower part of the mineral inclusion (green dashed line).

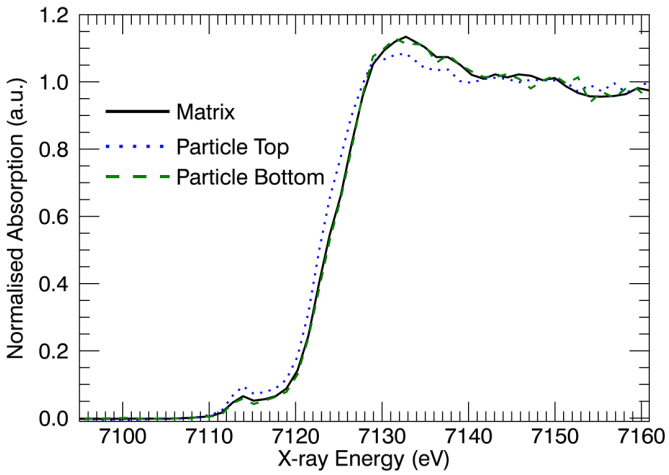

Figure 7.14: Fluorescence XANES spectra extracted from three regions in a Nitisol soil sample, studied with the SLcam using a 6:1 polycapillary optic.

time. Additionally, higher efficiency X-ray optics could be used to improve on the spatial resolution and to further reduce the measurement time.

To handle the large data set generated by the SLcam, a data reduction scheme has been applied using a combination of PCA and K-means clustering. While this approach showed promising results, nevertheless improved/dedicated algorithms may be required to differentiate between several chemical species in more complex samples.

Notwithstanding the current limitations of full-field emission mode micro-XANES imaging using the SLcam, mainly resulting from a limited X-ray beam flux, this method represents a substantial improvement on the way fluorescence mode XANES imaging is currently performed and opens up the possibility to perform XANES imaging experiments on dilute and/or non-transparent samples for which full-field transmission mode XANES cannot be applied.

7.4 Application: Confocal 3D Full-field XANES

This section is adapted from Tack *et al.*[b]

7.4.1 Introduction

As discussed earlier, X-ray absorption near edge structure (XANES) spectroscopy allows the experimentalist to extract information on the local chemical structure and oxidation state of a particular element in a sample matrix. By illuminating a sample with a focussed X-ray micro-beam and scanning the sample through this beam, spatially resolved information on the oxidation state and local chemical structure can be obtained.[50–55] However, when spatially resolved information is required, this approach has the disadvantage that samples need to be scanned through a beam, inducing sample movement. Thus one of the limiting factors is the precision and accuracy of motor positioning systems. Furthermore, when 3D information is required, an additional rotation step has to be introduced as in XANES computed tomography (CT).[56–58]

[b]P. Tack, B. Vekemans, B. Laforce, J. Rudloff-Grund, W.Y. Hernández, J. Garrevoet, G. Falkenberg, F.E. Brenker, P. Van Der Voort, L. Vincze, Application towards confocal full-field microscopic X-ray absorption near edge structure spectroscopy. Anal. Chem., doi:10.1021/acs.analchem.6b0482 (2017).

In order to circumvent this time consuming methodology, it is of great interest to develop so-called full-field methodologies. In these methodologies, a large field of view is investigated in a single measurement, without the need for sample movement, whilst maintaining the spatially resolved information. Initially, most full-field XANES techniques were based on transmission mode experiments,[1, 2, 5, 31, 59, 60] limiting the method to thin and transmitting samples. Another method, operating in fluorescence mode and thus allowing for the investigation of thick samples, consists of fast scanning using large solid angle X-ray detectors such as the Maia.[58, 61–66] Despite the method consisting of continuous sample movement, thus inducing uncertainties with respect to measurement position and movement stability, the method is favoured due to its impressively fast acquisition rates (order of a few ms/point/energy).

Another option for spatially resolved fluorescence mode XANES arises with the use of full-field methodology based on energy-dispersive CCD based detectors, such as the SLcam.[19, 20] The proof of principle for XANES using this device has been discussed in the previous section.[67] In this section, the method has been expanded to extract depth selective information by applying a confocal detection scheme, analogous to earlier X-ray fluorescence spectroscopy experiments performed with this detector.[68, 69] A virtual slice of the sample is illuminated using a focussed thin sheet beam, a part of which is selectively monitored by overlapping the sheet beam with the focal field of view of the detector, equipped with a polycapillary optic. By moving the sample through the sheet beam, making use of a single translation motor, and performing a monochromator energy scan at each position, 3D resolved XANES data is obtained. Here this method is applied to two samples: a) a Au/MgO catalyst particle which can be applied to several (photosensitive) catalytic processes(e.g. oxidation reactions,[70–72] hydrogenation reactions[73] and C-C coupling processes[74]), in which the local charge or oxidation state of Au has an important influence on the catalytic efficiency and sensitivity[75–80] and b) a natural alluvial diamond from Juina area, Mato Grosso, Brazil which may have an ultra deep origin as shown many samples of the same location.[81–83] The diamond contains inclusions, which have their stability field at least within the transition zone (410-670 km) and thus represents some of the only samples providing direct information on the materials from deep Earth.[82–84]

It is shown that the applied depth selective method, although still time consuming, is superior in speed compared to other currently applied XANES methodologies and is feasible to perform during a standard synchrotron radiation facility measurement session. Additionally, a method is discussed to facilitate handling and processing of the large amount

of created data, using a combination of principal component analysis (PCA) and K-means clustering. The XANES spectra can be overlapped with the spectra of reference compounds measured in transmission mode, proving the method allows for fingerprinting and linear combination data processing approaches.

7.4.2 Materials and Methods

Micro-CT

As a pre-characterization step, transmission X-ray computed tomography (CT) were performed on a laboratory instrument, details of which are described elsewhere.[85] The X-ray source, a W anode X-ray tube (XrayWorX GmbH, Garbsen, Germany), was operated at 70 kV voltage and 3 W power. The transmission signal was detected by a 20 MHz readout frequency VHR CCD camera (Photonic Science Ltd., Mountfield, UK) consisting of 4008×2672 9×9 μm^2 pixels and a Gd2OS:Tb scintillator screen. A 360 ° rotation was performed in 1501 steps with an exposure time of 1 s/rotation. Two consecutive measurements were performed at different sample heights in order to cover the full particle size. The data was backwards projected to obtain virtual slices of the sample, which were visualised using the Drishti software package.[86]

XANES

XANES experiments were performed at beamline P-06 at the PETRA-III synchrotron facility at DESY (Hamburg, Germany). The undulator generated primary X-ray beam was rendered monochromatic using a Si(111) double crystal monochromator, providing an energy resolution $\Delta E/E$ of approximately $1.4 \cdot 10^{-4}$. The second mirror of a Kirkpatrick-Baez (KB) mirror system was used to focus the beam to a vertically oriented sheet beam of approximately 1.8×0.007 mm^2 (V×H), with a horizontal divergence of approximately 2 mrad. No change in sheet beam position was observed by scanning through the primary X-ray beam energy.

Au L_3-edge (E_0: 11.919 keV) and Fe K-edge (E_0: 7.112 keV) XANES data were collected monitoring the excitation energy dependent X-ray fluorescence emission using the SLcam. Au L_3-edge XANES consisted of energy scans from 11.808 keV to 11.908 keV in 5 eV steps (5 min/step acquisition), 11.909 keV to 11.938 keV in 1 eV steps and from 11.941 keV to

12.079 keV in 3 eV steps (10 min/step acquisition); adding up to 98 energy steps. Fe K-edge XANES were performed by energy scans from 7.087 keV to 7.117 keV in 5 eV steps (9 min/step acquisition), 7.118 keV to 7.145 keV in 1 eV steps (18 min/step acquisition) and from 7.146 keV to 7.173 keV in 3 eV steps (18 min/step acquisition). Reference spectra were obtained from pure compounds (AuCN, Au foil, Fe foil), measured in transmission mode.

XANES spectra were normalised by subtracting the pre-edge background and fitting the post-edge region to a linear function, which was then normalised to 1 at E_0+50 eV.

Samples

A Au/MgO catalyst (having 1.0 wt% of Au) was prepared by a modified deposition-precipitation method described elsewhere,[87] using $HAuCl_4$ (Union Chimique Belge) as a gold precursor, urea (Sigma-Aldrich) as a precipitation agent and a meso-macroporous MgO support (prepared via a hydrothermal synthesis method adapted from Rezaei *et al.*[88]). A sintering step at 500 °C was performed in order to increase the Au particle sizes closer to the microscopic range, providing a more suitable size given the spatial resolution of the described technique ($\sim 8\,\mu$m resolution). The synthesized powder was then pressed to a pellet under a pressure of 300-400 bar for 5 minutes. A piece of suitable size ($\sim$2×2 mm^2) was cut from the pellet and attached to a graphite pin using clear liquid Pattex glue.

A second sample consists of a diamond from São Luiz placer diamond deposit in Juina, Mato Grosso, Brazil (SL FFM 08), containing Fe-rich inclusions from possible deep Earth sources. Juina provides large amounts of so-called ultra deep diamonds which were formed within ultra-deep parts of the Earth - the astenospheric upper mantle (<410 km), the transition zone (410-670 km) or even the lower mantle (>670 km).[81, 83, 89–91] Once the materials are encapsulated the inclusions remain chemically unchanged during exhumation due to the inert and stable nature of the host diamond.[83] Preliminary Raman investigation of diamond SL FFM 08 revealed the presence of walstromite and walstromite+CaTi-perovskite among other phases.

7.4.3 Results and Discussion

The SLcam was placed perpendicular to the primary X-ray beam under a 90 ° scattering geometry, in the plane of polarisation of the synchrotron radiation (Figure 7.15). This

effectively minimizes X-ray scattering by the sample to impinge on the detector; an important feature considering the low atomic number (Z) matrix of the investigated samples. A virtual slice of the sample was illuminated using the vertically focussed sheet beam and the SLcam field of view was co-aligned with the illuminated sample area, thus creating a confocal volume from which information is selectively acquired in an analogous manner to the confocal full-field XRF scheme as presented by Radtke et al. and Garrevoet *et al.*[68, 69]

By scanning over the energy of the primary X-ray beam and detecting the emitted fluorescence from the illuminated cross-section by the SLcam detector for each energy step, direct 3D X-ray absorption spectroscopy data is acquired. Considering the limited count rate of the SLcam (approximately 10 counts/s/pixel) and low detected flux due to the low transmission efficiency of the applied polycapillary optic, seemingly long acquisition times per energy step have to be applied (5-20 minutes/energy). However, one should realise this acquisition represents 20 minutes for a total of 69696 $8\times8\,\mu m^2$ pixels: the equivalent of 17 ms/point/energy. This is a count rate far superior to what is usually applied in confocal measurements,[36, 52, 55, 92–95] and very competitive to standard 3D XANES methodologies based on, for instance, tomographic reconstruction.

An Au/MgO catalyst particle was investigated in order to determine the spatially resolved chemical state of Au, as this can have a great effect on the catalytic activity of the particles.[75–80] As such, it is important to know whether a used reduction step during the synthesis affected only the outer Au particles, or whether the reduction also occurred inside the catalyst material. Using the applied methodology, this question can be answered.

An initial transmission tomography experiment was performed on the catalyst particle in order to obtain a rough overview of the Au particle distribution inside the catalyst (Figure 7.16A). It is clear this method does not provide information on the local chemical structure of the Au particles, as it mainly displays differences in local density. It is however a useful method to obtain a full 3D "roadmap" of the catalyst particle in a fairly short time, which allows for straightforward recognition of the investigated volumes during the confocal full-field experiments based on the emitted fluorescence and scattering radiation. The XRF Au-L_α intensity of the full-field XANES investigated area is compared to the transmission CT data in Figure 7.16B. The intensity gradient in the XRF data is explained by the absorption of the primary X-ray beam in the sample, as well as differences in sample thickness the emitted fluorescence radiation travels through. As such, the region that contains a similar Au concentration based on the transmission CT seems less concentrated

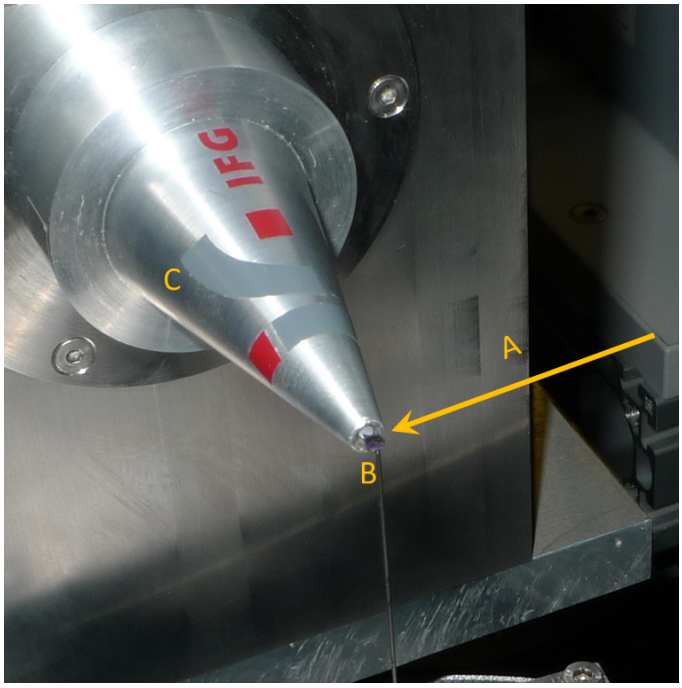

Figure 7.15: Photograph of the setup displaying the direction of primary X-ray sheet beam (A), the Au/MgO catalyst particle sample positioned on a XYZ translation and rotation stage (B) and the SLcam with 6:1 magnifying polycapillary optic (C).

based on the XRF data. This reduction in primary beam intensity is not problematic for the full-field XANES experiments however, as sufficient XRF intensity was detected over the entire illuminated sample region.

A major issue in full-field XANES spectroscopy concerns the handling of the large amount of data. Considering this experiment, for each energy step 69696 XRF spectra were generated. Multiplied by 98 energy steps (as for our Au L_3-edge XANES scan) and 2 sample positions in order to cover the entire sample cross section, one obtains over 13 million XRF spectra. Each of these spectra was processed to determine the relevant peak intensities, resulting in nearly 140000 XANES spectra. It is clear that this amount of spectra does not lend itself to the task of normalising and processing each spectrum manually. As such, a sequence of principal component analysis (PCA) and K-means clustering was performed in order to group and average XANES spectra with similar variations as a function of energy. During the initial steps of the in-house developed PCA analysis routine, a rough XANES normalisation is performed by fitting the pre-edge and post-edge regions by a linear function each. The pre-edge region is then normalised to 0, whereas the post-edge region is normalised to 1. This pre-normalisation effectively reduces concentration effects

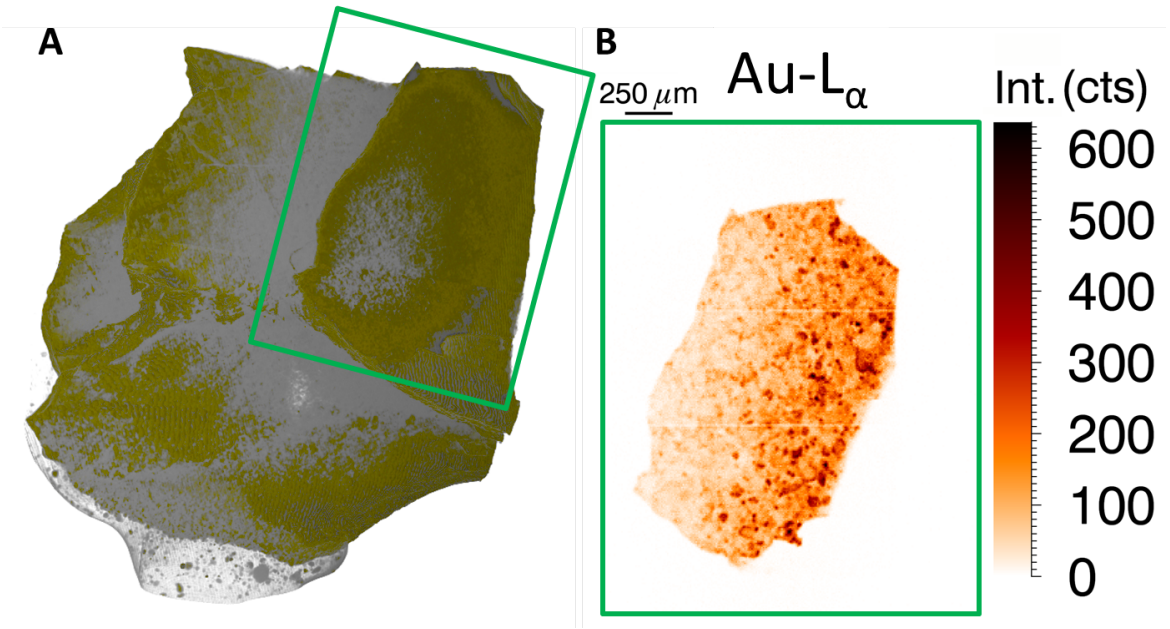

Figure 7.16: A) Transmission tomography rendered volume of a Au/MgO catalyst particle with gray parts representing the catalyst particle and gold/yellow parts representing the Au nanoparticles distributed through the volume. B) The full-field confocal Au-L_α XRF emission of the region marked in green. (E_0: 12.079 keV, t_m: 10 min)

that would otherwise cause the PCA to simply group spectra of similar intensity/edge jump.

Furthermore, voxels downstream in the sample are excited by a primary beam whose intensity has been energy dependently modified due to the energy dependent absorption by the sample upstream of the primary X-ray beam, that is the primary beam intensity illuminating the Au particles downstream is a product of the initial primary beam intensity and the attenuation of the X-rays by Au particles upstream.[52, 96] This effect is more pronounced at higher concentrations of the element over which edge is scanned are present in the sample. To correct for this, the Au-L_α and Fe-L_α intensities for each separate voxel were divided by the corresponding total intensity of energies lower than these XRF lines (I_{lowE}). This method essentially provides an I_0 normalisation on a point-by-point base that is independent of the absorption of the primary beam modulated by interactions occurring more upstream. In this particular case however, this normalisation was only used before the PCA and K-means clustering as I_{lowE} on a point-by-point basis suffered from poor counting statistics. Despite normalising for I_{lowE} providing clusters that correspond better with expected distributions based on for instance transmission CT experiments, using I_{lowE}

to normalise the final XANES spectra resulted in the disadvantageous addition of noise due to the high degree of noise in the I_{lowE} signal. As such, it was opted here to normalise the final (represented) XANES spectra using the general I_0 as registered by an ion chamber upstream of the KB mirror system, thus normalising each point in the full-field slice for the same value of I_0. In each case however the obtained XANES spectra had identical edge positions and XANES structure (within noise) when normalising with I_0 or I_{lowE}, thus proving both normalisation methods are viable in this case.

The results of clustering and the resulting extracted XANES profiles for the Au/MgO particle are shown in Figure 7.18. It is clear the clustering splits the Au/MgO in two large regions: the left and right region, where the left region is characterized by lower Au-L_α intensity (Figure 7.16) and the right region represents the more intense Au-L_α regions. In both cases, the extracted XANES spectra corresponding to these clusters show nearly identical XANES curves, which are in turn nearly identical to the reference spectrum of metallic Au. Only a very slight contribution of Au^+ can be seen at ∼11.928 keV, an interesting feature as the presence of a positive charge is advantageous for certain catalytic reactions, depending on the involved chemistry, such as the catalytic conversion of CO to CO_2 as is performed in air purification processes.[75–80]

The Single voxel XANES spectra of three randomly selected voxels are displayed in Figure 7.17. It is clear that significant noise levels are present in the post-edge region of the spectra, which complicate the performed PCA routine. Nevertheless, the main absorption edge is clearly visible and the general trend of the characteristic metallic Au features at approximately 11.95 and 11.97 keV can be differentiated slightly as well, showing the PCA is sufficiently sensitive in order to differentiate between compounds containing different oxidation states of the element of interest.

From the XRF data set it is also clear that in nearly the entire Au/MgO catalyst particle, Au particles are to be found. However, some regions are locally enriched in Au particles, characterised by the Au-L_α XRF hot spots (Figure 7.16B). Nevertheless, all particles are of mainly metallic Au (Au^0) with perhaps a small charge.

A second sample, a natural deep Earth diamond containing Fe rich inclusions, was investigated. This experiment benefits significantly from the confocal detection scheme, that is inherent to the full-field XANES methodology using the SLcam, as the diamond carbon matrix has a high Compton scattering cross section. In traditional detection schemes (e.g. XANES tomography) the scattering induced by the diamond would be sufficient to

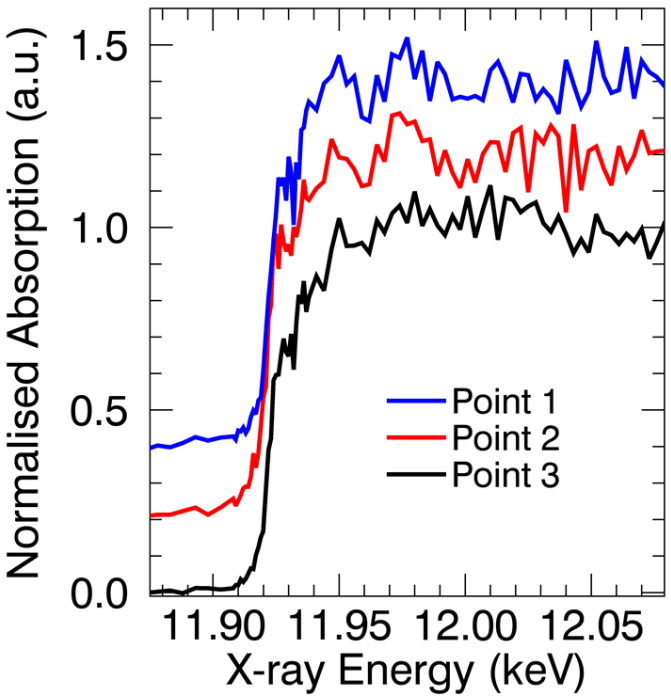

Figure 7.17: Single voxel Au L_3-edge XANES spectra for three randomly selected voxels in the Au/MgO sample data set. Noise levels are fairly high in the post-edge region, but a clear edge position is distinguishable.

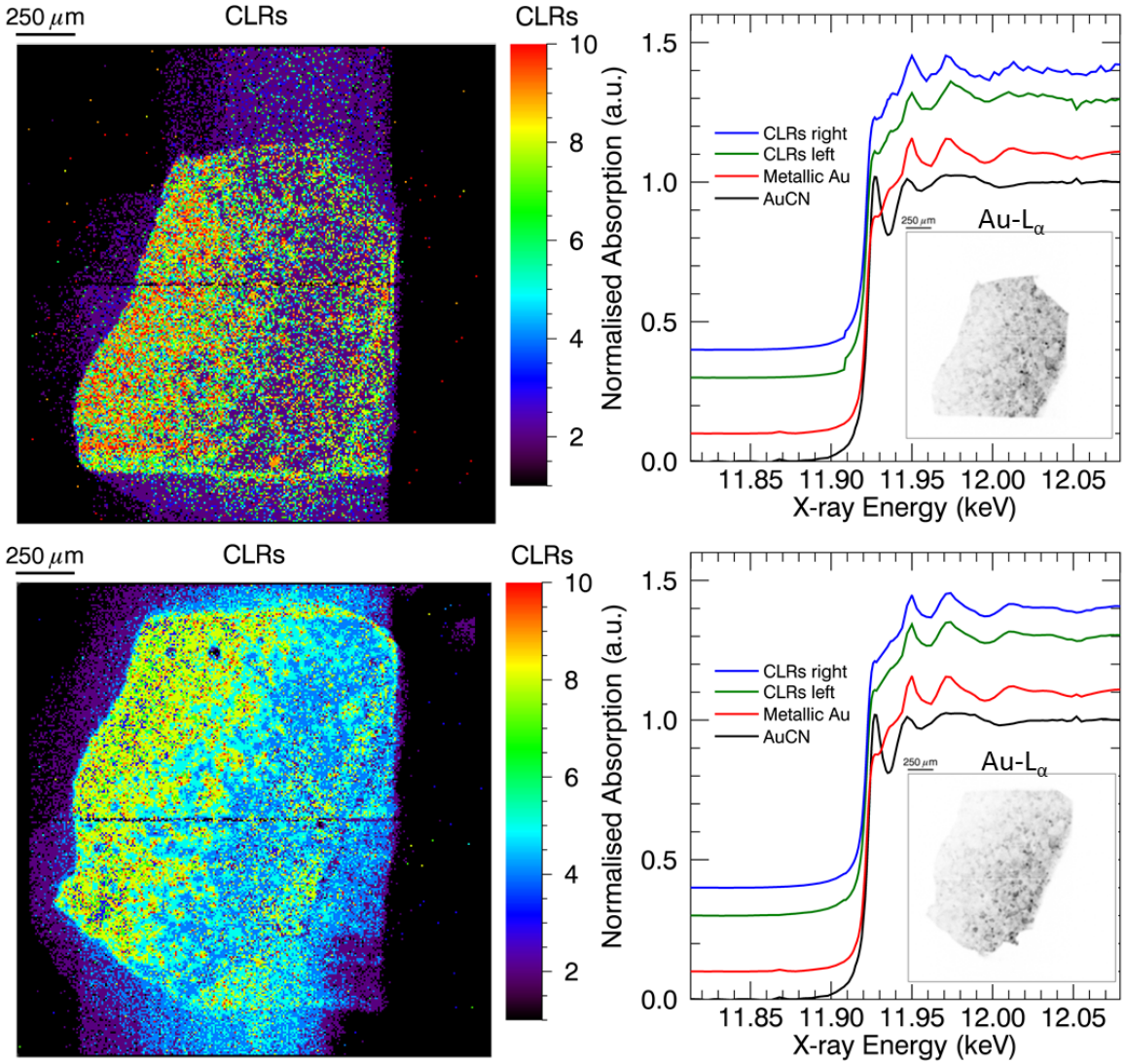

Figure 7.18: K-means clustering on PCA scores result (left) and corresponding Au L_3-edge XANES spectra for two large groups of clusters (CLRs) (right) for a Au/MgO catalyst particle, along with the spectra of reference compounds. An inset XRF Au distribution image is shown for each region. 'CLRs right' corresponds to the clusters on the right side of the particle, whereas 'CLRs left' corresponds to the clusters on the left side of the particle, as displayed on the PCA score results.

even overload most common fluorescence detectors, significantly reducing signal-to-scatter ratios achievable by the experiment. By applying the confocal method however, most of the scattering by the carbon matrix can be suppressed due to the restricted scattering volume combined with the 90 ° detection angle. The results of the clustering, obtained using an analogous procedure described above, and the resulting XANES spectra are displayed in Figure 7.19. Again it appears all the Fe in the inclusions has the same or very similar chemical signature, which is according to expectation for this particular specimen. The obtained XANES curve is very similar to that of a magnetite Fe_3O_4 reference compound, allowing us to deduce that the Fe in the investigated diamond inclusions consists of a mixture of Fe^{2+} and Fe^{3+} ions ordered in a magnetite-like structure. It should be noted that the pre-edge peak at ∼7.115 keV, visible for pure Fe_3O_4, is not visible in the confocal full-field XANES spectrum. This is either because the Fe surrounding inside the diamond inclusion, in contrast to magnetite, is characterized by an inversion symmetry (e.g. octahedral surrounding) or because the counting statistics in this energy region of the spectrum were insufficient to detect any pre-edge features. Additionally, the features around ∼7.146 keV are missing from the full-field XANES spectrum as well. This is unlikely due to poor counting statistics as the corresponding peak in the Fe_3O_4 spectrum is larger than the noise fluctuations visible in the full-field spectrum. This further strengthens the hypothesis that the Fe surrounding inside the diamond inclusions is similar but not identical to pure magnetite.

7.4.4 Conclusion

A confocal full-field XANES experiment was performed by illuminating a sample with a thin sheet beam, and selectively detecting the emitted fluorescence radiation as a function of primary X-ray beam energy in a spatially resolved manner using an energy dispersive pnCCD detector, the SLcam, characterized by a $2\times2\,mm^2$ field of view with 8 μm spatial resolution. Despite the seemingly long measurement times (12-15 hours/XANES scan consisting of 98 energy points) this depth sensitive methodology is revolutionary fast considering the large field of view and amount of simultaneously monitored voxels (69696). In comparison, to perform a similar XANES scan on a point-by-point scanning regime, each XANES scan should take only 750 ms/point including motor movement overhead time, which becomes significant at such movement rates.

Furthermore, as this technique is confocal in nature, it is possible to extract depth resolved

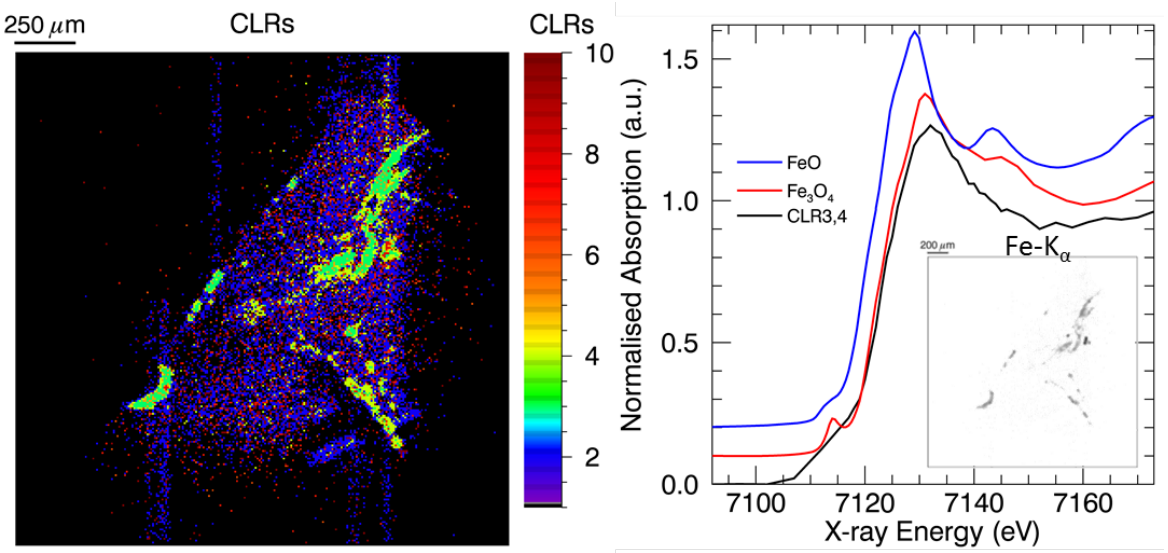

Figure 7.19: K-means clustering on PCA scores result (left) and corresponding Fe K-edge XANES spectra for two large groups of clusters (right) for a natural diamond with Fe containing deep Earth inclusions, along with the spectra of reference compounds. An inset XRF Fe distribution image is shown for the investigated subvolume.

2D information from a virtual slice in a sample without the requirement of rotating or otherwise moving the sample during measurement. Additionally, full 3D chemical state information can in principle be acquired by extending the described method by a lateral movement of the sample through the sheet beam, along the normal of the detector chip surface and performing an energy scan at each sample position.

In order to be able to handle the large amount of data acquired during this methodology, a clustering method based on PCA and K-means clustering was proposed in order to group similar XANES profiles, providing a semi-automated way of data reduction.

The methodology was applied to two samples: a) a Au/MgO catalyst sample in which the spatial chemical state distribution of the Au particles was monitored as this can have an impact catalytic activity, as well as b) a natural diamond containing Fe-rich inclusions, in which the chemical state of the Fe can give information on the redox conditions of the Earth's interior and as such can have great implications towards the understanding of our planet. In both cases the method resulted in XANES spectra which showed great agreement to reference compound spectra obtained in transmission mode.

Future improvements to this method are expected to be made mainly in the development of new X-ray detector optics, providing a higher transmission efficiency and better spatial

resolution. Additionally, new technologies could also result in obtaining faster detector readout and larger fields of view whilst maintaining similar or even better spatial resolution.

7.5 Summary

Full-field XAS allows for the spatially resolved investigation of local chemical structures over large sample areas in time frames which would be unattainable for common step-by-step scanning mode approaches. Here, the use of spatially resolved energy dispersive detectors was displayed for emission mode XAS and XRF, allowing for the investigation of thick and diluted samples which cannot be investigated using transmission mode approaches.

Several spatially resolved, energy dispersive detectors are currently available. Amongst them, the SLcam is characterised by one of the thickest (450 μm) and largest (12.7×12.7 mm^2 area with 48×48 μm^2 pixels) Si crystal chips. Additionally, the spatial resolution can be tuned by using one of two polycapillary optics: a 6:1 magnifying conical polycapillary optic resulting in a spatial resolution of 8×8 μm^2, or a 1:1 straight polycapillary optic resulting in a spatial resolution of 48×48 μm^2. Furthermore, the SLcam is characterised by a ∼150 eV energy resolution, similar to common SDD detectors, and a 400 Hz readout frequency.

Information from a large surface area of a sample can be obtained by illuminating the sample with a broad beam, and detecting the emitted radiation with the SLcam. By applying a sample rotation, 3D information can be obtained following a computed tomography reconstruction scheme. Alternatively, direct 3D information can be obtained from a sample by illuminating it with a thin sheet beam, operating in a confocal full-field mode. By scanning the sample through the sheet beam, even larger 3D volumes can be investigated without the need of computationally demanding reconstruction algorithms or extensive sample movement. The SLcam was applied to specific case studies such as the investigation of geologically relevant soils (Nitisol), Fe rich inclusions in deep Earth diamonds and the Au state distribution in a catalyst particle.

The main disadvantage of the use of the 6:1 magnifying polycapillary optic is its low X-ray photon transmission efficiency: only a small part of the X-rays emitted by the sample reach the detector chip. As such, longer measurement times are applied than what would be achievable with better transmitting optics. Thus, the use of different X-ray

optics in combination with the SLcam will mean one of the biggest advances in full-field emission mode XAS. Nevertheless, full-field XAS and XRF using the SLcam means a significant advance in measurement time compared to common scanning approaches and is even similarly fast as the most recent scanning approaches making use of large solid angle detectors.

References

[1] Mangold, S., Steininger, R., Rolo, T. d. S. & Göttlicher, J. Full field spectroscopic imaging at the anka-xas- and -sul-x-beamlines. *Journal of Physics: Conference Series* **430**, 012130 (2013).

[2] Fayard, B., Pouyet, E., Berruyer, G., Bugnazet, D., Cornu, C., Cotte, M., Andrade, V. D., Chiaro, F. D., Hignette, O., Kieffer, J., Martin, T., Papillon, E., Salomé, M. & Sole, V. A. The new id21 xanes full-field end-station at esrf. *Journal of Physics: Conference Series* **425**, 192001 (2013).

[3] Muñoz, M., Pascarelli, S., Aquilanti, G., Narygina, O., Kurnosov, A. & Dubrovinsky, L. Hyperspectral µ-xanes mapping in the diamond-anvil cell: analytical procedure applied to the decomposition of (mg,fe)-ringwoodite at the upper/lower mantle boundary. *High Pressure Research* **28**, 665–673 (2008).

[4] Liu, Y. J., Meirer, F., Wang, J. Y., Requena, G., Williams, P., Nelson, J., Mehta, A., Andrews, J. C. & Pianetta, P. 3d elemental sensitive imaging using transmission x-ray microscopy. *Analytical and Bioanalytical Chemistry* **404**, 1297–1301 (2012).

[5] Nelson, G. J., Harris, W. M., Izzo, J. R., Grew, K. N., Chiu, W. K. S., Chu, Y. S., Yi, J., Andrews, J. C., Liu, Y. & Pianetta, P. Three-dimensional mapping of nickel oxidation states using full field x-ray absorption near edge structure nanotomography. *Applied Physics Letters* **98**, 173109 (2011).

[6] Meirer, F., Cabana, J., Liu, Y., Mehta, A., Andrews, J. C. & Pianetta, P. Three-dimensional imaging of chemical phase transformations at the nanoscale with full-field transmission x-ray microscopy. *J Synchrotron Radiat* **18**, 773–781 (2011).

[7] Procz, S., Lübke, J., Zwerger, A., Mix, M. & Fiederle, M. Optimization of medipix-2 threshold masks for spectroscopic x-ray imaging. *IEEE Transactions on Nuclear Science* **Vol. 56 No. 4**, 1795–1799 (2009).

[8] Ballabriga, R., Campbell, M., Heijne, E. H. M., Llopart, X. & Tlustos, L. The medipix3 prototype, a pixel readout chip working in single photon counting mode with improved spectrometric performance. *Ieee Transactions on Nuclear Science* **54**, 1824–1829 (2007).

[9] Wright, V. A., Davidson, W. D., Melone, J., O'Shea, V., Smith, K. M., Donnohue, L., Lea, L., Robb, K., Nenonen, S. & Silpila, H. 3-d medipix: A new generation of x-ray detectors. *Nuclear Instruments & Methods in Physics Research Section a-Accelerators Spectrometers Detectors and Associated Equipment* **546**, 319–323 (2005).

[10] Wright, V. A., Davidson, W. D., Melone, J. J., O'Shea, V., Smith, K. M., Donohue, L., Lea, L., Robb, K., Nenonen, S. & Sipila, H. Three-dimensional medipix - a new generation of x-ray detectors. *Ieee Transactions on Nuclear Science* **52**, 1873–1876 (2005).

[11] Jakubek, J., Pospisil, S., Vavrik, D. & Visschers, J. L. Resolution and stability tests of a medipix-1 pixel detector for x-ray dynamic defectoscopy. *Nuclear Instruments & Methods in Physics Research Section a-Accelerators Spectrometers Detectors and Associated Equipment* **509**, 294–301 (2003).

[12] Llopart, X., Campbell, M., Dinapoli, R., Segundo, D. S. & Pernigotti, E. Medipix2: a 64-k pixel readout chip with 55-μm square elements working in single photon counting mode. *IEEE Transactions on Nuclear Science* **Vol. 49 No. 5**, 2279–2283 (2002).

[13] Hartmann, R., Stephan, K.-H. & Strüder, L. The quantum efficiency of pn-detectors from the near infrared to the soft x-ray region. *Nuclear Instruments and Methods in Physics Research A* **439**, 216–220 (2000).

[14] Kimmel, N., Hartmann, R., Holl, P., Meidinger, N., Richter, R. & Strüder, L. Analysis of the charge collection process in pnccds (2006). Date od event: 2006-05-24 - 2006-05-27.

[15] Kimmel, N., Hiraga, J. S., Hartmann, R., Meidinger, N. & Struder, L. The direct measurement of the signal charge behavior in pnccds with subpixel resolution. *Nu-*

clear Instruments & Methods in Physics Research Section a-Accelerators Spectrometers Detectors and Associated Equipment **568**, 128–133 (2006).

[16] Alfeld, M., Janssens, K., Sasov, A., Liu, X., Kostenko, A., Rickers-Appel, K. & Falkenberg, G. The use of full-field xrf for simultaneous elemental mapping. *X-Ray Optics and Microanalysis, Proceedings* **1221**, 111–118 (2010).

[17] Jungmann-Smith, J. H. *et al.* Towards hybrid pixel detectors for energy-dispersive or soft x-ray photon science. *J Synchrotron Radiat* **23**, 385–394 (2016).

[18] Jungmann-Smith, J. H., Bergamaschi, A., Cartier, S., Dinapoli, R., Greiffenberg, D., Johnson, I., Maliakal, D., Mezza, D., Mozzanica, A., Ruder, C., Schaedler, L., Schmitt, B., Shi, X. & Tinti, G. Jungfrau 0.2: prototype characterization of a gain-switching, high dynamic range imaging system for photon science at swissfel and synchrotrons. *Journal of Instrumentation* **9**, 12013–12013 (2014).

[19] Scharf, O. *et al.* Compact pnccd-based x-ray camera with high spatial and energy resolution: a color x-ray camera. *Anal Chem* **83**, 2532–2538 (2011).

[20] Ordavo, I., Ihle, S., Arkadiev, V. & Scharf, O. A new pnccd-based color x-ray camera for fast spatial and energy-resolved measurements. *Nuclear Instruments and Methods in Physics Research A* **doi:10.1016/j.nima.2011.05.080** (2010).

[21] Garrevoet, J. *Development of Full-Field and Scanning X-ray Fluorescence Microspectroscopy.* Ph.D. thesis, Ghent University (2015).

[22] Boone, M. N., Garrevoet, J., Tack, P., Scharf, O., Cormode, D. P., Van Loo, D., Pauwels, E., Dierick, M., Vincze, L. & Van Hoorebeke, L. High spectral and spatial resolution x-ray transmission radiography and tomography using a color x-ray camera. *Nuclear Instruments and Methods in Physics Research Section A: Accelerators, Spectrometers, Detectors and Associated Equipment* **735**, 644–648 (2014).

[23] Hartmann, R., Buttler, W. & Gorke, H. A high-speed pnccd detector system for optical applications. *Nuclear Instruments and Methods in Physics Research A* **568**, 118–123 (2006).

[24] Nowak, S. H., Bjeoumikhov, A., Borany, J. v., Buchriegler, J., Munnik, F., Petric, M., Radtke, M., Renno, A. D., Reinholz, U., Scharf, O. & Wedell, R. Sub-pixel resolution with color x-ray camera slcam. *arXiv* **1501.06825** (2015).

[25] Feng, L. Y., Iwanczyk, J. S., Patt, B. E., Barkan, S. & Tull, C. R. Vortex - a new high performance silicon multicathode detector for xrd and xrf applications. *Hard X-Ray and Gamma-Ray Detector Physics V* **5198**, 103–110 (2004).

[26] Scharf, O. Slcam setup, operating guidelines and the ixcc-imaging software version 1.0.0 (2012).

[27] Calvin, S. *XAFS for Everyone* (Taylor & Francis, 2013).

[28] Koningsberger, D. & Prins, R. *X-ray absorption: Principles, applications, techniques of EXAFS, SEXAFS and XANES* (Wiley, 1987).

[29] Grunwaldt, J.-D., Hannemann, S., Schroer, C. G. & Baiker, A. 2d-mapping of the structure of a heterogeneous catalyst inside a catalytic micro-reactor during the partial oxidation of methane. *Journal of Physical Chemistry B* **110**, 8674 (2006).

[30] Marcus, M. A. X-ray photon-in/photon-out methods for chemical imaging. *Trac-Trends in Analytical Chemistry* **29**, 508–517 (2010).

[31] Meirer, F., Pemmer, B., Pepponi, G., Zoeger, N., Wobrauschek, P., Sprio, S., Tampieri, A., Goettlicher, J., Steininger, R., Mangold, S., Roschger, P., Berzlanovich, A., Hofstaetter, J. G. & Streli, C. Assessment of chemical species of lead accumulated in tidemarks of human articular cartilage by x-ray absorption near-edge structure analysis. *J Synchrotron Radiat* **18**, 238–244 (2011).

[32] Liu, Y., Wang, J., Hong, Y., Wang, Z., Zhang, K., Williams, P. A., Zhu, P., Andrews, J. C., Pianetta, P. & Wu, Z. Extended depth of focus for transmission x-ray microscope. *Opt Lett* **37**, 3708–3710 (2012).

[33] Kachenko, A. G., Grafe, M., Singh, B. & Heald, S. M. Arsenic speciation in tissues of the hyperaccumulator p. calomelanos var. austroamericana using x-ray absorption spectroscopy. *Environmental Science & Technology* **44**, 4735–4740 (2010).

[34] Gonella, F., Quaranta, A., Padovani, S., Sada, C., D'Acapito, F., Maurizio, C., Battaglin, G. & Cattaruzza, E. Copper diffusion in ion-exchanged soda-lime glass. *Applied Physics A* **81**, 1065–1071 (2004).

[35] Silversmit, G., Vekemans, B., Nikitenko, S., Schmitz, S., Schoonjans, T., Brenker, F. E. & Vincze, L. Spatially resolved 3d micro-xanes by a confocal detection scheme. *Phys Chem Chem Phys* **12**, 5653–5659 (2010).

[36] Silversmit, G., Vekemans, B., Appel, K., Schmitz, S., Schoonjans, T., Brenker, F. E., Kaminsky, F. & Vincze, L. Three-dimensional fe speciation of an inclusion cloud within an ultradeep diamond by confocal μ-x-ray absorption near edge structure: Evidence for late stage overprint. *Anal. Chem.* **83**, 6294–6299 (2011).

[37] Kühn, A., Scharf, O., Ordavo, I., Riesemeier, H., Reinholz, U., Radtke, M., Berger, A., Ostermann, M. & Panne, U. Pushing the limits for fast spatially resolved elemental distribution patterns. *J. Anal. At. Spectrom.* **26**, 1986–1989 (2011).

[38] Broothaerts, N., Kissi, E., Poesen, J., Van Rompaey, A., Getahun, K., Van Ranst, E. & Diels, J. Spatial patterns, causes and consequences of landslides in the gilgel gibe catchment, sw ethiopia. *Catena* **97**, 127–136 (2012).

[39] Manyala, B., Yves-Dady, Nemes, A., Mafuka, P., Van Ranst, E. & Cornelis, W. Prediction of water retention of soils from the humid tropics by the nonparametric k-nearest neighbor approach. *VADOSE ZONE JOURNAL* **12** (2013).

[40] de Wispelaere, L. *Characterization and genesis of Nitisols in the south-western Ethiopian highlands.* Ph.D. thesis, Ghent University (2012-2013).

[41] Working Group WRB, I. World reference base for soil resources 2006, first update 2007. *World Soil Resources Reports* **103** (2007).

[42] Beckhoff, B., Kanngießer, B., Langhoff, N., Wedell, R. & Wolff, H. *Handbook of Practical X-Ray Fluorescence Analysis* (Springer, 2007).

[43] Grieken, R. E. V. & Markowicz, A. A. *Handbook of X-Ray Spectrometry Second Edition, Revised and Expanded* (Marcel Dekker, Inc., 2002).

[44] Proost, K., Vincze, L., Janssens, K., Gao, N., Bulska, E., Schreiner, M. & Falkenberg, G. Characterization of a polycapillary lens for use in micro-xanes experiments. *X-Ray Spectrometry* **32**, 215–222 (2003).

[45] Nikitenko, S., Beale, A. M., van der Eerden, A. M., Jacques, S. D., Leynaud, O., O'Brien, M. G., Detollenaere, D., Kaptein, R., Weckhuysen, B. M. & Bras, W. Implementation of a combined saxs/waxs/qexafs set-up for time-resolved in situexperiments. *J Synchrotron Radiat* **15**, 632–640 (2008).

[46] Pearce, N. J. G., Perkins, W. T., Westgate, J. A., Gorton, M. P., Jackson, S. E., Neal, C. R. & Chenery, S. P. A compilation of new and published major and trace

element data for nist srm 610 and nist srm 612 glass reference materials. *Geostandards Newsletter-the Journal of Geostandards and Geoanalysis* **21**, 115–144 (1997).

[47] Vekemans, B., Janssens, K., Vincze, L., Adams, F. & Vanespen, P. Analysis of x-ray-spectra by iterative least-squares (axil) - new developments. *X-Ray Spectrometry* **23**, 278–285 (1994).

[48] Vekemans, B., Vincze, L., Brenker, F. E. & Adams, F. Processing of three-dimensional microscopic x-ray fluorescence data. *Journal of Analytical Atomic Spectrometry* **19**, 1302–1308 (2004).

[49] Tirez, K., Silversmit, G., Vincze, L., Servaes, K., Vanhoof, C., Mertens, M., Bleux, N. & Berghmans, P. Speciation and fractionation of nickel in airborne particulate matter: comparison between selective leaching and xas spectroscopy. *Journal of Analytical Atomic Spectrometry* **26**, 517–527 (2011).

[50] Tack, P., Cotte, M., Bauters, S., Brun, E., Banerjee, D., Bras, W., Ferrero, C., Delattre, D., Mocella, V. & Vincze, L. Tracking ink composition on herculaneum papyrus scrolls: quantification and speciation of lead by x-ray based techniques and monte carlo simulations. *Scientific Reports* **6**, 20763 (2016).

[51] Mino, L., Borfecchia, E., Groppo, C., Castelli, D., Martinez-Criado, G., Spiess, R. & Lamberti, C. Iron oxidation state variations in zoned micro-crystals measured using micro-xanes. *Catalysis Today* **229**, 72–79 (2014).

[52] Luhl, L., Hesse, B., Mantouvalou, I., Wilke, M., Mahlkow, S., Aloupi-Siotis, E. & Kanngiesser, B. Confocal xanes and the attic black glaze: the three-stage firing process through modern reproduction. *Anal Chem* **86**, 6924–6930 (2014).

[53] Terzano, R., Mimmo, T., Vekemans, B., Vincze, L., Falkenberg, G., Tomasi, N., Schnell Ramos, M., Pinton, R. & Cesco, S. Iron (fe) speciation in xylem sap by xanes at a high brilliant synchrotron x-ray source: opportunities and limitations. *Anal Bioanal Chem* **405**, 5411–5419 (2013).

[54] Terabayashi, M., Matsui, T., Okamoto, K., Ozawa, H., Kaneko, Y. & Maruyama, S. Micro-x-ray absorption near edge structure determination of $fe^{3+}/\sigma fe$ in omphacite inclusion within garnet from dabie eclogite, east-central china. *Island Arc* **22**, 37–50 (2013).

[55] Tack, P., Bauters, S., Mauro, J. C., Smedskjaer, M. M., Vekemans, B., Banerjee, D., Bras, W. & Vincze, L. Confocal depth-resolved micro-x-ray absorption spectroscopy study of chemically strengthened boroaluminosilicate glasses. *RSC Adv.* **6**, 24060–24065 (2016).

[56] Rau, C., Somogyi, A. & Simionovici, A. Microimaging and tomography with chemical speciation. *Nuclear Instruments & Methods in Physics Research Section B-Beam Interactions with Materials and Atoms* **200**, 444–450 (2003).

[57] Rau, C., Somogyi, A., Bytchkov, A. & Simionovici, A. Xanes microimaging and tomography. *Proceedings of SPIE* **4503**, 249–255 (2002).

[58] Ryan, C. G. *et al.* Maia x-ray fluorescence imaging: Capturing detail in complex natural samples. *22nd International Congress on X-Ray Optics and Microanalysis* **499**, 012002 (2014).

[59] Andrews, J. C., Meirer, F., Liu, Y., Mester, Z. & Pianetta, P. Transmission x-ray microscopy for full-field nano imaging of biomaterials. *Microsc Res Tech* **74**, 671–681 (2011).

[60] Meirer, F., Liu, Y., Pouyet, E., Fayard, B., Cotte, M., Sanchez, C., Andrews, J. C., Mehta, A. & Sciau, P. Full-field xanes analysis of roman ceramics to estimate firing conditions—a novel probe to study hierarchical heterogeneous materials. *Journal of Analytical Atomic Spectrometry* **28**, 1870 (2013).

[61] Kopittke, P. M., de Jonge, M. D., Wang, P., McKenna, B. A., Lombi, E., Paterson, D. J., Howard, D. L., James, S. A., Spiers, K. M., Ryan, C. G., Johnson, A. A. & Menzies, N. W. Laterally resolved speciation of arsenic in roots of wheat and rice using fluorescence-xanes imaging. *New Phytol* **201**, 1251–1262 (2014).

[62] Monico, L., Janssens, K., Alfeld, M., Cotte, M., Vanmeert, F., Ryan, C. G., Falkenberg, G., Howard, D. L., Brunetti, B. G. & Miliani, C. Full spectral xanes imaging using the maia detector array as a new tool for the study of the alteration process of chrome yellow pigments in paintings by vincent van gogh. *J. Anal. At. Spectrom.* **30**, 613 (2015).

[63] Howard, D. L., de Jonge, M. D., Lau, D., Hay, D., Varcoe-Cocks, M., Ryan, C. G., Kirkham, R., Moorhead, G., Paterson, D. & Thurrowgood, D. High-definition x-ray fluorescence elemental mapping of paintings. *Anal Chem* **84**, 3278–3286 (2012).

[64] Ryan, C. G., Kirkham, R., Hough, R. M., Moorhead, G., Siddons, D. P., de Jonge, M. D., Paterson, D. J., De Geronimo, G., Howard, D. L. & Cleverley, J. S. Elemental x-ray imaging using the maia detector array: The benefits and challenges of large solid-angle. *Nuclear Instruments & Methods in Physics Research Section a-Accelerators Spectrometers Detectors and Associated Equipment* **619**, 37–43 (2010).

[65] Kirkham, R. *et al.* The maia spectroscopy detector system: Engineering for integrated pulse capture, low-latency scanning and real-time processing. In *The 10th International Conference on Synchrotron Radiation Instrumentation*, vol. CP1234, 240–243 (American Institute of Physics, 2010).

[66] Etschmann, B. E., Ryan, C. G., Brugger, J., Kirkham, R., Hough, R. M., Moorhead, G., Siddons, D. P., De Geronimo, G., Kuczewski, A., Dunn, P., Paterson, D., de Jonge, M. D., Howard, D. L., Davey, P. & Jensen, M. Reduced as components in highly oxidized environments: Evidence from full spectral xanes imaging using the maia massively parallel detector. *American Mineralogist* **95**, 884–887 (2010).

[67] Tack, P., Garrevoet, J., Bauters, S., Vekemans, B., Laforce, B., Van Ranst, E., Banerjee, D., Longo, A., Bras, W. & Vincze, L. Full-field fluorescence mode micro-xanes imaging using a unique energy dispersive ccd detector. *Anal Chem* **86**, 8791–8797 (2014).

[68] Radtke, M., Buzanich, G., Curado, J., Reinholz, U., Riesemeier, H. & Scharf, O. Slicing – a new method for non destructive 3d elemental sensitive characterization of materials. *J. Anal. At. Spectrom.* **29**, 1339–1344 (2014).

[69] Garrevoet, J., Vekemans, B., Tack, P., De Samber, B., Schmitz, S., Brenker, F. E., Falkenberg, G. & Vincze, L. Methodology toward 3d micro x-ray fluorescence imaging using an energy dispersive charge-coupled device detector. *Anal Chem* **86**, 11826–11832 (2014).

[70] Wang, Z., Xu, C. L. & Wang, H. F. A facile preparation of highly active au/mgo catalysts for aerobic oxidation of benzyl alcohol. *Catalysis Letters* **144**, 1919–1929 (2014).

[71] Wang, L., Yang, D., Wang, J., Zhu, Z. B. & Zhou, K. B. Ambient temperature co oxidation over gold nanoparticles (14 nm) supported on mg(oh)(2) nanosheets. *Catalysis Communications* **36**, 38–42 (2013).

[72] Jia, C. J., Liu, Y., Bongard, H. & Schuth, F. Very low temperature co oxidation over colloidally deposited gold nanoparticles on mg(oh)2 and mgo. *J Am Chem Soc* **132**, 1520–1522 (2010).

[73] Guzman, J. & Gates, B. C. A mononuclear gold complex catalyst supported on mgo: spectroscopic characterization during ethylene hydrogenation catalysis. *Journal of Catalysis* **226**, 111–119 (2004).

[74] Hammond, C., Lopez-Sanchez, J. A., Hasbi Ab Rahim, M., Dimitratos, N., Jenkins, R. L., Carley, A. F., He, Q., Kiely, C. J., Knight, D. W. & Hutchings, G. J. Synthesis of glycerol carbonate from glycerol and urea with gold-based catalysts. *Dalton Transactions* **40**, 3927–3937 (2011).

[75] Rodriguez, J. A., Si, R., Evans, J., Xu, W., Hanson, J. C., Tao, J. & Zhu, Y. Active gold-ceria and gold-ceria/titania catalysts for co oxidation: From single-crystal model catalysts to powder catalysts. *Catalysis Today* **240**, 229–235 (2015).

[76] Meire, M., Tack, P., De Keukeleere, K., Balcaen, L., Pollefeyt, G., Vanhaecke, F., Vincze, L., Van Der Voort, P., Van Driessche, I. & Lommens, P. Gold/titania composites: An x-ray absorption spectroscopy study on the influence of the reduction method. *Spectrochimica Acta Part B: Atomic Spectroscopy* **110**, 45–50 (2015).

[77] Zamponi, F., Penfold, T. J., Nachtegaal, M., Lubcke, A., Rittmann, J., Milne, C. J., Chergui, M. & van Bokhoven, J. A. Probing the dynamics of plasmon-excited hexanethiol-capped gold nanoparticles by picosecond x-ray absorption spectroscopy. *Phys Chem Chem Phys* **16**, 23157–23163 (2014).

[78] Pacchioni, G. Electronic interactions and charge transfers of metal atoms and clusters on oxide surfaces. *Phys Chem Chem Phys* **15**, 1737–1757 (2013).

[79] Zhang, C., Michaelides, A. & Jenkins, S. J. Theory of gold on ceria. *Phys Chem Chem Phys* **13**, 22–33 (2011).

[80] Zhang, C., Michaelides, A., King, D. A. & Jenkins, S. J. Positive charge states and possible polymorphism of gold nanoclusters on reduced ceria. *J Am Chem Soc* **132**, 2175–2182 (2010).

[81] Kaminsky, F. V., Zakharchenko, O. D., Davies, R., Griffin, W. L., Khachatryan-Blinova, G. K. & Shiryaev, A. A. Superdeep diamonds from the juina area, mato grosso state, brazil. *Contributions to Mineralogy and Petrology* **140**, 734–753 (2001).

[82] Brenker, F. E., Vollmer, C., Vincze, L., Vekemans, B., Szymanski, A., Janssens, K., Szaloki, I., Nasdala, L., Joswig, W. & Kaminsky, F. Carbonates from the lower part of transition zone or even the lower mantle. *Earth and Planetary Science Letters* **260**, 1–9 (2007).

[83] Pearson, D. G., Brenker, F. E., Nestola, F., McNeill, J., Nasdala, L., Hutchison, M. T., Matveev, S., Mather, K., Silversmit, G., Schmitz, S., Vekemans, B. & Vincze, L. Hydrous mantle transition zone indicated by ringwoodite included within diamond. *Nature* **507**, 221–224 (2014).

[84] Kaminsky, F. Mineralogy of the lower mantle: A review of 'super-deep' mineral inclusions in diamond. *Earth-Science Reviews* **110**, 127–147 (2012).

[85] Laforce, B., Vermeulen, B., Garrevoet, J., Vekemans, B., Hoorebeke, L. V., Janssen, C. & Vincze, L. Laboratory scale x-ray fluorescence tomography: Instrument characterization and application in earth and environmental science. *Anal Chem* **88**, 3386–3391 (2016).

[86] Ajay Limaye, D. Volume exploration and presentation tool, poster presentation. *Vis Baltimore* (2006).

[87] Estrada, M., Costa, V. V., Beloshapkin, S., Fuentes, S., Stoyanov, E., Gusevskaya, E. V. & Simakov, A. Aerobic oxidation of benzyl alcohol in methanol solutions over au nanoparticles: Mg(oh)(2) vs mgo as the support. *Applied Catalysis a-General* **473**, 96–103 (2014).

[88] Rezaei, M., Khajenoori, M. & Nematollahi, B. Preparation of nanocrystalline mgo by surfactant assisted precipitation method. *Materials Research Bulletin* **46**, 1632–1637 (2011).

[89] B., H. & J.W., H. Lower mantle mineral associations preserved in diamonds. *Mineralogical Magazine* **58A**, 384–385 (1994).

[90] Brenker, F. E., Vincze, L., Vekemans, B., Nasdala, L., Stachel, T., Vollmer, C., Kersten, M., Somogyi, A., Adamsb, F., Joswig, W. & Harris, J. W. Detection of a ca-rich lithology in the earth's deep (>300 km) convecting mantle. *Earth and Planetary Science Letters* **236**, 579– 587 (2005).

[91] Hayman, P. C., Kopylova, M. G. & Kaminsky, F. V. Lower mantle diamonds from rio soriso (juina area, mato grosso, brazil). *Contributions to Mineralogy and Petrology* **149**, 430–445 (2005).

[92] Laclavetine, K., Ager, F. J., Arquillo, J., Respaldiza, M. n. & Scrivano, S. Characterization of the new mobile confocal micro x-ray fluorescence (cxrf) system for in situ non-destructive cultural heritage analysis at the cna: μxrf-concha. *Microchemical Journal* **125**, 62–68 (2016).

[93] Luhl, L., Mantouvalou, I., Schaumann, I., Vogt, C. & Kanngiesser, B. Three-dimensional chemical mapping with a confocal xrf setup. *Anal Chem* **85**, 3682–3689 (2013).

[94] Kanngiesser, B., Malzer, W., Mantouvalou, I., Sokaras, D. & Karydas, A. G. A deep view in cultural heritage—confocal micro x-ray spectroscopy for depth resolved elemental analysis. *Applied Physics A* **106**, 325–338 (2011).

[95] Silversmit, G., Vekemans, B., T.Schoonjans, Voorde, L. V. D., Schmitz, S., Appel, K., Brenker, F. & Vincze, L. Three-dimensional confocal μ-xanes on mineral inclusions in natural diamonds. *Photon Science 2009 : highlights and HASYLAB annual report : author contributions* (2010).

[96] Luhl, L., Mantouvalou, I., Malzer, W., Schaumann, I., Vogt, C., Hahn, O. & Kanngiesser, B. Reconstruction procedure for 3d micro x-ray absorption fine structure. *Anal Chem* **84**, 1907–1914 (2012).

Chapter 8

Summary and Conclusions

X-ray fluorescence (XRF) spectroscopy provides qualitative and quantitative information on the elemental composition of a sample by illuminating it with X-rays and monitoring the emitted characteristic radiation. X-ray absorption spectroscopy (XAS) provides information on the local chemical structure of an element of interest in a sample by tuning the primary X-ray beam energy over an absorption edge of the element of interest, and monitoring the amount of absorbed X-rays. Based on the energy position of the absorption edge, information is retrieved on the oxidation state whereas the energy dependent fluctuations provide information on the type, amount and distance of neighbouring atoms. (Chapter 2)

XAS can be performed in transmission mode, monitoring the amount of primary X-ray beam photons transmitted through the sample, or in emission mode, monitoring the emitted characteristic radiation or photoelectrons. Although transmission mode measurements have the advantage of better counting statistics, allowing for shorter measurement times, this approach is limited to thin (allowing for >10 % X-ray beam transmission) and concentrated samples. In this work, mainly emission mode experiments were discussed as they allow for the investigation of a wider range of samples.

In particular, this work presents several XAS/XRF methods in order of increasing methodological complexity:

- Bulk XAS: although this method does not provide microscopic spatially resolved information, it remains the method of choice for samples where spatially resolved information is not essential. It was shown that bulk mode XAS usually provides

better counting statistics for similar measurement times compared to the more technologically demanding methods. Additionally, the sample environment is fairly easily modified rendering this method ideal to monitor e.g. *in-situ* experiments. The use of this method was presented by the investigation of vanadium- and gold-based catalysts (Chapter 4).

- Focal XAS: A micro-focal polycapillary based setup was designed for the DUBBLE XAS beamline (BM26A, ESRF, Grenoble), providing a $8\times8\,\mu m^2$ beam size and presenting a milestone in introducing the DUBBLE XAS beamline to microscopic analysis. Detection limits for 1 s exposure time on a NIST SRM 1577c bovine liver sample amount to 2-35 ppm for elements with atomic number between 19 (K) and 29 (Cu). Additionally, the application of a Kirkpatrick-Baez mirror system to focus down the beam at an undulator source beam line (ID21, ESRF) was displayed for the purpose of investigating carbonized Herculaneum papyrus scrolls, providing information on the writing in these unique and precious scrolls (Chapter 5).

- Confocal XAS: In this approach a (micro)volume is generated from which information is selectively acquired. The focal setup at the DUBBLE XAS station was improved to allow for a confocal detection scheme, providing a confocal volume of $8\times8\times10\,\mu m^3$ at $\sim$18 keV(Chapter 6). Detection limits of 3-40 ppm are found for elements with atomic number between 19 (K) and 29 (Cu) when illuminating a NIST SRM 1577c bovine liver sample for 1 s allowing for trace element analysis. The Fe coordination in chemically strengthened boroaluminosilicate glass as well as in natural deep Earth diamond inclusions was investigated.

- Full-field XAS: In this approach a sample is illuminated with a large X-ray beam and the emitted characteristic radiaton is detected in a spatially resolved manner, providing direct 2D information. Here, the use of the SLcam was discussed, providing a 450 μm thick pnCCD-type Si chip with 264 by 264 $48\times48\,\mu m^2$ energy dispersive pixels, a 400 Hz detector readout and 150 eV energy resolution at the Mn-K_α fluorescence line (Chapter 7). A spatial resolution down to $8\times8\,\mu m^2$ was obtained by applying a 6:1 magnifying polycapillary optic in front of the detector. The SLcam was used at the DUBBLE beamline for 2D XAS applications on geological Nitisol soil samples.

- Confocal full-field XAS: by illuminating the sample with a thin sheet beam and monitoring a large area ($2.1\times2.1\,mm^2$) with 8 μm spatial resolution simultaneously,

spatially resolved XAS can be performed in record times: a XAS scan measured in 12 hours with the SLcam is equivalent to a measurement time of 620 ms per XAS scan in a point-by-point measurement approach, including the motor movement, in order to cover an area consisting of 69696 points. This experiment was performed at beam line P-06 (PETRA-III, DESY, Hamburg) to investigate a Au/MgO catalyst particle and natural deep Earth diamond inclusions.

Future prospects for the (con)focal approaches include the application of different X-ray optics (e.g. mirror-based optics) providing higher X-ray photon transmission efficiencies and better spatial resolution. Additionally, newer versions of the SLcam have a 1 kHz readout speed, providing even shorter measurement times if sufficient radiation is emitted by the sample. These developments potentially push the limits of SLcam spatial resolution to the sub-micron scale and full-field XANES acquisition of nearly 70 thousand data points in less than 10 hours, further increasing the applicability in the fields of geology, chemistry, cosmology and catalysis research.

Appendix A

English Summary

X-ray fluorescence (XRF) spectroscopy provides qualitative and quantitative information on the elemental composition of a sample by illuminating it with X-rays and monitoring the emitted characteristic radiation.[1, 2] X-ray absorption spectroscopy (XAS) provides information on the local chemical structure of an element of interest in a sample by tuning the primary X-ray beam energy over an absorption edge of the element of interest, and monitoring the amount of absorbed X-rays.[3, 4] Based on the energy position of the absorption edge, information is retrieved on the oxidation state whereas the energy dependent fluctuations provide information on the type, amount and distance of neighbouring atoms.

Due to the requirement of beam energy tunability and high X-ray photon fluxes, most XAS experiments are performed at synchrotron radiation (SR) facilities. The most basic approach towards XAS is the bulk mode approach, making use of a wide X-ray beam. This approach only provides averaged information on the relatively large probed sample volume of several mm^3.

In order to differentiate between sample heterogeneities, a scanning approach can be performed in which the primary X-ray beam is focussed down to microscopic dimensions. The sample is then raster scanned through this beam, providing spatially resolved information. 3D resolved information can be achieved by applying a tomographic detection scheme. However, this approach demands much time, rendering it less ideal for most SR experiments due to the limited access and measurement time constraints.

The confocal detection scheme partially resolves this issue as it allows for direct 3D information extraction from subvolumes in a sample. However, the investigation of large

volumes is still limited due to the inherently long measurement times of XAS experiments on diluted samples.

For this reason, full-field XAS was developed in which spatially resolved information is retrieved directly and simultaneously from a large sample volume. To achieve this, the SLcam was used providing information from a $2.1 \times 2.1\,\mathrm{mm}^2$ sample area with $8\,\mu$m spatial resolution in measurement times equivalent to the acquisition of a XANES spectrum each 620 ms following the default point-by-point scanning method.

The several approaches towards emission mode XAS presented above are discussed, along with several applications displaying the strengths of each of the separate measurement approaches.

A.1 Materials and Methods

A.1.1 BM26A

Beamline BM26A or the DUBBLE beamline (Dutch-Belgian beamline) at the ESRF (Grenoble, France) provides an X-ray beam originating from a 0.4 T bending magnet, rendered monochromatic using a Si(111) monochromator. Higher harmonics are rejected and vertically focussed by a Si and Pt coated mirror behind the monochromator.[5] The primary and transmitted beam intensities are monitored using ionization chambers, filled with gasses to provide approximately 10 % and 70 % absorption before and after the sample position respectively.

A.1.2 P-06

The PETRA-III P-06 beamline at DESY (Hamburg, Germany) operates an undulator generating primary X-ray beam was rendered monochromatic using a Si(111) double crystal monochromator, providing an energy resolution dE/E of approximately $1.4 \cdot 10^{-4}$. A Kirkpatrick-Baez (KB) mirror system was used to focus the beam to a vertically oriented sheet beam of approximately $1.8 \times 0.007\,\mathrm{mm}^2$ (V×H), with a horizontal divergence of approximately 2 mrad. No change in sheet beam position was perceived by scanning through the primary X-ray beam energy.

A.1.3 (Con)focal Setup

A polycapillary X-ray optic based confocal setup was built at the BM26A beamline. Primary X-ray beam focussing occurs with an XOS (X-ray Optical Systems, NY, USA) designed focussing optic, characterised by a large acceptance window ($7.5\times3\,mm^2$), a focal distance of approximately 2.5 mm and an estimated focal spot size of 10 μm at 6.4 keV. The 6 cm long polycapillary optic is contained in a housing with entrance window diameter of 10 mm and exit window diameter of 2.8 mm. Due to the large acceptance window, a large fraction of the BM26A X-ray beam is guided through the optic, resulting in a flux as high as possible impinging the microscopic beam spot on the sample.

By applying a second polycapillary optic to the Vortex-EM SDD detector (Hitachi High-Technologies Science America Inc.) and coinciding the focii of both optics, a confocal detection scheme is achieved. As confocal optic a 4 cm long XOS manufactured collimating optic with a 2 mm diameter entrance window, 10 mm diameter exit window and 2 mm focal spot distance was used. Purging holes to flow He through the polycapillary optics, decreasing absorption of X-ray photons by air, are foreseen in the optic's housing design. An image of the confocal setup is displayed in Figure A.1.

A.1.4 SLcam

The SLcam (Strüder-Langhoff camera, or Colour X-ray Camera) is a Si based pnCCD type energy dispersive X-ray detector, consisting of a 450 μm thick Si layer with 264 by 528 $48\times48\,\mu m^2$ pixels, mutually developed by PNSensor GmbH (Munich, Germany), the Institute for Scientific Instruments GmbH (IFG, Berlin, Germany), the BAM Federal Institute for Materials Research and Testing (Berlin, Germany), and the Institut für Angewandte Photonik e.V. (IAP, Berlin, Germany).[6] The outer 264 by 132 pixels of the chip are covered to prevent illumination by X-rays. The chip is read out with a 400 Hz frequency, in which a fast sideways transfer of the central 264 by 264 pixels to the sides, the so-called 'dark frame storage mode', is combined with the slower read out of the dark frames by two CAMEX chips each, effectively splitting the SLcam readout window in four quarters. Two polycapillary optics are available: a straight 1:1 magnification optic resulting in $48\times48\,\mu m^2$ spatial resolution and a conical 6:1 magnification optic for $8\times8\,\mu m^2$ spatial resolution (Figure A.2).

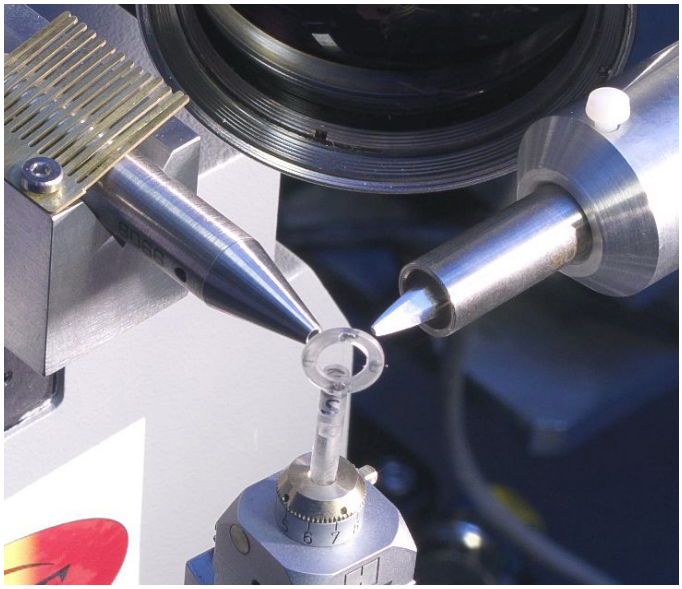

Figure A.1: Photograph of the polycapillary based confocal setup at beam line BM26A (DUBBLE, ESRF) showing the focussing optic on the left, confocal optic on the right and a 10 μm stainless steel wire cross in a plastic holder ring as a sample.

The detector chip was cooled to -20 °C to reduce electronic noise and provide an energy resolution of ∼150 eV for the Mn-K_α fluorescence line energy.

A.2 Results and Discussion

In the bulk mode approach, the sample is illuminated by a 'large' X-ray beam with a size in the order of a few millimetre. The resulting absorption and fluorescence spectrum is then the average of the entire illuminated sample volume. Despite the current synchrotron radiation development trend towards smaller beam sizes, currently achieving sizes down to only a few nanometre,[7] bulk XAS experiments remain very popular as they are the ideal approach when studying samples with millimetre sized homogeneity length scales. Due to the high flux attainable at synchrotron radiation facilities, bulk XANES experiments can be performed at a rate of less than a minute per spectrum, even down to a sub-second frequency, creating the opportunity of *in-situ* experiments such as following catalytic processes.[8–11]

Vanadium containing MOF catalysts were measured to investigate the chemical and structural changes around V during the breathing process of this MOF as well as the influence

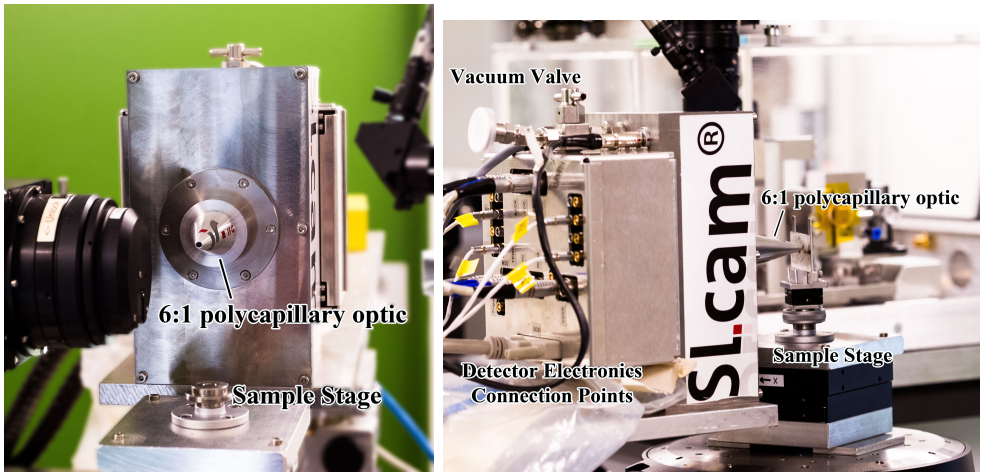

Figure A.2: Photographs of the SLcam installed at beamline P-06 of PETRA-III at DESY, Hamburg. Left: frontal view, right: side view.

of the Al/V content of the catalyst on the V state.[12] Additionally, a Au/TiO_2 catalyst particle was investigated to determine the effects of different reduction synthesis methods on the Au oxidation state.[13] As spatially resolved information was not required for these experiments, bulk mode XAS presented the ideal method due to the higher photon flux impending the samples. This resulted in shorter measurement times per sample, thus allowing for the investigation of more samples. Additionally, the fairly straightforward measurement setup allows for the implementation of specialized sample environments such as cryogenic conditions and He atmosphere.

Micro-focal emission mode XAS experiments were performed at the ID21 and BM26A beamlines, investigating carbonized Herculaneum papyrus scrolls.[14, 15] Here, spatially resolved information is of the essence as elemental composition images displayed the correlation between several elements, as well as showed the elemental constituents of the writing on the papyrus. Micro-XAS provided additional information on the compounds present in the papyrus writing, providing insights on the ink or pigment that was potentially used when drafting the manuscript. Due to the implementation of an X-ray optic in the primary beam path a slight decrease in sensitivity is observed due to the slightly reduced X-ray beam flux: 1-20 ppm for bulk mode and 2-35 ppm for micro-focal measurements with 1 s exposure time and atomic number Z from 19 to 29. However, the brilliance increases significantly, allowing for fast data acquisition. XAS images in which a XAS spectrum is recorded for each pixel of a predetermined array are however rarely applied due to the long measurement times involved in this method. It should be noted that due to the recent

developments in large solid angle detectors this scanning method does become feasible, even when considering 3D tomographic detection schemes.[16–21]

To obtain 3D spatially resolved information in manageable measurement times, a confocal detection scheme can be applied. At the BM26A beamline information was extracted selectively from a $\sim 8 \times 8 \times 10\,\mu m^3$ volume, with detection limits that are only a fraction higher than those obtained for micro-focal experiments (4-40 ppm). The confocal setup was applied for the investigation of Fe in chemically strengthened boroaluminosilicate glasses to monitor the change of Fe with sample depth and Al content.[22] Additionally, natural diamonds with deep Earth inclusions were investigated to determine the Fe minerals contained in these inclusions as they provide a unique way in which deep Earth can be sampled directly.

Nevertheless, scanning a 3D sample volume rapidly increases in measurement time with increasing array size using the confocal point-by-point measurement scheme. As a result, full-field XAS was applied making use of the SLcam, providing XRF and XAS spectra of 69696 pixels simultaneously. Although a single full-field XAS measurement easily takes over 10 hours of measurement time, it should be noted this corresponds to measuring a XAS spectrum every 620 ms for each point, including sample movement, in order to cover the same sample area. It is clear the SLcam presents a vast increase in 2D and 3D XAS data acquisition.

An initial 2D full-field XAS experiment with the SLcam was performed at BM26A, investigating geological Nitisol soil samples and reference structures.[23] A data reduction method based on a combination of PCA and K-means clustering was applied to combine similar XANES spectra, rendering the evaluation of nearly 70 thousand XAS spectra more manageable (Figure A.3).

Due to the illumination of the sample with a broad beam which was spread out over the sample surface to illuminate an area nearly as large as the SLcam field of view, the detected information originates from varying depths with respect to the sample surface. As such, the information is spatially resolved in two dimensions, however the third dimension remains unknown. By illuminating the sample with a sheet beam with known width, a confocal detection scheme can be obtained using the SLcam, providing full-field confocal XAS measurements. This was displayed with a Au/MgO catalyst particle, measured at beamline P-06 (PETRA-III, DESY, Hamburg). A virtual 3D slice of the sample was made with $8 \times 8 \times 8\,\mu m^3$ spatial resolution, which could be overlapped with transmission

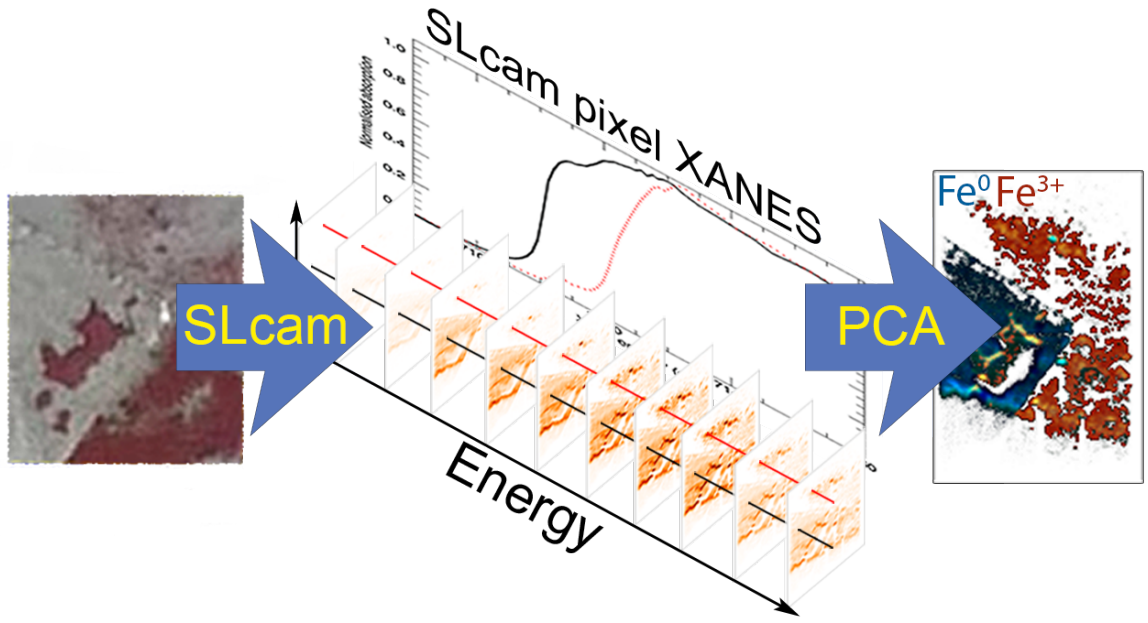

Figure A.3: Schematic overview of the full-field emission mode XANES experiment in which the Fe-K_α signal of an Fe^0/Fe_2O_3 model sample is monitored as a function of incident X-ray beam energy, using the SLcam. A multivariate analysis method is used to reduce the data set consisting of 69696 simultaneously acquired XRF spectra per incident beam energy step. Figure adapted from Tack *et al.*[23]

tomographic data acquired at a lab source (Figure A.4). Based on the extracted XANES curves the gold clusters in the sample could be identified as metallic.

A.3 Conclusions

Several approaches towards emission mode XAS data acquisition were discussed: bulk mode, focal, confocal and ultimately full-field and confocal full-field XAS. The methods were compared based on the investigation of different types of samples, including geological, catalytic and industrial applications.

The applications presented in this work present insights in the respective fields of research providing advances in the synthesis or interpretation of previously obtained data, displaying XAS is a powerful tool to study the local chemical environment in a sample.

Furthermore, it can be concluded that each XAS method is characterised by its own strengths and weaknesses. The discussed applications present samples and research questions appropriate for the corresponding methodologies. It is advised to consider the type of information one hopes to obtain from a sample before deciding on a XAS methodology: *in-situ* reactions may prove difficult to monitor with sufficient time resolution if one opts to perform full-field experiments, whilst investigating local hot spots in a larger sample matrix is not ideal with bulk mode XAS. This comparison of methodologies helps in determining the appropriate detection method for a given research question.

Full-field emission mode XAS is shown to provide microscopic spatially resolved information of large sample volumes in previously unattainable measurement times, rendering this approach feasible for thick and diluted samples at synchrotron radiation facilities.

References

[1] Beckhoff, B., Kanngießer, B., Langhoff, N., Wedell, R. & Wolff, H. *Handbook of Practical X-Ray Fluorescence Analysis* (Springer, 2007).

[2] Grieken, R. E. V. & Markowicz, A. A. *Handbook of X-Ray Spectrometry Second Edition, Revised and Expanded* (Marcel Dekker, Inc., 2002).

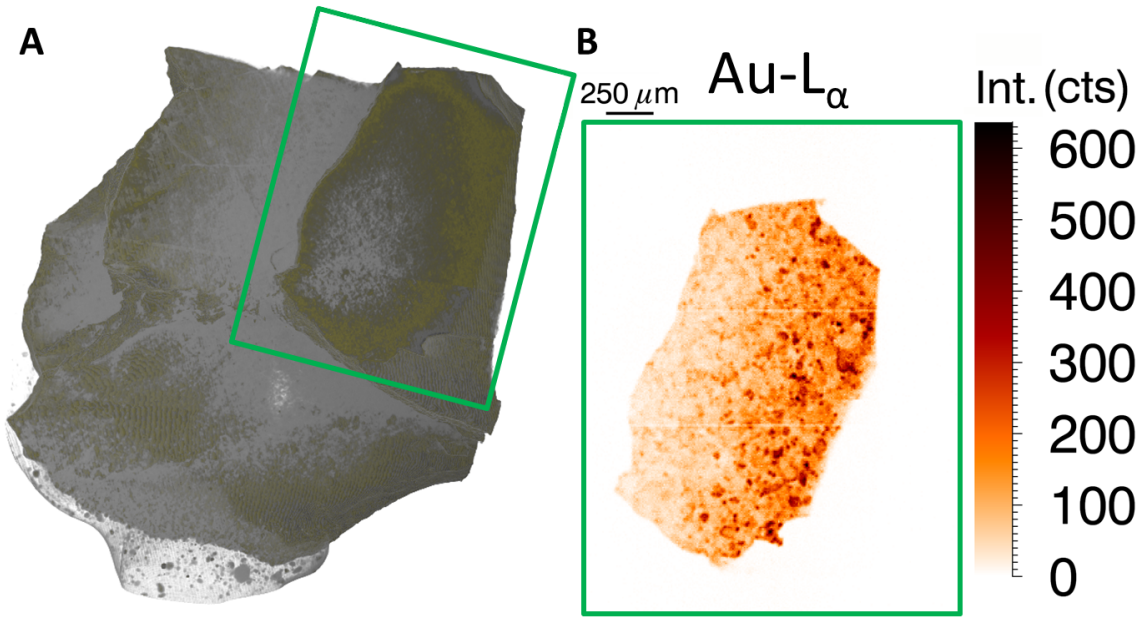

Figure A.4: A) Transmission tomography rendered volume of a Au/MgO catalyst particle with gray parts representing the catalyst particle and gold/yellow parts representing the Au nanoparticles distributed through the volume. B) The full-field confocal Au-L_α XRF emission of the region marked in green. (E_0: 12.079 keV, t_m: 10 min)

[3] Calvin, S. *XAFS for Everyone* (Taylor & Francis, 2013).

[4] Koningsberger, D. & Prins, R. *X-ray absorption: Principles, applications, techniques of EXAFS, SEXAFS and XANES* (Wiley, 1987).

[5] Nikitenko, S., Beale, A. M., van der Eerden, A. M., Jacques, S. D., Leynaud, O., O'Brien, M. G., Detollenaere, D., Kaptein, R., Weckhuysen, B. M. & Bras, W. Implementation of a combined saxs/waxs/qexafs set-up for time-resolved in situexperiments. *J Synchrotron Radiat* **15**, 632–640 (2008).

[6] Scharf, O. *et al.* Compact pnccd-based x-ray camera with high spatial and energy resolution: a color x-ray camera. *Anal Chem* **83**, 2532–2538 (2011).

[7] Laforce, B., Schmitz, S., Vekemans, B., Rudloff, J., Garrevoet, J., Tucoulou, R., Brenker, F. E., Martinez-Criado, G. & Vincze, L. Nanoscopic x-ray fluorescence imaging of meteoritic particles and diamond inclusions. *Anal Chem* **86**, 12369–12374 (2014).

[8] Sherborne, G. J. & Nguyen, B. N. Recent xas studies into homogeneous metal catalyst in fine chemical and pharmaceutical syntheses. *Chem Cent J* **9**, 37 (2015).

[9] Silversmit, G., Poelman, H., Sack, I., Buyle, G., Marin, G. B. & De Gryse, R. An in-situ reduction/oxidation xas study on the el10v8 vox/tio2(anatase) powder catalyst. *Catalysis Letters* **107**, 61–71 (2006).

[10] Silversmit, G., Poelman, H., Balcaen, V., Heynderickx, P. M., Olea, M., Nikitenko, S., Bras, W., Smet, P. F., Poelman, D., Gryse, R. D., Reniers, M.-F. & Marin, G. B. In-situ xas study on the cu and ce local structural changes in a cuo–ceo2/al2o3 catalyst under propane reduction and re-oxidation. *Journal of Physics and Chemistry of Solids* **70**, 1274–1284 (2009).

[11] Bazin, D. & Guczi, L. A review of in situ xas study on co-based bimetallic catalysts relevant to co hydrogenation. *Natural Gas Conversion Vii* **147**, 343–348 (2004).

[12] Wang, G., Leus, K., Couck, S., Tack, P., Depauw, H., Liu, Y. Y., Vincze, L., Denayer, J. F. & Van Der Voort, P. Enhanced gas sorption and breathing properties of the new sulfone functionalized comoc-2 metal organic framework. *Dalton Trans* **45**, 9485–9491 (2016).

[13] Meire, M., Tack, P., De Keukeleere, K., Balcaen, L., Pollefeyt, G., Vanhaecke, F., Vincze, L., Van Der Voort, P., Van Driessche, I. & Lommens, P. Gold/titania composites: An x-ray absorption spectroscopy study on the influence of the reduction method. *Spectrochimica Acta Part B: Atomic Spectroscopy* **110**, 45–50 (2015).

[14] Tack, P., Cotte, M., Bauters, S., Brun, E., Banerjee, D., Bras, W., Ferrero, C., Delattre, D., Mocella, V. & Vincze, L. Tracking ink composition on herculaneum papyrus scrolls: quantification and speciation of lead by x-ray based techniques and monte carlo simulations. *Scientific Reports* **6**, 20763 (2016).

[15] Brun, E., Cotte, M., Wright, J., Ruat, M., Tack, P., Vincze, L., Ferrero, C., Delattre, D. & Mocella, V. Revealing metallic ink in herculaneum papyri. *Proc Natl Acad Sci U S A* **113**, 3751–3754 (2016).

[16] Ryan, C. G., Kirkham, R., Hough, R. M., Moorhead, G., Siddons, D. P., de Jonge, M. D., Paterson, D. J., De Geronimo, G., Howard, D. L. & Cleverley, J. S. Elemental x-ray imaging using the maia detector array: The benefits and challenges of large solid-angle. *Nuclear Instruments & Methods in Physics Research Section a-Accelerators Spectrometers Detectors and Associated Equipment* **619**, 37–43 (2010).

[17] Ryan, C., Siddons, D., Kirkham, R., Dunn, P., Kuczewski, A., Moorhead, G., Geronimo, G. D., Paterson, D., Jonge, M. d., Hough, R., Lintern, M., Howard, D., Kappen, P. & Cleverley, J. The new maia detector system: Methods for high definition trace element imaging of natural material. In Denecke, M. & Walker, C. (eds.) *X-ray Optics and Microanalysis, Proceedings of the 20th International Congress*, vol. CP1221, 9–17 (American Intitute of Physics, 2010).

[18] Howard, D. L., de Jonge, M. D., Lau, D., Hay, D., Varcoe-Cocks, M., Ryan, C. G., Kirkham, R., Moorhead, G., Paterson, D. & Thurrowgood, D. High-definition x-ray fluorescence elemental mapping of paintings. *Anal Chem* **84**, 3278–3286 (2012).

[19] Kirkham, R. *et al.* The maia spectroscopy detector system: Engineering for integrated pulse capture, low-latency scanning and real-time processing. In *The 10th International Conference on Synchrotron Radiation Instrumentation*, vol. CP1234, 240–243 (American Institute of Physics, 2010).

[20] Ryan, C. G. *et al.* Maia x-ray fluorescence imaging: Capturing detail in complex natural samples. *22nd International Congress on X-Ray Optics and Microanalysis* **499**, 012002 (2014).

[21] Monico, L., Janssens, K., Alfeld, M., Cotte, M., Vanmeert, F., Ryan, C. G., Falkenberg, G., Howard, D. L., Brunetti, B. G. & Miliani, C. Full spectral xanes imaging using the maia detector array as a new tool for the study of the alteration process of chrome yellow pigments in paintings by vincent van gogh. *J. Anal. At. Spectrom.* **30**, 613 (2015).

[22] Tack, P., Bauters, S., Mauro, J. C., Smedskjaer, M. M., Vekemans, B., Banerjee, D., Bras, W. & Vincze, L. Confocal depth-resolved micro-x-ray absorption spectroscopy study of chemically strengthened boroaluminosilicate glasses. *RSC Adv.* **6**, 24060–24065 (2016).

[23] Tack, P., Garrevoet, J., Bauters, S., Vekemans, B., Laforce, B., Van Ranst, E., Banerjee, D., Longo, A., Bras, W. & Vincze, L. Full-field fluorescence mode micro-xanes imaging using a unique energy dispersive ccd detector. *Anal Chem* **86**, 8791–8797 (2014).

Appendix B

Nederlandstalige Samenvatting

X-straal fluorescentie (XRF) spectroscopie voorziet kwalitatieve en kwantitatieve informatie over de elementaire samenstelling van een monster door het te bestralen met X-stralen en de uitgezonden karakteriestieke straling te detecteren.[1, 2] X-straal absorptie spectroscopie (XAS) biedt informatie over de locale chemische structuur van een element van interesse in een monster door de primaire X-straalbundel energie te variëren over een absorptiesprong van het element van interesse, het aantal geabsorbeerde X-straalfotonen metende.[3, 4] Gebasseerd op de energetische waarde van de absorptiesprong wordt informatie verkregen over de oxidatietoestand, waar de energie afhankelijke fluctuaties informatie schenken omtrent de soort, aantal en afstand van naburige atomen.

Wegens de nood om energetisch varieerbare en zeer intense X-straalbundels worden de meeste XAS experimenten uitgevoerd aan synchrotronstraling faciliteiten. De meest eenvoudige aanpak is de bulk modus methode die gebruik maakt van een brede X-straal bundel. Deze aanpak biedt enkel uitgemiddelde informatie van het betrekkelijk grote belichte monster volume van verscheidene mm^3.

Om monster heterogeniteiten te onderscheiden van elkaar kan een rasterende aanpak gebruik worden. Hier wordt de exciterende X-straal bundel gefocusseerd tot microscopische dimensies, waarop het monster doorheen de bundel wordt bewogen en ruimtelijk verdeelde informatie wordt verkregen. 3D informatie kan verkregen worden door een tomografische reconstructie meting uit te voeren. Deze methode vergt echter veel tijd waardoor ze minder optimaal is voor synchrotron experimenten wegens de beperkte toegankelijkheid en meettijd constricties.

De confocale detectie methode lost dit probleem gedeeltelijk op daar het toelaat direct 3D informatie te extraheren van subvolumes in een monster. Het onderzoeken van grote volumes blijft echter beperkt wegens de inherent lange XAS meettijden op verdunde monsters.

Daardoor werd full-field XAS ontwikkeld waar ruimtelijk verdeelde informatie onmiddelijk en gelijktijdig wordt vergaard van een groot monster volume. Om dit te bekomen werd gebruikt gemaakt van de SLcam die informatie verzamelt van een $2.1 \times 2.1\,\mathrm{mm}^2$ monster oppervlak met $8\,\mu$m ruimtelijke resolutie in een meettijd equivalent met het opmeten in 620 ms van een XAS spectrum gebruik makende van de punt-na-punt rasterende meet methode.

De verscheidene aanpakken voor emissie modus XAS experimenten hierboven beschreven worden besproken, samen met verscheidene applicatie die de sterktes van elk van deze methodologiëen aantonen.

B.1 Materialen en Methodes

B.1.1 BM26A

Bundellijn BM26A of de DUBBLE bundellijn (Dutch-Belgian beamline) aan het ESRF (Grenoble, Frankrijk) biedt een X-straal bundel afkomstig van een 0.4 T *bending magnet*, monochromatisch gemaakt met een Si(111) monochromator. Hogere orde harmonieken worden geabsorbeerd en de X-straal bundel wordt verticaal gefocusseerd door een Si en Pt gelaagde spiegel na de monochromator.[5] De primaire en getransmitteerde bundelintensiteiten worden gemeten met ionisatiekamers, gevuld met gassen die ongeveer 10 % en 70 % van de straling absorberen respectievelijk voor en na de monster positie.

B.1.2 P-06

De PETRA-III P-06 bundellijn aan DESY (Hamburg, Duitsland) maakt gebruik van een *undulator* om X-stralen op te weken, die gemonochromatiseerd werden met een Si(111) dubbel kristal monochromator gekarakteriseerd door een energieresolutie dE/E van ongeveer $1.4{\cdot}10^{-4}$. Een Kirkpatrick-Baez (KB) spiegel systeem werd gebruikt om de bundel te

focusseren tot een verticaal georiënteerde $1.8\times0.007\,\mathrm{mm}^2$ (V×H) vlakke bundel met een horizontale divergentie van ongeveer 2 mrad. Geen verandering in bundelpositie werd opgemerkt bij het veranderen van de primaire X-straalbundel energie.

B.1.3 (Con)focal Setup

Een polycapillaire X-straal optica gebasseerde confocale opstelling werd aan bundellijn BM26A gebouwd. Primaire X-straalbundel focussering gebeurt met een door XOS (X-ray Optical Systems, NY, USA) ontworpen focusserende optica, gekarakteriseerd door een groot acceptantieoppervlak ($7.5\times3\,\mathrm{mm}^2$), een focale afstand van ongeveer 2.5 mm en een geschatte focale punt diameter van 10 μm bij 6.4 keV. Het 6 cm lange polycapillair is bevat in een omhulsel met 10 mm ingangsvenster diameter en 2.8 mm uitgangsvenster diameter. Door het grote acceptantievenster wordt een grote fractie van de BM26A X-straal bundellijn gegidst doorheen het optica, resulterend in een zo hoog mogelijke flux die het monster bereikt in een microscopisch oppervlak.

Door een tweede polycapillaire optica te plaatsen voor de Vortex-EM SDD detector (Hitachi High-Technologies Science America Inc.) en de focii van beide optica te overlappen wordt een confocale detectie verkregen. Als confocaal optica werd een 4 cm lang XOS gefabriceerde collimerende optica met 2 mm diameter ingangsvenster, 10 mm diameter uitgangsvenster en 2 mm focale afstand gebruikt. Purgeergaten werden voorzien in de behuizing om He gas te blazen doorheen de optica om zo absorptie van X-straal fotonen in de lucht te verminderen. Een afbeelding van de confocale opstelling is weergegeven in Figuur B.1.

B.1.4 SLcam

De SLcam (Strüder-Langhoff camera, of *Colour X-ray Camera*) is een Si gebasseerde pnCCD type energie dispersieve X-straal detector, bestaande uit een 450 μm dik Si kristal met 264 bij 528 $48\times48\,\mu\mathrm{m}^2$ pixels, gezamenlijk ontwikkeld door PNSensor GmbH (Munchen, Duitsland), het Instituut voor Wetenschappelijke Instrumenten GmbH (IFG, Berlijn, Duitsland), het BAM Federaal Instituut voor Materiaal Onderzoek en Tests (Berlijn, Duitsland), en het Institut für Angewandte Photonik e.V. (IAP, Berlijn, Duitsland).[6] De chip wordt uitgelezen met een 400 Hz frequentie waarin een snelle zijdelingse overdracht van

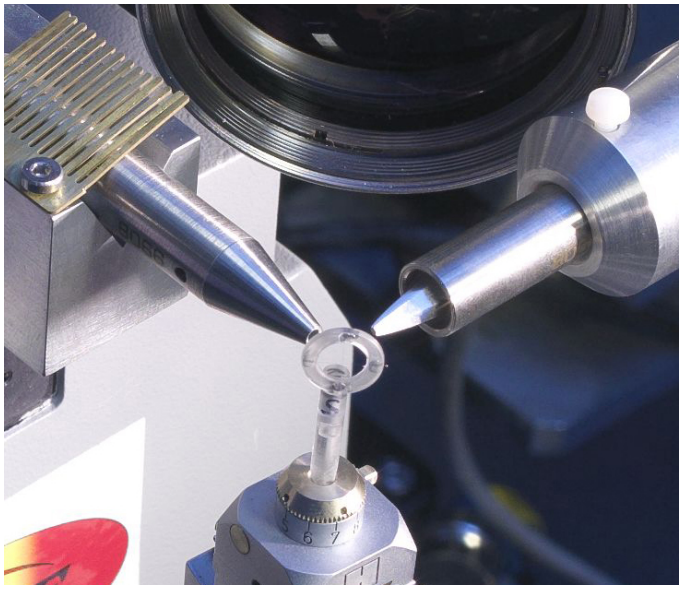

Figure B.1: Foto van de polycapillair gebasseerde confocale opstelling aan bundellijn BM26A (DUBBLE, ESRF) die het focusserende optica (links), confocale optica (rechts) en een 10 μm roestvrij stalen draad kruis in een plastiek houder ring als monster weergeeft.

de centrale 264 bij 264 pixels naar de zijkanten, de zo-geheten *'dark frame storage mode'*, wordt gecombineerd met het tragere uitlezen van de *dark frames* door twee CAMEX chips elk, effectief het SLcam venster in vier kwadranten delende. Twee polycapillaire optica zijn beschikbaar: een parallel 1:1 vergrotend optica met $48\times48\,\mu m^2$ ruimtelijke resolutie en een conisch 6:1 vergrotend optica met $8\times8\,\mu m^2$ ruimtelijke resolutie (Figuur B.2).

De detector chip werd gekoeld tot -20 °C om elektronisch ruis te verminderen, wat leidt tot een energie resolutie van ∼150 eV voor de Mn-K_α fluorescentie lijn energie.

B.2 Resultaten and Discussie

In de bulk modus aanpak wordt het monster bestraald met een 'grote' X-straalbundel in de orde van enkele millimeter. Het bekomen absorptie en fluorescentie spectrum is dan het gemiddelde van het volledig belichtte monster volume. Ondanks de huidige trend van synchrotronfaciliteiten naar kleine bundelgroottes, momenteel dimensies van slechts enkele nanometer behalende,[7] blijven bulk XAS experimenten zeer populair daar ze de ideale methode zijn wanneer men monsters onderzoekt met millimeter-grootte homogeniteiten. Door de hoge flux verkrijgbaar aan synchrotronfaciliteiten kunnen bulk XANES experi-

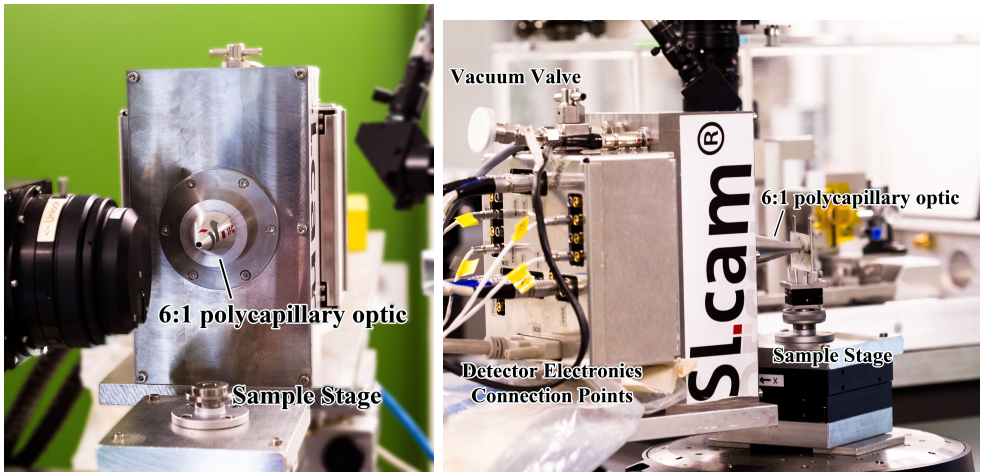

Figure B.2: Foto's van de SLcam geïnstalleerd aan bundellijn P-06 van PETRA-III aan DESY, Hamburg. Links: frontaal zicht. Rechts: zijzicht.

menten uitgevoerd worden in meettijden minder dan een minuut per spectrum, zelfs tot sub-seconde frequentie, wat de opportuniteit biedt om *in-situ* experimenten zoals katalytische processen te volgen.[8–11]

Vanadium bevattende MOF katalysatoren werden opgemeten om de chemische en structurele veranderingen rond V tijdens het ademingsproces van deze MOF alsook de invloed van de Al/V ratio te onderzoeken.[12] Bovendien werd een Au/TiO_2 katalysator onderzocht om de effecten van verschillende reductie synthese methoden op de Au oxidatietoestand te bepalen.[13] Daar ruimtelijk verdeelde informatie niet noodzakelijk was voor deze experimenten bleek bulk modus XAS de ideale methode om toe te passen wegens de hogere fotonenflux die het monster belichtte. Dit resulteerde in kortere meettijden per monster waardoor een grotere hoeveelheid monsters kon onderzocht worden. Daarenboven laat de betrekkelijk eenduidige meetopstelling ook toe om gespecialiseerde monsteromgevingen te implementeren zoals een He atmosfeer en cryogene condities.

Micro-focale emissiemodus XAS experimenten werden uitgevoerd aan de ID21 en BM26A bundellijnen, waar verkoolde Herculaneum papyrus rollen werden onderzocht.[14, 15] Hier is ruimtelijk verdeelde informatie van groot belang daar elementcompositie afbeeldingen de correlatie aantoonden tussen verscheidene elementen, alsook de samenstelling van het schrift op de papyrus prijs gaven. Micro-XAS bood additionele informatie omtrent de samenstelling van de componenten in het schrift, informatie verschaffende over de inkt of pigmenten die mogelijks gebruikt werden bij het opstellen van het manuscript. Wegens de implementatie van een X-straal optica in de primaire X-straalbundel werd een lichte daling

in gevoeligheid geobserveerd, verklaard door de licht verlaagde X-straalbundel intensiteit: 1-20 ppm voor bulk modus en 2-35 ppm voor micro-focale metingen met 1 s meettijd en atoomnummer Z van 19 tot 29. De brilliantie van de bundel stijgt echter significant, wat snelle data acquisitie mogelijk maakt. XAS beelden waarin een XAS spectrum wordt opgenomen voor elke pixel van een vooraf bepaalde matrix worden echter zelden toegepast wegens de te lange meettijden met betrekking tot deze methode. Het dient opgemerkt dat wegens recente ontwikkelingen in grote ruimtehoek detectoren deze aanpak mogelijk wordt, zelfs voor 3D tomografische detectie methodes.[16–21]

Om 3D ruimtelijk verdeelde informatie te bekomen in handelbare meettijden kan een confocale detectie methode gebruikt worden. Aan de BM26A bundellijn werd informatie selectief gedetecteerd van een $\sim 8\times 8\times 10\,\mu m^3$ volume, met detectielimieten die slechts een fractie hoger zijn dan die verkregen voor micro-focale experimenten (4-40 ppm). De confocale opstelling werd gebruikt om de variaties in Fe te onderzoeken met monsterdiepte en Al concentratie in chemisch versterkte boro-aluminosilicaat glazen.[22] Bovendien werden ook diep Aarde inclusies in natuurlijke diamanten onderzocht om de ijzer houdende mineralen bevat in deze inclusies te identificeren daar deze een unieke directe monstername van diep Aarde betekenen.

Desalniettemin verhoogt het opmeten van een 3D volume met de confocale punt-na-punt methode de meettijd significant. Daarom werd full-field XAS toegepast gebruik makende van de SLcam, waarin XRF en XAS spectra simultaan worden opgemeten voor 69696 pixels. Ook al neemt een enkele full-field XAS meting gemakkelijk meer dan 10 uur in beslag, het dient opgemerkt dat dit overeenkomt met het opmeten van een XAS spectrum elke 620 ms per punt, monster bewegingen inbegrepen, om eenzelfde gebied op te meten. Het is duidelijk dat de SLcam een significante versnelling in het opmeten van 2D en 3D XAS data betekent.

Een initieel 2D full-field XAS experiment met de SLcam werd uitgevoerd aan BM26A waarin geologische Nitisol bodemstalen en referentie structuren werden opgemeten.[23] Een data reductie methode gebasseerd op een combinatie van PCA en K-means clusteren werd toegepast om gelijkaardige XANES spectra te combineren, wat de evaluatie en verwerking van bijna 70 duizend XAS spectra handelbaarder maakt (Figuur B.3).

Daar het monster belicht werd met een brede bundel die uitgesmeerd werd over het monster oppervlak om een gebied te belichten zo groot als het meetbaar oppervlak van de SLcam, komt de gedetecteerde informatie van variërende monster dieptes. Op deze wijze

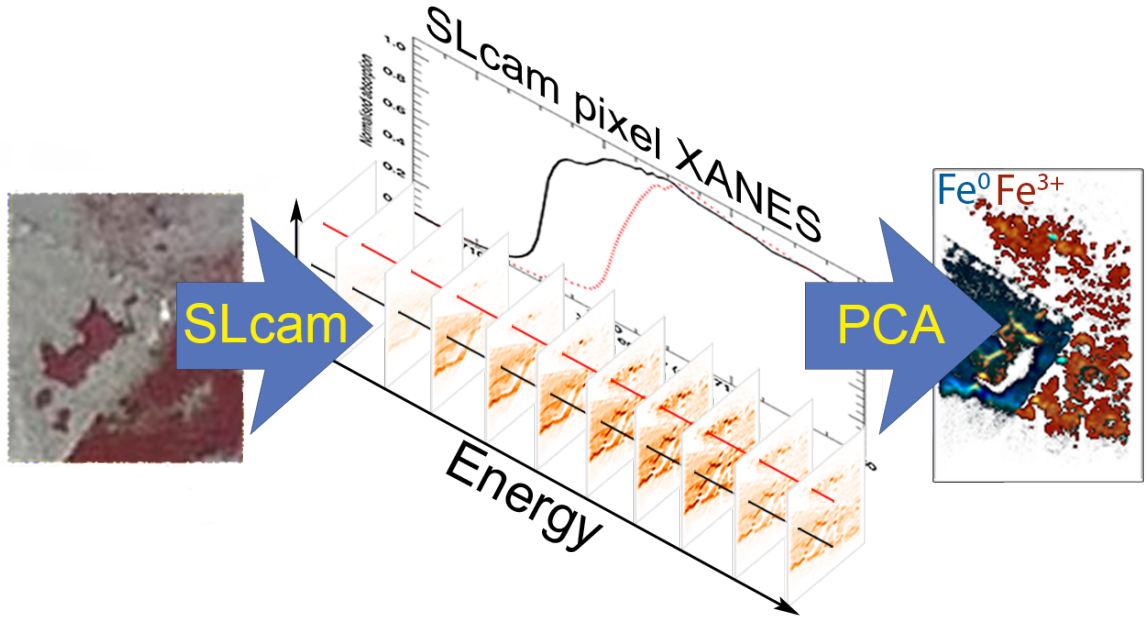

Figure B.3: Schematisch overzicht van een full-field emissie mode Schematic overview of the full-field emission modus XANES experiment waarin het Fe-K_α signaal van een Fe^0/Fe_2O_3 model monster werd opgemeten in functie van de primaire X-straal bundel energie, gebruik makende van de SLcam. Een multivariate analyse methode is gebruikt om de data set, bestaande uit 69696 gelijktijdig verzamelde XRF spectra per primaire X-straalbundel energie stap, te reduceren. Figuur overgenomen uit Tack *et al.*[23]

is de verkregen informatie ruimtelijk verdeeld in twee dimensies, echter de derde dimensie is niet gekend. Door het monster met een vlakke bundel met gekende dikte te belichten wordt een confocale detectie bekomen met de SLcam, resulterend in full-field XAS metingen. Deze methode werd aangetoond aan de hand van een Au/MgO katalysator deeltje, opgemeten aan bundellijn P-06 (PETRA-III, DESY, Hamburg). Een virtuele 3D doorsnede van het monster werd gemaakt met een ruimtelijke resolutie van $8\times8\times8\,\mu m^3$. De verkregen doorsnede kon overlapt worden met transmissie tomografische data opgenomen in een laboratorium toestel (Figuur B.4). Gebasseerd op de onttrokken XANES curves van de goud clusters in het monster konden deze partikels geïdentificeerd worden als metallisch goud.

B.3 Conclusies

Verscheidene benaderingen tot emissie modus XAS dataname werden besproken: bulk modus, focaal, confocaal en uiteindelijk full-field en confocale full-field XAS. Deze methodes werden vergeleken op basis van het onderzoeken van verscheidene monsters, waaronder geologische, katalytische en industriele toepassingen.

De toepassingen besproken in dit werken bieden inzichten in de respectievelijke onderzoeksvelden die leidden tot vooruitgang in de synthese of interpretatie van eerder verkregen data, bewijzend dat XAS een krachtige methode is om de locale chemische omringing in een monster te onderzoeken.

Bovendien kan geconcludeerd worden dat elke XAS methode gekarakteriseerd wordt door zijn eigen voor- en nadelen. De besproken applicaties behandelen monsters en onderzoeksvragen die gepast zijn voor de corresponderende methodologiën. Het is aangeraden om de gewenste soort informatie te overwegen alvorens een XAS methodologie te kiezen: *in-situ* reacties kunnen moeilijk te volgen zijn met voldoende tijdsresolutie indien men full-field experimenten wenst uit te voeren, terwijl de locale *hot spots* in een grotere monster matrix niet ideaal te onderzoeken zijn met bulk XAS. Deze vergelijking van methodologieën is een steun om de gepaste detectie methode voor een gegeven onderzoeksvraag te bepalen.

Het werd aangetoond dat full-field emissie modus XAS in staat is om microscopisch ruimtelijk verdeelde informatie in grote monster volumes te vergaren in eerder onhaal-

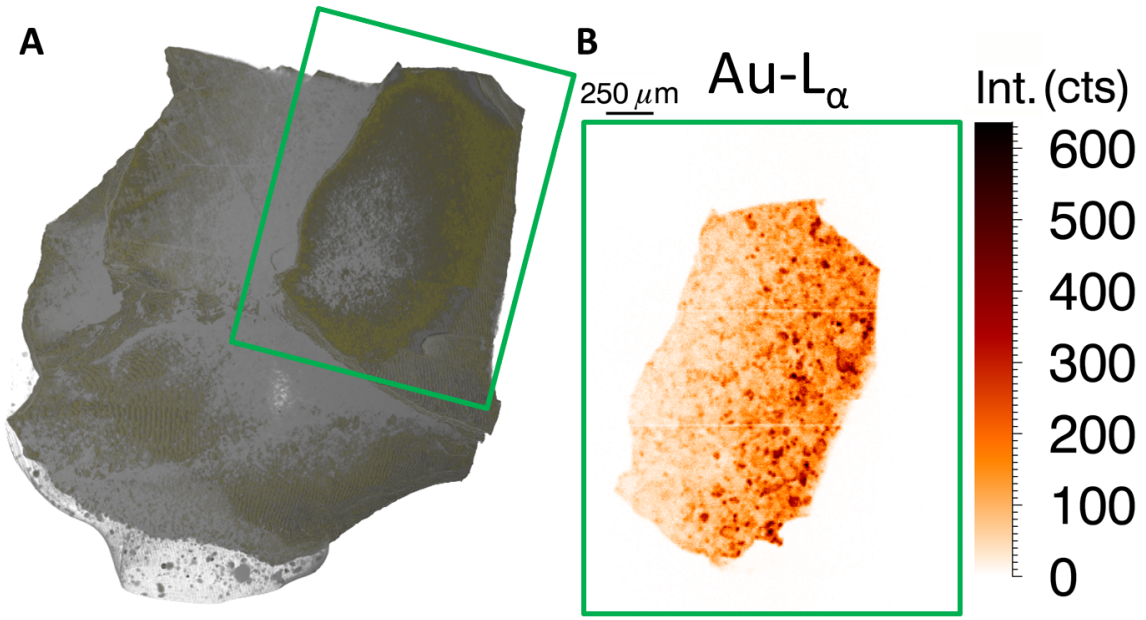

Figure B.4: A) Transmissie tomografie ontwikkeld volume van een Au/MgO katalysator deeltje waar de grijze delen het deeltje voorstellen en de goud/gele delen de Au nanoparticles die verdeeld zijn doorheen het monster volume. B) De full-field confocale Au-L_α XRF emissie van de regio aangeduid in het groen. (E_0: 12.079 keV, t_m: 10 min)

bare meettijden, waardoor deze aanpak een mogelijkheid wordt voor het onderzoeken van dikke en verdunde monsters aan synchrotronstraling faciliteiten.

Referenties

[1] Beckhoff, B., Kanngießer, B., Langhoff, N., Wedell, R. & Wolff, H. *Handbook of Practical X-Ray Fluorescence Analysis* (Springer, 2007).

[2] Grieken, R. E. V. & Markowicz, A. A. *Handbook of X-Ray Spectrometry Second Edition, Revised and Expanded* (Marcel Dekker, Inc., 2002).

[3] Calvin, S. *XAFS for Everyone* (Taylor & Francis, 2013).

[4] Koningsberger, D. & Prins, R. *X-ray absorption: Principles, applications, techniques of EXAFS, SEXAFS and XANES* (Wiley, 1987).

[5] Nikitenko, S., Beale, A. M., van der Eerden, A. M., Jacques, S. D., Leynaud, O., O'Brien, M. G., Detollenaere, D., Kaptein, R., Weckhuysen, B. M. & Bras, W. Imple-

mentation of a combined saxs/waxs/qexafs set-up for time-resolved in situexperiments. *J Synchrotron Radiat* **15**, 632–640 (2008).

[6] Scharf, O. *et al.* Compact pnccd-based x-ray camera with high spatial and energy resolution: a color x-ray camera. *Anal Chem* **83**, 2532–2538 (2011).

[7] Laforce, B., Schmitz, S., Vekemans, B., Rudloff, J., Garrevoet, J., Tucoulou, R., Brenker, F. E., Martinez-Criado, G. & Vincze, L. Nanoscopic x-ray fluorescence imaging of meteoritic particles and diamond inclusions. *Anal Chem* **86**, 12369–12374 (2014).

[8] Sherborne, G. J. & Nguyen, B. N. Recent xas studies into homogeneous metal catalyst in fine chemical and pharmaceutical syntheses. *Chem Cent J* **9**, 37 (2015).

[9] Silversmit, G., Poelman, H., Sack, I., Buyle, G., Marin, G. B. & De Gryse, R. An in-situ reduction/oxidation xas study on the el10v8 vox/tio2(anatase) powder catalyst. *Catalysis Letters* **107**, 61–71 (2006).

[10] Silversmit, G., Poelman, H., Balcaen, V., Heynderickx, P. M., Olea, M., Nikitenko, S., Bras, W., Smet, P. F., Poelman, D., Gryse, R. D., Reniers, M.-F. & Marin, G. B. In-situ xas study on the cu and ce local structural changes in a cuo–ceo2/al2o3 catalyst under propane reduction and re-oxidation. *Journal of Physics and Chemistry of Solids* **70**, 1274–1284 (2009).

[11] Bazin, D. & Guczi, L. A review of in situ xas study on co-based bimetallic catalysts relevant to co hydrogenation. *Natural Gas Conversion Vii* **147**, 343–348 (2004).

[12] Wang, G., Leus, K., Couck, S., Tack, P., Depauw, H., Liu, Y. Y., Vincze, L., Denayer, J. F. & Van Der Voort, P. Enhanced gas sorption and breathing properties of the new sulfone functionalized comoc-2 metal organic framework. *Dalton Trans* **45**, 9485–9491 (2016).

[13] Meire, M., Tack, P., De Keukeleere, K., Balcaen, L., Pollefeyt, G., Vanhaecke, F., Vincze, L., Van Der Voort, P., Van Driessche, I. & Lommens, P. Gold/titania composites: An x-ray absorption spectroscopy study on the influence of the reduction method. *Spectrochimica Acta Part B: Atomic Spectroscopy* **110**, 45–50 (2015).

[14] Tack, P., Cotte, M., Bauters, S., Brun, E., Banerjee, D., Bras, W., Ferrero, C., Delattre, D., Mocella, V. & Vincze, L. Tracking ink composition on herculaneum

papyrus scrolls: quantification and speciation of lead by x-ray based techniques and monte carlo simulations. *Scientific Reports* **6**, 20763 (2016).

[15] Brun, E., Cotte, M., Wright, J., Ruat, M., Tack, P., Vincze, L., Ferrero, C., Delattre, D. & Mocella, V. Revealing metallic ink in herculaneum papyri. *Proc Natl Acad Sci U S A* **113**, 3751–3754 (2016).

[16] Ryan, C. G., Kirkham, R., Hough, R. M., Moorhead, G., Siddons, D. P., de Jonge, M. D., Paterson, D. J., De Geronimo, G., Howard, D. L. & Cleverley, J. S. Elemental x-ray imaging using the maia detector array: The benefits and challenges of large solid-angle. *Nuclear Instruments & Methods in Physics Research Section a-Accelerators Spectrometers Detectors and Associated Equipment* **619**, 37–43 (2010).

[17] Ryan, C., Siddons, D., Kirkham, R., Dunn, P., Kuczewski, A., Moorhead, G., Geronimo, G. D., Paterson, D., Jonge, M. d., Hough, R., Lintern, M., Howard, D., Kappen, P. & Cleverley, J. The new maia detector system: Methods for high definition trace element imaging of natural material. In Denecke, M. & Walker, C. (eds.) *X-ray Optics and Microanalysis, Proceedings of the 20th International Congress*, vol. CP1221, 9–17 (American Intitute of Physics, 2010).

[18] Howard, D. L., de Jonge, M. D., Lau, D., Hay, D., Varcoe-Cocks, M., Ryan, C. G., Kirkham, R., Moorhead, G., Paterson, D. & Thurrowgood, D. High-definition x-ray fluorescence elemental mapping of paintings. *Anal Chem* **84**, 3278–3286 (2012).

[19] Kirkham, R. *et al.* The maia spectroscopy detector system: Engineering for integrated pulse capture, low-latency scanning and real-time processing. In *The 10th International Conference on Synchrotron Radiation Instrumentation*, vol. CP1234, 240–243 (American Institute of Physics, 2010).

[20] Ryan, C. G. *et al.* Maia x-ray fluorescence imaging: Capturing detail in complex natural samples. *22nd International Congress on X-Ray Optics and Microanalysis* **499**, 012002 (2014).

[21] Monico, L., Janssens, K., Alfeld, M., Cotte, M., Vanmeert, F., Ryan, C. G., Falkenberg, G., Howard, D. L., Brunetti, B. G. & Miliani, C. Full spectral xanes imaging using the maia detector array as a new tool for the study of the alteration process of chrome yellow pigments in paintings by vincent van gogh. *J. Anal. At. Spectrom.* **30**, 613 (2015).

[22] Tack, P., Bauters, S., Mauro, J. C., Smedskjaer, M. M., Vekemans, B., Banerjee, D., Bras, W. & Vincze, L. Confocal depth-resolved micro-x-ray absorption spectroscopy study of chemically strengthened boroaluminosilicate glasses. *RSC Adv.* **6**, 24060–24065 (2016).

[23] Tack, P., Garrevoet, J., Bauters, S., Vekemans, B., Laforce, B., Van Ranst, E., Banerjee, D., Longo, A., Bras, W. & Vincze, L. Full-field fluorescence mode micro-xanes imaging using a unique energy dispersive ccd detector. *Anal Chem* **86**, 8791–8797 (2014).

Appendix C

Thickness Sensitive XAS Self-absorption Correction

X-ray absorption spectra measured in emission mode can be influenced by self-absorption effects when the element of interest is concentrated in a sample. In this case, the measured fluorescence signal I_f is no longer proportional to the absorption coefficient of interest.[1] As a consequence, the obtained spectrum will be attenuated and edge energies may appear to have shifted. Fortunately, mathematical algorithms exist to correct for these self-absorption effects, provided the investigated sample's chemical composition is known.

C.1 Infinite Thickness Approximation

Conventionally, this self-absorption correction assumes an infinitely thick sample. Provided the reaction scheme as shown in Figure C.1, the fluorescence intensity I_f of an element of interest, originating from a sample slice at depth z_n with thickness dz is given by Equation C.1.[2]

$$I_f(z_n)dz_n = \left(\frac{\Omega}{4\pi}\right) I_0 e^{-\mu_t(\omega)z_n/sin\theta_i} \varepsilon_f(\omega)\mu_e(\omega)\frac{dz_n}{sin\theta_i} e^{-\mu_t(\omega_f)z_n/sin\theta_f} \tag{C.1}$$

with:

- Ω the detector solid angle

- I_0 the incident primary X-ray beam intensity
- $\mu_t(\omega)$ the total absorption coefficient for photons with energy ω
- θ_i the incident angle (Figure C.1)
- $\varepsilon_f(\omega)$ the fluorescence yield
- $\mu_e(\omega)$ the absorption coefficient with contributions from the edge of interest, opposed to the contributions from other atoms and edges of the element of interest denoted $\mu_b(\omega)$. $\mu_t(\omega) = \mu_e(\omega) + \mu_b(\omega)$
- ω_f the energy of the fluorescent photon
- θ_f the detection angle (Figure C.1)

By integrating Equation C.1 over the sample thickness z_n, the fluorescence signal is obtained:

$$\int_0^{z_s} I_f(z_n) dz_n = I_f(\omega) \tag{C.2}$$

$$\frac{I_f(\omega)}{I_0(\omega)} = \left(\frac{\Omega}{4\pi}\right) \frac{\varepsilon_f(\omega)\mu_e(\omega)}{\mu_t(\omega) + \mu_t(\omega_f) \cdot \frac{sin\theta_i}{sin\theta_f}} \left[1 - e^{-\left(\mu_t(\omega) + \mu_t(\omega_f) \cdot \frac{sin\theta_i}{sin\theta_f}\right) \frac{z_s}{sin\theta_i}}\right] \tag{C.3}$$

For an infinitely thick sample $\mu_t(\omega) \gg z_s^{-1}$ and thus $[\mu_t(\omega) + \mu_t(\omega_f)] \gg z_s^{-1}$. Additionally, usually $0 \leq (\theta_{i,f} \leq 90\,\text{deg})$ resulting in:

$$\left[\frac{\mu_t(\omega)}{sin\theta_i} + \frac{\mu_t(\omega_f)}{sin\theta_f}\right] \gg z_s^{-1} \tag{C.4}$$

And, subsequently

$$\frac{I_f(\omega)}{I_0(\omega)} = \left(\frac{\Omega}{4\pi}\right) \frac{\varepsilon_f(\omega)\mu_e(\omega)}{\mu_t(\omega) + \mu_t(\omega_f) \cdot \frac{sin\theta_i}{sin\theta_f}} \tag{C.5}$$

I_f/I_0 corresponds to the pre-edge background subtracted XAS data and is zero below the absorption edge of interest. Adding an edge-step normalisation one obtain the normalised signal N:

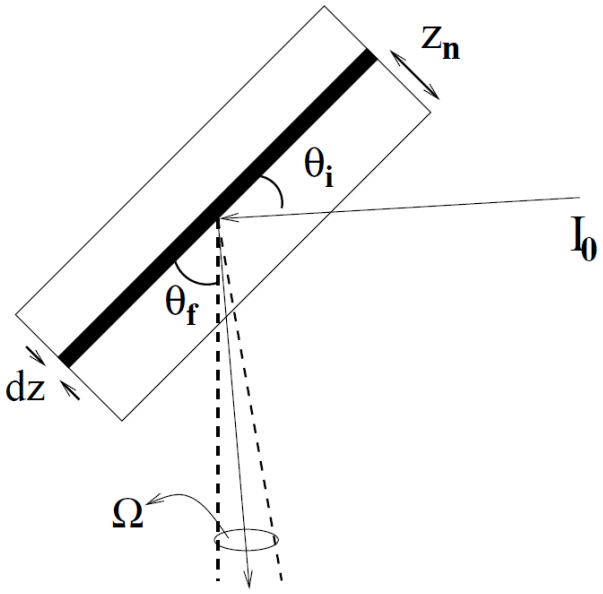

Figure C.1: Schematic representation of fluorescence experimental setup. Figure adapted from Haskel.[2]

$$N = \frac{\frac{I_f}{I_0}\omega}{\frac{I_f}{I_0}\omega_0^+} = \left[\frac{\varepsilon_f(\omega)\mu_e(\omega)}{\varepsilon_f(\omega_0^+)\mu_e(\omega_0^+)}\right]\left[\frac{\mu_t(\omega_0^+) + \mu_t(\omega_f)\cdot\frac{sin\theta_i}{sin\theta_f}}{\mu_t(\omega) + \mu_t(\omega_f)\cdot\frac{sin\theta_i}{sin\theta_f}}\right] \tag{C.6}$$

with ω_0^+ an energy above the main absorption edge. By dividing numerator and denominator by $\mu_e(\omega_0^+)$ and solving for $\mu_e(\omega)/\mu_e(\omega_0^+)$ on gets the equation for the self-absorption corrected X-ray absorption curve:

$$\frac{\mu_e(\omega)}{\mu_e(\omega_0^+)} = \frac{N\left(\frac{\mu_t(\omega_f)}{\mu_e(\omega_0^+)}\frac{sin\theta_i}{sin\theta_f} + \frac{\mu_b(\omega)}{\mu_e(\omega_0^+)}\right)}{\left(\frac{\mu_t(\omega_f)}{\mu_e(\omega_0^+)}\frac{sin\theta_i}{sin\theta_f} + \frac{\mu_b(\omega_0^+)}{\mu_e(\omega_0^+)} + 1\right) - N} \tag{C.7}$$

Where N is the experimentally measured I_f/I_0.

C.2 Thickness Sensitive Approach

If however one needs to correct for self-absorption effects in thin samples for which the infinite thickness approximation (Equation C.4) does not hold, the self-absorption correction

equation becomes the following, analogous to the section above:

$$\frac{\mu_e(\omega)}{\mu_e(\omega_0^+)} = \frac{N \cdot [\mu_t(\omega_f) \cdot c_1 + \mu_b(\omega)]}{\varepsilon \cdot \left[\mu_t(\omega_f) \cdot c_1 + \mu_e(\omega_0^+) + \mu_b(\omega_0^+)\right] \cdot \frac{1-e^{-\left(\mu_e(\omega)+\mu_b(\omega)+\mu_t(\omega_f)\cdot c_1\right)c_2}}{1-e^{-\left(\mu_e(\omega_0^+)+\mu_b(\omega_0^+)+\mu_t(\omega_f)\cdot c_1\right)c_2}} - N \cdot \mu_e(\omega_0^+)} \tag{C.8}$$

With:

- $\varepsilon = \frac{\varepsilon_f(\omega)}{\varepsilon_f(\omega_0^+)} \approx 1$
- $c_1 = \frac{sin\theta_i}{sin\theta_f}$
- $c_2 = \frac{z_s}{sin\theta_i}$

It is clear this equation cannot be solved directly as the term $\mu_e(\omega)$ is contained in both sides of the equation. To solve this equation a functional half-interval iterative method was applied which ends when the self-absorption corrected function is determined within an error of 0.05 %.

References

[1] Pfalzer, P., Urbach, J. P., Klemm, M., Horn, S., denBoer, M. L., Frenkel, A. I. & Kirkland, J. P. Elimination of self-absorption in fluorescence hard-x-ray absorption spectra. *Physical Review B* **60**, 9335–9339 (1999).

[2] Haskel, D. Fluo: Correcting xanes for self-absorption in fluorescence measurements. *Computer program and documentation [online]. Available from http://www.aps.anl.gov/xfd/people/haskel/fluo. html (accessed January 4, 2009)* (1999).

Appendix D

List of Beamtimes

2013:

- June 18 - June 21: Uranium speciation in rat bone slices and environmental sludge samples, P-06 beamline PETRA-III (DESY, Hamburg, Germany)
- June 21 - June 24: Full-field micro-XRF measurements on inclusions in rare natural diamonds, P-06 beamline PETRA-III (DESY, Hamburg, Germany), 10009686
- July 8 - July 16: Confocal micro-XANES/EXAFS investigation of high surface compressive strength, DUBBLE beamline BM26A (ESRF, Grenoble, France), BM26-01-976
- November 18 - November 25: Slcam application for XANES on geological soil samples, DUBBLE beamline BM26A (ESRF, Grenoble, France), Inhouse

2014:

- January 29 - February 1: Full-field micro-XRF measurements using the Slcam on mammalian teeth and rat, ID19 beamline (ESRF, Grenoble, France), Inhouse
- February 12 - February 17: Confocal micro-XANES investigation of FCC and zeolitic extrudate particles, DUBBLE beamline BM26A (ESRF, Grenoble, France), BM26-01-985
- July 2 - July 6: Copper K-edge grazing incidence XAFS: Study of Cu and Ag oxidation of silver alloys during sulphidation in Na2S solution, DUBBLE beamline BM26A (ESRF, Grenoble, France), BM26-01-990

- July 6 - July 8: Gold XANES on titania/gold photocatalytic materials to determine the oxidation state as a function of reduction synthesis, DUBBLE beamline BM26A (ESRF, Grenoble, France), Inhouse
- July 9 - July 14: Cu XANES on biological model organisms, DUBBLE beamline BM26A (ESRF, Grenoble, France), IH-CH-853
- July 14 - July 20: Confocal micro-XANES investigation of high surface compressive strength alkali-aluminosilicate glasses, DUBBLE beamline BM26A (ESRF, Grenoble, France), BM26-01-989
- August 25 - September 2: Ba determination in chimp and neanderthal teeth to study dietary conditions, ID19 beamline (ESRF, Grenoble, France), IH-LS-1976

2015:

- January 30 - February 3: Full-field XRF imaging to examine the 3D distribution of metals in the developing mouse brain, ID19 beamline (ESRF, Grenoble, France), IH-LS-2344
- February 10 - February 17: Construction of a confocal micro-XAS setup and its application in cultural heritage and ecotoxicological research, DUBBLE beamline BM26A (ESRF, Grenoble, France), IH-CH-918
- April 2 - April 6: Assessing the mechanisms of copper toxicity in the marine environment, DUBBLE beamline BM26A (ESRF, Grenoble, France), BM26-01-1035
- May 18 - May 24: Wavelength dispersive XRF/XAS of rare earth elements in diamond inclusions, P-06 beamline PETRA-III (DESY, Hamburg, Germany), I-20140708 EC
- June 24 - June 27: Three-dimensional confocal XAS/XRF analyses of polyphase lower mantle and transition zone inclusions trapped in ultra deep diamonds, DUBBLE beamline BM26A (ESRF, Grenoble, France), BM26-01-1036
- July 22 - July 28: 3D texture scanning on bone osteons using a novel method of white beam and energy dispersive 2D detector, XMAS beamline BM28 (ESRF, Grenoble, France), SC-4041
- October 27 - October 29: Depth resolved EXAFS experiments on ion-exchanged glasses, DUBBLE beamline BM26A (ESRF, Grenoble, France), IH-CH-1017

- November 4 - November 9: Longterm Project: (Con)focal XRF and XANES on Ming dynasty porcelain glasses, DUBBLE beamline BM26A (ESRF, Grenoble, France), BM26-01-1053

2016:

- February 20 - February 25: Development of a serie of Al-V-bimetallic metal organic frameworks, DUBBLE beamline BM26A (ESRF, Grenoble, France), BM26-01-1046
- March 21 - March 23: Test experiment for (con)focal XAFS measurements on ancient geographical map inks, DUBBLE beamline BM26A (ESRF, Grenoble, France), IH-CH-1053
- May 8 - May 14: Nondestructive REE Measurements of Carbonate and Carbonatitic Inclusions in Unique Deep Mantle Diamonds, P-06 beamline PETRA-III (DESY, Hamburg, Germany), II-20150052 EC
- June 1 - June 7: Crystal orientation in healthy and diseased bone osteons: submicron texture scanning by a one-shot energy-dispersive Laue diffraction approach, BM32 beamline (ESRF, Grenoble, France), BM32-SC-4241
- July 26 - August 1: Why teeth hit hard: Understanding the structure-function relationship in teeth by white-beam energy dispersive 3D texture determination, XMAS beamline BM28 (ESRF, Grenoble, France), SC-4249
- September 8 - September 14: Nondestructive REE Measurements of Carbonate and Carbonatitic Inclusions in Unique Deep Mantle Diamonds, P-06 beamline PETRA-III (DESY, Hamburg, Germany), II-20150052 EC

Appendix E

List of Publications

A1 Publications:

- M. N. Boone, J. Garrevoet, P. Tack, O. Scharf, D. P. Cormode, D. Van Loo, E. Pauwels, M. Dierick, L. Vincze, L. Van Hoorebeke, High spectral and spatial resolution X-ray transmission radiography and tomography using a Color X-ray Camera. *Nuclear Instruments and Methods in Physics Research Section A: Accelerators, Spectrometers, Detectors and Associated Equipment* **735**, 644-648, doi:10.1016/j.nima.2013.10.044 (2014).

- P. Tack, J. Garrevoet, S. Bauters, B. Vekemans, B. Laforce, E. Van Ranst, D. Banerjee, A. Longo, W. Bras, L. Vincze, Full-Field Fluorescence Mode Micro-XANES Imaging Using a Unique Energy Dispersive CCD Detector. *Anal. Chem.* **86**, 8791-8797, doi:10.1021/ac502016b (2014).

- J. Garrevoet, B. Vekemans, P. Tack, B. De Samber, S. Schmitz, F. E. Brenker, G. Falkenberg, L. Vincze, Methodology toward 3D micro X-ray fluorescence imaging using an energy dispersive charge-coupled device detector. *Anal. Chem.* **86**, 11826-11832, doi:10.1021/ac503410s (2014).

- M. Meire, P. Tack, K. De Keukeleere, L. Balcaen, G. Pollefeyt, F. Vanhaecke, L. Vincze, P. Van Der Voort, I. Van Driessche, P. Lommens, Gold/titania composites: An X-ray absorption spectroscopy study on the influence of the reduction method. *Spectrochimica Acta Part B: Atomic Spectroscopy* **110**, 45-50, doi:10.1016/j.sab.2015.05.007 (2015).

- L. Van de Voorde, B. Vekemans, E. Verhaeven, P. Tack, R. De Wolf, J. Garrevoet, P. Vandenabeele, L. Vincze, Analytical characterization of a new mobile X-ray fluorescence and X-ray diffraction instrument combined with a pigment identification case study. *Spectrochimica Acta Part B: Atomic Spectroscopy* **110**, 14-19, doi:10.1016/j.sab.2015.05.002 (2015).
- D. Bourgeois, B. Burt-Pichat, X. Le Goff, J. Garrevoet, P. Tack, G. Falkenberg, L. Van Hoorebeke, L. Vincze, M. A. Denecke, D. Meyer, C. Vidaud, G. Boivin, Microdistribution of uranium in bone after contamination: new insight into its mechanism of accumulation into bone tissue. *Analytical and bioanalytical chemistry* **407**, 6619-6625, doi:10.1007/s00216-015-8835-7 (2015).
- P. Tack, S. Bauters, J. C. Mauro, M. M. Smedskjaer, B. Vekemans, D. Banerjee, W. Bras, L. Vincze, Confocal depth-resolved micro-X-ray absorption spectroscopy study of chemically strengthened boroaluminosilicate glasses. *RSC Adv.* **6**, 24060-24065, doi:10.1039/C6RA01839D10.1039/c6ra01839d (2016).
- P. Tack, M. Cotte, S. Bauters, E. Brun, D. Banerjee, W. Bras, C. Ferrero, D. Delattre, V. Mocella, L. Vincze, Tracking ink composition on Herculaneum papyrus scrolls: quantification and speciation of lead by X-ray based techniques and Monte Carlo simulations. *Scientific Reports* **6**, 20763, doi:10.1038/srep20763 (2016).
- E. Brun, M. Cotte, J. Wright, M. Ruat, P. Tack, L. Vincze, C. Ferrero, D. Delattre, V. Mocella, Revealing metallic ink in Herculaneum papyri. *Proceedings of the National Academy of Sciences of the United States of America* **113**, 3751-3754, doi:10.1073/pnas.1519958113 (2016).
- G. Wang, K. Leus, S. Couck, P. Tack, H. Depauw, Y. Y. Liu, L. Vincze, J. F. Denayer, P. Van Der Voort, Enhanced gas sorption and breathing properties of the new sulfone functionalized COMOC-2 metal organic framework. *Dalton transactions* **45**, 9485-9491, doi:10.1039/c6dt01355d (2016).
- O. Schalm, A. Crabbé, P. Storme, R. Wiesinger, A. Gambirasi, E. Grieten, P. Tack, S. Bauters, C. Kleber, M. Favaro, D. Schryvers, L. Vincze, H. Terryn, A. Patelli, The corrosion process of sterling silver exposed to a Na2S solution: monitoring and characterizing the complex surface evolution using a multi-analytical approach. *Appl. Phys. A* **122**, doi:10.1007/s00339-016-0436-6 (2016).
- T. A. Grunewald, H. Rennhofer, P. Tack, J. Garrevoet, D. Wermeille, P. Thompson,

W. Bras, L. Vincze, H. C. Lichtenegger, Photon Energy Becomes the Third Dimension in Crystallographic Texture Analysis. *Angew. Chem. Int. Ed. Engl.* **55**, 1 - 6, doi:10.1002/anie.201603784 (2016).

- P. Tack, B. Vekemans, B. Laforce, J. Rudloff-Grund, W. Y. Hernández, J. Garrevoet, G. Falkenberg, F. E. Brenker, P. Van Der Voort, L. Vincze, Application towards confocal full-field microscopic X-ray absorption near edge structure spectroscopy. *Anal. Chem.* **89**, 2123−2130, doi:10.1021/acs.analchem.6b0482 (2017).

A2 Publications:

- D. Goossens, F. Mees, E. V. Ranst, P. Tack, L. Vincze, J. Poesen, Rock fragments with dark coatings in slope deposits of the Famenne region, southern Belgium. *Belgeo* **4**, doi:belgeo.revues.org/17625 (2015).